Polymer Fixed-Targets for Time-Resolved Serial Protein Crystallography at XFELs and Synchrotrons

Inauguraldissertation

zur

Erlangung der Würde eines Doktors der Philosophie
vorgelegt der
Philosophisch-Naturwissenschaftlichen Fakultät
der Universität Basel

von

Melissa Carrillo

Basel, 2024

Genehmigt von der Philosophisch-Naturwissenschaftlichen Fakultät

auf Antrag von

Erstbetreuer: Prof. Dr. Thomas R. Ward

Zweitbetreuer: Prof. Dr. Florian P. Seebeck

Externe Expertin: Prof. Dr. Arwen R. Pearson

zusätzlicher Erstbetreuer: Dr. Celestino Padeste

Basel, 30.04.2024

Prof. Dr. Marcel Mayor

Dekan

“What you learn from a life in science is the vastness of our ignorance.”

- David Eagleman (1971-present)

To my parents
Para mis papás

ACKNOWLEDGMENTS

First and foremost, I would like to thank God for all of the blessings He has given me. The opportunity to move overseas and live in Switzerland provided me the opportunity for growth in my academic, professional, and personal life. I am grateful for the abundant support, knowledge and experience obtained, mentors gained, and friendships built during my Ph.D. God is good, all the time, and all the time, God is good.

To my parents, Moms, Pops, *gracias por todos los sacrificios que han hecho por mí. Sin ustedes, no estaría donde estoy ahora. Aprecio todo el apoyo que me han brindado y por siempre estar disponibles en cualquier momento que necesitaba apoyo durante mi tiempo en Suiza.* To my brother, thank you for all of the help and support you have provided me throughout my academic career. Lastly, to my fiancé, Jesús, we managed to do what seemed to be the impossible. You were my biggest supporter through this entire journey, always motivating me to push through. Your patience, support, availability, and encouragement have been my rock, providing me with the motivation to persevere through the challenges and celebrate the triumphs. This thesis would not have been possible without the love, support, and encouragement of you, thank you.

To my supervisor, Dr. Celestino Padeste. First and foremost, I would like to express my gratitude for entrusting me with the opportunity to undertake this project. Developing these chips and engaging in numerous beamtimes has deepened my passion for protein crystallography. Thank you for your unwavering support, expertise, and guidance throughout my doctoral journey. Your mentorship, insightful feedback, and knowledge have not only shaped my research but have also enriched my academic and personal growth profoundly. I am thankful for your encouragement, mentorship, and belief in my abilities. I have grown both professionally and personally under your mentorship. Dr. John H. Beale, thank you for taking me under your wing and teaching me about crystallography and sharing your knowledge on beamlines with me. It has been a pleasure to have performed all of the Cristallina-MX commissioning beamtimes together, I have learned so much from you on how to be a great beamline scientist, provide user support, and troubleshoot during beamtimes. Dr. Tobias Weinert, thank you so much for taking the time to teach me how to process data. Your patience,

skill to teach, as well as passion does not go unnoticed. It was a pleasure working with you during beamtimes and discussing developments of the chip. I learned a lot from you. Dr. Jörg Standfuss, thank you for adopting me into your group and trusting me during the group's beamtimes. My time in your group had a large impact in my doctoral studies. Dr. Thomas R. Ward, thank you for your support and guidance during my doctoral studies. You, as well as your group, were an impactful part of my PhD, without you and your team's support, this project could have not been done. Konrad Vogelsang, you were a big part of our success with the chips during the development and production stage. Thank you for always providing a helping hand and taking the time to teach me around the process room, I learned a lot from you. It was a pleasure to have shared my experience with you. Thank you to the clean room staff for providing the assistance needed during the developmental stages of the MISP-chips. Dr. Emma Beale, thank you for your guidance, the chats we would have really grounded me during the times I needed support. Dr. Michal Kepa, you were a great mentor, I learned so much from you when preparing for beamtimes, during our night shifts, and while commissioning the chips. It was honestly a pleasure to have worked with you. Thank you to the Swiss Nano Institute (SNI 1904) for the funding that made this research project possible.

And to the team: Georgii and Quentin, thank you for having the patience to teach me how to process data and always ready to answer any questions I had, I cannot stress enough, thank you for your support! Hannah, thank you for providing support and guidance through my PhD. Tom, Matthias, and Max, it was always nice to have you around in the office to unwind when things became stressful. Fabienne, your support and mentorship cannot go unnoticed. Thank you for holding down the fort during beamtimes.

I would like to express my gratitude towards Dr. Celestino Padeste, Dr. John H. Beale and Dr. Tobias Weinert for providing guidance and proofreading my thesis manuscript during my writing stage. Additionally, I would like to acknowledge the use of AI tools as they were used for editing prose in my manuscript.

PREFACE

The present Ph.D. thesis summarizes the scientific work conducted at the Paul Scherrer Institute (PSI) in Villigen, Switzerland in collaboration with the University of Basel in Basel, Switzerland and was funded by the Swiss Nanoscience Institute (SNI). The work was conducted under the research groups of Prof. Dr. G. V. Shivashankar at PSI and Prof. Dr. T. R. Ward at the University of Basel during the years 2020-2024 under the supervision of Dr. Celestino Padeste and guidance of Dr. John H. Beale and Dr. Tobias Weinert.

This thesis centers on the study of protein crystallography. Chapter 1 provides an overview of this discipline, serving as an introductory foundation for the research showcased within this thesis. The main part of this research was to develop, produce, and establish a new sample delivery method for serial crystallography for synchrotrons and XFELs, specifically for SwissFEL's newly constructed experimental station, CristallinaMX. Cristallina MX completed its construction in 2022, with the commissioning of the Swiss-MX endstation starting in late 2022 and continuing throughout 2023. Swiss-MX, which stands for Serial WIth Solid Support MX (protein crystallography), is CristalinaMX's endstation designed for the sole purpose of performing serial protein crystallography on solid supports, also known as fixed-targets. With this said, the fixed-target developed during my PhD would become the standard fixed-target implemented at Cristallina-MX. The objective was to ensure that the fixed-target would have minimal background noise, be cost-effective during production, be user-friendly during handling, be durable, have a high reusability rate, and be able to be implemented for both serial crystallography and pump-probe serial crystallography. As a result, a new aperture-aligned, polymer based fixed-target called the MIcro-Structured Polymer based fixed-target (MISP-chip) was produced. Chapter 2, a publication on the MISP-chips, focuses on the production and usage of this fixed-target, providing details on the initial experimental results utilizing lysozyme. Once the MISP-chips became established at Swiss-MX, my focus then shifted towards developing a MISP-chip suitable for pump-probe serial crystallography experiments. Chapter 3, a manuscript accepted in IUCrJ, reveals the first study on pump-probe serial crystallography using the MISP-chips, demonstrating their versatility for serial crystallography.

A secondary aim during my doctoral studies was to investigate ligand binding interactions involving caged compounds. More specifically, this study used photocaged-biotin and a streptavidin variant called T7-SA as a model system for time-resolved serial crystallography. By utilizing optical light to control and cleave the protecting group from biotin we are able to control the initiation of the reaction. Chapter 4 describes the iterations and advancements of the photocaged biotin compounds that were created. An evaluation of the caged compounds was conducted through soaking trials and illumination tests. In this chapter, I investigate the cryogenic structure of T7-SA in its apo state, as well as when bound to biotin and biotin derivatives. Initial studies at room temperature were performed using MISP-chips at Cristallina-MX, focusing on the structural determination of a photocaged biotin compound.

Throughout my doctoral studies, I was also actively participating in serial crystallography experiments, utilizing liquid and viscous jetting techniques for sample delivery. Chapter 5 provides a comprehensive list and summary of the experiments to which I contributed.

TABLE OF CONTENTS

1

INTRODUCTION

1.1 Protein Crystallography

Protein crystallography is a method that enables the determination of the three-dimensional structure of proteins at an atomic level using X-ray diffraction of protein crystals. X-ray crystallography began in the late 19th and early 20th century with the discovery of X-rays by Max von Laue and the work of William Henry Lawrence Bragg and William Lawrence Bragg with their discovery of the relationship between the angles of incidence and diffraction of X-rays at crystal planes, also known as Bragg's Law (Bragg, 1913; Perutz, 1990). Initially, crystallography was limited to the study of small molecules but was soon applied to protein crystals. The first protein diffraction pattern was published in 1938 (Drenth et al., 1968) on papain. However, the number of atoms in protein molecules presented an increased challenge, as the phases of the diffracted beams could not be obviously interpreted. Max Ferdinand Perutz and John Cowdery Kendrew laid the foundation for understanding protein structures and their functions in protein crystallography with the solution of the structures of hemoglobin (Perutz, 1963) and myoglobin (Kendrew et al., 1958; Kendrew & Parrish, 1957). This led them to win a Nobel prize in 1962. Since then, protein crystallography has established itself as a standard method for determining the three-dimensional structures of proteins with a systematic series of steps including protein crystallization, data collection, data reduction and phase determination, model building and refinement (Figure 1.1). Due to these developments, X-ray crystallography continues to play a pivotal role in advancing our understanding of biological macromolecules, facilitating breakthroughs in structural biology and drug discovery.

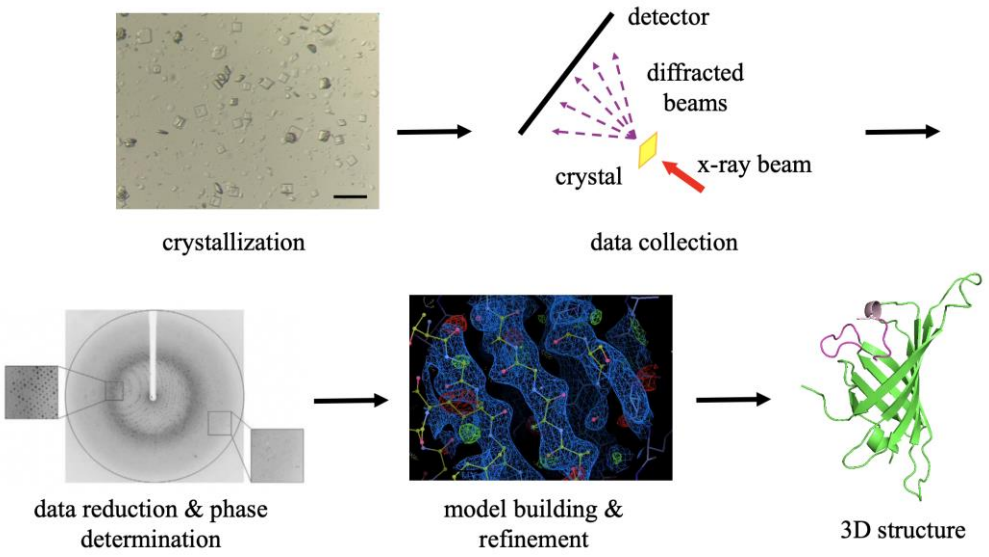

Figure 1.1: Overview of the crystallographic process of obtaining a protein structure from protein crystals*. The protein is crystallized (scalebar represents 100μm) then exposed to an X-ray source. Diffraction patterns are collected and reduced, phases are solved, and an electron density map is constructed. Amino acids are placed in the right location and orientation to construct the final 3D structure.*

1.2 Protein Crystals

The initial step in protein crystallography is to obtain a highly purified, monodispersed protein sample. This is commonly done through the expression of the protein of interest recombinantly in *Escherichia coli* or *Saccharomyces cerevisiae*, although some protein can be purified directly from their source (Hansen et al., 1999; Safo & Abraham, 2003). Expression cells are then lysed, and the cell pellet removed by centrifugation. The protein remaining in the supernatant solution is purified *via* chromatography (Hunte et al., 2003; Kim et al., 2011; Labrou, 2014). Once purified, the protein of interest can be crystallized, often requiring many optimization steps. Protein crystals are composed of protein molecules arranged in a highly ordered three-dimensional lattice constructed by translating a common unit in x, y, and z. The protein molecules are held together by interactions between neighboring proteins such as hydrogen bonding, polar interactions, salt bridges and hydrophobic interactions. The order within crystal domains with respect to each other will be affected by imperfections or variations

in the packing of protein molecules within the lattice and this will ultimately have an effect on the broadness of the diffraction peaks and the final resolution attained.

For a protein to undergo crystallization it must undergo a phase transition, from solution to a crystalline phase, rather than an amorphous solid (precipitate). Parameters such as protein concentration, precipitant, temperatures, or pH are often varied to find the best conditions for crystallization. The relationship between the protein, a precipitant, and water can be visualized through the crystallization phase diagram (Figure 1.2). The diagram depicts four regions that describe the thermodynamic state of the protein, precipitant and water mixture (Beale et al., 2019; Chayen, 2005; Chayen & Saridakis, 2008; Ducruix & Giegé, 1999). The zones are described as follows:

1. The undersaturation zone, where the protein and precipitant concentration is low enough such that both can be fully dissolved in water. The limit of this zone is defined by the solubility line.
2. The supersaturation region, comprising the metastable, nucleation and precipitation zone. Past the solubility line the protein-precipitant mixture becomes thermodynamically unstable and will want to separate into a solid and solution phase.
    a. In the metastable zone, the solution is thermodynamically unstable. Crystal growth can occur, but nucleation will not happen independently.
    b. The nucleation zone, where the protein will begin to precipitate from the solution but in an ordered manner such that spontaneous nucleation can occur and enable further crystal growth.

c. In the precipitation zone, the protein precipitates but in an amorphous manner, although sometimes crystals can form after some amorphous protein has precipitated.

In order for crystallization to occur, the protein must reach the nucleation zone and drop down to the metastable zone for growth (Beale & Marsh, 2021).

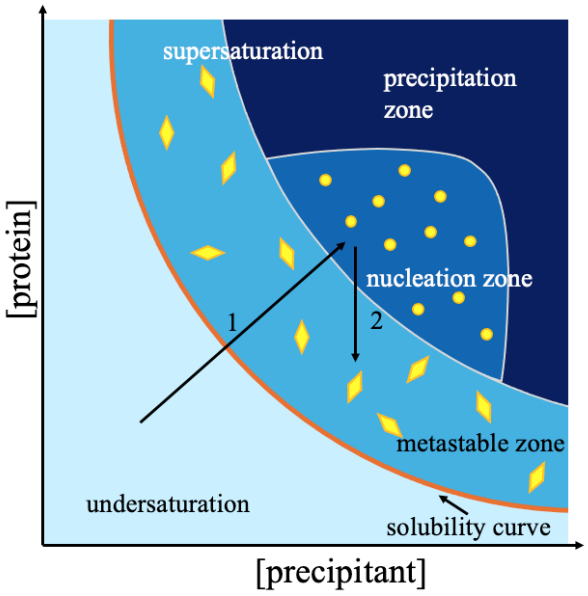

Figure 1.2: Phase diagram of a protein crystallization experiment. *Arrows 1 and 2 indicate the trajectory a protein will follow across the phase diagram to ultimately result in the formation of a mature crystal through vapor diffusion. Arrow 2 indicates the trajectory a protein would follow in the phase diagram to form micro crystals through batch crystallization. Important to note that the conditions may start anywhere from the undersaturation zone, metastable zone, or nucleation zone. As long as they pass the solubility line, reach the nucleation zone, and drop to the metastable zone, crystals will most likely develop.*

There are several crystallization methods available, but by far the most commonly used is vapor diffusion. Vapor diffusion is typically performed in two varieties, hanging drop, and sitting drop, depending on whether the crystallization droplet is placed on an elevated post or suspended under the lid of the chamber (Figure 1.3A). In a vapor diffusion experiment a concentration difference between a reservoir solution and precipitant-protein mixture is exploited to drive the protein crystallization. This is practically done by filling up a reservoir

with a potential crystallization solution (also known as mother liquor) which typically is composed of a combination of a buffer, salt, and high-molecular weight poly-ethylene glycol. A droplet of the protein and a precipitant solution are mixed and sealed within a chamber with the reservoir. As soon as the system is sealed, the vapor phase above the solution begins to equilibrate. This equilibration typically causes a net transfer of water from the crystallization droplet to the reservoir until the droplet reaches a point where the osmolarity of the drop and precipitant are equal. As the system equilibrates, the concentration of the protein and precipitant in the protein-precipitant mixture will gradually increase and supersaturate these components. In the phase diagram this can be visualized by the movement of the droplet conditions into the metastable region across the solubility line and ultimately into the nucleation zone (Figure 1.2: arrow 1). The solution is now in a thermodynamically unstable state and will want to separate into a solid and solution phase (Rupp, 2015). The crystallization is successful if spontaneous nucleation occurs at this point. Once nucleates have formed and as more protein comes out of solution, the concentration of protein in the solution drops and the crystal grows until a stable thermodynamic equilibrium at the solubility line is reached (Figure 1.2: arrow 2).

In batch crystallization, the concentrated protein and precipitant solution are mixed directly together. The idea is to place the mixture straight into its nucleation zone. In optimized systems nucleation usually starts immediately after mixing, followed by crystal growth (Figure 1.2: arrow 2) (Beale et al., 2019; Dessau & Modis, 2011; Nam, 2023; Stevens, 2000). Batch crystallization typically enables the use of larger volumes compared to vapor diffusion systems, e.g. 1.5 mL in centrifuge tubes or 100 μL in plate wells and may need constant agitation such as using a rotational or rocking platform (Figure 1.3B).

A.

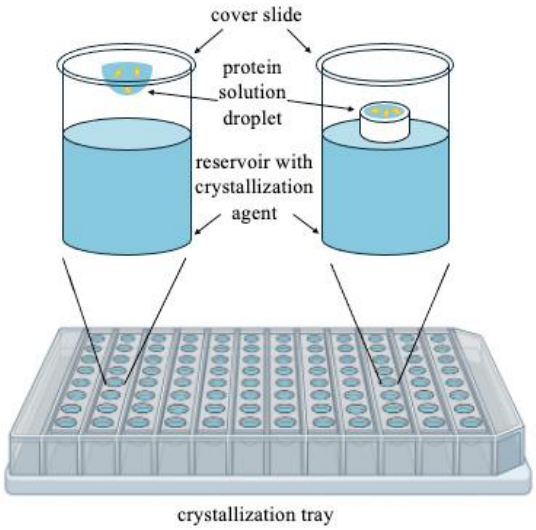

B.

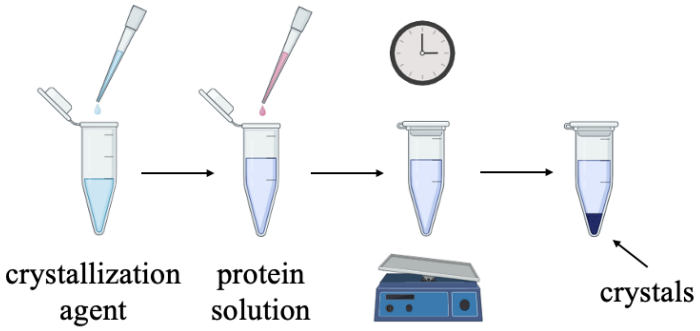

Figure 1.3: Two methods to crystallize protein. *(A.) Illustration of hanging drop and sitting drop crystallization. Every well of the crystallization tray contains a protein solution droplet and a reservoir with crystallization agent and is sealed with a cover slide. (B.) Illustration of batch crystallization. Crystallization agent is placed first into a centrifuge tube, then the concentrated protein solution. It is mixed and after some time micro-crystals form. (Figures made with Biorender).*

The selection of vapor diffusion or batch crystallization will vary depending on what experimental stage, type of experiment, or facility is required. Vapor diffusion tends to produce larger crystals, suitable for rotational cryo-crystallography. Moreover, crystallization trays of vapor diffusion serve as a means to finely optimize crystallization conditions. Once crystallization conditions are optimized and crystals are grown in the proper shape, size, and space group, batch crystallization can be performed if one needs a large number of crystals; particularly smaller crystals. An option to optimize batch crystallization involves seeding, which introduces a small amount of pre-formed crushed crystals into a supersaturated solution.

This provides a template for the formation of additional crystals, promoting the growth of a larger and more uniform crystal structure (Zhang et al., 2021). In contrast to vapor diffusion, batch crystallization can more easily produce micro-crystals in large quantities. Such crystals are typically required for room temperature studies using serial crystallography.

1.3 X-ray diffraction of protein crystals

A unit-cell represents the smallest repeatable translatable unit of a crystal. The unit cell, in many cases and depending on the crystal symmetry, can be further reduced to asymmetry units (Figure 1.4) related by rotational symmetry operations within the unit-cell. As a protein forms into a crystal, its unit cells will create a crystal lattice and extend itself.

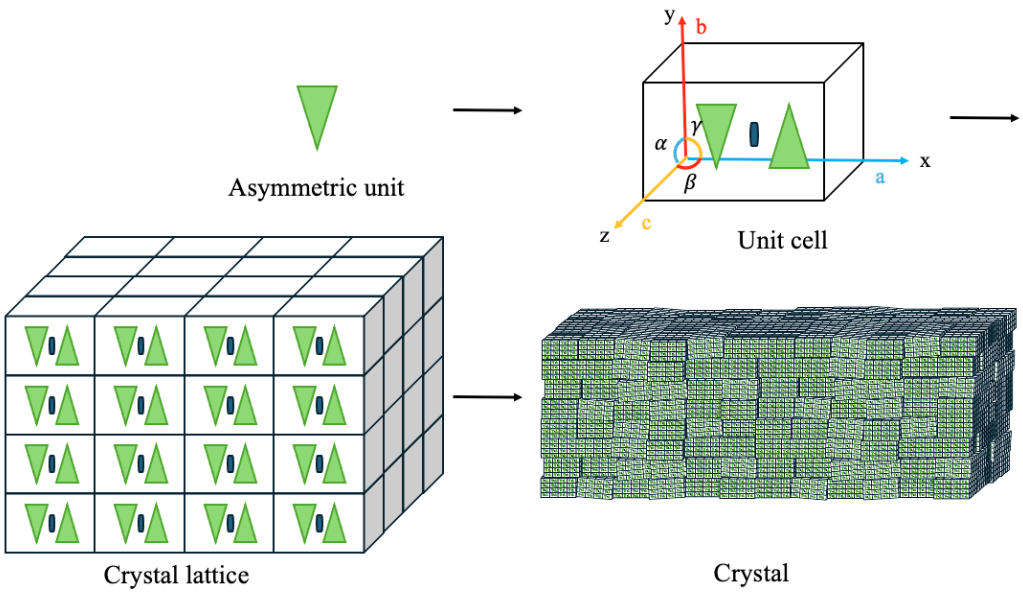

Figure 1.4: Formation of a crystal from its asymmetric unit to its unit cell to the crystal lattice. The crystal lattice makes up the crystal, but clusters of the crystal lattice may align in a non-uniform manner, demonstrated in the last section, known as the mosaicity of the crystal.

A unit cell's geometric arrangement determines the crystal's symmetry. The cell constants and angles, depicted in Figure 1.4 and Table 1.1, define one of the seven primitive crystal symmetries (Table 1.1).

Table 1.1: The seven crystal symmetries.

Name	Cell Constants	Angles
Cubic	$a = b = c$	$\alpha = \beta = \gamma = 90°$
Tetragonal	$a = b \neq c$	$\alpha = \beta = \gamma = 90°$
Orthorhombic	$a \neq b \neq c$	$\alpha = \beta = \gamma = 90°$
Rhombohedral	$a = b = c$	$\alpha = \beta = \gamma \neq 90°$
Hexagonal	$a = b = c$	$\alpha = \beta = 90°$ $\gamma = 120°$
Monoclinic	$a \neq b \neq c$	$\alpha = \beta = 90°$ $\gamma \neq 90°$
Triclinic	$a \neq b \neq c$	$\alpha \neq \beta \neq \gamma \neq 90°$

Once crystals are obtained, they can be exposed to X-rays. The vast majority of X-rays delivered to the crystal will pass straight through. Some will be absorbed, but some will also scatter elastically from the electrons they encounter. If these electrons are arranged in an ordered matrix, like in a crystal, their scattered waves will interfere and give rise to constructive and destructive patterns. The Braggs, a father and son duo, formulated the Bragg's Law (1) which gives the relationship between the incident and scattered waves and the distance between adjacent crystal lattice planes. It says that **only** an integer number of wavelengths (λ), with an interplanar spacing (d) and within a lattice at angle (θ) with respect to the incident beam will give rise to constructive interference and lead to a diffraction spot (Figure 1.5, eq. 1.1).

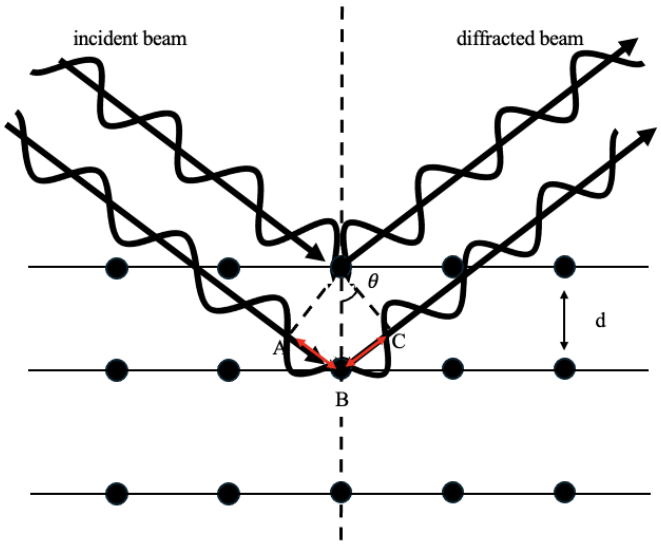

Figure 1.5: Bragg's law. *Bragg's Law of X-ray diffraction defines the relationship between the angle of incidence of a wave with crystal lattice, the wavelength of the light and the resulting constructive interference of the scattered waves. Constructive interference occurs when the path difference between the scattered waves from neighboring planes with distance (d) overlap and their amplitudes reinforce each other, producing diffraction patterns.*

$$AB + BC = 2d \sin\theta$$

$$\boldsymbol{2dsin\theta = n\lambda} \qquad \textbf{eq. (1.1)}$$

In the 1920s, Paul Peter Ewald constructed the Ewald's sphere, which provides an enhanced three-dimensional model for representing the conditions of diffraction (Figure 1.6, Eq. 1.1). Ewald's sphere construction is a representation of reciprocal space where the origin (O) (where the wave leaves the sphere) is on the surface of the sphere. Each wave resulting from constructive interference in reciprocal space from atoms in real space can be represented as a dot indexed using Miller indicies (*h*,*k*,*l*). The *h*,*k*,*l* lengths are determined by the unit cell of the crystal in real space.

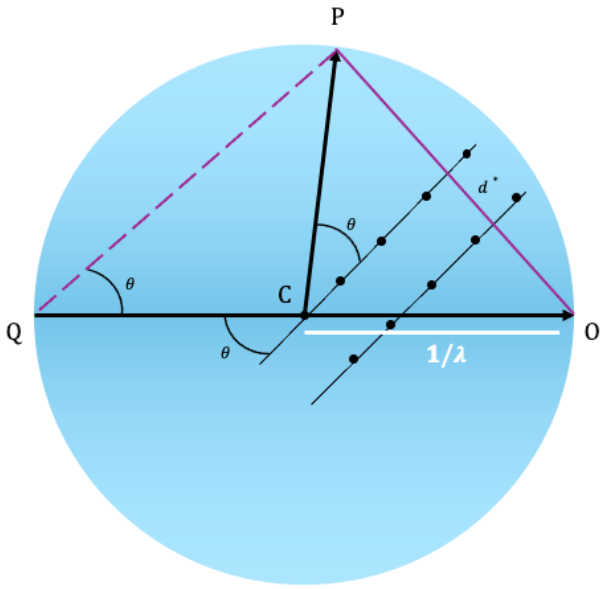

Figure 1.6: A representation of Ewald's sphere. *The beam passes through the origin of the reciprocal lattice (O) and interacts with an atom (C) and the origin (O). This in turn causes the diffracted beam (P) to leave the sphere. Vector PO becomes the structure factor* $\boldsymbol{F_{hkl}}$*. Through trigonometry, θ can be calculated. Ewald's sphere allows to geometrically represent and analyze the reciprocal lattice of a crystal.*

$$d^* = \frac{1}{d}$$

$$\sin\theta = \frac{OP}{OQ}$$

$$\sin\theta = \frac{\left(\frac{1}{d}\right)}{\frac{2}{\lambda}}$$

$$\sin\theta = \frac{\lambda}{2d}$$

$$\boldsymbol{2dsin\theta = n\lambda} \qquad \textbf{eq. (1.1)}$$

Now, to further understand diffraction and the significance of the X-ray wavelength, we can look at Figure 1.7. Assuming that the crystal has a collection of atoms evenly spaced (intersections of orange grids) the reflections of it would also be a collection of points in the reciprocal space. When an Ewald's sphere is drawn within the crystal lattice and rotated 360 degrees at point O, the limiting sphere can then construct. Rotating the sphere of reflections 360 degrees in the diagram mimics data collection during cryo-crystallography. Any reflections beyond this sphere are not accessible with this wavelength which brings awareness to the role

of the wavelength. A larger wavelength would decrease the diameter of both the limiting sphere and the sphere of reflections, minimizing the number of reflections. On the contrary, a shorter wavelength would increase the spheres and increase the number of reflections.

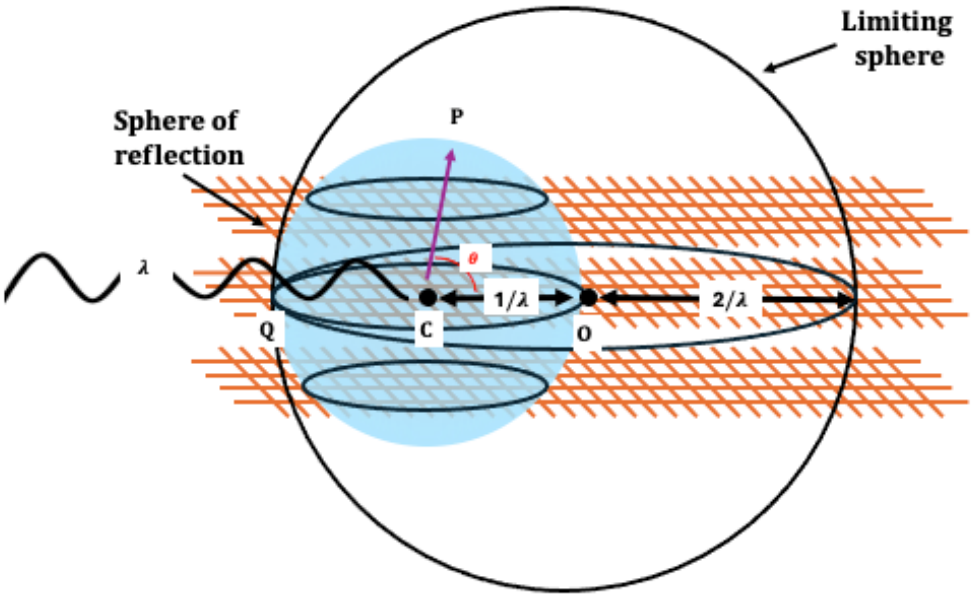

Figure 1.7: A representation of the limiting sphere. *The beam passes through the origin of the reciprocal lattice (O) and interacts with an atom (C) and the origin (O). This in turn causes the diffracted beam (P) to leave the sphere. Through trigonometry, θ can be calculated. Ewald's sphere allows to geometrically represent and analyze the reciprocal lattice of a crystal.*

1.4 Data Processing

During a data collection, these diffraction patterns are recorded. The key information for reconstructing the real-space unit cell volume (x,y,z) are the spot locations in reciprocal space (h,k,l) and their intensities. The data collected from the experiment goes through an analyzes that can be divided into six major stages (Figure 1.8).

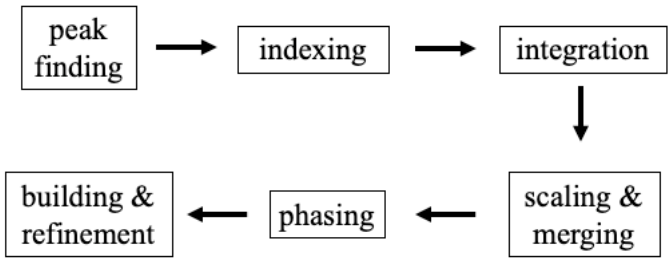

Figure 1.8: The six main stages for data reduction and processing.

Peak finding and indexing. Typically, during a cryo-crystallographic data collection, the diffraction peaks are recorded from a single rotating crystal. A dataset of images from this crystal will consist of consecutive rotating slices of the reciprocal space lattice. In serial crystallography, a large number of images are recorded and saved during a beamtime in which a smaller subset is likely to contain a crystal diffraction patterns. In order to distinguish images of crystal diffraction patterns from either empty shots or diffraction patterns, potential Bragg peaks are identified (Hadian-Jazi et al., 2017; Powell, 2017, 2021) by looking for a small number of strong reflections with pixel intensities above a background threshold. This is followed by indexing, which determines the space group, crystal orientation, and unit cell dimensions from the identified diffraction spots. This step also assigns each diffraction spot an index value (*hkl*) in reciprocal space corresponding to the crystal planes in real space.

Peak integration. Once the patterns are indexed and known, the intensity of the spots are measured as the number of photons recorded in each individual pixel. To identify the intensities of a peak, the photons in the pixels are compared to neighboring pixels in order to differentiate the background to the peak. This then draws the peak's circumference and classifies the signal to background. The final results from the integration step yields a three-dimensional array of *hkl*s with corresponding intensities and measurement error (σ). Since the intensities are the only information recorded, the phase information is lost. This loss means that scattering phase information can only be estimated/calculated rather than directly measured.

Scaling and merging. Scaling focuses on correcting and adjusting the diffraction spot intensities difference found across all collected images in order to assure that independent varying factors such as crystal sizes, orientations, exposure time or beam intensities, of all data can be on a consistent scale. Afterwards, all the intensities recorded over the entire dataset are then merged, depending on the symmetry, into a single coherent data set (Powell, 2017, 2021).

Phasing. The Fourier transform eq. (1.3) gives the relationship between the scattered structure factors eq. (1.2) and the electron density.

$$\boldsymbol{F = |F_{hkl}|e^{-2\pi\phi}} \qquad \textbf{eq. (2)}$$

$$\boldsymbol{\rho(x,y,z) = \frac{1}{V}\sum_h \sum_k \sum_l |F_{hkl}| e^{-2\pi i\phi(hk+ky+lz)}} \qquad \textbf{eq. (3)}$$

Where $\rho(x, y, z)$ is the electron density at a given point in space with coordinates (x, y, z), V is the volume of the unit cell, $|F_{hkl}|$ is the amplitudes, and ϕ are the phases of each reflection. Since crystallographic data acquisition only records the intensities of the diffracted beams, the phase information, which is an essential part for determining the electron density, is lost, causing the so-called phase problem. There are three common methods for overcoming this barrier: heavy atom method (also known as isomorphous replacement), anomalous scattering (also known as anomalous dispersion) and molecular replacement. These three options helps resolve the phasing problem.

Isomorphous replacement is a method that obtains the phase by introducing one or a small number of atoms to identical sites in all unit cells of the crystal. These atoms need to be "heavy atoms", or more precisely, strong diffractors with significantly higher atomic number than most of the other atoms in the protein (C, O, N, S and H). It is often done by soaking a few crystals with a heavy atom solution to produce heavy atom derivatives of the sample. This

allows for diffraction patterns with different intensity distributions to be recorded, which is then used for initial estimates of phases using the relationship of the structure factors eq. (1.4).

$$\boldsymbol{F_{PH} = F_P + F_H} \qquad \textbf{eq. (1.4)}$$

Where F_{PH} is the structure factor of the corresponding heavy atom derivate reflection, F_P is the structure factor of the native reflection, and F_H is the structure factor for the heavy atom. Techniques such as Single Isomorphous Replacement (SIR) and Multiple Isomorphous Replacement (MIR) solve the phase ambiguity from heavy atom derivatives by using either single or multiple heavy atoms bound at a different site in the molecule. Once having two different heavy atoms bound onto the molecule, the phases of F_H would both be the same, providing the same information for both phase determinations. At times there may even be a need to use more than two heavy atoms bound to the protein molecule.

Anomalous scattering uses the heavy atoms' capacity to absorb specific wavelengths of the X-ray source. More specifically, these elements both absorb and emit X-rays. However, when the wavelengths reach right below their characteristic emission wavelengths the absorption drops sharply. This sudden drop in absorption is called an absorption edge, a point at which an element will exhibit anomalous scattering (Rhodes, 2010) and can be easily recorded for heavy atoms. Techniques such as single-wavelength anomalous diffraction (SAD) and multi-wavelength anomalous diffraction (MAD) use either single- or multi- wavelengths to resolve the phase issue.

The last method to solve the phase problem is molecular replacement, where the phases of a known structure that is similar to the protein of interest are used for initial estimates. If the phasing model and the target model of interest are isomorphous, *i.e.*, their structures and unit cells are very similar, then the phases can be calculated by simply adjusting the Fourier sum

equation eq. (1.5) where F_{hkl}^{target} is derived from the intensities of the target model of interest and $\alpha_{hkl}^{\prime model}$ are the phase of the model.

$$\boldsymbol{\rho(x,y,z) = \frac{1}{V}\sum_h \sum_k \sum_l \left|F_{hkl}^{target}\right| e^{-2\pi i(hk+ky+lz-\alpha_{hkl}^{\prime model})}} \qquad \textbf{eq. (1.5)}$$

However, if the phasing model and the target model of interest are not isomorphous, due to difference in orientation and position of both models, phase calculation must be done by superimposing the structure of the model onto the structure of the target model of interest' unit cell. After such calculation the phases can be used for the target model of interest.

Model building and refinement. Once the phases have been determined, the electron density of the unit-cell contents can be calculated eq. (1.3) and used to build the model. However, since the phases are estimates, first electron density maps are usually imprecise. This can be improved by an iterative process (at times known as bootstrapping) where features can be removed or integrated into the phasing model for subsequent maps. If needed, once the map has been improved to the extent that atoms can be placed and located, the atoms are integrated into the model where new structure factors are then calculated with atomic structure factors rather than electron densities eq. (1.6):

$$\boldsymbol{F_{hkl} = \sum_{j=1}^{n} f_j e^{2\pi i(hx_j+ky_j+lz_j)}} \qquad \textbf{eq. (1.6)}$$

After a few iterations, the model becomes more detailed which improves the phases, which in return improves the model.

1.5 Synchrotrons & synchrotron crystallography

X-ray diffraction experiments of proteins are most commonly performed at synchrotron light sources due to their versatile use and availability with over 60 facilities around the world. The first successful diffraction experiment of cryo-cooled protein-crystals at a synchrotron was

conducted in 1970, but the method became a popular and well-established by the 1990s (Haas & Rossmann, 1970; Haas, 2020). Since the beginning, four generations of synchrotrons have been developed. The first-generation of synchrotrons, constructed in the 1940s-1950s, were primarily built, and used for particle and nuclear physics and had relatively low energy compared the modern synchrotrons. Synchrotron radiation, initially observed as parasitic radiation (Robinson & Booklet, 2001) in the storage rings, emitted from highly accelerated electrons travelling through the bending ring magnets, was later recognized as a potent source of X-rays, leading to the classification of synchrotron sources. This first generation of synchrotron sources, produced intense X-ray beams, fundamental for advancements in structural biology such as Ada Yonath's Nobel Prize-winning work on the ribosome (Schluenzen et al., 2000), although the high intensity necessitated innovative cooling methods to mitigate radiation damage. Advancements in technology have propelled synchrotrons into their fourth generation. Most recently the MAX IV laboratory in Sweden (Eriksson et al., 2016) finished being constructed, being one of the first fourth generation synchrotrons to be built, improving beam quality, coherence and brightness allowing for time-resolved serial crystallography to be performed with a resolution time in the microsecond range.

The principle of a synchrotron can be broken down into six stages (Figure 1.9), starting with generating electrons through an electron gun (Figure 1.9-1). Within the electron gun, a high electric voltage of approximately 200,000 volts applied to a heated metal cathode (most commonly copper, molybdenum or chromium) under vacuum. This provides the electrons in the metal cathode enough thermal energy to “evaporate” from the surface of the cathode and escape through thermionic emission, which produces pulses of electrons. A nearby screen provides a brief but intense positive charge, which draws the electrons away from the cathode. Through applied electric fields, the electrons collected from the electron gun undergo acceleration towards the linear accelerator, also known as the linac.

In the linac (Figure 1.9-2), the electrons produced in the electron gun gain a speed of upwards to 299,792 km/s (186,282 miles/s), nearly the speed of light. In the linac, the charged particles are placed in a magnetic field, undergoing a force as dictated by the Lorentz force law eq. (1.8) where **q** is the electron charge, $\vec{E}$ is the electric filed, $\vec{v}$ is the particle velocity, and $\vec{B}$ is the magnetic field.

$$\vec{F} = q\vec{E} + q\vec{v} \times \vec{B} \qquad \textbf{Eq. (1.8)}$$

As the electrons enter the vacuum chamber of the linac (to avoid any collisions with gas molecules), the electrons enter a series of radio frequent (RF) cavities driven by a source of voltage with alternating electric fields (positive or negative) in a timed manner. This transfer of energy to the electrons accelerates them along the linac. It is important to note that due to this specific type of acceleration from the alternative electric fields, the electrons are forced to travel as bunches of electrons (Edwards & Syphers, 2008).

The electrons are then ejected into the booster ring (Figure 1.9-3) where they circulate with the help of bending electromagnets and increase their kinetic energy with RF cavities until they reach the desired energy. Once at the desirable speed, the electrons then move to the storage ring (Figure 1.9-4), where they pass through bending magnets to keep them rotating in the storage ring. Magnetic fields such as undulators and wigglers are placed in specific locations throughout the storage as well. As electrons pass through an undulator they pass through alternating polar magnetic field causing them to undergo an oscillatory motion. This results in the emission of highly focused, intense, tunable wavelengths. The electrons passing through a wiggler, which has a similar setup as the undulator, will emit a wider range of wavelengths. The bending magnets are essential for bending the trajectory of the electrons to circle in the storage ring, leading to further photon emission.

The photons are emitted tangentially to the electron path towards the experimental stations as illustrated in Figure 1.9-5. Within this trajectory, they traverse a segment known as optics, enabling the selection of particular wavelengths and the precise focusing of the photon beam which is then transmitted to the experimental hutch (Figure 1.9-6) for interaction with the sample and data collection.

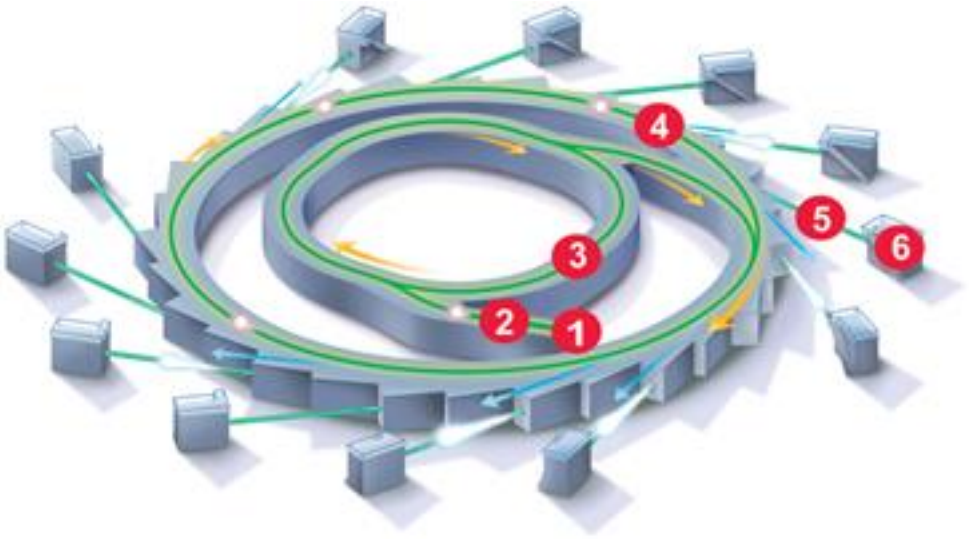
4
5
6
3
2
1

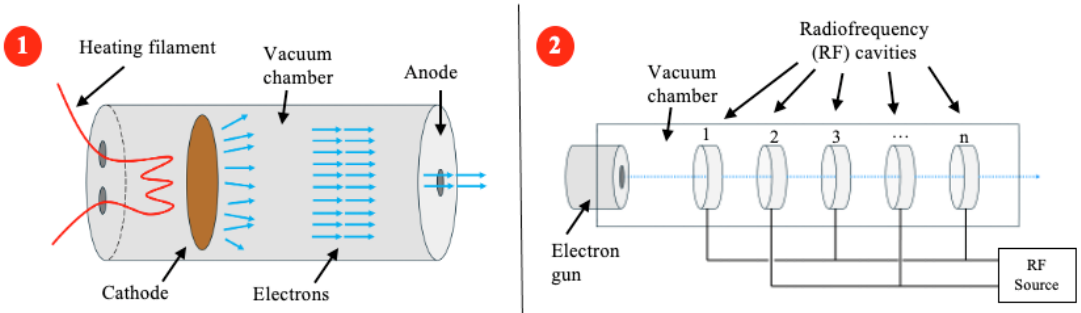
1
Heating filament
Vacuum chamber
Anode
Cathode
Electrons

2
Radiofrequency (RF) cavities
Vacuum chamber
1
2
3
⋯
n
Electron gun
RF Source

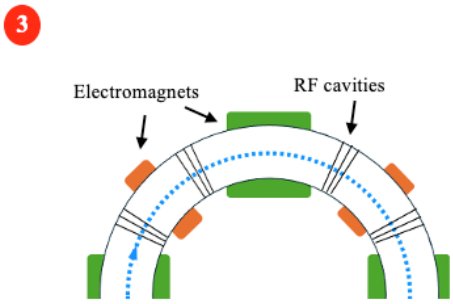
3
Electromagnets
RF cavities

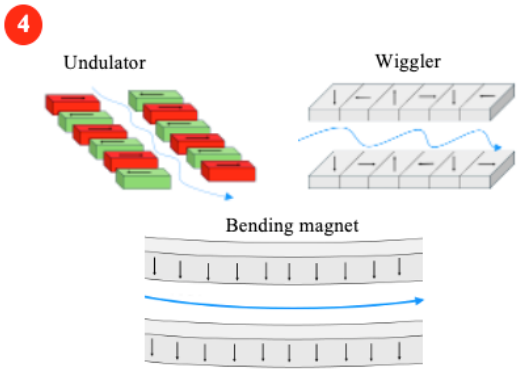
4
Undulator
Wiggler
Bending magnet

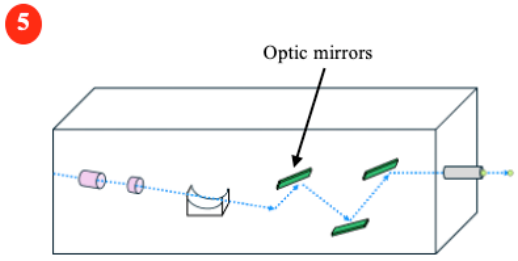
5
Optic mirrors

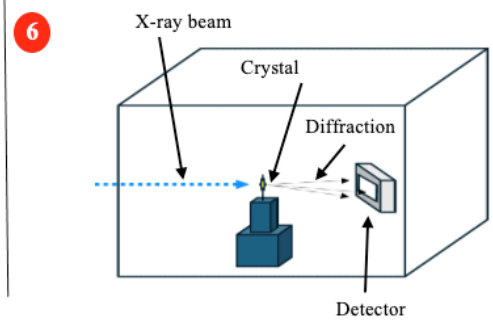
6
X-ray beam
Crystal
Diffraction
Detector

Figure 1.9. An explanation of the functioning principles of synchrotrons. *Top figure: overview of a synchrotron. (Top figure of a synchrotron was taken from* http://archive.synchrotron.org.au/synchrotron-science/how-is-synchrotron-light-created.) *Synchrotrons can be broken into six sections to produce x-ray beams for data collection. (1) Electrons are first generated in the electron gun where a heating filament heats a metal cathode for the electrons to evaporate. The anode then pulls the electrons away from the metal cathode and pulls them into (2) the linear accelerator (linac). The linac accelerates the electrons in bunches, due to electromagnetic forces caused by the radiofrequency (RF) cavities. The electrons are then emitted into (3) the booster ring where the electron bunches are further accelerated to nearly the speed of light with electromagnets and RF cavities. Once accelerated, the electron bunched then travel to (4) the storage ring where they pass through bending magnets to maintain their trajectory, encountering undulators and wigglers which induce oscillatory motions, resulting in the emission of highly focused, intense, and tunable wavelengths. The bending magnets further bend their trajectory, leading to additional photon emission. The photon bunches are emitted towards the (5) beamline where they go through a series of optical lenses to filter out wavelengths and focus the beam to a specific size. Finally, the x-rays reach the (6) experimental station where experiments are conducted.*

1.6 Cryogenic (Cryo)-crystallography

Protein crystallography is most commonly conducted at synchrotrons where the prevalent technique used is cryogenic crystallography. This technique consists of rapidly flash cooling the protein crystal to ~100K in order to avoid ice nucleation on the sample. This results in a rigid glass that encases the protein crystal (Rodgers, 1994) thus allowing for significant reduction of radiation damage during data collection and preserving crystal integrity as well. The sample is mounted onto a goniometer and is rotated across the X-ray beam to collect a rotational series dataset. Although this method is commonly used, it is unsuitable for protein time-resolved structural studies as the cryo temperatures and inhibit any movement within the protein molecules.

1.7 XFELs, serial crystallography and pump-probe methods

The first hard X-ray free electron laser (XFEL) was built in 2009 in California, USA and was called the Linac Coherent Light source (LCLS) (Emma et al., 2010). XFELs possess the capability to produce femtosecond pulses at specific wavelengths. They provide repetition rates of a few hertz to hundreds of kilohertz, with pulse energies, depending on the facility and photon energy, in the millijoule range. Importantly, XFELs can produce highly focused x-ray

beams with spot sizes to sub-micron range to study sub-micron particles (Altarelli, 2011; Huang et al., 2021; Kang et al., 2017).

XFELs are composed of five mayor sections (Figure 1.10). Like in synchrotrons, XFELs produce their electrons through an electron gun. These electrons then pass through a linac, with lengths of 0.5-3km, where they gain speeds upward to nearly the speed of light. As electrons pass through undulators, they emit X-ray radiation as a result of their oscillatory motion induced by the magnetic field, which subsequently triggers additional emissions from other electrons, leading to the amplification of X-ray pulses. This lasing effect in XFELs generates tightly focused and powerful X-ray beams, possessing characteristics well-suited for various scientific investigations, such as exploring atomic and molecular structures, studying ultrafast dynamics, and advancing materials science. The electrons are then pulled away into the dump and the X-ray light continues through an optics section and into the experimental hutch for data collection.

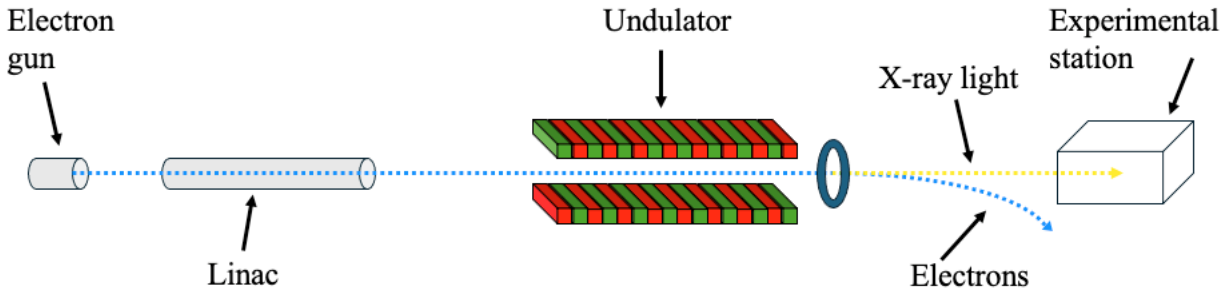

Figure 1.10. A breakdown of XFELs. *X-ray free electron lasers are composed similarly to synchrotrons containing elements such as electron guns, linacs and undulators to help speed electrons to nearly the speed of light with high precision, ultimately having the X-ray light of the electrons arrive in the experimental station for their usage in studies.*

In an effort to overcome the constraints associated with cryo-crystallography and to expand the capabilities of protein crystallography, a proposal was submitted in the year 2000 to use the first soon to be constructed XFEL for protein crystallography. In the proposal, a relatively new data collection method called serial crystallography (SX) (Figure 1.11) was

proposed in order to take advantage of the XFEL beam properties. Due to the XFEL's ultra-short and intense X-ray pulses, serial crystallography only allows for single diffraction patterns to be collected on individual crystals, as the crystal is immediately destroyed by the laser pulse. Interestingly, it was shown that diffraction takes place before the onset of radiation damage, an effect labeled as "diffraction before destruction" (Chapman et al., 2014; Doerr, 2011). Due to this phenomenon, as the name implies, a series of fresh crystals (usually several ten thousands) must be delivered across the beam in order to collect a full data set (Barends et al., 2022).

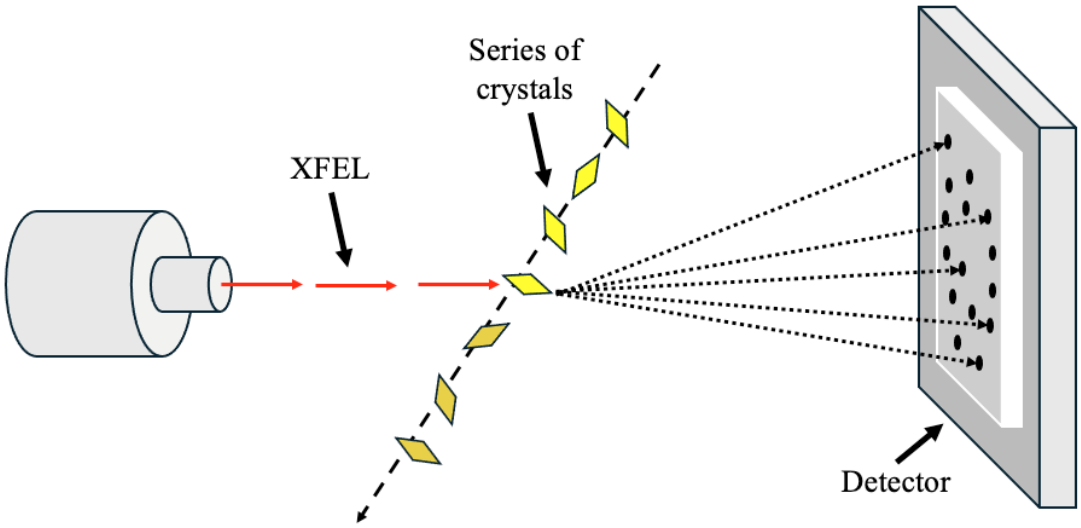

Figure 1.11: Illustration of serial crystallography at an XFEL. *A series of crystals are individually exposed to the X-ray beam where data is collected at room temperature before undergoing radiation damage. The sample delivery method varies depending on sample, sample size, sample quantity, experimental set up and facility.*

The establishment of serial crystallography at XFELs allows for microcrystals to be studied at room temperature, which enables time-resolved measurements by capturing snapshots of dynamic processes at atomic level in molecules over time after a triggering event. Time-resolved serial crystallography (TR-SX) can be conducted through different triggering methods such as temperature change, mixing of solutions or, most commonly, through photo-activation (Carrillo et al., 2021; Schmidt, 2013; Alexander M Wolff et al., 2023; Wranik, Weinert, Slavov, Masini, Furrer, Gaillard, Gioia, Ferrarotti, James, & Glover, 2023). The term

pump-probe is used for the two-step technique that allows for TR-SX studies of light reacting systems. The “pump” pulse is provided by an optical laser that is pulsed at a crystal sample to initiate a change or excitement in a photodynamic sample. This is followed by a “probe” pulse of the XFEL beam, which is pulsed at the same crystal sample at a specific time delay, in order to measure the consequences of the pump pulse. This allows to capture TR-SX data on photodynamic samples (Nango et al., 2019; Suraj Pandey et al., 2020). While serial crystallography was first developed at XFELs, its utilization is increasingly expanding to third and fourth-generation synchrotron facilities.

1.8 Photoswitches and photocages for pump-probe measurements

Substantial focus has recently been directed towards ligand binding in protein crystallography due to its significance in providing functional insights, for drug discoveries and designs, and for enzyme catalysis and allosteric regulation. One method to control and trigger the onset of ligand binding is the usage of light. This is relatively straight forward when the proteins themselves incorporate a photoactive moiety such as the rhodopsins, phytochromes and florescent proteins (Carrillo et al., 2021; Coquelle et al., 2018; Panneels et al., 2015; Sorigué et al., 2021) but causes challenges for non-photosensitive proteins. To broaden the scope of light activation in non-photoactive samples for TR-SX studies, photoswitches and photocages have been engineered to control the binding activities with specific optical wavelengths. Photoswitches are often derivatives of azobenzene (Ankenbruck et al., 2018; Bandara & Burdette, 2012) or stilbenes (Ji et al., 2020; Villarón & Wezenberg, 2020) in which isomerization takes places respectively around the N=N or C=C double bond between two phenyl groups.

Photocages offer an alternative method, enabling the selective removal of a photosensitive protecting group from a molecule when exposed to particular wavelengths of

light (Li et al., 2023). More specifically, photocages are composed of photolabile protecting groups covalently bound to a protein or ligand, causing the system to become inactive (D. C. Monteiro et al., 2021). The system can be activated when the photocage is photoexcited with a specific wavelength of light causing the photocage to cleave off, freeing the system. This provides scientists with control over the onset of specific binding interactions. However, there a several factors to consider when designing a suitable photocaged molecule. Factors such as quantum yield (ϕ), solubility, cleavage rate (s^{-1}), molar extinction coefficient ε_{max} ($mM^{-1}cm^{-1}$), and wavelength λ_{max} (nm) are critical for specific proteins, samples, and facility limitations on pump-probe TR-SX studies (D. C. F. Monteiro et al., 2021). These factors rely on the diverse scaffolds that constitute photocages. The primary scaffolds for photocaging include coumarin derivatives, *ortho*-nitrobenzyl derivatives, *para*-hydroxyphenyls, and nitrodibenzofurans (Figure 1.12).

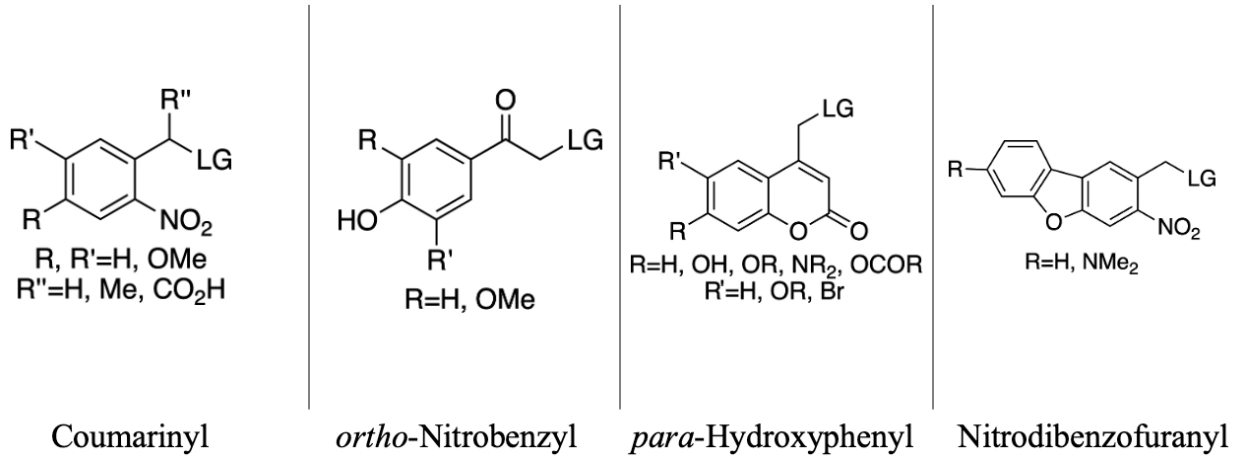

Figure 1.12: The four main scaffolds of photocages. *R represents various chemical groups that can be appended to the overall scaffold, while LG denotes the leaving group, which is the molecular fragment liberated upon photoexcitation. Figure taken from (D. C. F. Monteiro et al., 2021).*

Each photocaged scaffold offers different properties in terms of absorption wavelength, quantum yield, solubility, cleavage rate, and molar extinction coefficient which may be detrimental for specific experiments. Coumarins have an absorption maximum in the range of

320-390 nm, with an extinction coefficient of 6,000-20,000 $M^{-1}cm^{-1}$. The photodecaging rate of coumarins ranges from $1x10^8$ to $2x10^9$ s^{-1}, associated with a quantum yield of 0.02-0.30. However, solubility of these molecules is classified as poor-medium. On the other hand, *Ortho*-nitrobenzyl derivatives show some of the slowest photo-decaging rates, releasing molecules on the $1x10^4$ to $3x10^4$ s^{-1}. Their absorption maximum (λ) ranges from 254-345 nm, with a molar extinction coefficient of 600-27,000 $M^{-1}cm^{-1}$. Quantum yield of o*rtho*-nitrobenzyl derivatives range from 0.01-0.64 and like coumarins, they are classified to have poor-medium solubility. *Para*-hydroxyphenyls work with the lowest wavelengths from all four scaffolds at 280-304nm. They have an extinction coefficient of 9,000-15,000 $M^{-1}cm^{-1}$ and quantum yields of 0.03-0.9. They have photo-uncaging rates similar to coumarins at $1x10^7$ to $2x10^9$ s^{-1}, and show the highest solubilities from all four scaffolds, classified as good. Lastly, nitrodibenzofuranyls have the highest absorption wavelength at 310-420nm and an extinction coefficient of 10,000-19,000 $M^{-1}cm^{-1}$. Their quantum yields range from 0.2-0.7 and their photo-uncaging rates are $2x10^4$ s^{-1} with poor to medium solubilities. (D. C. Monteiro et al., 2021).

1.9 Sample delivery methods

Although a lot of emphasis needs to be placed on samples to conduct a successful experiment, one should not overlook the importance of the experimental set-up for TR-SX, specifically sample delivery methods. With the establishment of XFELs and the developments of SX and TR-SX, a critical problem emerged: how to effectively deliver a series of samples? Initial developments on sample delivery methods for SX at XFELs were conducted at LCLS with the introduction of a Gas Dynamic Virtual Nozzle (GDVN) which consisted of a 4μm diameter, continuous liquid jet (Henry N Chapman et al., 2011; DePonte et al., 2008). This GDVN allowed for crystal samples to be continuously streamed across the XFEL beam, delivering new samples for each X-ray pulse. The GDVN set the standard for future sample

delivery jet developments where the main focus is to stream a continuous series of micro-crystals across the X-ray beam in a focused and steady rate in a jet-like device. Further developments on jets continued to have the same focus, while at the same time improving jet stability and reducing the consumption of crystal sample. This was achieved with the Double-Flow Focusing Nozzle (DFFN) (Oberthuer et al., 2017), the Microfluidic electrokinetic sample holder (MESH) (Raymond G Sierra et al., 2012) and the High-Viscosity Extrusion injector (HVE) (Figure 1.13). Although there have been a lot of developments in jet extrusions for sample delivery proving it to be a valuable method for serial crystallography, issues such as sample clogging, sample waste and unstable jet position do often arise.

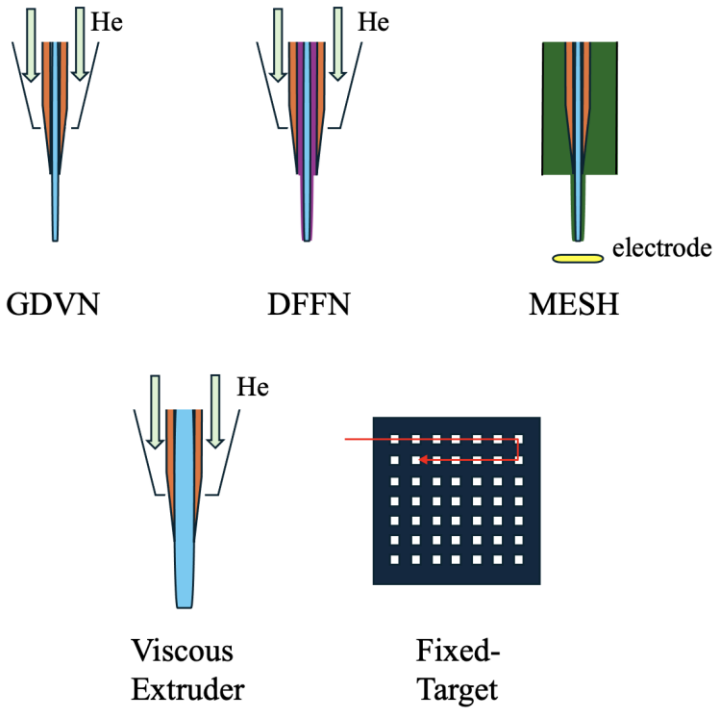

Figure 1.13: Sample delivery methods for serial crystallography. *The first four sample delivery methods can be classified as extruder jets where the crystal slurry (in baby blue) is ejected out of the nozzle (orange) as a stream of crystals. To focus the stream of crystals and maintained the consistency of the stream, an embracing stream of helium is implemented (for GDVN, DFFN and viscous extruders). The DFFN has an additional liquid stream to focus the crystal stream. GDVN uses an electrode to focus its stream and the viscous extruder is used for viscous media such as LCP. Fixed-targets are an alternative sample delivery method where crystals are placed on the surface of a membrane and scanned through.*

Sample delivery using fixed-targets, also known as chips or solid supports, uses a different philosophy. Instead of having the crystals flowing across the X-ray beam, the crystals can be placed onto a platform and be scanned across the beam. There are two categories of fixed-targets, the directed-raster chips and the aperture-aligned chips (M. Carrillo et al., 2023). Directed rastered fixed-targets distribute crystals in random locations throughout the surface a thin film or membrane. Due to the structure of the flat surface, crystals often times lay flat which can result in issues such as preferential orientation. A raster scan is conducted on these chips to gather data from individual crystals. Since the crystals are distributed randomly, only a small fraction of the loaded crystals will be utilized for data collection, as only those intersecting the path of the X-ray beam will create diffraction patterns (Figure 1.14). Increasing the density of the crystals placed on the chip will help increasing the hit-rate (fraction of X-ray pulses leading to a recorded diffraction pattern), but it also increases the number of multi-hits from single pulses, which are hard to process, and it leads to higher waste of material. With this said, a main drawback of this relatively simple approach is the uncertainty regarding the precise location of crystals relative to the X-ray beam. Furthermore, the application of optical excitation for pump-probe measurements is limited, as scattered photons may lead to cross-talk by activation of neighboring crystals.

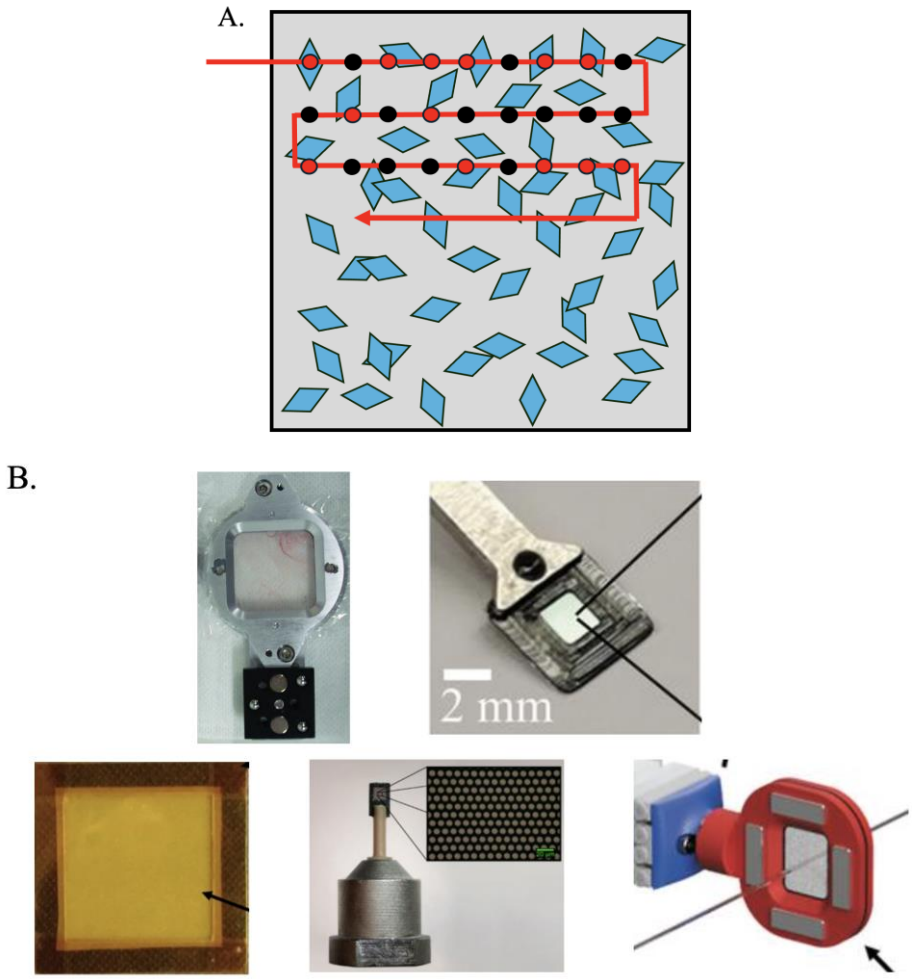

Figure 1.14: Directed-rastered fixed-targets for protein serial crystallography. *(A.) Schematic representation of a directed-rastered fixed-target during a raster grid scan data collection. Every dot represents a shot. Note that not all shots hit a crystal, leaving many empty shots and non-targeted crystals behind. (B.) Examples of directed raster fixed-targets. (Baxter et al., 2016; R. B. Doak et al., 2018; Karpik et al., 2020; Lee et al., 2019; Roedig et al., 2017; Darren A Sherrell et al., 2022).*

While there have been numerous advancements and iterations of directed-raster fixed-targets over time, there has been only one version of an aperture-aligned chips since 2015. (Mueller, Marx, Epp, Zhong, Kuo, Balo, Soman, Schotte, Lemke, & Owen, 2015; Oghbaey et al., 2016a). Aperture-aligned fixed-targets exhibit a greater degree of structure and organization. Their membranes are composed of organized and structured wells that serve to position the crystals inside of the membrane. This is unique as the crystals are now no longer randomly distributed throughout the membrane but instead lay in a pre-determined location

where the X-ray beam is programed to hit (Figure 1.15). For alignment with respect to the beam, they contain reference structures (fiducials) in the outer corners. This provides an optimized approach for data collection, minimizing the occurrence of empty shots or unused crystals. To minimize optical cross-talk in pump-probe experiments, aperture aligned fixed targets should be made from opaque material, absorbing light scattered from exposed crystals.

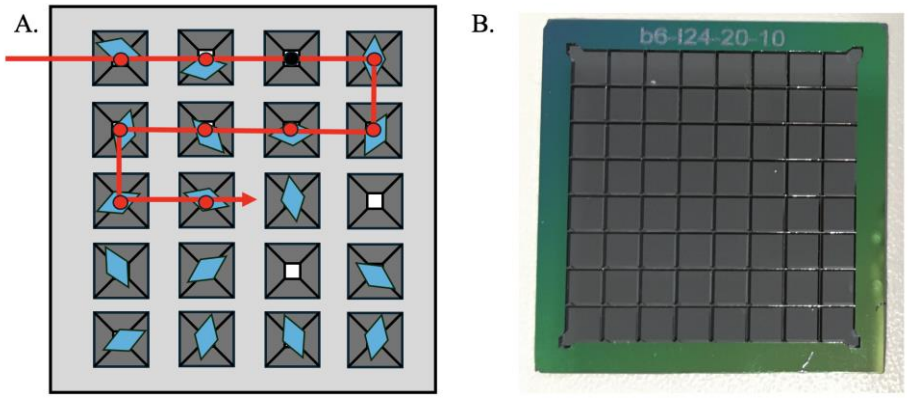

Figure 1.15: Aperture-aligned fixed-targets for protein serial crystallography. (A.) Schematic of an aperture-aligned fixed-target, demonstrating the wells within the membrane where crystals can position themselves during data collection. (B.) An image of the aperture-aligned fix-target design, constructed from silicon and initially developed in 2015 (Mueller, Marx, Epp, Zhong, Kuo, Balo, Soman, Schotte, Lemke, & Owen, 2015).

In addition to the fixed-target, other materials such as chip mounting devices and strategies for preventing crystal dehydration are crucial aspects to take into account when working with fixed-targets. Fixed targets are usually mounted onto the beamlines through chip holders which contain a magnetic base for goniometers (Martiel et al., 2021; Roedig et al., 2017) allowing them to be adaptable in various synchrotron beamlines. One important consideration is maintaining the hydration of crystals throughout the data collection process. Fixed-targets can prevent their crystals from dehydrating by incorporating methods to maintain an appropriate level of hydration during data collection. By using humidity chambers or streams or by sealing the chip with polymer films (M. Carrillo et al., 2023; R. B. Doak et al.,

2018; Darren A Sherrell et al., 2022) serve as effective measures to prevent crystals from dehydrating during the process of data collection.

1.10 Thesis aims

The aims of this research were two: first, to develop and establish a novel sample delivery method for serial crystallography at synchrotrons and XFELs, specifically tailored for SwissFEL's CristallinaMX experimental station; and second, to investigate ligand binding interactions involving caged compounds, particularly photocaged-biotin and T7-SA, in order to enhance understanding through protein crystallography. The primary focus was on creating a standard fixed-target, the MIcro-Structured Polymer based fixed-target (MISP-chip), optimized for minimal background noise, cost-effective production, user-friendly handling, durability, high reusability, and applicability to both serial crystallography and pump-probe experiments. Chapter 2 details the production and utilization of the MISP-chips, with initial experimental results on lysozyme, while Chapter 3 explores their suitability for pump-probe experiments. Simultaneously, efforts were dedicated to investigating ligand binding interactions, with cryogenic data collected at the Swiss Light Source and room-temperature data acquired at CristallinaMX using the MISP-chips, culminating in Chapter 4's findings.

1.11 References

Adams, P. D., Grosse-Kunstleve, R. W., Hung, L.-W., Ioerger, T. R., McCoy, A. J., Moriarty, N. W., Read, R. J., Sacchettini, J. C., Sauter, N. K., & Terwilliger, T. C. (2002). PHENIX: building new software for automated crystallographic structure determination. *Acta Crystallographica Section D: Biological Crystallography*, *58*(11), 1948-1954.

Afonine, P. V., Poon, B. K., Read, R. J., Sobolev, O. V., Terwilliger, T. C., Urzhumtsev, A., & Adams, P. D. (2018). Real-space refinement in PHENIX for cryo-EM and crystallography. *Acta Crystallographica Section D: Structural Biology*, *74*(6), 531-544.

Altarelli, M. (2011). The European X-ray free-electron laser facility in Hamburg. *Nuclear Instruments and Methods in Physics Research Section B: Beam Interactions with Materials and Atoms*, *269*(24), 2845-2849.

Ankenbruck, N., Courtney, T., Naro, Y., & Deiters, A. (2018). Optochemical control of biological processes in cells and animals. *Angewandte Chemie International Edition*, *57*(11), 2768-2798.

Argarana, C. E., Kuntz, I. D., Birken, S., Axel, R., & Cantor, C. R. (1986). Molecular cloning and nucleotide sequence of the streptavidin gene. *Nucleic acids research*, *14*(4), 1871-1882.

Bandara, H. D., & Burdette, S. C. (2012). Photoisomerization in different classes of azobenzene. *Chemical Society Reviews*, *41*(5), 1809-1825.

Barends, T. R., Stauch, B., Cherezov, V., & Schlichting, I. (2022). Serial femtosecond crystallography. *Nature Reviews Methods Primers*, *2*(1), 59.

Baxter, E. L., Aguila, L., Alonso-Mori, R., Barnes, C. O., Bonagura, C. A., Brehmer, W., Brunger, A. T., Calero, G., Caradoc-Davies, T. T., & Chatterjee, R. (2016). High-density grids for efficient data collection from multiple crystals. *Acta Crystallographica Section D: Structural Biology*, *72*(1), 2-11.

Bayer, E. A., & Wilchek, M. (1990). Application of avidin-biotin technology to affinity-based separations. *J Chromatogr*, *510*, 3-11. https://doi.org/10.1016/s0021-9673(01)93733-1

Beale, J. H., Bolton, R., Marshall, S. A., Beale, E. V., Carr, S. B., Ebrahim, A., Moreno-Chicano, T., Hough, M. A., Worrall, J. A., & Tews, I. (2019). Successful sample preparation for serial crystallography experiments. *Journal of Applied Crystallography*, *52*(6), 1385-1396.

Beale, J. H., & Marsh, M. E. (2021). Optimizing the Growth of Endothiapepsin Crystals for Serial Crystallography Experiments. *JoVE (Journal of Visualized Experiments)*(168), e61896.

Botha, S., Nass, K., Barends, T. R. M., Kabsch, W., Latz, B., Dworkowski, F., Foucar, L., Panepucci, E., Wang, M., Shoeman, R. L., Schlichting, I., & Doak, R. B. (2015). Room-temperature serial crystallography at synchrotron X-ray sources using slowly flowing free-standing high-viscosity microstreams. *Acta Crystallographica Section D Biological Crystallography*, *71*(2), 387-397. https://doi.org/10.1107/s1399004714026327

Bragg, W. L. (1913). The structure of some crystals as indicated by their diffraction of X-rays. *Proceedings of the Royal Society of London. Series A, Containing papers of a mathematical and physical character*, *89*(610), 248-277.

Brändén, G., & Neutze, R. (2021). Advances and challenges in time-resolved macromolecular crystallography. *Science*, *373*(6558). https://doi.org/10.1126/science.aba0954

Carrillo, M., Beale, J., & Padeste, C. (2022). Fixed-targets for serial protein crystallography at SwissFEL. *Acta Crystallographica*, *A78*, a279.

Carrillo, M., Mason, T. J., Karpik, A., Martiel, I., Kepa, M. W., McAuley, K. E., Beale, J. H., & Padeste, C. (2023). Micro-structured polymer fixed targets for serial crystallography at synchrotrons and XFELs. *IUCrJ*, *10*(Pt 6), 678-693. https://doi.org/10.1107/S2052252523007595

Carrillo, M., Pandey, S., Sanchez, J., Noda, M., Poudyal, I., Aldama, L., Malla, T. N., Claesson, E., Wahlgren, W. Y., & Feliz, D. (2021). High-resolution crystal structures of transient intermediates in the phytochrome photocycle. *Structure*, *29*(7), 743-754. e744.

Chaiet, L., & Wolf, F. J. (1964). The Properties of Streptavidin, a Biotin-Binding Protein Produced by Streptomycetes. *Arch Biochem Biophys*, *106*, 1-5. https://doi.org/10.1016/0003-9861(64)90150-x

Chapman, H. N., Caleman, C., & Timneanu, N. (2014). Diffraction before destruction. *Philos Trans R Soc Lond B Biol Sci*, *369*(1647), 20130313. https://doi.org/10.1098/rstb.2013.0313

Chapman, H. N., Fromme, P., Barty, A., White, T. A., Kirian, R. A., Aquila, A., Hunter, M. S., Schulz, J., DePonte, D. P., Weierstall, U., Doak, R. B., Maia, F. R., Martin, A. V., Schlichting, I., Lomb, L., Coppola, N., Shoeman, R. L., Epp, S. W., Hartmann, R., . . . Spence, J. C. (2011). Femtosecond X-ray protein nanocrystallography. *Nature*, *470*(7332), 73-77. https://doi.org/10.1038/nature09750

Chayen, N. E. (2005). Methods for separating nucleation and growth in protein crystallisation. *Progress in biophysics and molecular biology*, *88*(3), 329-337.

Chayen, N. E., & Saridakis, E. (2008). Protein crystallization: from purified protein to diffraction-quality crystal. *Nature methods*, *5*(2), 147-153.

Claesson, E., Wahlgren, W. Y., Takala, H., Pandey, S., Castillon, L., Kuznetsova, V., Henry, L., Panman, M., Carrillo, M., Kubel, J., Nanekar, R., Isaksson, L., Nimmrich, A., Cellini, A., Morozov, D., Maj, M., Kurttila, M., Bosman, R., Nango, E., . . . Westenhoff, S. (2020). The primary structural photoresponse of phytochrome proteins captured by a femtosecond X-ray laser. *Elife*, *9*. https://doi.org/10.7554/eLife.53514

Coquelle, N., Sliwa, M., Woodhouse, J., Schirò, G., Adam, V., Aquila, A., Barends, T. R., Boutet, S., Byrdin, M., & Carbajo, S. (2018). Chromophore twisting in the excited state of a photoswitchable fluorescent protein captured by time-resolved serial femtosecond crystallography. *Nature Chemistry*, *10*(1), 31-37.

Dasgupta, M., Budday, D., de Oliveira, S., Madzelan, P., Marchany-Rivera, D., Seravalli, J., Hayes, B., Sierra, R. G., Boutet, S., Hunter, M. S., Alonso-Mori, R., Batyuk, A., Wierman, J., Lyubmiov, A., Brewster, A. S., Sauter, N. K., Applegate, G. A., Tiwari, V. K., Berkowitz, D. B., . . . Wilson, M. A. (2019). Mix-and-inject XFEL crystallography reveals gated conformational dynamics during enzyme catalysis. *PNAS*, *116*(51), 25634-25640.

DeLano, W. (2020). The PyMOL Molecular Graphics System, Version 2.0 Schrödinger, LLC.

DeLano, W. L. (2002). Pymol: An open-source molecular graphics tool. *CCP4 Newsl. Protein Crystallogr*, *40*(1), 82-92.

DePonte, D., Doak, R., Hunter, M., Zhenquan, L., Weierstall, U., & Spence, J. (2009). SEM imaging of liquid jets. *Micron*, *40*(4), 507-509.

DePonte, D., Weierstall, U., Schmidt, K., Warner, J., Starodub, D., Spence, J., & Doak, R. (2008). Gas dynamic virtual nozzle for generation of microscopic droplet streams. *Journal of Physics D: Applied Physics*, *41*(19), 195505.

Dessau, M. A., & Modis, Y. (2011). Protein crystallization for X-ray crystallography. *JoVE (Journal of Visualized Experiments)*(47), e2285.

Doak, R., Kovacs, G., Gorel, A., Foucar, L., Barends, T., Grünbein, M., Hilpert, M., Kloos, M., Roome, C., Shoeman, R., Stricker, M., Tono, K., You, D., Ueda, K., Sherrell, D. A.,

Owen, R. L., & Schlichting, I. (2018). Crystallography on a chip - without the chip: sheet-on-sheet sandwich. *Acta Crystallographica*, *D74*(10), D1000-1007.

Doak, R. B., Nass Kovacs, G., Gorel, A., Foucar, L., Barends, T. R., Grünbein, M. L., Hilpert, M., Kloos, M., Roome, C. M., & Shoeman, R. L. (2018). Crystallography on a chip–without the chip: Sheet-on-sheet sandwich. *Acta Crystallographica Section D: Structural Biology*, *74*(10), 1000-1007.

Doerr, A. (2011). Diffraction before destruction. *Nature methods*, *8*(4), 283-283.

Drenth, J., Jansonius, J., Koekoek, R., Swen, H., & Wolthers, B. (1968). Structure of papain. *Nature*, *218*(5145), 929-932.

Ducruix, A., & Giegé, R. (1999). *Crystallization of nucleic acids and proteins: a practical approach* (Vol. 210). OUP Oxford.

Ebrahim, A., Appleby, M., Axford, D., Beale, J., Moreno-Chicano, T., Sherrell, D. A., Strange, R. W., Hough, M. A., & Owen, R. L. (2019). Resolving polymorphs and radiation-driven effects in microcrystals using fixed-target serial synchrotron crystallography. *Acta Crystallographica*, *D75*(2), 151-159.

Edwards, D. A., & Syphers, M. J. (2008). *An introduction to the physics of high energy accelerators*. John Wiley & Sons.

Emma, P., Akre, R., Arthur, J., Bionta, R., Bostedt, C., Bozek, J., Brachmann, A., Bucksbaum, P., Coffee, R., & Decker, F.-J. (2010). First lasing and operation of an ångstrom-wavelength free-electron laser. *nature photonics*, *4*(9), 641-647.

Emsley, P., & Cowtan, K. (2004). Coot: model-building tools for molecular graphics. *Acta Crystallographica Section D: Biological Crystallography*, *60*(12), 2126-2132.

Eriksson, M., Al-Dmour, E., Andersson, Å., Johansson, M., Leemann, S., Malmgren, L., Tavares, P., & Thorin, S. (2016). *Commissioning of the MAX IV light source*. eScholarship, University of California.

Fedorov, R., Schlichting, I., Hartmann, E., Domratcheva, T., Fuhrmann, M., & Hegemann, P. (2003). Crystal structures and molecular mechanism of a light induced signaling switch: the Phot-LOV1 domain from Chlamydomonas reinhardtii. *Biophysics J*, *84*, 2474-2482.

Fromme, R., Ishchenko, A., Metz, M., Chowdhury, S. R., Basu, S., Boutet, S., Fromme, P., White, T. A., Barty, A., Spence, J. C. H., Weierstall, U., Liu, W., & Cherezov, V. (2015). Serial femtosecond crystallography of soluble proteins in lipidic cubic phase. *International Union of Crystallography Journal*, *2*(5), 545-551.

Gevorkov, Y., Yefanov, O., Barty, A., White, T. A., Mariani, V., Brehm, W., Tolstikova, A., Grigat, R. R., & Chapman, H. N. (2019). XGANDALF - extended gradient descent algorithm for lattice finding. *Acta Crystallogr A Found Adv*, *75*(Pt 5), 694-704. https://doi.org/10.1107/S2053273319010593

Gotthard, G., Mous, S., Weinert, T., Maia, R. N. A., James, D., Dworkowski, F., Gashi, D., Furrer, A., Ozerov, D., Panepucci, E., Wang, M., Schertler, G. F. X., Heberle, J., Standfuss, J., & Nogly, P. (2023). Capturing the blue-light activated state of the Phot-LOV1 domain from Chlamydomonas reinhardtii using time-resolved serial synchrotron crystallography. *bioRxiv*, *preprint*. https://doi.org/10.1101/2023.11.06.565770

Gretch, D., Suter, M., & Stinski, M. (1987). The use of biotinylated monoclonal antibodies and streptavidin affinity chromatography to isolate herpesvirus hydrophobic proteins or glycoproteins. *Analytical biochemistry*, *163*(1), 270-277.

Haas, D., & Rossmann, M. (1970). Crystallographic studies on lactate dehydrogenase at–75° C. *Acta Crystallographica Section B: Structural Crystallography and Crystal Chemistry*, *26*(7), 998-1004.

Haas, D. J. (2020). The early history of cryo-cooling for macromolecular crystallography. *IUCrJ*, *7*(2), 148-157.

Habeeb, A., & Hiramoto, R. (1968). Reaction of proteins with glutaraldehyde. *Archives of biochemistry and biophysics*, *126*(1), 16-26.

Hadian-Jazi, M., Messerschmidt, M., Darmanin, C., Giewekemeyer, K., Mancuso, A. P., & Abbey, B. (2017). A peak-finding algorithm based on robust statistical analysis in serial crystallography. *Journal of Applied Crystallography*, *50*(6), 1705-1715.

Hansen, S., Hough, E., & Andersen, K. (1999). Purification, crystallization and preliminary X-ray studies of two isoforms of Rubisco from Alcaligenes eutrophus. *Acta Crystallographica Section D: Biological Crystallography*, *55*(1), 310-313.

Holzer, W., Penzkofer, A., Fuhrmann, M., & Hegemann, P. (2002). Spectroscopic characterization of flavin mononucleotide bound to the LOV1 domain of phototropin from Chlamydomonas reinhardtii. *Photochem Photobiol*, *75*, 479-487.

Hosaka, T., Katsura, K., Ishizuka-Katsura, Y., Hanada, K., Ito, K., Tomabechi, Y., Inoue, M., Akasaka, R., Takemoto, C., & Shirouzu, M. (2022). Crystal Structure of an Archaeal Tyrosyl-tRNA Synthetase Bound to Photocaged L-Tyrosine and Its Potential Application to Time-Resolved X-ray Crystallography. *Int J Mol Sci*, *23*(18). https://doi.org/10.3390/ijms231810399

Hosaka, T., Nomura, T., Kubo, M., Nakane, T., Fangjia, L., Sekine, S. I., Ito, T., Murayama, K., Ihara, K., Ehara, H., Kashiwagi, K., Katsura, K., Akasaka, R., Hisano, T., Tanaka, T., Tanaka, R., Arima, T., Yamashita, A., Sugahara, M., . . . Shirouzu, M. (2022). Conformational alterations in unidirectional ion transport of a light-driven chloride pump revealed using X-ray free electron lasers. *Proc Natl Acad Sci U S A*, *119*(9). https://doi.org/10.1073/pnas.2117433119

Huang, N., Deng, H., Liu, B., Wang, D., & Zhao, Z. (2021). Features and futures of X-ray free-electron lasers. *The Innovation*, *2*(2).

Hunte, C., Von Jagow, G., & Schagger, H. (2003). *Membrane protein purification and crystallization: a practical guide*. Elsevier.

Hunter, M. S., Segelke, B., Messerschmidt, M., Williams, G. J., Zatsepin, N. A., Barty, A., Benner, W. H., Carlson, D. B., Coleman, M., Graf, A., Hau-Riege, S. P., Pardini, T., Seibert, M. M., Evans, J., Boutet, S., & Frank, M. (2014). Fixed-target protein serial microcrystallography with an X-ray free-electron laser. *Nature Scientific Reports*, *4*, 6026.

James, D., Weinert, T., Skopintsev, P., Furrer, A., Gashi, D., Tanaka, T., Nango, E., Nogly, P., & Standfuss, J. (2019). Improving High Viscosity Extrusion of Microcrystals for Time-resolved Serial Femtosecond Crystallography at X-ray Lasers. *J Vis Exp*(144). https://doi.org/10.3791/59087

Ji, G., Wang, N., Yin, X., & Chen, P. (2020). Substituent Effect Induces Emission Modulation of Stilbene Photoswitches by Spatial Tuning of the N/B Electronic Constraints. *Organic Letters*, *22*(15), 5758-5762.

Josts, I., Niebling, S., Gao, Y., Levantino, M., Tidow, H., & Monteiro, D. (2018). Photocage-initiated time-resolved solution X-ray scattering investigation of protein dimerization. *IUCrJ*, *5*(Pt 6), 667-672. https://doi.org/10.1107/S2052252518012149

Kaminski, J. W., Vera, L., Stegmann, D. P., Vering, J., Eris, D., Smith, K. M. L., Huang, C. Y., Meier, N., Steuber, J., Wang, M., Fritz, G., Wojdyla, J. A., & Sharpe, M. E. (2022). Fast fragment- and compound-screening pipeline at the Swiss Light Source. *Acta Crystallogr D Struct Biol*, *78*(Pt 3), 328-336. https://doi.org/10.1107/S2059798322000705

Kang, H.-S., Min, C.-K., Heo, H., Kim, C., Yang, H., Kim, G., Nam, I., Baek, S. Y., Choi, H.-J., & Mun, G. (2017). Hard X-ray free-electron laser with femtosecond-scale timing jitter. *nature photonics*, *11*(11), 708-713.

Karpik, A., Martiel, I., Kristiansen, P. M., & Padeste, C. (2020). Fabrication of ultrathin suspended polymer membranes as supports for serial protein crystallography. *Micro and Nano Engineering*, *7*, 100053.

Kendrew, J. C., Bodo, G., Dintzis, H. M., Parrish, R., Wyckoff, H., & Phillips, D. C. (1958). A three-dimensional model of the myoglobin molecule obtained by x-ray analysis. *Nature*, *181*(4610), 662-666.

Kendrew, J. C., & Parrish, R. (1957). The crystal structure of myoglobin III. Sperm-whale myoglobin. *Proceedings of the Royal Society of London. Series A. Mathematical and Physical Sciences*, *238*(1214), 305-324.

Kim, Y., Babnigg, G., Jedrzejczak, R., Eschenfeldt, W. H., Li, H., Maltseva, N., Hatzos-Skintges, C., Gu, M., Makowska-Grzyska, M., & Wu, R. (2011). High-throughput protein purification and quality assessment for crystallization. *Methods*, *55*(1), 12-28.

Klehr, J., Zhao, J., Kron, A. S., Ward, T. R., & Köhler, V. (2020). Streptavidin (Sav)-based artificial Metalloenzymes: cofactor design considerations and large-scale expression of host protein variants. *Peptide and Protein Engineering: From Concepts to Biotechnological Applications*, 213-235.

Kottke, T., Heberle, J., Hehn, D., Dick, B., & Hegemann, P. (2003). Phot LOV1: photocycle of a blue-light receptor domain from the green alga Chlamydomonas reinhardtii. *Biophys J*, 1192-1201.

Kubo, M., Nango, E., Tono, K., Kimura, T., Owada, S., Song, C., Mafune, F., Miyajima, K., Takeda, Y., Kohno, J. Y., Miyauchi, N., Nakane, T., Tanaka, T., Nomura, T., Davidsson, J., Tanaka, R., Murata, M., Kameshima, T., Hatsui, T., . . . Iwata, S. (2017). Nanosecond pump-probe device for time-resolved serial femtosecond crystallography developed at SACLA. *J Synchrotron Radiat*, *24*(Pt 5), 1086-1091. https://doi.org/10.1107/S160057751701030X

Labrou, N. E. (2014). Protein purification: an overview. *Protein Downstream Processing: Design, Development and Application of High and Low-Resolution Methods*, 3-10.

Le Trong, I., Humbert, N., Ward, T. R., & Stenkamp, R. E. (2006). Crystallographic analysis of a full-length streptavidin with its C-terminal polypeptide bound in the biotin binding site. *J Mol Biol*, *356*(3), 738-745. https://doi.org/10.1016/j.jmb.2005.11.086

Le Trong, I., Wang, Z., Hyre, D. E., Lybrand, T. P., Stayton, P. S., & Stenkamp, R. E. (2011). Streptavidin and its biotin complex at atomic resolution. *Acta Crystallogr D Biol Crystallogr*, *67*(Pt 9), 813-821. https://doi.org/10.1107/S0907444911027806

Lee, D., Baek, S., Park, J., Lee, K., Kim, J., Lee, S. J., Chung, W. K., Lee, J.-L., Cho, Y., & Nam, K. H. (2019). Nylon mesh-based sample holder for fixed-target serial femtosecond crystallography. *Scientific reports*, *9*(1), 6971.

Letondor, C., Humbert, N., & Ward, T. R. (2005). Artificial metalloenzymes based on biotin-avidin technology for the enantioselective reduction of ketones by transfer hydrogenation. *Proc Natl Acad Sci U S A*, *102*(13), 4683-4687. https://doi.org/10.1073/pnas.0409684102

Li, H., Nakajima, Y., Nomura, T., Sugahara, M., Yonekura, S., Chan, S. K., Nakane, T., Yamane, T., Umena, Y., Suzuki, M., Masuda, T., Motomura, T., Naitow, H., Matsuura, Y., Kimura, T., Tono, K., Owada, S., Joti, Y., Tanaka, R., . . . Suga, M. (2021). Capturing structural changes of the S(1) to S(2) transition of photosystem II using time-resolved serial femtosecond crystallography. *IUCrJ*, *8*(Pt 3), 431-443. https://doi.org/10.1107/S2052252521002177

Li, Y., Wang, M., Wang, F., Lu, S., & Chen, X. (2023). Recent progress in studies of photocages. *Smart Molecules*, e20220003.

Liebschner, D., Afonine, P. V., Baker, M., Bunkoczi, G., Chen, V. B., Croll, T. I., Hintze, B., Hung, L.-W., Jain, S., McCoy, A. J., Moriarty, N. W., Oeffner, R. D., Poon, B. K.,

Prisant, M. G., Read, R. J., Richardson, J. S., Richardson, D. C., Sammito, M. D., Sobolev, O. V., . . . Adams, P. D. (2019). Macromolecular structure determination using X-rays, neutrons and electrons: recent developments in Phenix. *Acta Crystallographica*, *D75*, 861-877.

Liu, X., Liu, P., Li, H., Xu, Z., Jia, L., Xia, Y., Yu, M., Tang, W., Zhu, X., Chen, C., Zhang, Y., Nango, E., Tanaka, R., Luo, F., Kato, K., Nakajima, Y., Kishi, S., Yu, H., Matsubara, N., . . . Wang, J. (2022). Excited-state intermediates in a designer protein encoding a phototrigger caught by an X-ray free electron laser. *Nat Chem*, *14*, 1054-1060.

Loosli, A., Rusbandi, U. E., Gradinaru, J., Bernauer, K., Schlaepfer, C. W., Meyer, M., Mazurek, S., Novic, M., & Ward, T. R. (2006). (Strept)avidin as host for biotinylated coordination complexes: stability, chiral discrimination, and cooperativity. *Inorg Chem*, *45*(2), 660-668. https://doi.org/10.1021/ic051405t

Maestre-Reyna, M., Yang, C. H., Nango, E., Huang, W. C., Putu, E. P. G. N., Wu, W. J., Wang, P. H., Badur-Franz, S., Saft, M., Emmerich, H. J., Wu, H. Y., Lee, C. C., Huang, K. F., Chang, Y. K., Liao, J. H., Weng, J. H., Gad, W., Chang, C. W., Pang, A. H., . . . Tsai, M. D. (2022). Serial crystallography captures dynamic control of sequential electron and proton transfer events in a flavoenzyme. *Nat Chem*, *14*, 677-685.

Mallin, H., Hestericová, M., Reuter, R., & Ward, T. R. (2016). Library design and screening protocol for artificial metalloenzymes based on the biotin-streptavidin technology. *Nature protocols*, *11*(5), 835-852.

Malmerberg, E., M. Bovee-Geurts, P. H., Katona, G., Deupi, X., Arnlund, D., Wickstrand, C., Johansson, L. C., Westenhoff, S., Nazarenko, E., & X. Schertler, G. F. (2015). Conformational activation of visual rhodopsin in native disc membranes. *Science signaling*, *8*(367), ra26-ra26.

Martiel, I., Beale, J. H., Karpik, A., Huang, C. Y., Vera, L., Olieric, N., Wranik, M., Tsai, C. J., Muhle, J., Aurelius, O., John, J., Hogbom, M., Wang, M., Marsh, M., & Padeste, C. (2021). Versatile microporous polymer-based supports for serial macromolecular crystallography. *Acta Crystallogr D Struct Biol*, *77*(Pt 9), 1153-1167. https://doi.org/10.1107/S2059798321007324

Mehrabi, P., Müller-Werkmeister, H. M., Leimkohl, J. P., Schikora, H., Ninkovic, J., Krivokuca, S., Andricek, L., Epp, S. W., Sherrell, D. A., Owen, R. L., Pearson, A. R., Tellkamp, F., Schulz, E. C., & Miller, R. J. D. (2020). The HARE chip for efficient time-resolved serial synchrotron crystallography. *Journal of Synchrotron Radiation*, *27*(2), 360-370.

Mehrabi, P., Schulz, E. C., Agthe, M., Horrell, S., Bourenkov, G., von Stetten, D., Jan-Philipp, L., Schikora, H., Schneider, T. R., Pearson, A. R., Tellkamp, F., & Miller, R. J. D. (2019). Liquid application method for time-resolved analyses by serial synchrotron crystallography. *Nature Methods*, *16*, 979-982.

Mehrabi, P., Schulz, E. C., Dsouza, R., Mueller-Werkmeister, H. M., Tellkamp, F., Miller, R. J. D., & Pai, E. F. (2019). Time-resolved crystallography reveals allosteric communication aligned with molecular breathing. *Science*, *365*, 1167-1170.

Monteiro, D. C. F., Amoah, E., Rogers, C., & Pearson, A. R. (2021). Using photocaging for fast time-resolved structural biology studies. *Acta Crystallogr D Struct Biol*, *77*(Pt 10), 1218-1232. https://doi.org/10.1107/S2059798321008809

Mous, S., Gotthard, G., Ehrenberg, D., Sen, S., Weinert, T., Johnson, P. J., James, D., Nass, K., Furrer, A., Kekilli, D., Ma, P., Bruenle, S., Casadei, C. M., Martiel, I., Dworkowski, F., Gashi, D., Skopintsev, P., Wranik, M., Knopp, G., . . . Nogly, P. (2022). Dynamics and mechanism of a light-driven chloride pump. *Science*, *375*, 845-851.

Mueller, C., Marx, A., Epp, S. W., Zhong, Y., Kuo, A., Balo, A. R., Soman, J., Schotte, F., Lemke, H. T., Owen, R. L., Pai, E. F., Pearson, A. R., Olson, J. S., Anfinrud, P. A., Ernst,

O. P., & Miller, R. J. D. (2015). Fixed target matrix for femtosecond time-resolved and in situ serial micro-crystallography. *Structural Dynamics*, *2*(5), 054302.

Nam, K. H. (2023). Real-time monitoring of large-scale crystal growth using batch crystallization for serial crystallography. *Journal of Crystal Growth*, *614*, 127219.

Nam, K. H., Kim, J., & Cho, Y. (2021). Polyimide mesh-based sample holder with irregular crystal mounting holes for fixed-target serial crystallography. *Sci Rep*, *11*(1), 13115. https://doi.org/10.1038/s41598-021-92687-x

Nango, E., Kubo, M., Tono, K., & Iwata, S. (2019). Pump-probe time-Resolved serial femtosecond crystallography at SACLA: current status and data collection strategies. *Applied Sciences*, *9*(24), 5505.

Nango, E., Royant, A., Kubo, M., Nakane, T., Wickstrand, C., Kimura, T., Tanaka, T., Tono, K., Song, C., Tanaka, R., Arima, T., Yamashita, A., Kobayashi, J., Hosaka, T., Mizohata, E., Nogly, P., Sugahara, M., Nam, D., Nomura, T., . . . Iwata, S. (2016). A three-dimensional movie of structural changes in bacteriorhodopsin. *Science*, *354*(6319), 1552-1557.

Nass Kovacs, G., Colletier, J. P., Grunbein, M. L., Yang, Y., Stensitzki, T., Batyuk, A., Carbajo, S., Doak, R. B., Ehrenberg, D., Foucar, L., Gasper, R., Gorel, A., Hilpert, M., Kloos, M., Koglin, J. E., Reinstein, J., Roome, C. M., Schlesinger, R., Seaberg, M., . . . Schlichting, I. (2019). Three-dimensional view of ultrafast dynamics in photoexcited bacteriorhodopsin. *Nat Commun*, *10*(1), 3177. https://doi.org/10.1038/s41467-019-10758-0

Neutze, R., Wouts, R., van der Spoel, D., Weckert, E., & Hajdu, J. (2000). Potential for biomolecular imaging with femtosecond X-ray pulses. *Nature*, *406*(6797), 752-757.

Nogly, P., James, D., Wang, D., White, T., Zatsepin, N., Shilova, A., Nelson, G., Liu, H., Johansson, L., Heymann, M., Jaeger, K., Metz, M., Wickstrand, C., Wenting, W., Bath, P., Berntsen, P., Oberthuer, D., Panneels, V., Cherezov, V., . . . Weierstall, U. (2015). Lipidic cubic phase serial milisecond crystallography using synchrotron radiation. *International Union of Crystallography Journal*, *2*(2), 168-176.

Nogly, P., Panneels, V., Nelson, G., Gati, C., Kimura, T., Milne, C., Milathianaki, D., Kubo, M., Wu, W., Conrad, C., Coe, J., Bean, R., Zhao, Y., Bath, P., Dods, R., Harimoorthy, R., Beyerlein, K. R., Rheinberger, J., James, D., . . . Standfuss, J. (2016). Lipidic cubic phase injector is a viable crystal delivery system for time-resolved serial crystallography. *Nat Commun*, *7*, 12314. https://doi.org/10.1038/ncomms12314

Nogly, P., Weinert, T., James, D., Carbajo, S., Ozerov, D., Furrer, A., Gashi, D., Borin, V., Skopintsev, P., Jaeger, K., Nass, K., Bath, P., Bosman, R., Koglin, J., Seaberg, M., Lane, T., Kekilli, D., Bruenle, S., Tanaka, T., . . . Standfuss, J. (2018). Retinal isomerization in bacteriorhodopsin captured by a femtosecond X-ray laser. *Science*, *361*(6398).

Oberthuer, D., Knoška, J., Wiedorn, M. O., Beyerlein, K. R., Bushnell, D. A., Kovaleva, E. G., Heymann, M., Gumprecht, L., Kirian, R. A., & Barty, A. (2017). Double-flow focused liquid injector for efficient serial femtosecond crystallography. *Scientific reports*, *7*(1), 44628.

Oghbaey, S., Sarracini, A., Ginn, H. M., Pare-Labrosse, O., Kuo, A., Marx, A., Epp, S. W., Sherrell, D. A., Eger, B. T., Zhong, Y., Loch, R., Mariani, V., Alonso-Mori, R., Nelson, S., Lemke, H. T., Owen, R. L., Pearson, A. R., Stuart, D. I., Ernst, O. P., . . . Miller, R. J. (2016a). Fixed target combined with spectral mapping: approaching 100% hit rates for serial crystallography. *Acta Crystallogr D Struct Biol*, *72*(Pt 8), 944-955. https://doi.org/10.1107/S2059798316010834

Olmos, J. L., Jr., Pandey, S., Martin-Garcia, J. M., Calvey, G., Katz, A., Knoska, J., Kupitz, C., Hunter, M. S., Liang, M., Oberthuer, D., Yefanov, O., Wiedorn, M., Heyman, M., Holl, M., Pande, K., Barty, A., Miller, M. D., Stern, S., Roy-Chowdhury, S., . . . Schmidt, M.

(2018). Enzyme intermediates captured "on the fly" by mix-and-inject serial crystallography. *BMC Biol*, *16*(1), 59. https://doi.org/10.1186/s12915-018-0524-5
Orville, A. M. (2020). Recent results in time resolved serial femtosecond crystallography at XFELs. *Curr Opin Struct Biol*, *65*, 193-208. https://doi.org/10.1016/j.sbi.2020.08.011
Pande, K., Hutchison, C., Groenhof, G., Aquila, A., Robinson, J., Tenboer, J., Basu, S., Boutet, S., DePonte, D. P., Liang, M., White, T. A., Zatsepin, N., Yefanov, O., Morozov, D., Oberhuer, D., Gati, C., Subramanian, G., James, D., Zhao, Y., . . . Schmidt, M. (2016). Femtosecond structural dynamics drives the trans/cis isomerization in photoactive yellow protein. *Science*, *352*(6286), 725-729.
Pandey, S., Bean, R., Sato, T., Poudyal, I., Bielecki, J., Cruz Villarreal, J., Yefanov, O., Mariani, V., White, T. A., Kupitz, C., Hunter, M., Abdellatif, M. H., Bajt, S., Bondar, V., Echelmeier, A., Doppler, D., Emons, M., Frank, M., Fromme, R., . . . Schmidt, M. (2020). Time-resolved serial femtosecond crystallography at the European XFEL. *Nat Methods*, *17*(1), 73-78. https://doi.org/10.1038/s41592-019-0628-z
Pandey, S., Poudyal, I., & Malla, T. N. (2020). Pump-probe time-resolved serial femtosecond crystallography at X-ray free electron lasers. *Crystals*, *10*(7), 628.
Panneels, V., Wu, W., Tsai, C.-J., Nogly, P., Rheinberger, J., Jaeger, K., Cicchetti, G., Gati, C., Kick, L. M., & Sala, L. (2015). Time-resolved structural studies with serial crystallography: A new light on retinal proteins. *Structural Dynamics*, *2*(4).
Park, S.-Y., Choi, H., Eo, C., Cho, Y., & Nam, K. (2020). Fixed-Target Serial Synchrotron Crystallography Using Nylon Mesh and Enclosed Film-Based Sample Holder. *Crystals*, *10*(9), 803.
Perutz, M. (1990). How WL Bragg invented X-ray analysis. *Acta Crystallographica Section A: Foundations of Crystallography*, *46*(8), 633-643.
Perutz, M. F. (1963). X-ray Analysis of Hemoglobin: The results suggest that a marked structural change accompanies the reaction of hemoglobin with oxygen. *Science*, *140*(3569), 863-869.
Piketty, M.-L., Polak, M., Flechtner, I., Gonzales-Briceño, L., & Souberbielle, J.-C. (2017). False biochemical diagnosis of hyperthyroidism in streptavidin-biotin-based immunoassays: the problem of biotin intake and related interferences. *Clinical Chemistry and Laboratory Medicine (CCLM)*, *55*(6), 780-788.
Powell, H. R. (2017). X-ray data processing. *Bioscience reports*, *37*(5), BSR20170227.
Powell, H. R. (2021). A beginner's guide to X-ray data processing. *The Biochemist*, *43*(3), 46-50.
Reyes, F. D., Romero, J. F., & de Castro, M. L. (2001). Determination of biotin in foodstuffs and pharmaceutical preparations using a biosensing system based on the streptavidin–biotin interaction. *Analytica chimica acta*, *436*(1), 109-117.
Rhodes, G. (2010). *Crystallography made crystal clear: a guide for users of macromolecular models*. Elsevier.
Robinson, A., & Booklet, X.-r. D. (2001). Section 2.2 History of synchrotron radiation. *X-ray data booklet*, *2*.
Rodgers, D. W. (1994). Cryocrystallography. *Structure*, *2*(12), 1135-1140.
Roedig, P., Ginn, H. M., Pakendorf, T., Sutton, G., Harlos, K., Walter, T. S., Meyer, J., Fischer, P., Duman, R., & Vartiainen, I. (2017). High-speed fixed-target serial virus crystallography. *Nature methods*, *14*(8), 805-810.
Rupp, B. (2015). Origin and use of crystallization phase diagrams. *Acta Crystallographica Section F: Structural Biology Communications*, *71*(3), 247-260.
Safo, M. K., & Abraham, D. J. (2003). X-ray crystallography of hemoglobins. *Hemoglobin Disorders: Molecular Methods and Protocols*, 1-19.

Sano, T., Pandori, M. W., Chen, X., Smith, C. L., & Cantor, C. R. (1995). Recombinant core streptavidins. A minimum-sized core streptavidin has enhanced structural stability and higher accessibility to biotinylated macromolecules. *J Biol Chem*, *270*(47), 28204-28209. https://doi.org/10.1074/jbc.270.47.28204

Schluenzen, F., Tocilj, A., Zarivach, R., Harms, J., Gluehmann, M., Janell, D., Bashan, A., Bartels, H., Agmon, I., & Franceschi, F. (2000). Structure of functionally activated small ribosomal subunit at 3.3 Å resolution. *cell*, *102*(5), 615-623.

Schmidt, M. (2013). Mix and inject: Reaction initiation by diffusion for time-resolved macromolecular crystallography. *Advances in Condensed Matter Physics*, *2013*.

Schmidt, M., Pande, K., Basu, S., & Tenboer, J. (2015). Room temperature structures beyond 1.5 Å by serial femtosecond crystallography. *Structural Dynamics*, *2*(4).

Schulz, E. C., Yorke, B. A., Pearson, A. R., & Mehrabi, P. (2022). Best practices for time-resolved serial synchrotron crystallography. *Acta Crystallographica*, *D78*(Pt 1), 14-29. https://doi.org/10.1107/S2059798321011621

Sherrell, D. A., Foster, A. J., Hudson, L., Nutter, B., O'Hea, J., Nelson, S., Pare-Labrosse, O., Oghbaey, S., Miller, R. J., & Owen, R. L. (2015). A modular and compact portable mini-endstation for high-precision, high-speed fixed target serial crystallography at FEL and synchrotron sources. *J Synchrotron Radiat*, *22*(6), 1372-1378. https://doi.org/10.1107/S1600577515016938

Sherrell, D. A., Lavens, A., Wilamowski, M., Kim, Y., Chard, R., Lazarski, K., Rosenbaum, G., Vescovi, R., Johnson, J. L., Akins, C., Chang, C., Michalska, K., Babnigg, G., Foster, I., & Joachimiak, A. (2022). Fixed-target serial crystallography at the Structural Biology Center. *J Synchrotron Radiat*, *29*(Pt 5), 1141-1151. https://doi.org/10.1107/S1600577522007895

Sierra, R. G., Laksmono, H., Kern, J., Tran, R., Hattne, J., Alonso-Mori, R., Lassalle-Kaiser, B., Glockner, C., Hellmich, J., Schafer, D. W., Echols, N., Gildea, R., Grosse-Kunstleve, R. W., Sellberg, J., McQueen, T. A., Fry, A. R., Messerschmidt, M., Miahnahri, A., Seibert, M. M., . . . Bogan, M. J. (2012). Nanoflow electrospinning serial femtosecond crystallography. *Acta Crystallographica*, *D68*, 1584-1587.

Skopintsev, P., Ehrenberg, D., Weinert, T., James, D., Kar, R. K., Johnson, P. J. M., Ozerov, D., Furrer, A., Martiel, I., Dworkowski, F., Nass, K., Knopp, G., Cirelli, C., Arrell, C., Gashi, D., Mous, S., Wranik, M., Gruhl, T., Kekilli, D., . . . Standfuss, J. (2020). Femtosecond-to-millisecond structural changes in a light-driven sodium pump. *Nature*, *583*(7815), 314-318. https://doi.org/10.1038/s41586-020-2307-8

Smolentsev, G., Guda, A., Zhang, X., Haldrup, K., Andreiadis, E., Chavarot-Kerlidou, M., Canton, S. E., CNachtegaal, M., Artero, V., & Sundstrom, V. (2013). Pump-flow-probe X-ray absorption spectroscopy as a tool for studying intermediate states of photocatalytic systems. *J Phys Chem C Nanom Interf*, *117*(34), 17367-17375.

Sorigué, D., Hadjidemetriou, K., Blangy, S., Gotthard, G., Bonvalet, A., Coquelle, N., Samire, P., Aleksandrov, A., Antonucci, L., & Benachir, A. (2021). Mechanism and dynamics of fatty acid photodecarboxylase. *Science*, *372*(6538), eabd5687.

Stevens, R. C. (2000). High-throughput protein crystallization. *Current opinion in structural biology*, *10*(5), 558-563.

Studier, F. (2005). Protein production by auto-induction in high-density shaking cultures. *Protein Expression and Purification*, *41*(1), 207-234.

Suga, M., Akita, F., Sugahara, M., Kubo, M., Nakajima, Y., Nakane, T., Yamashita, K., Umena, Y., Nakabayashi, M., Yamane, T., Nakano, T., Suzuki, M., Masuda, T., Inoue, S., Kimura, T., Nomura, T., Yonekura, S., Yu, L. J., Sakamoto, T., . . . Shen, J. R. (2017). Light-induced structural changes and the site of O=O bond formation in PSII caught by XFEL. *Nature*, *543*(7643), 131-135. https://doi.org/10.1038/nature21400

Tsai, C.-J., Pamula, F., Nehmé, R., Mühle, J., Weinert, T., Flock, T., Nogly, P., Edwards, P. C., Carpenter, B., & Gruhl, T. (2018). Crystal structure of rhodopsin in complex with a mini-Go sheds light on the principles of G protein selectivity. *Science advances*, *4*(9), eaat7052.

Villarón, D., & Wezenberg, S. J. (2020). Stiff-stilbene photoswitches: from fundamental studies to emergent applications. *Angewandte Chemie*, *132*(32), 13292-13302.

Ward, T. R. (2005). Artificial metalloenzymes for enantioselective catalysis based on the noncovalent incorporation of organometallic moieties in a host protein. *Chemistry*, *11*(13), 3798-3804. https://doi.org/10.1002/chem.200401232

Weierstall, U., James, D., Wang, C., White, T. A., Wang, D., Liu, W., Spence, J. C. H., Doak, R. B., Nelson, G., Fromme, P., Fromme, R., Grotjohann, I., Kupitz, C., Zatsepin, N. A., Liu, H., Basu, S., Wacker, D., Han, G. W., Katritch, V., . . . Cherezov, V. (2014). Lipidic cubic phase injector facilitates membrane protein serial femtosecond crystallography. *Nature Communications*, *5*, 3309.

White, T. A. (2019). Processing serial crystallography data with CrystFEL: a step-by-step guide. *Acta Crystallographica Section D: Structural Biology*, *75*(2), 219-233.

White, T. A., Kirian, R. A., Martin, A. V., Aquila, A., Nass, K., Barty, A., & Chapman, H. N. (2012). CrystFEL: a software suite for snapshot serial crystallography. *Journal of Applied Crystallography*, *45*(2), 335-341.

Wilmanns, M. (2000). Future structural biology applications with a free-electron laser - more than wild dreams? *Journal of Synchrotron Radiation*, *7*(1), 41-46.

Winn, M. D., Ballard, C. C., Cowtan, K. D., Dodson, E. J., Emsley, P., Evans, P. R., Keegan, R. M., Krissinel, E. B., Leslie, A. G., McCoy, A., McNicholas, S. J., Murshudov, G. N., Pannu, N. S., Potterton, E. A., Powell, H. R., Read, R. J., Vagin, A., & Wilson, K. S. (2011). Overview of the CCP4 suite and current developments. *Acta Crystallogr D Biol Crystallogr*, *67*(Pt 4), 235-242. https://doi.org/10.1107/S0907444910045749

Wojdyla, J. A., Kaminski, J. W., Panepucci, E., Ebner, S., Wang, X., Gabadinho, J., & Wang, M. (2018). DA+ data acquisition and analysis software at the Swiss Light Source macromolecular crystallography beamlines. *J Synchrotron Radiat*, *25*(Pt 1), 293-303. https://doi.org/10.1107/S1600577517014503

Wolff, A. M., Nango, E., Young, I. D., Brewster, A. S., Kubo, M., Nomura, T., Sugahara, M., Owada, S., Barad, B. A., Ito, K., Bhowmick, A., Carbajo, S., Hino, T., Holton, J. M., Im, D., O'Riordan, L. J., Tanaka, T., Tanaka, R., Sierra, R. G., . . . Thompson, M. C. (2023). Mapping protein dynamics at high spatial resolution with temperature-jump X-ray crystallography. *Nat Chem*, *15*(11), 1549-1558. https://doi.org/10.1038/s41557-023-01329-4

Wranik, M., Weinert, T., Slavov, C., Masini, T., Furrer, A., Gaillard, N., Gioia, D., Ferrarotti, M., James, D., Glover, H., Carrillo, M., Kekilli, D., Stipp, R., Skopintsev, P., Brünle, S., Mühlethaler, T., Beale, J., Gashi, D., Nass, K., . . . Standfuss, J. (2023). Watching the release of a photopharmacological drug from tubulin using time-resolved serial crystallography. *Nature Communications*, *14*(1). https://doi.org/10.1038/s41467-023-36481-5

Yan, E.-K., Cao, H.-L., Zhang, C.-Y., Lu, Q.-Q., Ye, Y.-J., He, J., Huang, L.-J., & Yin, D.-C. (2015). Cross-linked protein crystals by glutaraldehyde and their applications. *Rsc Advances*, *5*(33), 26163-26174.

Yonath, A., Sielecki, A., Moult, J., Podjarny, A., & Traub, W. (1977). Crystallographic studies of protein denaturation of renaturation. 1. Effects of denaturants on volume and x-ray pattern of crosslinked triclinic lysozyme crystals. *Biochemistry*, *16*(7), 1413-1417.

Zarrine-Afsar, A., Barends, T. R. M., Müller, C., Fuchs, M. R., Lomb, L., Schlichting, I., & Miller, R. J. D. (2012). Crystallography on a chip. *Acta Crystallographica*, *D68*(3), 321-323.

Zhang, F., Shan, B., Wang, Y., Zhu, Z., Yu, Z.-Q., & Ma, C. Y. (2021). Progress and opportunities for utilizing seeding techniques in crystallization processes. *Organic Process Research & Development*, *25*(7), 1496-1511.

2

Micro-Structured Polymer Fixed-Target for Serial Crystallography at Synchrtrons and XFELs

The following section has been published in
IUCRj. ***2023***
doi: 10.1107/S2052252523007595
Contributions: Designed, produced, collected data, and commissioned the MISP-chips

Micro-structured polymer fixed-targets for serial crystallography at synchrotrons and XFELs

Melissa Carrillo [a, b, c], Thomas J. Mason [a], Agnieszka Karpik [a, d], Isabelle Martiel [a], Michal W. Kepa [a], Katherine E. McAuley [a], John H. Beale [a] and Celestino Padeste [a*]

[a] Paul Scherrer Institut, Forschungsstrasse 111, 5232 Villigen, Switzerland
[b] Department of Chemistry, University of Basel, Mattenstrasses 24a, 4002 Basel, Switzerland
[c] Swiss Nanoscience Institute, Klingelbergstrasse 82, 4056 Basel, Switzerland
[d] Institute of Polymer Nanotechonology (INKA), FHNW Univeristy of Applied Sciences and Arts Northwestern Switzerland, School of Engineering, Klosterzelgstrasse 2, 5210 Windisch, Switzerland

Keywords: fixed-targets, serial crystallography, XFELs, SFX, SSX

Abstract

Fixed-targets are a popular form of sample delivery system used in serial crystallography at synchrotron and XFEL sources. They offer a wide range of sample preparation options and are generally easy to use. The supports are typically made from silicon, quartz, or polymer. Of these currently, only silicon offers the ability to perform an aperture-aligned data collection where crystals are loaded into cavities in precise locations and sequentially rastered through in step with the X-ray pulses. The polymer-based fixed-targets have lacked the precision fabrication to enable this data-collection strategy and have been limited to directed raster-scans with crystals randomly distributed across the polymer surface. Here, the fabrication and first results from a new polymer-based fixed-target, the MIcro-Structured Polymer fixed-targets (MISP-chips), are presented. The MISP-chips, like those made from silicon, have a precise array of cavities and fiducial markers. They consist of a structured polymer membrane and a stabilization frame. Crystals can be loaded into the cavities and the excess crystallization solution removed through apertures at their base. The fiducial markers allow for a rapid calculation of the aperture locations. The chips have a low X-ray background and, since they are optically transparent, also allow for an *a priori* analysis of crystal locations. This location mapping could, ultimately, optimize hit-rates towards 100%. A black version of the MISP-chip was produced to reduce light contamination for optical-pump/X-ray probe experiments. A study of the loading properties of the chips reveals that these types of fixed-targets are best optimized for crystals on the order of 25 µm, but quality data can be collected from crystals as small as 5 µm. With the development of these chips, it has been proved that polymer-based fixed-targets can be made with the precision required for aperture-alignment based data-collection strategies. Further work can now be directed towards more cost-effective mass fabrication to make their use more sustainable for serial crystallography facilities and users.

2.1 Introduction

Serial crystallography at X-ray free electron laser (XFEL) and synchrotron light sources, called serial femto-second crystallography (SFX) and serial synchrotron crystallography (SSX), respectively, has proved to be a successful and robust methodology. The method has perhaps best been exemplified by the regular practice of time-resolved crystallography (Redecke *et al.*, 2013; Barends *et al.*, 2015; Ishigami *et al.*, 2019; Nogly *et al.*, 2018; Weinert *et al.*, 2019), but also in damage-free, or low- dose structures (Fukuda *et al.*, 2016; Halsted *et al.*, 2018; Barnes *et al.*, 2019; Moreno-Chicano *et al.*, 2019) and micro *in cellulo* crystallography (Sawaya *et al.*, 2014; Jakobi *et al.*, 2016; Boudes *et al.*, 2017). Excitingly, serial crystallography continues to evolve and find new triggering technologies (Olmos *et al.*, 2018; Mehrabi *et al.*, 2019) and hybrid methods (Kern *et al.*, 2018; Rabe *et al.*, 2021; Kepa *et al.*, 2022).

To cater for these different experiments, a wide variety of delivery methods have been developed (Martiel *et al.*, 2019; Chen *et al.*, 2019). Amongst these, fixed-targets or chips have proved to be a robust and reliable approach (Barends *et al.*, 2022). Fixed-targets can enable two types of data-collection (Figure 2.1): aperture-aligned, where crystals are loaded into precisely positioned cavities at known locations and sequentially exposed, or, directed-raster, where a raster grid is defined over crystals in completely random locations. The utilization of the aperture-aligned mode has only been possible with the utilization of precision silicon fabrication techniques to create micro-structured solid-supports (Oghbaey *et al.*, 2016; Mehrabi *et al.*, 2020) and stage-motion (Sherrell *et al.*, 2015).

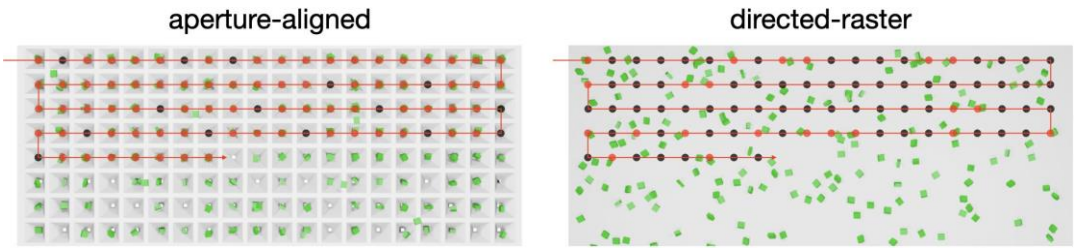

Figure 2.1: Schematic of the different data-collection types supported by fixed-targets. *The two methods of data collection performed on fixed-targets are aperture-aligned and directed-raster fixed-targets. Aperture-aligned fixed-targets allow for crystals to be deposited in precise locations where as directed-raster fixed-targets have the crystals randomly distributed throughout the surface of the chip.*

Although there is still considerable variation around different facilities, silicon fixed-target supports, approximately 30×30 mm^2 with around 25,000 etched cavities, are now commonly used in at least three facilities: Time-Resolved Experiments with Crystallography (TREXX)[1], PETRA III, Germany; ID29[2], ESRF-EBS, France; and I24[3], Diamond Light Source (DLS), UK. Due to the size of the chips, precise cavity placement must also be coupled to precise motion and alignment strategies. The silicon wafer offers a viable means to these ends. The silicon is rigid, inert, and can be precisely chemically etched. Any diffraction spots given by the silicon crystals are more aesthetically disagreeable rather than deleterious to the detector or experiment. The silicon chip has, therefore, been essential to the establishment of aperture-aligned methods in the serial crystallography toolbox.

However, the use of silicon also has a number of disadvantages. Though rigid, even when only 50µm thick, it is also highly brittle and prone to fracture. The silicon is also opaque, making it difficult to know *a priori* how well crystals have been loaded into the cavities.

[1] https://www.embl.org/groups/macromolecular-crystallography/p14-eh2/
[2] https://www.esrf.fr/id29
[3] https://www.diamond.ac.uk/Instruments/Mx/I24.html

Currently, silicon chips are also posing a significant cost to users. Given these issues, it is worthwhile pursuing alternative materials as the basis for such micro-structured supports. Here, polymers offer an advantageous substitute provided a comparable means of cavity fabrication and precision can be achieved.

The use of polymer supports is not new in protein crystallography. Loops and meshes, made from nylon or Kapton^{TM}, are common mounts in cryo-crystallography. Samples either encased or surrounded by pieces of thin-film are also routine under cryo-conditions or at room-temperature (Huang *et al.*, 2015; Axford *et al.*, 2016; Baxter *et al.*, 2016) and enable the directed-raster mode. Recently, more complex micro-structured supports specifically for room-temperature samples have started to become available. The Crystallography Sample Supports (MiTeGen) are mounted on standard SPINE pins but currently lack the larger area format of the silicon chips (Illava *et al.*, 2021). Large-area polymer supports have been developed but are also currently limited to directed-raster data-collection strategies. These range from simple thin-film sandwiches (Doak *et al.*, 2018; Rabe *et al.*, 2020; Park *et al.*, 2020; Lee *et al.*, 2020) [also possible in using quartz (Ren *et al.*, 2018)] to more regular structures encased within film (Lee *et al.*, 2019; Martiel *et al.*, 2021; Nam *et al.*, 2021; Sherrell *et al.*, 2022) or resting on film (Kepa *et al.*, 2022). A method to precisely fabricate a regular array of cavities in a polymer film is still lacking, resulting in the lack of polymer chips in aperture-aligned data-collection modes.

Here, the MIcro-Structured Polymer (MISP) chips are presented. The supports retain very high precision in cavity fabrication, similar to the silicon-based chips; however, their raw materials are a fraction of the cost of the silicon and offer greater flexibility in design and cavity shape. Their stabilizing frame proves to be beneficial in increasing the

hit-rate and sample efficiency. They are also more robust, making them easier to handle and user-friendly when compared to the silicon chips. The chips were tested at the SwissFEL Cristallina experimental station using the serial with solid-support MX (SwissMX) endstation. Due to the success of the chips in the commissioning experiments, they will be the principal work-horse fixed-target of the endstation.

2.2 Methods

2.2.1 Preparation of silicon masters

The fabrication of MISP-chips begins with the preparation of a silicon master from a double-sided, polished, 4" silicon wafer coated with 100 nm silicon nitride (Si_3N_4). The wafer is spin coated with a photosensitive resist (Microposit^{TM} S1813^{TM} G2, Micro Resist Technology) at 4000 rpm and soft-baked for 90s at 115°C. The design for the MISP-chips is created on KLayout software and transferred onto the wafer using laser lithography (Heidelberg Instruments – DWL 66^{+}). The wafer is then placed in a developer bath for 1 min to dissolve away the regions that were exposed to light. The structure is transferred onto the Si_3N_4 through reactive ion etching (RIE) (Oxford Instruments – PlasmaPro 100: 5 sccm O_2, 40 sccm CHF_3, 2min). Subsequently, the wafer is etched through with potassium hydroxide (KOH etching at 80°C, 1.5hr). The wafer is then rinsed with water and the remaining silicon nitride is removed using RIE. In preparation for the following steps, the silicon wafer's surface is activated in oxygen plasma (Oxford Instruments – PlasmaPro 80: 20 sccm O_2, 150 W, 2 min) and then coated with a fluorosilane anti-sticking layer (Schift *et al.*, 2005).

2.2.2 Fabrication of working stamps

A glass wafer is prepared by surface activation with oxygen plasma (Oxford

Instruments – PlasmaPro 80: 20 sccm O_2, 150 W, 2 min), spin-coated with Ormoprime®08 (Micro Resist Technology, 4,000 rpm, 1,000 rmp·s^{-1}, 60 s) then hard baked for 5min at 150°C. Ormostamp® (Micro Resist Technology) is dispensed on the silicon master and covered by the glass wafer, waiting until all cavities are filled. The assembly is then exposed to ultraviolet C (UV-C) radiation (Compact UV-LED Chamber BSL-01 – Opsytec Dr. Gröbel: 210 mW·cm^2, 2min) and hard baked on a hotplate for 30min at 130°C. The samples are then unmolded, resulting in a glass/Ormostamp working stamp used for membrane production. The surface is activated through oxygen plasma (Oxford Instrumets – PlasmaPro 80: 20sccm O_2, 20W, 20s) and finally coated with a fluorosilane anti-sticking layer.

2.2.3 Transparent COP & Black COC

Imprints were performed on transparent 50µm cyclic olefin polymer (COP) (microfluidic ChipShop) and black cyclic olefin copolymer (COC) film. Black COC films were manufactured in-house by first dispersing 1.7g of carbon black (Acetylene Carbon Black Li400, UBIQ, Japan) in 100mL toluene under ultrasound agitation for 1hr. 17.0g of COC granules (8007 x10, TOPAS Advanced Polymers, Oberhausen, Ger- many) were added and dissolved within 24hrs under constant stirring and heating to 60°C. The resulting viscous solution was spread out on glass plates using a ZAA automatic film applicator (Zehntner, Switzerland; barrel applicator with 500 µm gap, 15 mm/s) and dried at 60°C, yielding films with thicknesses in the range of 52-55µm.

2.2.4 Fabrication of fixed-targets

Fixed-target membranes were produced by hot embossing the working stamp into a COP or COC film, backed by 50-250µm of Kapton™ and 0.1 – 1.0mm of Teflon™, using a Jenoptic HEX 03 hot-press (180°C, 300N, 15min). After cooling down, the

structured films, were released from the stamp and underwent plasma activation (Oxford Instruments – PlasmaPro 80: 20sccm O_2, 150W, 2min) shortly before attachment of the frames. Acrylic frames were designed using the software Fusion 360 and 3D printed on a ProJet MJP 2500 Series 3D Printer. Frames were then glued onto the membrane with epoxy glue and left overnight to harden. Afterwards, they were cut and removed from the excess COC and COP film.

2.2.5 Sample preparation

Hen egg-white lysozyme (HEWL) (Sigma Aldrich) was dissolved to a final concentration of 50mg/mL in 0.1M sodium acetate, pH 3.0. The protein concentration was measured using a NanoDrop™ One UV-Vis spectrophotometer (Thermo Scientific) at 280nm using an extinction coefficient of 2,653g·L^{-1}. Different size HEWL micro-crystals were obtained by varying the protein and crystallization buffer concentrations (Table 2.1). The crystallization buffer was 0.1M sodium acetate pH 3.0, 28% (w/v) sodium chloride, 8% (w/v) PEG 6,000. To make the micro-crystal slurry, 500µL of protein and crystallization buffer were mixed in a 1.5mL centrifuge tube and immediately vortexed for 10 s. The centrifuge tube was then left stationary overnight (~16hr) at 20°C. The number of crystals and their sizes were then estimated using a hemocytometer (Hausser Scientific™) and a HIROX RH-2000 digital microscope with a MXB-5000REZ zoom-lens.

Table 2.1. ***Crystal sizes and concentrations grown from different HEWL solutions and crystallization buffer concentrations.*** *All values are given as final concentrations after 1:1 mixing of protein and crystallization buffer solutions.*

[HEWL] (mg/ml)	[crystallization buffer] [% (v/v)]	[crystal] (crystals·mL^{-1})	longest dimension (µm)
25.0	40	3.2×10^8	5 ±1
25.0	35	1.0×10^8	10 ±2
12.5	40	6.9×10^6	25 ±7

2.2.6 Sample loading

A loading station was built for sample loading into the MISP-chips. It consists of a loading platform, a vacuum pump to extract the excess mother liquor, and a humidity stream to keep the crystals from dehydrating during preparation. Vacuum pump suction was controlled with a valve and provided control over the intensity and timing of excess mother-liquor extraction [see SI, Figure 2.9].

The loading platform was designed on Fusion 360 and 3D printed on a ProJet MJP 2500 Series 3D printer [SI Figure 2.9(*b*)]. This loading platform provides a support for the membrane of the MISP-chips whilst under suction, prolonging the lifespan of the MISP-chips. The loading surface contains a gasket cut from a polydimethylsiloxane (PDMS) sheet, serving as a vacuum seal.

The samples were loaded by pipetting the crystal slurry onto the top surface of the chip when placed on the holder and removing the excess mother liquor by applying a vacuum. Loading was performed under a constant humidity stream. The chip was then transferred to a chip holder (designed on Fusion 360 and 3D printed on a ProJet MJP 2500 Series 3D printer) and enclosed with two layers of 6 µm Mylar® film (SI 2.9). Typically, five MISP-chips were loaded, one after another, placed in a chamber, and kept at a constant 80 % humidity before the entire chamber was transported to the hutch. Previous work indicated that samples could be stored in a humidified environment for up to 7 days prior to measurement without apparent loss of diffraction quality (Huang *et al.*, 2022).

2.2.7 Data collection

Data were collected over three beamtimes in May, September, and October 2022 at the Cristallina experimental station of SwissFEL using the SwissMX endstation. Consistent self-amplified spontaneous emission (SASE) parameters were achieved across all three beamtimes with pulse width, peak energy, and repetition rate set to 35fs [20fs root mean square (RMS)], approximately $40 - 50\mu J$, and 100Hz, respectively. The achieved photon energy varied slightly between beamtimes, with central energies of 11.36 ± 0.05, 11.30 ± 0.05, and 11.26 ± 0.05 keV.

All data were collected in air but with scatter guards upstream and downstream of the sample position such that scattering from only a 15mm section of the beam path could reach the detector. The detector distance varied over the three beamtimes from 150 to 110mm which corresponded to an achievable resolution difference of 1.65 to 1.35Å on an 8 Mpixel JUNGFRAU detector.

The MISP-chips are designed with fiducials in known locations to assist aperture alignment (Oghbaey *et al.*, 2016). The *x*/*y*/*z* coordinates of these fiducials were recorded with respect to the X-ray beam. The locations of cavity apertures could then be inferred by a coordinate transformation (Sherrell *et al.*, 2015). Due to the slight shrinkage of chips from their design specifications during the hot-embossing process, the intra-aperture distances needed to be scaled. To do this on a per-chip basis, the mean fiducial distance (FiD_{obs}) was determined by averaging the distance between the four recorded motor positions of each fiducial. The ratio between the designed fiducial distance (FiD_{calc}) could then be used as a 'shrinkage-factor' to be applied to all the other intra-

aperture distances.

$$\text{shrinkage factor} = \frac{\text{Fid}_{obs}}{Fid_{calc}} \quad \text{(eq. 2.1)}$$

2.2.8 Data processing and analysis

CrystFEL (White *et al.*, 2012) version 0.10.0 was used to analyze the data. peakfinder8 and xgandalf were used to find spots and index images, respectively, with the following settings: –threshold=10, –int-radius=3,4,7, –min-snr=5.0, –min-peaks=10, and – min-pix-count=2. Data from the resulting stream files were then individually extracted for downstream analysis. To calculate $CC_{\frac{1}{2}}$'s values, approximately 30,000 integrated patterns for each HEWL crystal sizes were merged using partialator with –model=unity, –iterations=1.

Initial phases were calculated using Phaser (McCoy *et al.*, 2007) and the previously solved HEWL structure, PDB ID 6ABZ, (Seraj & Seyedarabi, 2020) as a search model. Refinement was completed using Phenix (Liebschner *et al.*, 2019) and model building was performed using Coot (Emsley & Cowtan, 2004). Final refinement statistics for all structures are shown in SI, Table 2.2. Figures were made using PyMOL (Schrödinger, LLC, 2015).

2.3 Results

2.3.1 Chip fabrication

2.3.1.1 Membrane manufacturing

The procedure to manufacture the structured polymer membrane, representing the central part of the MISP-chips, is shown in Figure 2.2. It starts with the fabrication of a silicon master; taking advantage of well-established and highly precise silicon micro-

fabrication techniques. More specifically, cavities shaped as inverted pyramids are wet-etched into a silicon ⟨100⟩ wafer [Figure 2.2(*a*)]. A silicon nitride layer structured with laser lithography and reactive ion etching serves as a hard mask during the anisotropic KOH etching. This follows, due to preferential etching in the parallel direction, exactly with the silicon ⟨100⟩-planes, resulting in an angle of the sidewalls of 54.74° with respect to the wafer surface. This angle defines the exact geometry of the pyramids (relation of the base plane and height) and results in constraints for the membrane design (see below).

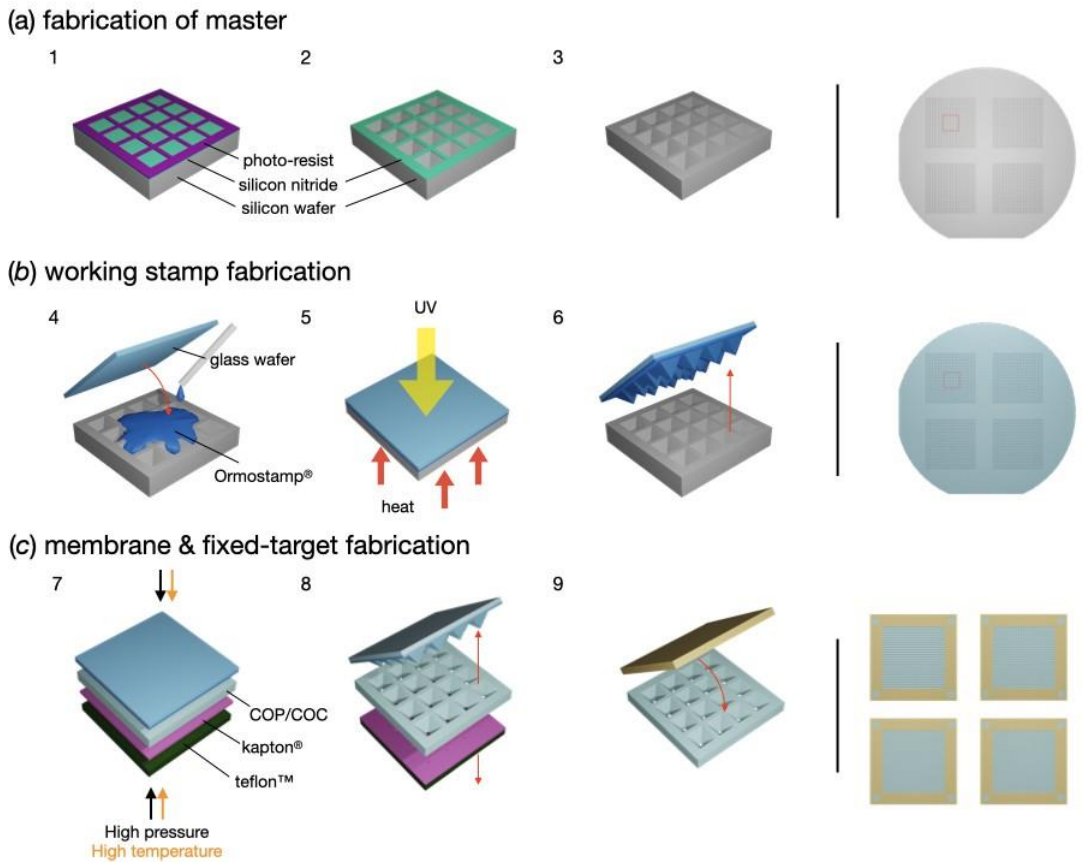

Figure 2.2: Fabrication overview of MISP-chip. *(a) 1. The design of the MISP-chip is translated into a silicon nitride layer on a silicon wafer using laser lithography and reactive ion etching (RIE). 2. KOH etching forms the inverted pyramidal wells at the surface of the silicon wafer. 3. The remaining silicon nitride is removed using RIE, resulting in the master stamp. (b) 4. Ormostamp® is pipetted onto the master and a prepared glass wafer is slowly placed on the top. 5. By applying UV-light and heat the Ormostamp® hardens and molds into the silicon wafer wells. 6. The working stamp is lifted*

off resulting in pyramids on the working stamp. (c) 7. The working stamp is used to imprint the cavities into the COC or COP film through hot-embossing. 8. Film is demolded from the working stamp. 9. Frames are glued onto the film resulting in the final product of the polymer fixed-targets. Images on the right show the final product of the master stamp, working stamp and fixed- targets.

From the master structure, a working stamp copy is made using OrmoStamp®, a UV-curable hybrid material that enables high-fidelity replication of micro-structures and is suitable as a material for nano-imprint lithography [Figure 2.2(*b*)]. This working stamp is then hot-embossed into a film of a thermoplastic material such as COC or COP [Figure 2.2(*c*)]. The exact balance of structure sizes and film thickness as well as material combinations used as backing layers play important roles to obtain cavities in the films with defined apertures at the bottom. As backing of the COC or COP film a polyimide is placed directly underneath, which does not soften at the process temperature. This is followed by Teflon™, which is relatively soft and can level out forces on a larger scale. Pyramid heights must exceed the film thickness by more than the intended punching-through height, as the polymer displaced in the process results in an apparent increase in film thickness (see SI A.2.1). For instance, when using 50µm thick COP films and pyramid structures of 100µm side length (70.80µm height) at 120µm pitch, the formed holes had dimensions of about 5-7µm, indicating that only the top 4-5µm of the pyramids were punching through the film.

2.3.1.2 Parameterization of chips

The MISP-chips are globally defined by three parameters [Figure 2.3(*a*)]:

- the fiducial spacing – the distance between corner fiducials;
- the aperture pitch – the distance between adjacent aperture centers;
- the number of apertures – the number of openings per row of apertures.

Initial designs featured 12.5mm fiducial spacing, 120µm aperture pitch, and an array of 78x78 apertures. This was done to prototype the manufacturing process as well as the fiducial-alignment software. After the first commissioning of the SwissMX instrumentation and confirmation that the MISP-chips were compatible with a fiducial-alignment based data-collection, the MISP-chips were enlarged to increase the total number of available apertures per chip. These larger chips have 23.0mm fiducial spacing, 120µm aperture pitch, and 172x172 apertures, giving an increase in total aperture number from 6,084 to 26,244 per chip.

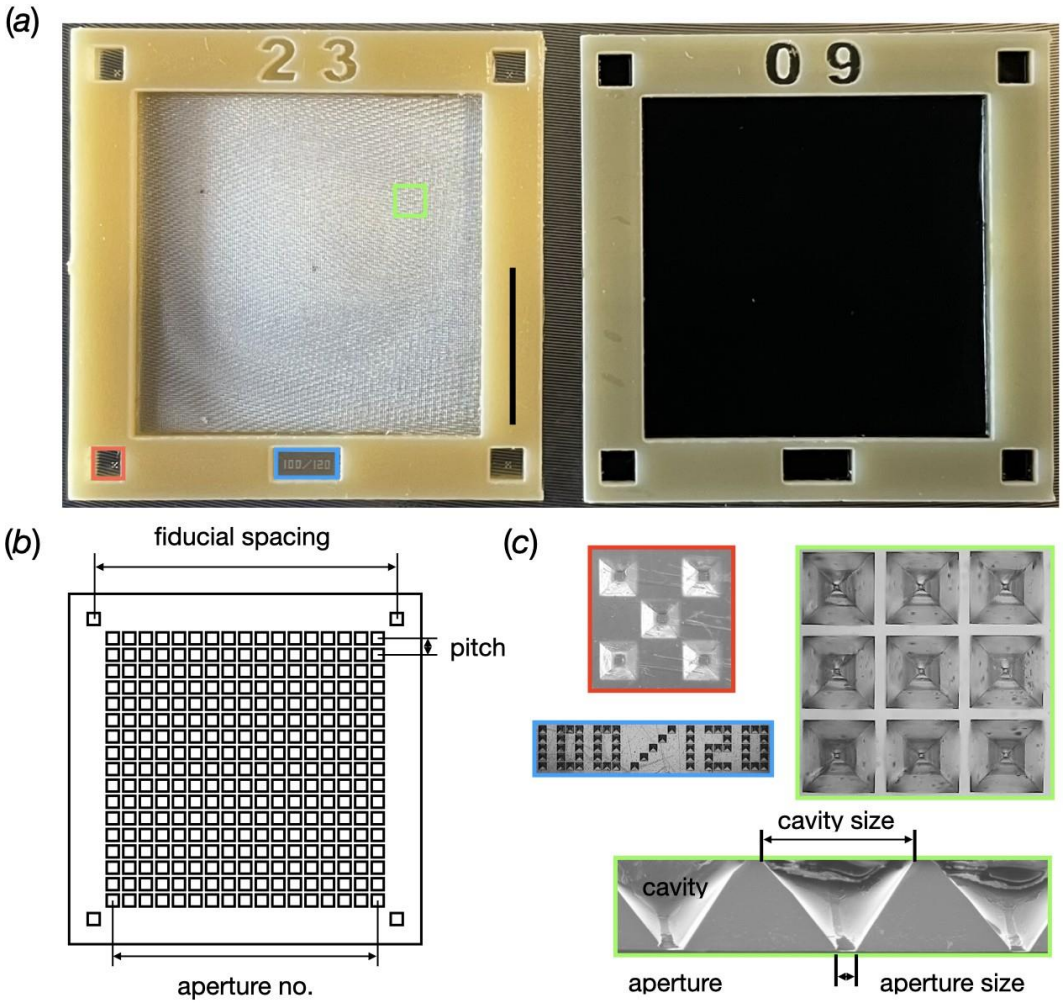

Figure 2.3: An overview of the MISP-chips. *(a) The two current versions of the MISP-chip with transparent COP and black COC membrane. The black scale bar shown on the frame of the transparent COP MISP-chip represents 10mm. (b) The*

parameters used to define the chips. (c) Magnified fiducials (red box), cavities (green box), cavity profiles (green), and label.

MISP-chips were developed on transparent COP and black COC film with thicknesses of 50 ± 1 and 52 ± 3 µm, respectively (see SI A.2.1). There was good agreement between the original layout and the structured replicates in both, the transparent and black films. However, a linear shrinkage of the dimensions of about 1 % was determined on both types of films, which was assigned to a contraction of the material when cooling down from the embossing temperature. The aperture sizes in the center of the membrane area varied between the two film types [Figure 2.3(*b*)]. For the transparent chips, they were consistently between 5 and 7µm. On the black chips, they were more dependent on the batch of film and fluctuated in a range from 4 to 12µm.

For both the transparent and black chips, there were consistent variations in aperture sizes around the edges of the membrane. This was due to the build-up of excess material shifting during hot embossing. The rows on the edge of the cavity arrays consistently showed larger apertures. For the transparent and black chips, the maximum observed apertures measured about 13 and 20µm, respectively (for details see SI A.2.1). However, issues that may have arisen from this phenomenon were limited since most of the enlarged apertures were covered when the chip frames were glued onto the film surface.

2.3.1.3 Overcoming chip bending

In the first round of chip making, the chips showed a pronounced bending orthogonal to the membrane, sometimes as large as 100 − 200µm from base to apex. This was found to be caused by the fixation of the frame to the COP and COC

membrane. The fixation was performed in the same manner as reported earlier (Karpik *et al.*, 2020), *i.e.*, by directly printing a polylactic acid (PLA) frame onto the COP film using a filament printer. However, direct printing caused the membrane to heat and the bending was a result of the different thermal expansion coefficients of the film and PLA filament. To overcome this issue, frames were 3D printed on a multi-jet printer using acrylic and then fixed onto the membrane with epoxy glue. This change rectified the pronounced bending.

2.3.2 Loading analyzes

Loading of crystals onto the MISP-chips was done using a humidity sample loading station constructed specifically for the MISP-chips [(see SI A.2.2)(*a*)]. This setup provided a humidity stream over the sample loading platform [SI A.2.2)(*b*)] which was attached to a vacuum pump. This allowed for the excess mother-liquor to be removed while keeping the crystals hydrated. A chip was placed onto the sample loading platform and then the crystal slurry was pipetted onto the surface of the chip. The valve to the pump was then opened and excess mother-liquor was removed. Once done, the chip was placed into a chip holder, sealed [see SI A.2.2)(*c*)], and placed in a humidity chamber.

Two different strategies were used to load the sample onto the chips. Initially, crystals were loaded with just enough solution such that the slurry could be spread over the surface of the chip [Figure 2.4(*a*)]. This ‘high-conc/low-vol’ strategy proved effective for 25µm HEWL crystals and was comparable, in terms of hit-rate, to the silicon chips with 25µm insulin crystals loaded in a similar manner [Figure 2.4(*c*)] (Davy *et al.*, 2019).

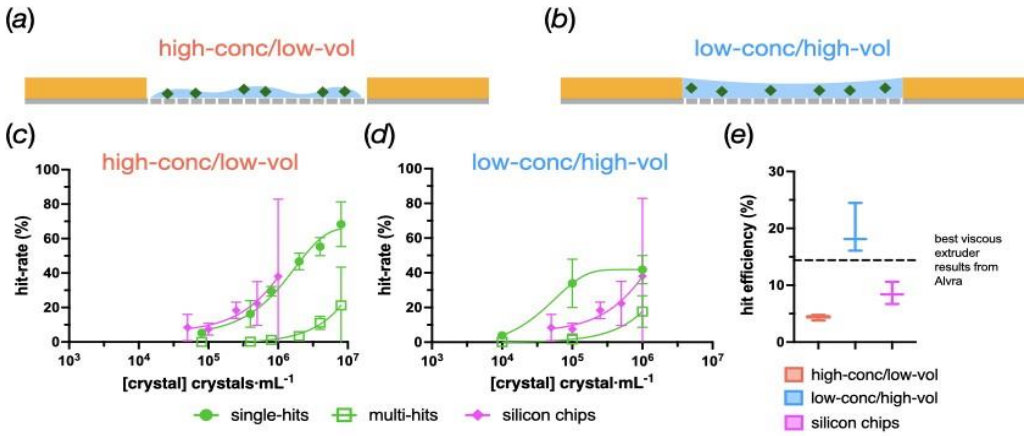

Figure 2.4: A comparison of different loading methods. *(a) and (b) schemes showing the practical difference between the loading methods. In 'high-conc/low-vol' experiments, low volumes of highly concentrated slurries were tested (a). In 'low-conc/high-vol' experiments, the reverse was true; higher volumes of less concentrated slurries were used (b). (c) and (d) graphs plotting aperture hit-rates as a function of crystal concentration for 25µm HEWL crystals for the high-conc and low-conc methods, respectively. The aperture hits have been divided into single and multi-hits to indicate whether one or more than one crystal was found in the well. Data obtained from 25µm insulin crystals deposited on silicon chips at a synchrotron (Davy et al., 2019) has also been plotted for comparison. (e) An assessment of the loading efficiency given as a percentage of the absolute number of crystals used vs exposed. The single-hit data from silicon chips (Davy et al., 2019) have also between plotted and an estimate of the efficiency of a viscous extruder, with comparably sized crystals, from a beamtime at the SwissFEL Alvra endstation.*

However, moving to a low-concentration/high-volume method was found to be beneficial for the sample deposition. Here, a larger volume of solution was used to load the same number of crystals such that the entire well surrounded by the acrylic frame was filled with liquid [Figure 2.4(*b*)]. This change meant that a much lower crystal concentration was required to achieve comparable hit-rates [Figure 2.4(*d*)]. It also proved to drastically improved the sample efficiency.

Figure 2.4(*e*) shows the absolute hit-rate with respect to the actual number of crystals that were loaded onto the chips. The low-conc/high-vol strategy shows an approximate 4 and 2-fold increase in sample efficiency compared to the high-conc/low-vol method and data obtained from silicon chips, respectively. An estimated sample efficiency

is also shown from a viscous extruder experiment measured at Alvra. The low-conc/high-vol method is on par with this as well. All subsequent data shown in this paper were collected using this low-conc/high-vol loading method.

2.3.3 The effect of crystal size and concertation on hit-rate

It became clear from the first experiments that crystal size was a significant factor in determining the eventual hit-rate. To test this systematically, 5, 10, and 25 µm HEWL crystals were prepared. Chips were then loaded with different concentrations of these crystals and the hit-rates were recorded (Figure 2.5). Apertures that gave rise to hits have been split into either single-hit or multi-hit, signifying that either only a single diffraction pattern or overlaid patterns were observed, respectively.

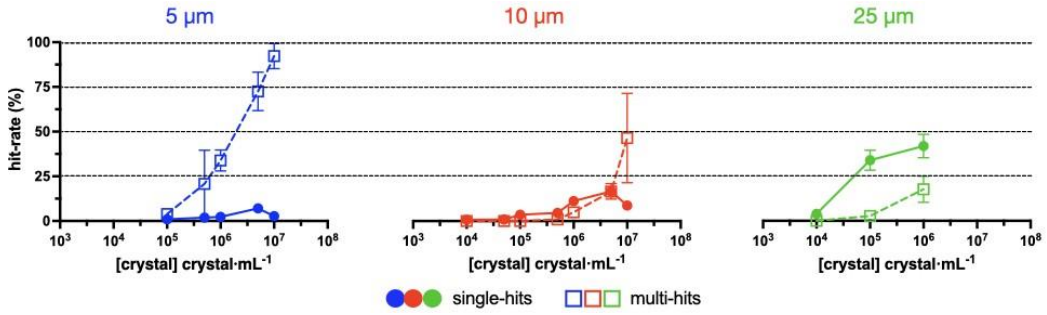

Fig. 2.5: The effect of HEWL crystal size and concentration on hit-rate. *The mean and 95 % confidence interval for each data point have been plotted. Each data point was based upon at least three measurements. Single and multi-hit denote either single or multiple crystal lattices observed in each well, respectively.*

The results indicate that it is very challenging to obtain a high rate of single hits (> 30 %) for crystals ≤10µm. It appears that for smaller crystals, a higher concentration is required to locate crystals in the chip apertures. This can best be observed by comparing the hit-rates at a concentration of 1×10^5 crystals·mL^{-1}. This is enough to obtain a hit-rate of over 30 % in the 25µm crystals, but only 2% in the 10µm and 1% in the 5µm

crystals. As the concentration in the 5µm and 10µm crystals is increased, the hit-rates do improve, but both in the number of single and multi-hits observed. This effect is particularly pronounced for the 5µm crystals.

2.3.4 Comparing calculated and observed hit-rates

One of the benefits of the fixed-targets, when compared to other delivery methods, is that it should be possible to determine crystal distribution before data collection. The logical extension of this idea is 'chip-mapping' (Oghbaey *et al.*, 2016), where all crystal locations on the chip are known, such that empty apertures can be avoided and close to 100% hit-rates obtained. However, crystals loaded on opaque silicon chips proved difficult to see under a microscope and, so far, could only be spectroscopically observed when the protein crystals were colored (Oghbaey *et al.*, 2016).

The clear COP chips changed this. Crystals loaded are now clearly observable under a standard microscope [Figure 2.6(*a*) and (*b*)]. These images give us a better understanding of the low hit rates when using 5 and 10µm crystals. Smaller crystals appear to be scattered throughout the surface of the chip rather than being drawn into the apertures at the center of the cavities.

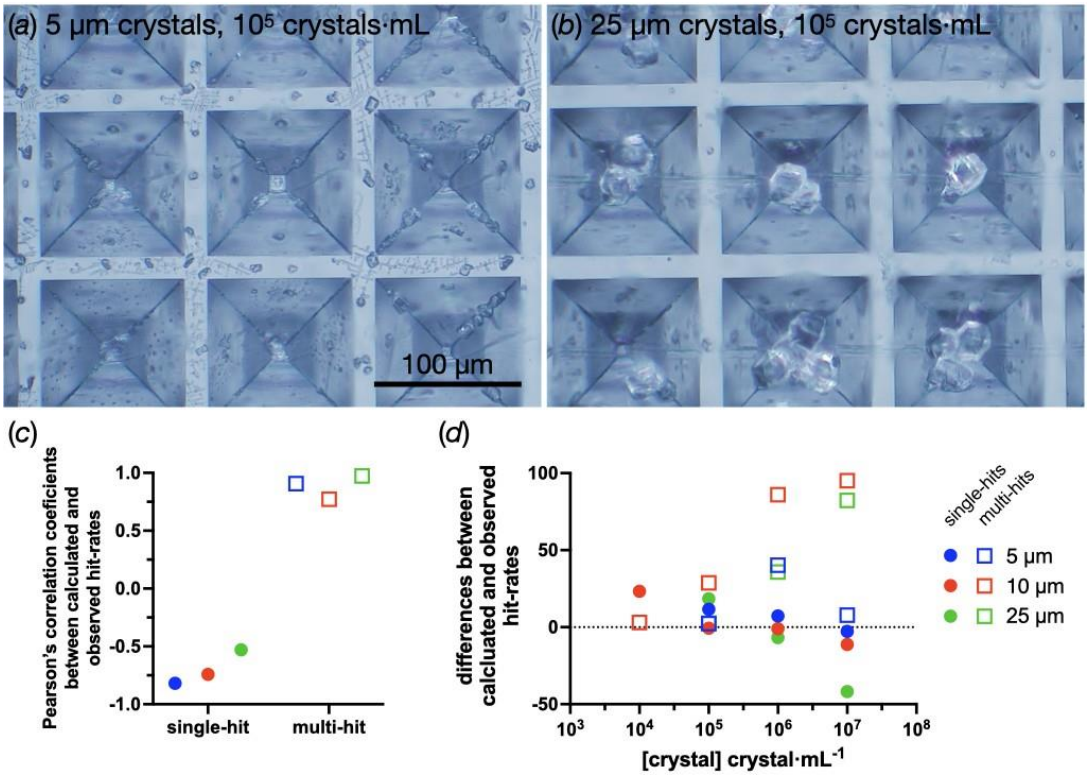

Figure 2.6: The opportunities and problems with observing crystal locations under a microscope. *(a) and (b) Wells from chips loaded with 5 and 25µm crystals at 1 × 10^5 crystals·mL^{-1}, respectively. (c) The correlation between calculated (counted under a microscope) and observed (diffraction detected) hit-rates for the 5, 10, and 25µm crystals. (d) The residual differences between the observed and calculated hit-rates.*

Given the fact that crystals are clearly visible on the clear chips, it should be possible to check the loading of the fixed-target once it has been prepared, giving users real-time feedback on sample preparation. However, the natural excitement towards this opportunity should be tempered as the human eye and mind can be easily fooled. Figure 2.6(*c*) shows the Pearson's correlation coefficient between the 'microscope-calculated' and diffraction-observed hit-rates for both single and multi-hits. Even a favorable interpretation of these data with regard to the multi-hit correlation should be tempered. Figure 2.6(*d*) shows the differences between the calculated and observed rates in terms of real numbers, showing that even positive correlations can be widely inaccurate.

2.3.5 Diffraction quality

Finally, it is worth looking at the quality of the data that can be obtained when using the MISP-chips. Unlike other delivery methods, fixed-targets will usually place solid material in the path of X-rays, therefore, the background is a serious consideration. Figure 2.7(*a*) shows the mean radial integral of the detector from a MISP-chip in air collected at 11.34keV and a pulse energy of approximately 50µJ. For comparison, a radial integral from a 50µm viscous jet collected in the SwissFEL's Alvra gas-chamber at 200mbar He and 12.4keV is also shown. Pleasingly, both are very comparable. In the near future, SwissMX will also be capable of data collections in a helium environment, reducing background noise even further.

Figure 2.7(*b*) shows the $CC_{\frac{1}{2}}$ plots for the three HEWL samples used to evaluate the chip loading. There is a gradual decline in the quality of the data, based on $CC_{\frac{1}{2}}$, as a function of the crystal size. The difference is almost negligible between the 25 and 10µm crystals but is quite pronounced for the 5µm crystals. A drop in resolution using the 0.3 criterion from 1.41 to 1.54Å was determined.

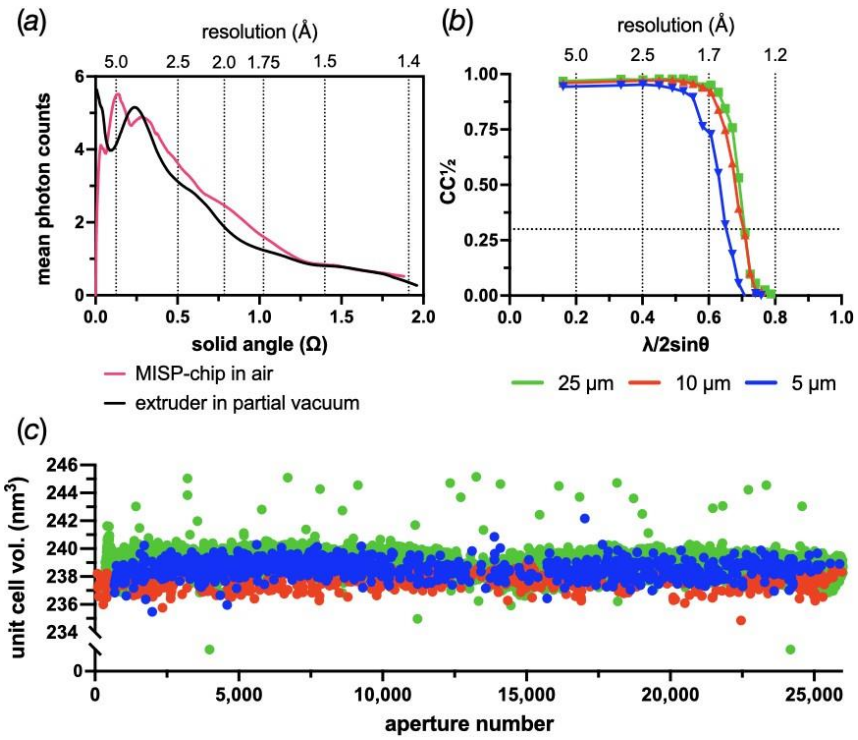

Figure 2.7: Data quality indicators from chip data-collections. *(a) A comparison of the total background observed between the MISP-chips collected at Cristallina and the viscous extruder collected in the Alvra gas-chamber with 200 mbar He. The background is shown as a radial integral given in mean photon counts. The solid angle shown has been limited to the effective size of a 4 Mpixel detector. The total background from the MISP-chip will also include contributions from the air, sealing films and sample. (b) $CC^{1}/2$ plots for the 25, 10, and 5µm HEWL crystals. Each is based on approximately 30,000 integrated and merged images. The 0.3 criterion line has been shown. (c) The unit-cell volume plotted as a function of aperture number for representative chips loaded with 25, 10, and 5µm HEWL crystals.*

To see if there was any degradation of crystal quality as the chip is exposed to the beam, the unit cell volume was calculated for every single crystal hit. The volumes were then plotted as a function of the aperture number to see if any change was observable. No change was detected throughout the 5 minutes of collection time for either the 25, 10, or 5 µm HEWL crystals; typical results are shown in Figure 2.7(*c*).

When working with fixed-targets, one must keep in mind that the crystals are being placed onto a surface which can raise concern to preferential orientation. Evaluation of the crystal orientation [(SI A.2.4)] indeed showed a certain degree of preferential

orientation, but the small magnitude did not affect the structure determination in the present case. However, preferential orientation is expected to be more pronounced for highly anisotropic crystal shapes such as platelets and needles and needs to be evaluated for individual cases. Structures were solved for all three different crystal sizes [(SI A.2.5)], with a resolution of 1.54Å for the 5µm crystals, and 1.40Å for the 10 and 25µm crystals, and in good agreement with published room temperature HEWL data.

2.4 Discussion

The MISP-chips are an attempt to combine the precision of the silicon micro-structured chips (Oghbaey *et al.*, 2016; Ebrahim *et al.*, 2019; Mehrabi *et al.*, 2020) with the ease of use and low cost of the polymer supports. By creating a precise array of apertures in a polymer, aperture-alignment style data-collection strategies can be performed. Like many such endeavors aimed at trying to capture all that is best and none that is worst, some compromises were required.

2.4.1 MISP-chip characterization

The first priority was to devise a fabrication process that had the precision to facilitate aperture-alignment style data collections. This was achieved using a combination of silicon micro-fabrication and hot-embossing techniques. The first prototype was 8 × 8 mm (4,356 cavities) then scaled to 12.5 × 12.5 mm (7,056 cavities) and currently 23 × 23 mm (29,584 cavities) from fiducial to fiducial. The increase in size had no side effects to its precision.

The hot embossing step during film membrane fabrication (Figure 2.2) slightly affects the precision of the MISP-chip, in that the film contracts by about 1 % when cooling down from the imprinting temperature. Once shrinkage is determined, all intra-

aperture distances could be appropriately scaled. This information is added into the alignment algorithm, leading to very high accuracy of aperture alignment. When apertures are missed, the resulting increase in the background appears to be small [Figure 2.7(*a*)] and the hit-rates remain comparable to the silicon chips.

During the hot embossing of the pyramid structures, the material of the film gets pushed to the outer edges of the pyramids, causing a substantial increase in film thickness. To compensate for this, pyramid heights were recalculated and modified on both master and working stamps to reach desired aperture sizes. Material drift also causes edge apertures to have an increase size as material is able to be distributed to the outer parts of the membrane. The larger edge apertures do not appear to affect the loading of crystals as high hit-rates could be achieved when compared to the silicon supports [Figure 2.4(*c*) and (*d*)]. It is possible that a higher density of multiple hits found towards the edges of the membranes is partly caused by these larger apertures (SI Figure 2.10).

The intrinsic flexibility of the films used for membrane fabrication necessitated the attachment of a stabilization frame. This turned out to be an advantage as it allowed for larger volumes of solution to be loaded onto the surface of the chip, improving the crystal loading efficiency (Figure 2.4). The frame provided rigidity to the MISP-chip and allows the chip to be robust and user friendly. The principal disadvantage of the frame is that it necessitates an extra fabrication step and needs to be precisely fixed to the membrane. Wells can be covered by the chip frame which reduces the number of available chip apertures that can be exposed; this non-ideal solution will be refined in time in future chip iterations.

An essential piece of the loading process is the loading stage and set-up. Initial trials of excess mother-liquor extraction consisted of blotting paper where the main aim

was to blot out the liquid from the back of the MISP-chip. However, this was not efficient, resulting in excess mother liquor, high background and low hit-rates. This led to the development of the loading stage, resulting to be extremely beneficial as it provided an efficient method for extraction of excess mother-liquor with the use of a vacuum pump. This improved the distribution of crystals, hit-rate, background and provided an additional membrane support, protecting and prolonging the life of the membrane. Several types of proteins and crystals have been loaded on the chips and successfully tested during beamtimes, such as soluble proteins and membrane proteins, in the form of cubic, rod and plate shaped crystals.

The MISP-chips are reusable due to the stability of the polymer film, the rigidity provided by the frames and the loading stage. On average a chip can be used 5-10 times without impacting crystal deposition, misalignment or increasing background noise, depending on protein type, crystal size, crystal concentration, solution viscosity, additives, and formation of protein aggregates. To reuse the chips, they are soaked or sonicated in water or any polar solvent and air-dried afterwards.

To make better usage of limited beamtimes at X-ray sources, an even higher density of cavities on a chip might be desirable. For instance, going from a 120µm to a 100µm pitch would increase the density of cavities by more than 40%. Here, the current fabrication method poses limitations given by the angle of the pyramid sidewalls, defined by the KOH etching process of silicon and the film thickness. Reducing the pitch of the structures leads to smaller pyramids, which may only punch through films of smaller thicknesses. However, polymer films of similar quality and precise thicknesses in the range of 30-40µm are not available off the shelf, and the production of dedicated films is very expensive given the low volume needed even for the production of several hundred chips.

Production of pyramid arrays of higher aspect ratios might be feasible using non-silicon-based microfabrication methods. However, it will be difficult to reach similar precision of the structures to be used as embossing stamp, terms of positioning, sharpness of the tip and of the aspect ratios.

2.4.2 Opaque MISP-chips for time-resolved serial crystallography

Pump-probe time-resolved serial crystallography (TR-SX) allows for observation of real-time changes in light triggering systems (Moffat, 2001). In order to perform such experiments with the MISP-chips further developments were required. In fixed- target laser-pumped SFX, the key concern is ensuring that neighboring wells are not contaminated by light. This is partly controlled by the size of the laser spot and the alignment of the laser and X-ray beam with respect to the chip. Efficiency removal of excess mother liquor is also important. However, is also critical to guarantee that light is not transmitted through the chip between wells. Due to this concern, a focus to explore opaque films was prioritized, resulting in the fabrication of black COC MISP-chips.

Film production was done in-house since an opaque, thin, and consistent COC or COP film is not commercially available. Methods such as film extrusion at a pilot plant was explored but, ultimately, solvent casting resulted in the most consistent thickness distribution for the film. The thickness range of films obtained in this process did play a slight role in the consistency of the aperture sizes in the membrane, causing a larger distribution of aperture sizes throughout the membrane. To further optimize the consistency of the aperture sizes of the black COC MISP-chips film extrusion or other methods of film production will be considered in the future.

The black film provides a barrier for the light used to illuminate specific wells not to trespass onto its neighboring wells, inhibiting light contamination through the chip. It is now feasible to conduct laser-pump TR-SX experiments using the black

MISP-chips. Initial studies and results conducted with the black MISP-chips will be presented in an upcoming paper.

2.4.3 A question of crystal size

The study into the effects of crystal size and concentration on fixed-target loading is essentially a more systematic continuation of those performed by Davy *et al*. (2019). The results show that single-hits are far easier to attain for 25µm crystals than for 5µm crystals (Figure 2.5). Based on first tests, this appears true independent of crystal shape (e.g. rod and plate shaped crystals). Multi-hits may not be a significant problem for static serial crystallography experiments such as radiation-damage-free structures, but they are not ideal in time-resolved pump-probe experiments.

In time-resolved experiments, protein molecules inside the crystal need to be triggered, typically by a pump-laser but potentially also a substrate solution (Schulz *et al.*, 2022). The size and number of crystals in a fixed-target cavity will greatly affect the activation efficiency of a trigger as they will determine its penetration into the crystals. This determines the excited fraction of the proteins within the crystal and, hence, the observable signal in the diffraction pattern (Schmidt, 2013; Grünbein *et al.*, 2020). Small, single crystals are ideal for such studies.

Our data on loading of the MISP-chips, and in fact other micro-structured solid supports suggest that the > 30% hit-rates promised by fixed-targets is only possible for

single crystals on the order of 25µm rather than 5µm. This is of particular concern for substrate-mixing experiments where <5µm crystals are not only essential for excited fraction but also the activation time (Schmidt, 2013). It is possible that a different loading method, such as with an acoustic droplet ejector, can help resolving this problem (Davy *et al.*, 2019). However, it is also possible that an alternative chip design, specifically for use with small crystals would help.

The modelling of serial crystallography hit-rates is typically done using Poissonstatistics (Park *et al.*, 2013; Hunter *et al.*, 2014). Anecdotally, these predictions never quite fit with the experience of actually using the apertured fixed-targets which tended to give a better ratio of single to multi-hits than would have been predicted by a Poisson distribution. The explanation for this was that the crystals were no longer randomly distributed on a plane, but funneled into locations [Figure 2.6(*b*)]. It is very possible that this feeling of non-conformity was primarily based on samples where crystals were >10µm and that fixed-targets users self-selected for these types of samples.

The 5µm crystals, by comparison to the 25µm, are much more randomly distributed upon the chip surface at the 10^5 crystals·mL^{-1} or, approximately, 400 crystals·mm^2 [Figure 2.6(*a*) and (*b*)]. At these concentrations, the 5µm crystals don't appear to be drawn into the center of the apertures. A future development here could be to increase the number of chip apertures by decreasing the thickness of the film, pitch size and cavity size, thereby, increase the number of focusing points for the crystals to funnel into as the mother liquor is removed by either blotting or vacuum.

The diffraction quality of the 5 µm crystals is also a slight concern given the reduction in observed resolution as measured by the $CC^{1}/_{2}$ [Figure 2.7(*b*)]. However, here an increase in the XFEL transmission is probably the simplest solution. The 50µJ pulse

used in all the commissioning experiments was initially chosen as the 25µm HEWL crystals gave rise to overloads on the JUNGFRAU detector. This pulse energy represented a transmission of 10% of the beam. Given the lower resolution diffraction, an increase in transmission could probably be safely attempted.

2.4.4 Towards 100% hit-rates

The promise of 100% hit-rates has often been touted by many serial crystallography sample delivery techniques. Fixed-targets have, at least, presented a possible method to achieve this: crystal location mapping. For the opaque silicon fixed-targets, a method to achieve this has already been shown using absorption spectroscopy; albeit for a colored protein (Oghbaey *et al.*, 2016). Therefore, the mapping of the silicon chips has currently failed to progress further.

Transparent polymer targets present the possibility of using light microscopy to find crystal located randomly on a mesh or encased between thin-films (Martiel *et al.*, 2021). Problems can arise if crystals are able to move but if imaging and software can be developed to reliably find crystals, mapping is possible. This is now also true for the transparent MISP-chips.

Although, microscopic inspection of areas did not match well with observed hits (Figure 2.6), a more systematic, automated approach could be successful. The main problem to overcome is the heterogeneous crystal loading (see SI A.2.3). If this problem is solved, the possibility for an aperture-aligned data-collection with crystals in known locations can be realized. Then empty apertures can be ignored, thus further increasing the project turnover of the endstation. For data-collections using the SwissMX at Cristallina

this could considerably increase throughput. With the implementation of a robotic sample changer, 6 full-chip (23 x 23 mm chip) data collections per hour will be easily possible. If only wells with crystals were exposed, 9-10 chips per hour might be possible.

2.5 Conclusions

The MISP-chips were developed to enable aperture-aligned style data-collections in polymer-based fixed-targets. From the results presented here, the hot-embossing of thermoplastics has been shown to be a valid method to create cavities with well- defined apertures at their bottom in a 50µm thick polymer film. The resulting fixed- targets were shown to be robust and preferable to other fixed-targets and delivery methods in terms of quantity and quality of data that can be recorded. There are still areas of these chips that require on-going optimization, particularly in sample loading and for 5 and 10µm crystals. The 23 × 23 mm chip, however, has proven to be a good first iteration and after expansion to 25 × 25 mm, it will be the workhorse of the SwissMX endstation at Cristallina, SwissFEL, for experiments such as time-resolved pump-probe and substrate mixing over the next years. The chips are normally reusable up to 5-10times and could have a price point below that of similar silicon chips. The production is still complex and expensive due to the multi-stage silicon micro-fabrication and hot embossing process. It may be possible to move towards combination of roll-embossing and injection molding style manufacturing processing, which after set-up costs could drastically reduce the fabrication costs. Ultimately, it is hoped that the MISP-chip can reduce the barriers to serial crystallography and further its reach in the structural biologist's toolbox.

2.6 References

Axford, D., Aller, P., Sanchez-Weatherby, J., & Sandy, J. (2016). Applications of thin-film sandwich crystallization platforms. *Acta Crystallogr F Struct Biol Commun*, *72*(Pt 4), 313-319. https://doi.org/10.1107/S2053230X16004386

Barends, T. R., Foucar, L., Ardevol, A., Nass, K., Aquila, A., Botha, S., Doak, R. B., Falahati, K., Hartmann, E., Hilpert, M., Heinz, M., Hoffmann, M. C., Kofinger, J., Koglin, J. E., Kovacsova, G., Liang, M., Milathianaki, D., Lemke, H. T., Reinstein, J., . . . Schlichting, I. (2015). Direct observation of ultrafast collective motions in CO myoglobin upon ligand dissociation. *Science*, *350*(6259), 445-450. https://doi.org/10.1126/science.aac5492

Barends, T. R., Foucar, L., Botha, S., Doak, R. B., Shoeman, R. L., Nass, K., Koglin, J. E., Williams, G. J., Boutet, S., Messerschmidt, M., & Schlichting, I. (2014). De novo protein crystal structure determination from X-ray free-electron laser data. *Nature*, *505*(7482), 244-247. https://doi.org/10.1038/nature12773

Barends, T. R. M., Stauch, B., Cherezov, V., & Schlichting, I. (2022). Serial femtosecond crystallography. *Nat Rev Methods Primers*, *2*. https://doi.org/10.1038/s43586-022-00141-7

Barnes, C. O., Wu, Y., Song, J., Lin, G., Baxter, E. L., Brewster, A. S., Nagarajan, V., Holmes, A., Soltis, S. M., & Sauter, N. K. (2019). The crystal structure of dGTPase reveals the molecular basis of dGTP selectivity. *Proceedings of the National Academy of Sciences*, *116*(19), 9333-9339.

Baxter, E. L., Aguila, L., Alonso-Mori, R., Barnes, C. O., Bonagura, C. A., Brehmer, W., Brunger, A. T., Calero, G., Caradoc-Davies, T. T., Chatterjee, R., Degrado, W. F., Fraser, J. S., Ibrahim, M., Kern, J., Kobilka, B. K., Kruse, A. C., Larsson, K. M., Lemke, H. T., Lyubimov, A. Y., . . . Cohen, A. E. (2016). High-density grids for efficient data collection from multiple crystals. *Acta Crystallogr D Struct Biol*, *72*(Pt 1), 2-11. https://doi.org/10.1107/S2059798315020847

Chen, J. P. J., Donatelli, J. J., Schmidt, K. E., & Kirian, R. A. (2019). Shape transform phasing of edgy nanocrystals. *Acta Crystallogr A Found Adv*, *75*(Pt 2), 239-259. https://doi.org/10.1107/S205327331900113X

Davy, B., Axford, D., Beale, J. H., Butryn, A., Docker, P., Ebrahim, A., Leen, G., Orville, A. M., Owen, R. L., & Aller, P. (2019). Reducing sample consumption for serial

crystallography using acoustic drop ejection. *J Synchrotron Radiat*, *26*(Pt 5), 1820-1825. https://doi.org/10.1107/S1600577519009329

Doak, R. B., Nass Kovacs, G., Gorel, A., Foucar, L., Barends, T. R., Grünbein, M. L., Hilpert, M., Kloos, M., Roome, C. M., & Shoeman, R. L. (2018). Crystallography on a chip–without the chip: Sheet-on-sheet sandwich. *Acta Crystallographica Section D: Structural Biology*, *74*(10), 1000-1007.

Ebrahim, A., Appleby, M. V., Axford, D., Beale, J., Moreno-Chicano, T., Sherrell, D. A., Strange, R. W., Hough, M. A., & Owen, R. L. (2019). Resolving polymorphs and radiation-driven effects in microcrystals using fixed-target serial synchrotron crystallography. *Acta Crystallogr D Struct Biol*, *75*(Pt 2), 151-159. https://doi.org/10.1107/S2059798318010240

Fukuda, Y., Tse, K. M., Nakane, T., Nakatsu, T., Suzuki, M., Sugahara, M., Inoue, S., Masuda, T., Yumoto, F., Matsugaki, N., Nango, E., Tono, K., Joti, Y., Kameshima, T., Song, C., Hatsui, T., Yabashi, M., Nureki, O., Murphy, M. E., . . . Mizohata, E. (2016). Redox-coupled proton transfer mechanism in nitrite reductase revealed by femtosecond crystallography. *Proc Natl Acad Sci U S A*, *113*(11), 2928-2933. https://doi.org/10.1073/pnas.1517770113

Grunbein, M. L., Stricker, M., Nass Kovacs, G., Kloos, M., Doak, R. B., Shoeman, R. L., Reinstein, J., Lecler, S., Haacke, S., & Schlichting, I. (2020). Illumination guidelines for ultrafast pump-probe experiments by serial femtosecond crystallography. *Nat Methods*, *17*(7), 681-684. https://doi.org/10.1038/s41592-020-0847-3

Halsted, T. P., Yamashita, K., Hirata, K., Ago, H., Ueno, G., Tosha, T., Eady, R. R., Antonyuk, S. V., Yamamoto, M., & Hasnain, S. S. (2018). An unprecedented dioxygen species revealed by serial femtosecond rotation crystallography in copper nitrite reductase. *IUCrJ*, *5*(Pt 1), 22-31. https://doi.org/10.1107/S2052252517016128

Huang, C.-Y., Olieric, V., Ma, P., Panepucci, E., Diederichs, K., Wang, M., & Caffrey, M. (2015). In meso in situ serial X-ray crystallography of soluble and membrane proteins. *Acta Crystallographica Section D: Biological Crystallography*, *71*(6), 1238-1256.

Huang, C. Y., Aumonier, S., Engilberge, S., Eris, D., Smith, K. M. L., Leonarski, F., Wojdyla, J. A., Beale, J. H., Buntschu, D., Pauluhn, A., Sharpe, M. E., Metz, A., Olieric, V., & Wang, M. (2022). Probing ligand binding of endothiapepsin by ;temperature-resolved' macromolecular crystallography. *Acta Crystallogr D Struct Biol*, *78*(Pt 8), 964-974. https://doi.org/10.1107/S205979832200612X

Hunter, M. S., Segelke, B., Messerschmidt, M., Williams, G. J., Zatsepin, N. A., Barty, A., Benner, W. H., Carlson, D. B., Coleman, M., & Graf, A. (2014). Fixed-target protein serial microcrystallography with an x-ray free electron laser. *Scientific reports*, *4*(1), 6026.

Illava, G., Jayne, R., Finke, A. D., Closs, D., Zeng, W., Milano, S. K., Huang, Q., Kriksunov, I., Sidorenko, P., Wise, F. W., Zipfel, W. R., Apker, B. A., & Thorne, R. E. (2021). Integrated sample-handling and mounting system for fixed-target serial synchrotron crystallography. *Acta Crystallogr D Struct Biol*, *77*(Pt 5), 628-644. https://doi.org/10.1107/S2059798321001868

Ishigami, I., Lewis-Ballester, A., Echelmeier, A., Brehm, G., Zatsepin, N. A., Grant, T. D., Coe, J. D., Lisova, S., Nelson, G., Zhang, S., Dobson, Z. F., Boutet, S., Sierra, R. G., Batyuk, A., Fromme, P., Fromme, R., Spence, J. C. H., Ros, A., Yeh, S. R., & Rousseau, D. L. (2019). Snapshot of an oxygen intermediate in the catalytic reaction of cytochrome c oxidase. *Proc Natl Acad Sci U S A*, *116*(9), 3572-3577. https://doi.org/10.1073/pnas.1814526116

Jakobi, A. J., Passon, D. M., Knoops, K., Stellato, F., Liang, M., White, T. A., Seine, T., Messerschmidt, M., Chapman, H. N., & Wilmanns, M. (2016). In cellulo serial crystallography of alcohol oxidase crystals inside yeast cells. *IUCrJ*, *3*(2), 88-95.

Kepa, M. W., Tomizaki, T., Sato, Y., Ozerov, D., Sekiguchi, H., Yasuda, N., Aoyama, K., Skopintsev, P., Standfuss, J., Cheng, R., Hennig, M., & Tsujino, S. (2022). Acoustic levitation and rotation of thin films and their application for room temperature protein crystallography. *Sci Rep*, *12*(1), 5349. https://doi.org/10.1038/s41598-022-09167-z

Kern, J., Chatterjee, R., Young, I. D., Fuller, F. D., Lassalle, L., Ibrahim, M., Gul, S., Fransson, T., Brewster, A. S., & Alonso-Mori, R. (2018). Structures of the intermediates of Kok's photosynthetic water oxidation clock. *Nature*, *563*(7731), 421-425.

Lee, D., Baek, S., Park, J., Lee, K., Kim, J., Lee, S. J., Chung, W. K., Lee, J.-L., Cho, Y., & Nam, K. H. (2019). Nylon mesh-based sample holder for fixed-target serial femtosecond crystallography. *Scientific reports*, *9*(1), 6971.

Lee, K., Lee, D., Baek, S., Park, J., Lee, S. J., Park, S., Chung, W. K., Lee, J.-L., Cho, H.-S., & Cho, Y. (2020). Viscous-medium-based crystal support in a sample holder for fixed-target serial femtosecond crystallography. *Journal of Applied Crystallography*, *53*(4), 1051-1059.

Liebschner, D., Afonine, P. V., Baker, M. L., Bunkoczi, G., Chen, V. B., Croll, T. I., Hintze, B., Hung, L. W., Jain, S., McCoy, A. J., Moriarty, N. W., Oeffner, R. D., Poon, B. K., Prisant, M. G., Read, R. J., Richardson, J. S., Richardson, D. C., Sammito, M. D., Sobolev, O. V., . . . Adams, P. D. (2019). Macromolecular structure determination using X-rays, neutrons and electrons: recent developments in Phenix. *Acta Crystallogr D Struct Biol*, *75*(Pt 10), 861-877. https://doi.org/10.1107/S2059798319011471

Martiel, I., Beale, J. H., Karpik, A., Huang, C. Y., Vera, L., Olieric, N., Wranik, M., Tsai, C. J., Muhle, J., Aurelius, O., John, J., Hogbom, M., Wang, M., Marsh, M., & Padeste, C. (2021). Versatile microporous polymer-based supports for serial macromolecular crystallography. *Acta Crystallogr D Struct Biol*, *77*(Pt 9), 1153-1167. https://doi.org/10.1107/S2059798321007324

Martiel, I., Muller-Werkmeister, H. M., & Cohen, A. E. (2019). Strategies for sample delivery for femtosecond crystallography. *Acta Crystallogr D Struct Biol*, *75*(Pt 2), 160-177. https://doi.org/10.1107/S2059798318017953

McCoy, A. J., Grosse-Kunstleve, R. W., Adams, P. D., Winn, M. D., Storoni, L. C., & Read, R. J. (2007). Phaser crystallographic software. *J Appl Crystallogr*, *40*(Pt 4), 658-674. https://doi.org/10.1107/S0021889807021206

Mehrabi, P., Muller-Werkmeister, H. M., Leimkohl, J. P., Schikora, H., Ninkovic, J., Krivokuca, S., Andricek, L., Epp, S. W., Sherrell, D., Owen, R. L., Pearson, A. R., Tellkamp, F., Schulz, E. C., & Miller, R. J. D. (2020). The HARE chip for efficient time-resolved serial synchrotron crystallography. *J Synchrotron Radiat*, *27*(Pt 2), 360-370. https://doi.org/10.1107/S1600577520000685

Mehrabi, P., Schulz, E. C., Agthe, M., Horrell, S., Bourenkov, G., von Stetten, D., Leimkohl, J. P., Schikora, H., Schneider, T. R., Pearson, A. R., Tellkamp, F., & Miller, R. J. D. (2019). Liquid application method for time-resolved analyses by serial synchrotron crystallography. *Nat Methods*, *16*(10), 979-982. https://doi.org/10.1038/s41592-019-0553-1

Moffat, K. (2001). Time-resolved biochemical crystallography: a mechanistic perspective. *Chemical reviews*, *101*(6), 1569-1582.

Moreno-Chicano, T., Ebrahim, A., Axford, D., Appleby, M. V., Beale, J. H., Chaplin, A. K., Duyvesteyn, H. M. E., Ghiladi, R. A., Owada, S., Sherrell, D. A., Strange, R. W., Sugimoto, H., Tono, K., Worrall, J. A. R., Owen, R. L., & Hough, M. A. (2019). High-throughput structures of protein-ligand complexes at room temperature using serial

femtosecond crystallography. *IUCrJ*, *6*(Pt 6), 1074-1085. https://doi.org/10.1107/S2052252519011655

Nam, K. H., Kim, J., & Cho, Y. (2021). Polyimide mesh-based sample holder with irregular crystal mounting holes for fixed-target serial crystallography. *Scientific reports*, *11*(1), 13115.

Nogly, P., Weinert, T., James, D., Carbajo, S., Ozerov, D., Furrer, A., Gashi, D., Borin, V., Skopintsev, P., Jaeger, K., Nass, K., Bath, P., Bosman, R., Koglin, J., Seaberg, M., Lane, T., Kekilli, D., Brunle, S., Tanaka, T., . . . Standfuss, J. (2018). Retinal isomerization in bacteriorhodopsin captured by a femtosecond x-ray laser. *Science*, *361*(6398). https://doi.org/10.1126/science.aat0094

Oghbaey, S., Sarracini, A., Ginn, H. M., Pare-Labrosse, O., Kuo, A., Marx, A., Epp, S. W., Sherrell, D. A., Eger, B. T., Zhong, Y., Loch, R., Mariani, V., Alonso-Mori, R., Nelson, S., Lemke, H. T., Owen, R. L., Pearson, A. R., Stuart, D. I., Ernst, O. P., . . . Miller, R. J. (2016). Fixed target combined with spectral mapping: approaching 100% hit rates for serial crystallography. *Acta Crystallogr D Struct Biol*, *72*(Pt 8), 944-955. https://doi.org/10.1107/S2059798316010834

Olmos, J. L., Jr., Pandey, S., Martin-Garcia, J. M., Calvey, G., Katz, A., Knoska, J., Kupitz, C., Hunter, M. S., Liang, M., Oberthuer, D., Yefanov, O., Wiedorn, M., Heyman, M., Holl, M., Pande, K., Barty, A., Miller, M. D., Stern, S., Roy-Chowdhury, S., . . . Schmidt, M. (2018). Enzyme intermediates captured "on the fly" by mix-and-inject serial crystallography. *BMC Biol*, *16*(1), 59. https://doi.org/10.1186/s12915-018-0524-5

Park, J., Joti, Y., Ishikawa, T., & Song, C. (2013). Monte Carlo study for optimal conditions in single-shot imaging with femtosecond x-ray laser pulses. *Applied Physics Letters*, *103*(26).

Park, S.-Y., Choi, H., Eo, C., Cho, Y., & Nam, K. H. (2020). Fixed-target serial synchrotron crystallography using nylon mesh and enclosed film-based sample holder. *Crystals*, *10*(9), 803.

Rabe, P., Beale, J. H., Butryn, A., Aller, P., Dirr, A., Lang, P. A., Axford, D. N., Carr, S. B., Leissing, T. M., McDonough, M. A., Davy, B., Ebrahim, A., Orlans, J., Storm, S. L. S., Orville, A. M., Schofield, C. J., & Owen, R. L. (2020). Anaerobic fixed-target serial crystallography. *IUCrJ*, *7*(Pt 5), 901-912. https://doi.org/10.1107/S2052252520010374

Rabe, P., Kamps, J., Sutherlin, K. D., Linyard, J. D. S., Aller, P., Pham, C. C., Makita, H., Clifton, I., McDonough, M. A., Leissing, T. M., Shutin, D., Lang, P. A., Butryn, A., Brem, J., Gul, S., Fuller, F. D., Kim, I. S., Cheah, M. H., Fransson, T., . . . Schofield, C. J. (2021). X-ray free-electron laser studies reveal correlated motion during isopenicillin N synthase catalysis. *Sci Adv*, *7*(34). https://doi.org/10.1126/sciadv.abh0250

Redecke, L., Nass, K., DePonte, D. P., White, T. A., Rehders, D., Barty, A., Stellato, F., Liang, M., Barends, T. R. M., Boutet, S., Williams, G. J., Messerschmidt, M., Seibert, M. M., Aquila, A., Arnlund, D., Bajt, S., Barth, T., Bogan, M. J., Caleman, C., . . . Chapman, H. N. (2013). Natively inhibited Trypanosoma brucei cathepsin B structure determined by using an X-ray laser. *Science*, *339*(6116), 227-230. https://doi.org/10.1126/science.1229663

Ren, Z., Ayhan, M., Bandara, S., Bowatte, K., Kumarapperuma, I., Gunawardana, S., Shin, H., Wang, C., Zeng, X., & Yang, X. (2018). Crystal-on-crystal chips for in situ serial diffraction at room temperature. *Lab Chip*, *18*(15), 2246-2256. https://doi.org/10.1039/c8lc00489g

Sawaya, M. R., Cascio, D., Gingery, M., Rodriguez, J., Goldschmidt, L., Colletier, J. P., Messerschmidt, M. M., Boutet, S., Koglin, J. E., Williams, G. J., Brewster, A. S., Nass, K., Hattne, J., Botha, S., Doak, R. B., Shoeman, R. L., DePonte, D. P., Park, H. W., Federici, B. A., . . . Eisenberg, D. S. (2014). Protein crystal structure obtained at 2.9 A

resolution from injecting bacterial cells into an X-ray free-electron laser beam. *Proc Natl Acad Sci U S A*, *111*(35), 12769-12774. https://doi.org/10.1073/pnas.1413456111
Schift, H., Saxer, S., Park, S., Padeste, C., Pieles, U., & Gobrecht, J. (2005). Controlled co-evaporation of silanes for nanoimprint stamps. *Nanotechnology*, *16*(5), S171.
Schmidt, M. (2013). Mix and inject: Reaction initiation by diffusion for time-resolved macromolecular crystallography. *Advances in Condensed Matter Physics*, *2013*.
Schrödinger, L. The AxPyMOL Molecular Graphics Plugin for Microsoft PowerPoint, Version 1.8. 2015. *Google Scholar There is no corresponding record for this reference*.
Schulz, E. C., Yorke, B. A., Pearson, A. R., & Mehrabi, P. (2022). Best practices for time-resolved serial synchrotron crystallography. *Acta Crystallogr D Struct Biol*, *78*(Pt 1), 14-29. https://doi.org/10.1107/S2059798321011621
Seraj, Z., & Seyedarabi, A. (2020). The role of Cinnamaldehyde and Phenyl ethyl alcohol as two types of precipitants affecting protein hydration levels. *Int J Biol Macromol*, *146*, 705-715. https://doi.org/10.1016/j.ijbiomac.2019.12.204
Sherrell, D. A., Foster, A. J., Hudson, L., Nutter, B., O'Hea, J., Nelson, S., Pare-Labrosse, O., Oghbaey, S., Miller, R. J., & Owen, R. L. (2015). A modular and compact portable mini-endstation for high-precision, high-speed fixed target serial crystallography at FEL and synchrotron sources. *J Synchrotron Radiat*, *22*(6), 1372-1378. https://doi.org/10.1107/S1600577515016938
Sherrell, D. A., Lavens, A., Wilamowski, M., Kim, Y., Chard, R., Lazarski, K., Rosenbaum, G., Vescovi, R., Johnson, J. L., Akins, C., Chang, C., Michalska, K., Babnigg, G., Foster, I., & Joachimiak, A. (2022). Fixed-target serial crystallography at the Structural Biology Center. *J Synchrotron Radiat*, *29*(Pt 5), 1141-1151. https://doi.org/10.1107/S1600577522007895
Weinert, T., Skopintsev, P., James, D., Dworkowski, F., Panepucci, E., Kekilli, D., Furrer, A., Brunle, S., Mous, S., Ozerov, D., Nogly, P., Wang, M., & Standfuss, J. (2019). Proton uptake mechanism in bacteriorhodopsin captured by serial synchrotron crystallography. *Science*, *365*(6448), 61-65. https://doi.org/10.1126/science.aaw8634
White, T. A., Kirian, R. A., Martin, A. V., Aquila, A., Nass, K., Barty, A., & Chapman, H. N. (2012). CrystFEL: a software suite for snapshot serial crystallography. *Journal of Applied Crystallography*, *45*(2), 335-341.

Synopsis

The MISP-chip is a new polymer fixed-target support for serial crystallography experiments at synchrotrons and XFELs. These micro-structured supports contain a precise array of apertures that allow rapid aperture-alignment based data-collection strategies. In this paper, the chip fabrication process is presented and discussed, as well as an analysis of ideal crystal loading parameters and data quality.

2.7 Appendix: Supplementary Information

A. 2.1 Film thickness increase during hot embossing

During the embossing of pyramid structures, the material is squeezed towards the sides of the imprinting structures, increasing the average thickness of the polymer film (Figure 2.8). For the typically used parameters of 120 µm aperture pitch, and pyramids of 100 µm cavity size (71µm height) imprinted into a 50µm thick film, a theoretical thickness increase of about 16µm is calculated. This is well in line with a measured thickness increase of 14 ±3µm, and apertures sizes of about 5-7µm, indicating, that only the top 4-5µm of the pyramids are penetrating the film.

Interestingly, increasing the pyramid dimensions at a constant pitch has only a minor influence on the aperture size. The increase in height is mostly compensated by an additional increase in film thickness (see Table 2.2). This in turn also indicates that the fabrication process critically depends on the change of film thickness during the hot embossing. This can be clearly observed when using a different thickness of polymer film. The change cannot simply be compensated by adapting the pyramid size linearly; all design parameters including the structure pitch have to be reoptimized.

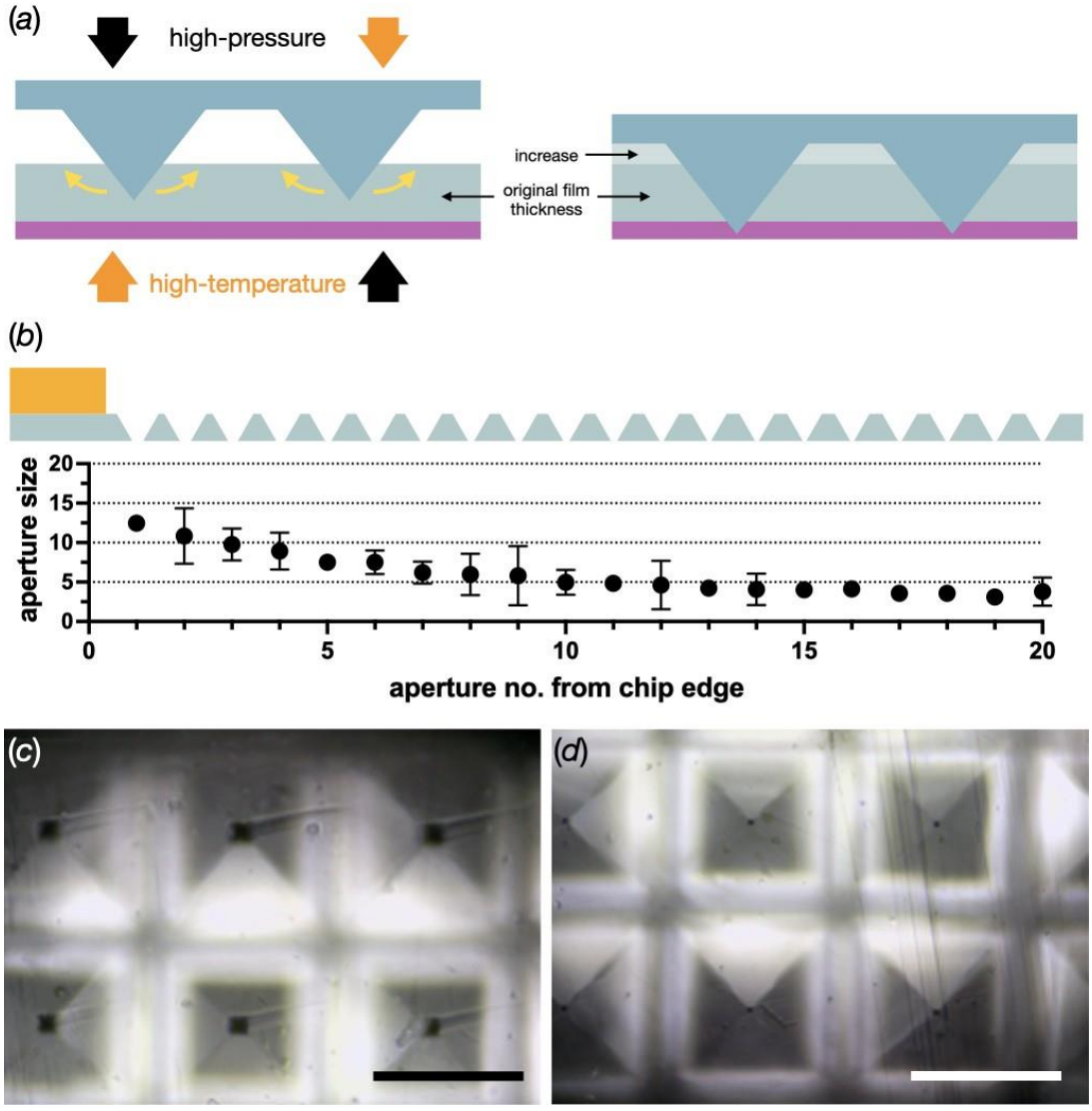

Figure 2.8: ***The effect of the material displacement from imprinting the pyramidal structures into COP film.*** *(a) Scheme for depicting the process of how the films thicken as a result of the hot embossing. (b) Diagram and plot showing the gradual decrease of the aperture size as a function of the distance from the edge of the membrane. The error bars in the plot show the 95 % confidence intervals. (c) and (d) images of rows 1 and 2, and 19 and 20, from (b). The scale bar in both images is 100 µm.*

The effect of film thickness increase is more pronounced in areas of high structure densities such as the center of the membranes and it levels out towards the borders of the structures. Figure 2.8(*b*) shows the aperture sizes measured as a function of row number, starting at the edge of the membranes. Within the first rows the aperture

sizes steadily decrease starting at about 12 µm, and level out at about 4 µm in the 15th row [Figure 2.8(*c*) and (*d*)].

In the areas of the fiducials, less material is displaced, leading to measured aperture sizes of about 18 ±2 µm for the 100 µm sized pyramids and the 50µm COP film. In future designs smaller pyramids will be used for the fiducials in order to increase the accuracy of positioning using the fiducials. This could be simply achieved by using smaller pyramid dimensions.

Table 2.2. ***Effect of imprinting pyramid arrays into 50 µm thick polymer films.*** *The periodicity (pitch) of the structures is 120µm. Calculations were done for pyramids with bases ranging from 90-110µm. The volume of the pyramids is a good estimate of the amount of polymer displaced leading to thickness increase. The punching height (fraction of the pyramid punching though the film) is equal to the thickness after thickness increase minus the pyramid height. The theoretical aperture size is given as the base of a pyramid of the same height.*

Pyramid width (µm)	Pyramid height (µm)	Pyramid volume (µm^3)	Film thickness increase (µm)	Punching height (µm)	Aperture size (µm)
90	63.7	172054	11.9	1.8	2.5
95	67.3	202352	14.1	3.2	4.6
100	70.8	236013	16.4	4.4	6.3
105	74.3	273215	19.0	5.4	7.7
110	77.9	314134	21.8	6.1	8.7

A. 2.2 MISP-chip accessories

A loading station was constructed and found to be essential for sample loading onto the MISP-chip. It consists of a loading platform, a vacuum pump to extract the excess mother liquor, and a humidity stream to keep the crystals from dehydrating during preparation. Vacuum pump suction was controlled with a valve and provided control over the force and timing of excess mother-liquor extraction [Figure 2.9].

The loading platform was designed on Fusion 360 and 3D printed on a ProJet MJP 2500 Series 3D printer [Figure 2.9 (*b*)]. This loading platform provides a support for the membrane of the MISP-chips whilst under suction, prolonging the lifespan of the MISP-chips. The loading surface contains a PDMS gasket, providing assistance with creating a vacuum seal.

Prepared chips are transferred over to the sample holder designed on Fusion 360 and 3D printed on a ProJet MJP 2500 Series 3D printer [Figure 2.9(*c*)]. It contains two Mylar films to retain humidity inside the chip and is closed with two screws.

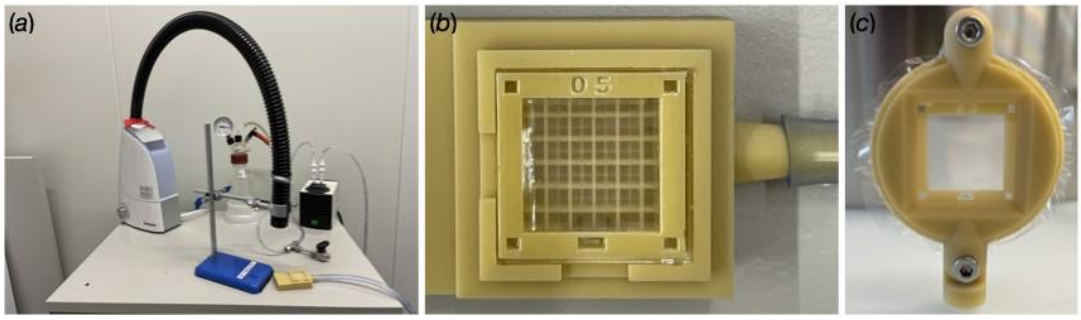

Figure 2.9: ***Essential items for the MISP-chip.*** *(a) Humidity sample loading station to prevent crystals from dehydrating during preparation. (b) Sample loading platform designed to extract excess mother liqour from the MISP-chip while providing sup- port on the membrane. (c) Sample holder is designed to seal the loaded crystals on the MISP-chip from dehydrating and is designed for mounting onto the goniometer at SwissMX.*

A. 2.3. Crystal location on the chip after loading

Distribution of crystals on the MISP-chip is partly understood by looking at an example bit-map of the hit locations on chip (Figure 2.10). The vacuum applied to the underside of the chips during loading appears to preferentially draw the solution and crystals towards the edges of the chip. This creates dense areas of multi-hits rather

than a more homogeneous spread of single-hits. The size of the loading support footprint

is also shown to be very large, obscuring some 3,000 of the chip's 26,000 available cavities. New versions will contain finer supports to reduce this issue.

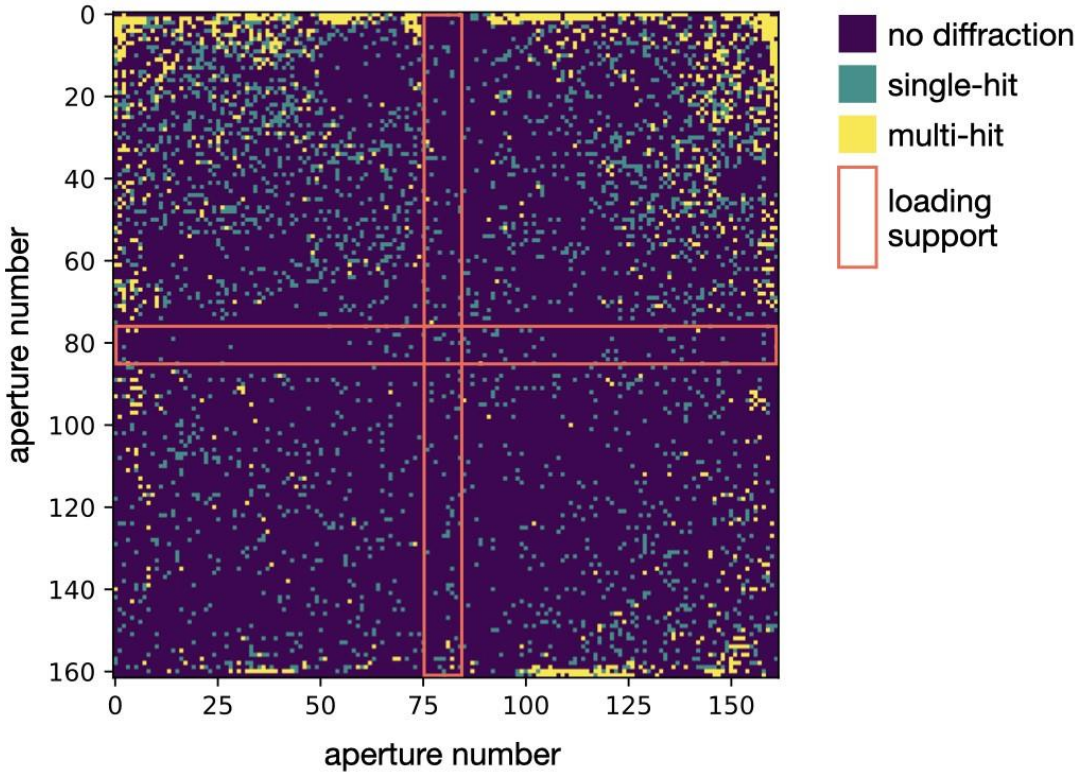

Figure 2.10: ***An example heat-map of single and multi-hit locations on the MISP-chip.*** *This map was generated using the 10 µm HEWL crystals loaded at a concentration of 5 × 10^5 crystals·mL^{-1}. The red box indicates the cavities that were partially obscured by the supports in the vacuum loader.*

A. 2.4 Crystal orientations on the chips

Crystal orientation of HEWL crystals for all the measured datasets was extracted and evaluated using the CrystFel stream files. Plots of the orientations are presented in Figure 2.11. Data points are not seen to be randomly distributed into a homogeneous circle, as would be expected for random orientations. The gaps and asymmetric localization observed in the figures are indications of multiple crystals containing a

similar preferential orientation. This small magnitude of preferential orientation is acceptable in the present case.

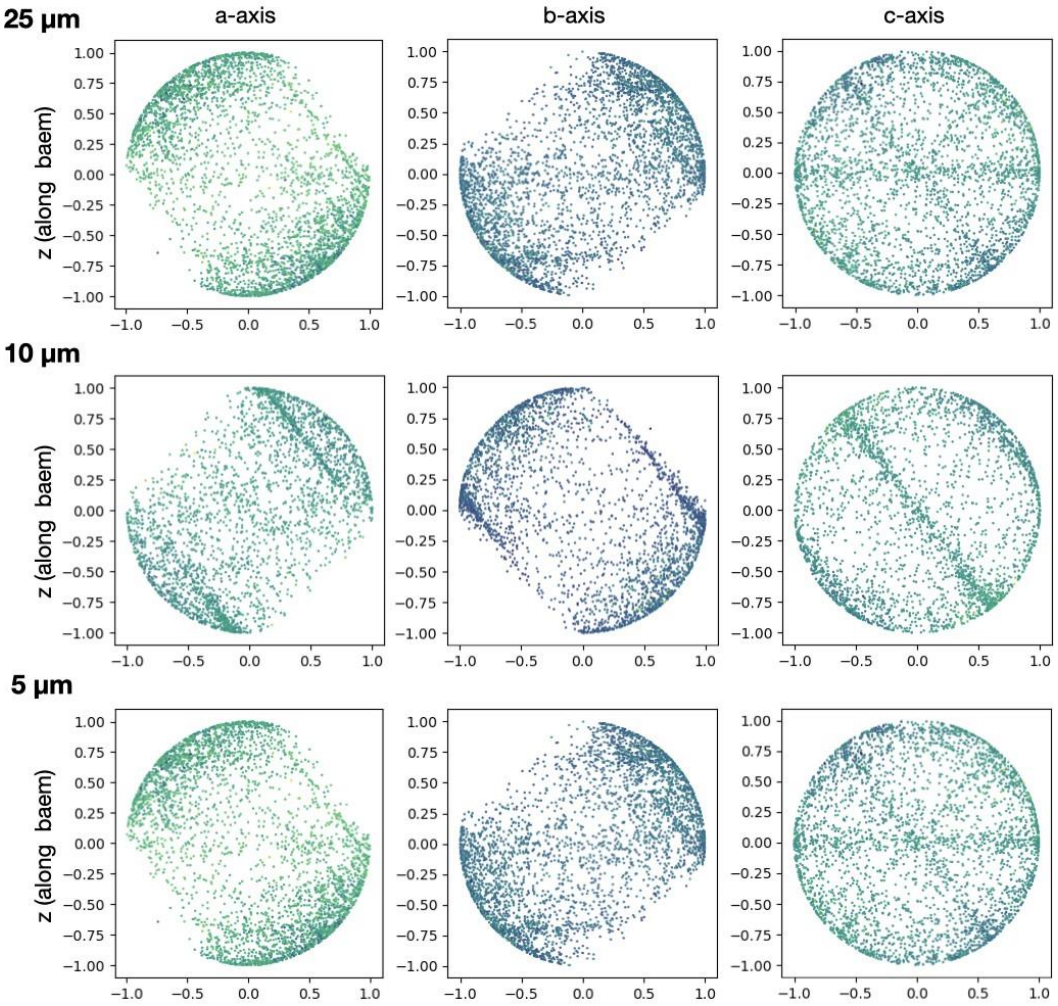

Figure 2.11: An analysis of the crystal orientation when loaded onto the MISP-chips. Analysis on 25 µm, 10 µm, and 5 µm HEWL crystals was performed to observe the orientation of the crystals to the beam. Each point on the diagram represents the crystal orientation on the a-, b-, or c-axis with respect to the beam.

A. 2.5 Structure determination

Structures were solved using the collected data sets of the three different crystal sizes. Final refinement statistics are summarized in Table 2.3. All determined structures are in good agreement with literature data.

Table 2.3: ***Data collection and refinement statistics for the three HEWL structure***

Dataset	**5** μm	**10** μm	**25** μm
Data collection			
Space group		P $4_3 2_1 2$	
a, b, c (Å)		79.2, 79.2, 38.2	
α, β, γ (°)		90, 90, 90	
Indexed patterns	31659	29436	69420
Indexing rate (%)	5.1	5.01	66.98
Resolution range (Å)	25.05 - 1.54	39.60 - 1.40	25.05 - 1.40
Completeness (%)	100 (100)	100 (100)	100 (100)
Multiplicity	354 (229)	375 (231)	405 (218)
Rsplit	0.021 (0.700)	0.025 (0.777)	0.027 (1.2)
CC1/2	0.943 (0.319)	0.977 (0.274)	0.982 (0.284)
$<I/\sigma(I)>$	5.67 (0.390)	6.25 (0.550)	7.34 (0.290)
R-work	17.11	14.41	15.3
R-free	20.15	17.86	19.66
protein atoms	1100	1101	1084
solvent atoms	112	91	107
RMS (bonds)	0.007	0.005	0.005
RMS (angles)	0.885	0.8	0.828
Ramachandran favored (%)	99.21	99.21	98.43
Ramachandran outliers (%)	0	0	0
mean B-factor	26.01	28.43	28.56
clashscore	2.77	1.84	2.34
PDB Code	8PYO	8PYQ	8PYP

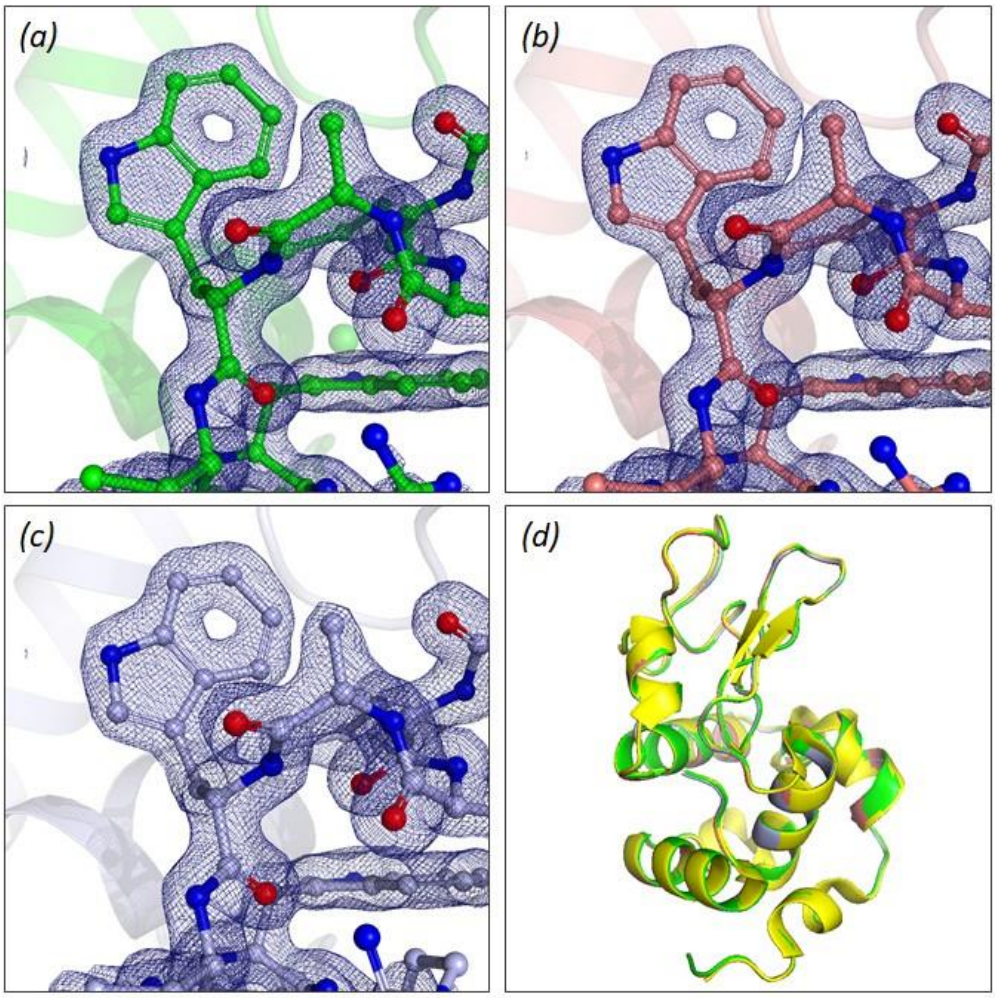

Figure 2.12: HEWL structures solved from different crystal sizes and alignment with previously published HEWL structure. Section of the solved HEWL structure and electron density for (a) 25 µm crystals, (b) 10 µm crystals, and (c) 5 µm crystals. Colors are consistent with previous figures. Electron density maps are shown in dark blue to 1.5 Å. (d) Superposition of our HEWL structures for 25 µm, 10 µm, and 5 µm crystals with the previously solved HEWL structure, PDB ID 4N5R (Barends *et al.*, 2014) (yellow), displaying high uniformity between our structures and those previously collected under room temperature conditions at an XFEL.

Acknowledgements: Thanks are due to Konrad Vogelsang, Dario Marty, Florian Graber and Moritz Würtenberg Paul Scherrer Institut (PSI) for assistance in the chip manufacturing process. This work was supported by the Swiss Nanoscience Institute, Project #1904. Many thanks to the MX Group for support during development and testing performed at the SwissFEL, specifically Sven Augustin, Emma Beale, Florian Dworkowski, Dmitry Ozerov, Georgii Khusainov, Tobias Weinert, Miao Liang, Greta Assman, Sylvain Aumonier, Filip Leonarski, May Sharpe, Dennis Stegmann and Meitian Wang. Many thanks also to the Quantum Photon Science Group for sup- port during the Cristallina, SwissFEL beamtimes, to the control room staff of both facilities for providing reliable and stable beam during beamtimes, and to Thomas Barends for providing the CrystFEL orientation analysis script used to generate the orientation projections. We acknowledge the Paul Scherrer Institut, Villigen, Switzer- land for provision of XFEL beamtime at the Cristallina endstation of SwissFEL.

3

Fixed-Target Pump-Probe SFX: Eliminating the Scourge of Light Contamination

The following section has been accepted in
IUCRj.
Contributions: Designed, produced, collected data, and commissioned the COC MISP-chips

Fixed-target pump-probe SFX: eliminating the scourge of light contamination

Guillaume Gotthard[1,2,3]*, Andrea Flores-Ibarra[4]*, Melissa Carrillo[5]*, Michal W Kepa[2], Thomas J Mason[2,3], Dennis P. Stegmann[3], Bence Olasz[4], Magdalena Pachota[4], Florian Dworkowski[6], Dmitry Ozerov[7], Bill F. Pedrini[8], Celestino Padeste[5], John H Beale[3‡], Przemyslaw Nogly[1,4‡]

[1]Institute of Molecular Biology and Biophysics, ETH Zurich, Rämistrasse 101, 8092 Zürich, Switzerland
[2]Laboratory of Biomolecular Research, Paul Scherrer Institut, Forschungsstrasse 111, 5232 Villigen, Switzerland
[3]Swiss Light Source, Paul Scherrer Institut, Forschungsstrasse 111, 5232 Villigen, Switzerland
[4]Dioscuri Center for Structural Dynamics of Receptors, Faculty of Biochemistry, Biophysics and Biotechnology, Jagiellonian University, Gronostajowa 7, 30-380 Krakow, Poland
[5]Laboratory of Nanoscale Biology, Paul Scherrer Institut, Forschungsstrasse 111, 5232 Villigen, Switzerland
[6]Laboratory for Synchrotron Radiation and Femtochemistry, Paul Scherrer Institut, Forschungsstrasse 111, 5232 Villigen, Switzerland
[7]Science IT Infrastructure and Services, Paul Scherrer Institut, Forschungsstrasse 111, 5232 Villigen, Switzerland
[8]Laboratory for X-ray Nanoscience and Technologies, Paul Scherrer Institut, Forschungsstrasse 111, 5232 Villigen, Switzerland
* Equal contribution
‡ Corresponding authors

Abstract

X-ray free electron laser (XFEL) light sources have enabled the rapid growth of time-resolved structural experiments which provide crucial information on the function of macromolecules and their mechanisms. In this study, we set out to commission the SwissMX fixed-target sample delivery system at the SwissFEL Cristallina experimental station using the PSI developed MISP-chip for pump-probe time-resolved experiments. To characterise the system, we used crystals of the light-sensitive protein Light-Oxygen-Voltage domain 1 (LOV1) from *Chlamydomonas reinhardtii.* Using different experimental settings, we examined the accidental illumination, referred to as light contamination, of crystals mounted in wells adjacent to those illuminated by the pump laser. We found that it was crucial to control the light scattering from and through the solid supports otherwise significant contamination occurred. However, our results also show that the opaque MISP-chips are suitable for defined pump-probe studies of a light-sensitive protein. Our experiment probed the sub-millisecond structural dynamics of LOV1 and indicated that at Δt=10 μs the covalent thioether bond is established between the reactive Cys57 and the FMN cofactor. This experiment validated the crystals to be suitable for in-depth follow up studies of this still poorly understood signal transduction mechanism. Importantly, the fixed-target delivery system also permitted a tenfold reduction in protein sample consumption compared to high-viscosity extrusion-based delivery system. This development creates the prospect of an increase in XFEL project throughput for the field.

Keywords: time-resolved crystallography; fixed-target, X-ray Free Electron Laser, room-temperature crystallography; pump probe, photoreceptor LOV domain

3.1 Introduction

The emergence of serial femtosecond crystallography (SFX) at X-ray free-electron laser (XFEL) sources and the development of its synchrotron counterpart, serial synchrotron crystallography (SSX), has furthered the reach of macromolecular crystallography (MX) in time-resolved sciences and the study of protein dynamics. Although continuous efforts are being made to adapt reaction-triggering technologies, such as substrate mixing (P. Mehrabi et al., 2019; Olmos et al., 2018), optical laser pumping of a light-absorbing molecule remains the default choice for the vast majority of pump-probe experiments. This is unsurprising given the SFX community's ongoing focus on light-sensitive proteins and/or ligands (Brändén & Neutze, 2021). However, continued efforts have been made to find general adaptations to expand the scope of laser pump-probe methods beyond intrinsically light-sensitive proteins. These include the laser-triggered release of photocages (Schulz et al., 2022), biological photoswitches (Wranik, Weinert, Slavov, Masini, Furrer, Gaillard, Gioia, Ferrarotti, James, Glover, et al., 2023), and temperature jump induction in non-photoactive targets (A. M. Wolff et al., 2023).

The very high peak brilliance of XFEL sources spurred the “diffraction before destruction” approach methodology (Boutet et al., 2012; H. N. Chapman et al., 2011; Neutze et al., 2000) and created the need for rapid and efficient sample delivery systems (also beneficial in SSX). The most widely used delivery systems include injectors using gas-focusing nozzles (DePonte et al., 2009), electrospun liquid microjets (R. G. Sierra et al., 2012) and the high-viscosity extruders, which have proved their utility for both crystals of membrane proteins grown in the lipidic cubic phase (LCP) and of soluble proteins (Botha et al., 2015; Fromme et al., 2015; Nogly et al., 2015; Weierstall et al., 2014). Together these technologies have resulted in many novel insights into protein dynamics and are widely used of time-resolved SFX (TR-SFX) experiments.

The sample efficiency of jet-based delivery methods in SFX measurements is dependent upon the repetition rate of the source, the diameter and flow-rate of the jet, and the X-ray energy. The flow-rates of liquid jets, such as the gas dynamic virtual nozzle (GDVN), needs to be high enough to maintain a liquid filament. In a continuous jet this is very sample consumptive at around 10 $\mu L \cdot min^{-1}$ for a jet running at 10 $m \cdot s^{-1}$, although this can be offset by pulsing or dripping the jet in sync with the XFEL pulse (Weierstall, 2014). Sample consumption can also be mitigated by increasing the repetition rate of the source to reduce gaps between the illuminated parts of the jet (Gisriel et al., 2019; Grunbein et al., 2018; Wiedorn et al., 2018). Using a 100 kHz, compared to a 100 Hz, source would reduce the distance between adjacent pulses within the jet from 100 to 0.1 mm, respectively.

The high viscosity extruder (HVE) operates at flow rates and jet speeds more suited to the majority of low repetition rate (>1 kHz) sources currently available (as of the time of writing May 2024). The development of the HVE significantly increased sample efficiency compared to the GDVNs, as stable filaments can be maintained with jet speeds in the 100s of micrometers per second. This translates to sample usage rates below 0.01 µL/min. However, despite this improvement for low repetition rate sources, sample consumption for the HVEs could still be improved as part of the injected sample is still not probed by the X-ray beam.

This sample efficiency is further reduced when performing pump-probe measurements. During a pump-probe experiment the jetting speed typically has to be increased to refresh the sample within the laser excitation area to preclude shot-to-shot light contamination. This increase is due to the larger beam profile of the pump laser with respect to the X-rays and the distance between adjacent XFEL shots needs to be safely larger than the width of the pump pulse (Smolentsev et al., 2013). Therefore, a trade-off has to be found between crystal concentration, repetition rate, and the jet width and velocities to ensure the sample is not overly

wasted and that the experiment is properly performed. A reduction of crystal concentration and/or XFEL repetition rate will negatively impact the beamtime efficiency. Preparations for experiments often require months of work invested in purifying and crystallizing sufficient protein quantities. Therefore, any improvement in sample and beamtime efficiency is of great interest to the structural biology field.

An alternative to jet-based systems is a fixed-target delivery system where protein micro-crystals are immobilized on a solid support or chip (Zarrine-Afsar et al., 2012). These techniques emerged later than their jet-based cousins but have proved to be robust and a user-friendly sample delivery system. Fixed-targets were first applied to SFX at LCLS where a micro-crystal slurry was applied to a silicon nitride membrane and rastered through in step with the XFEL pulse (Hunter et al., 2014). Since then, a large variety of different supports have emerged. These can be roughly grouped by whether or not they have apertures and whether those apertures are aligned to the beam during data collection (M. Carrillo et al., 2023). For these aperture-aligned fixed-targets, the key development was the coupling of precision silicon fabrication technique (Mueller, Marx, Epp, Zhong, Kuo, Balo, Soman, Schotte, Lemke, Owen, et al., 2015; Oghbaey et al., 2016b) to stage motion and alignment strategies (Sherrell et al., 2015). The three prominent examples of these apertured targets are the HARE chip (Mehrabi et al., 2020) the Oxford chip (Ebrahim et al., 2019) and the Micro-Structured Polymer (MISP) chip (M. Carrillo et al., 2023). Examples of the raster-based targets are the NAM-based sample holder (Nam et al., 2021; Park et al., 2020), the Advanced Lightweight Encapsulator for Crystallography (ALEX) mesh holder (D. A. Sherrell et al., 2022), and the MPI sheet-on-sheet (SOS) chip (R. Doak et al., 2018). Solid supports have typically shown a decrease in sample use compared to the jets without the need for gas flow or electrodes (R. Doak et al., 2018; Hunter et al., 2014; Mueller, Marx, Epp, Zhong, Kuo, Balo, Soman, Schotte, Lemke, Owen, et al., 2015). Given the utility of the fixed-targets and optical lasers for time-resolved

crystallography, chip developers must ensure that their tools are compatible with pump probe experiments using optical lasers.

As for all pump probe sample delivery systems, a significant issue when using fixed-targets is how to ensure that samples remain free from light prior to laser illumination and that only the desired crystals are illuminated at the designated moment. The former of these forms of light contamination can also be thought of as unintended pre-illumination from the environment. This environmental contamination can occur any moment from attempting to load the sample into the delivery system and could result from a poor choice of dark room lamps during sample loading, transporting loaded samples to the hutch or perhaps poor shielding of hutch lights/LEDs [Figure 3.1(*a*)]. The latter is from the contamination of adjacent crystals with respect to the desired crystal from the optical laser pulse [Figure 3.1(*b*) and (*c*)]. For example, data collected during a pump-probe experiment typically interleave dark and laser pumped XFEL exposures. If the laser and delivery system parameters are not properly characterised, significant light contamination of both the interleaved "light" and "dark" diffraction patterns can occur. This contamination, ultimately, prevents the correct interpretation of relevant structural changes and renders the experiment pointless.

In jet and extruder-based delivery systems, the oncoming crystals are housed in the opaque enclosure of the reservoir. Environmental pre-illumination is a concern during sample preparation and loading, but once complete, this risk is minimised due to the small area of environment exposure during data collection [Figure 3.1 (*a*)]. Adjacent crystal contamination is still a significant concern. However, contamination, if it does occur, will be limited to the single axis of jet and likely restricted to the immediately following shot/s [Figure 3.1 (*b*)].

Unfortunately, both of these risks are amplified when using fixed-targets. Firstly, the whole chip is left exposed to its surroundings and, therefore, the risk of environmental contamination is increased [Figure 3.1 (*a*)]. Pump-laser contamination in fixed-targets is also more pervasive than in the jet since the adjacent crystals are distributed in two dimensions. This means that light contamination can propagate much further in time from the deliberately pumped crystal [Figure 3.1 (*c*)]. This could be tens of milliseconds or even seconds depending on the location of contamination and repetition rate used for data collection. This uncertainty in the effective time-delay of the probed region can ultimately make any intelligent subsequent analysis very challenging or, most likely, impossible.

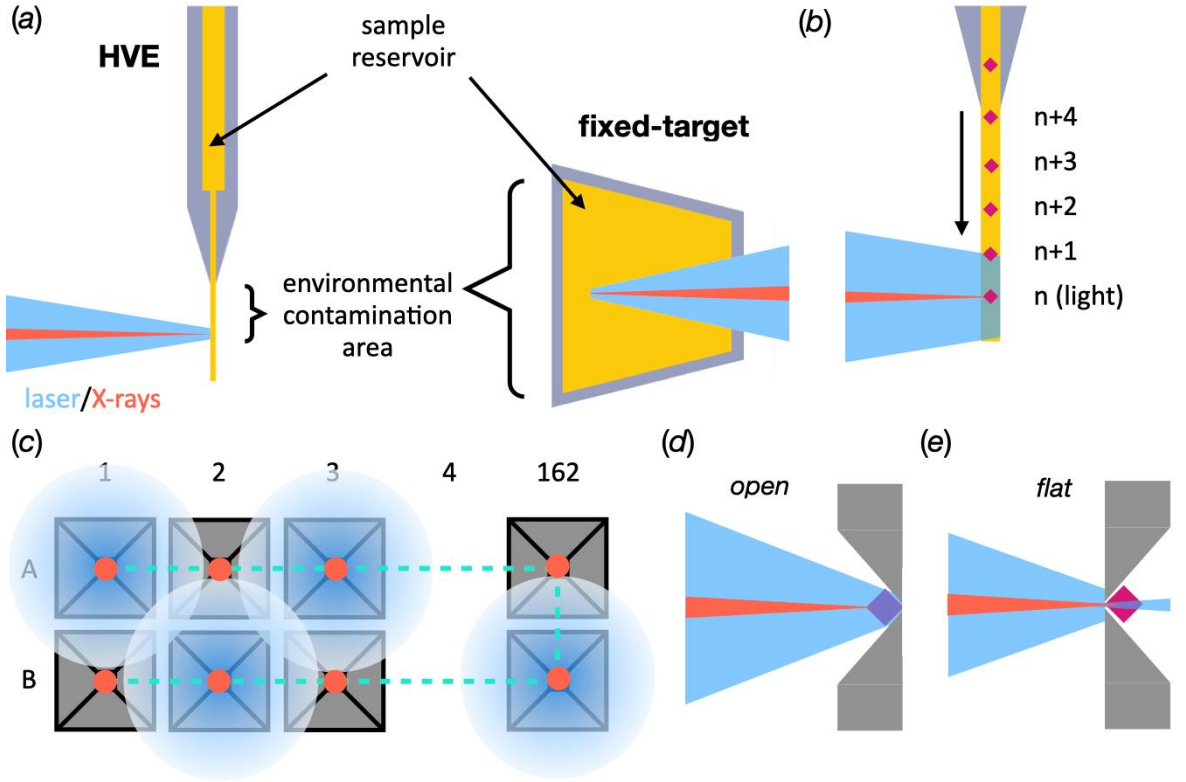

Figure 3.1: Practical differences between potential regions of light contamination in fixed-targets and HVEs. (*a*) A comparison of pump-probe in HVEs and fixed-targets highlighting the increased access of environmental stray photons to the sample when mounted in fixed-targets compared to jets. (b) A simplified schematic demonstrating pump-laser contamination in an HVE. Crystal *n* is currently illuminated with X-rays. As the jet descends, crystals *n*+1, *n*+2 etc, will descend into the X-ray path. The pump-laser is also currently illuminating *n*, but is also partially illuminating *n*+1 and leading to light contamination. (*c*) A schematic of a 1:1 interleaved light:dark setup in a MISP-chip with a incompatibly large laser spot for the experiment. Each "light well" (A1, A3, A5 etc) is correctly illuminated. The laser will also weakly illuminate any crystals in the "dark wells" (A2, A4, A6 etc) and lead to light contamination. Importantly however, the light contamination will occur both between consecutive apertures (A1 to A2, 10 ms at 100 Hz) and adjacent apertures, *i.e.*, A1 to B1. The contamination of these adjacent apertures gives rise to much longer reaction timescales; A1 to B1 = 3.24 s. (*d*) and (*e*) Schematic of the two potential orientations of an apertured fixed-target in a pump-probe experiment. The sample area is shown in yellow, the cavities grey, the X-ray are shown in red, the stage path is depicted as a dashed cyan line and the pump laser is shown in blue.

XFELs are uniquely suited to the study of ultrafast dynamics on the femtosecond-microsecond scale; however, fixed-targets have yet to be exploited for time-resolved work at XFELs; although their utility has been proven for similar experiments at synchrotrons (P Mehrabi et al., 2019). The serial crystallography with solid-support MX (SwissMX) endstation

at the SwissFEL Cristallina experimental station (Paul Scherrer Institute, Villigen, Switzerland) and PSI-developed MISP chips were designed to address this gap. However, extensive tests are obviously essential to validate these tools for optical pump X-ray probe experiments. This work describes a commissioning experiment conducted in November 2022 at the SwissFEL Cristallina experimental station. The aim was to find and understand the parameters that enable time-resolved pump-probe experiments using the SwissMX and MISP chips (Carrillo et al., 2022). To achieve this, a pump-probe experiment was performed collecting interleaved dark (no laser) and light (laser on) diffraction images (hereafter referred to as interleaved-light and interleaved-dark, respectively) in a 1:1 ratio with both transparent and opaque MISP chips. The protein used in these experiments was the Light-Oxygen-Voltage (LOV) domain 1 from *Chlamydomonas reinhardtii* (*Cr*LOV1). *Cr*LOV1 is a light-sensitive protein domain that undergoes a long photocycle (~200 s cycle time). This long photocycle is, therefore, ideal for the purpose of investigating light contamination in fixed-targets where any unsolicited light originating from stray photons from adjacent cavities can occur on the millisecond to tens of seconds scales. A covalent thioether bond forms between the flavin mononucleotide (FMN) cofactor and Cys57 in the flavin binding pocket after photoexcitation (Fedorov et al., 2003). This distinctive signature makes *Cr*LOV1 an ideal candidate to benchmark data collection schemes using fixed targets with respect to light contamination.

3.2 Material and methods

3.2.1 Expression and purification

The expression and purification protocols have been described previously (Gotthard et al., 2023). Briefly, the expressed protein sequence was amino acids 16-133 of the Phot1 protein LOV1 domain from *Chlamydomonas reinhardtii*. The protein possesses an N-terminal His-tag followed by a Factor Xa protease site. The protein was expressed in *Escherichia coli* BL21

DE3 using auto-inducible media (Studier, 2005). The expressed protein was purified by Ni^{2+} affinity followed by size exclusion chromatography. Fractions corresponding to the protein were pooled and concentrated to 10 mg·ml^{-1} for crystallization.

3.2.2 Crystallization

Limited proteolysis with trypsin allowed a more reproducible and controlled crystallization process (Gotthard et al., 2023). Microcrystals were grown at 293 K in batch with a 2:1 protein to precipitant condition ratio in 0.1 M Sodium cacodylate pH 6.5, 1.0 M Sodium citrate dibasic trihydrate. An average crystal size of 25 µm ± 7 µm was measured using a Leica microscope (Kaminski et al., 2022). The crystal concentration was measured using a cell counter and estimated to be 1.0-2.0 x 10^7 crystals·ml^{-1}.

3.2.3 Chip mounting

Firstly, the crystal concentration was adjusted by diluting the microcrystal slurry with crystallisation solution to a final concentration of 1-2×10^6 crystals·ml^{-1}. Subsequently, 400 µl of crystalline suspension was pipetted onto a MISP-chip that was either made with transparent cyclic olefin polymer (COP) film or an opaque film made by mixing 10 % (w/w) carbon black with cyclic olefin copolymer (COC) (M. Carrillo et al., 2023). Once loaded, the MISP-chip was placed on a loading stage connected to a vacuum pump that served to remove the excess mother liquor and funnel the crystals into the wells. Filter paper was occasionally required to blot away any excess solution. After this, the chip was placed onto the MISP-chip holders (M. Carrillo et al., 2023) that sealed the chip inside two pieces of 6 µm Mylar® film and maintained the crystal hydration. They were then placed inside a darkened humidity chamber kept at 80 % relative humidity and transported to the beamline. X-ray data collection was performed at the Cristallina experimental station of the SwissFEL using the SwissMX endstation. Due to

concerns over crystal hydration, only 5 chips were consecutively loaded and kept in the humidity chamber at a time. Chips were manually mounted from the humified chamber to the SwissMX.

3.2.4 Beamline setup and data collection

Data were collected over a 24-hr period on November the 27th 2022. The X-ray beam energy was 12.4 keV with a pulse energy at the sample position of approximately 50 μJ. The X-rays were focused using Kirkpatrick-Baez (KB) mirrors to a spot size of approximately 1.5 x 1.5 mm and the repetition rate was 100 Hz. The pulse width was approximately 35 fs root mean square (RMS). The diffraction data were recorded on a JUNGFRAU 8 M pixel detector. Collecting each set of 5 chips stored in the humidity chamber took approximately 50-60 minutes. The chips were kept at room temperature (23-25 ℃, depending on the location within SwissFEL).

3.2.5 Laser coupling

As of November 2022, the Cristallina hutch was not provided with a through-space connection to a pump laser. The SwissMX endstation was limited to a 70 m fiber connection to a nanosecond laser located in the SwissFEL laser room. Due to this constraint, the decision was taken to couple the laser to the sample position through the SwissMX on-axis-viewing (OAV) system. Such couplings have been demonstrated at synchrotron protein crystallography beamlines (Madden et al., 2013; Pompidor et al., 2013) and this solution offered the best compromise between the final achievable focus and the meshing with other instrumentation at the sample position.

For pump-probe experiments using fixed-targets for sample delivery the key parameter for avoiding light-contamination of unprobed crystals by the pump laser is the laser focal-spot size. The efficiency of the fixed-target is dependent upon the number crystal locations that can be squeezed onto the chip-surface. For the apertured fixed-targets this means having a small pitch between adjacent cavities. The achievable laser focus size, therefore, has a direct influence on the efficiency of the experiment as an increase in the diameter of the focus will necessitate an increase in the aperture pitch or the spacing of the XFEL probed cavities.

The laser spot size was estimated to be 50x50 μm^2 based on its reflection from a piece of opaque COC film held at the OAV focus. The OAV was calibrated against known distances, but it is impossible to accurately infer from this the $1/e^2$ or full-width half-maximum (FWHM) of the spot profile. The laser wavelength was set at 450 nm with a pulse energy of approximately 2 μJ at the sample position. The duration of the laser pulse was 3 ns and the laser was not polarized due to the fibre coupling. Given the average crystal dimensions of 25x25x25 μm^3, the ε_{450nm} for the flavin was estimated to be 11,300 $M^{-1}cm^{-1}$ for the free-Flavin. Since the beam profile could not be visualized, it is not possible to determine whether the beam profile was more top-hat or gaussian. Given this ambiguity, we estimate the mean number of photons per chromophore to be between 1.6 and 3.2 (Grunbein et al., 2020).

3.2.6 Pump-probe setup

X-ray data collection over the whole chip in a dark environment without any laser excitation was used as a 'reference' for the calculation of the Fourier difference electron density maps ($F_{obs}^{laser\text{-}off}$). Light contamination from the transparent and opaque chips and SwissMX setup was assessed using two chip orientations: *open*, with the wider side of the cavity directed towards the laser, and *flat*, with the wider side of the cavity facing the detector. All pump-probe

data were collected 1:1 interleaved light:dark, *i.e.*, XFEL at 100 Hz, ns laser at 50 Hz, giving a laser pulse in every other aperture.

3.2.7 Data processing

Serial data processing was performed using the CrystFEL version 0.10.1 software suite (T. White, 2019). Diffraction hits were identified using the peakfinder8 and XGANDALF (Gevorkov et al., 2019) algorithms with a hexagonal unit cell (a = b = 122, c = 46 Å). Peak integration was performed using the three-rings methods in indexamajig with integration radii of 2, 3, and 5 pixels. Indexing rates were between 50 and 80 %. Interleaved-dark and the interleaved-light image lists were generated by labelling images with a 'laser-on' event generated by the SwissFEL event master. This event was passed to the JUNGFRAU while data were collected and propagated with it thereafter. By following the laser events, the interleaved data could be indexed and integrated independently. Stream files were merged using partialator using the unity partiality model with a pushres option of 1.6-2.0 nm^{-1}. *hkl* files were converted into the *mtz* format with f2mtz from the CCP4 suite (M. D. Winn et al., 2011). A resolution cut-off was applied when $CC_{1/2}$ was falling below 30%. Dataset statistics are reported in Table 3.1.

Table 3.1: Data collection parameters and data reduction for the 1st experiment

Data collection parameters							
	Laser-off	Interleaved-dark	Interleaved light	Interleaved-dark	Interleaved light	Interleaved-dark	Interleaved light
Chip type	Transparent	Transparent	Transparent	Opaque	Opaque	Opaque	Opaque
Chip orientation	*Open*	*Open*	*Open*	*Open*	*Open*	*Flat*	*Flat*
Δt (µs)	10						
Beamline, Endstation	ARAMIS, Cristallina						
Detector	Jungfrau 8M						
X-ray energy (keV)	12.29						
Laser wavelength (nm)	450						
Laser profile (µm)	~50 x 50						
Repetition rate (Hz)	100						
Crystal size (µm^3)	25						
Data reduction							
Space group	$P6_522$						
Cell dimensions *a, b, c* (Å) *α, β, γ (°)*	122.6, 122.6, 46.6 90, 90, 120						
Collected images	210760	184413	184417	171246	171239	131725	131725
Indexed lattices	151790	101483	101688	72918	72229	68637	69208
Indexing rate (%)	72.0	55.0	55.1	42.6	42.2	52.1	52.5
Resolution (Å)	37.09-1.42 (1.44-1.42)	37.11-1.47 (1.50-1.47)	37.11-1.47 (1.50-1.47)	37.12-1.47 (1.50-1.47)	37.13-1.49 (1.52-1.49)	37.11-1.47 (1.50-1.47)	37.11-1.49 (1.52-1.49)
Number of reflections	6612099	3873108	4157075	3042546	3239469	2877548	3094253
Unique reflections	3846	3487	3484	3477	3365	3495	3360
Redundancy	2736.5 (1719.2)	1718.5 (1110.7)	1906.5 (1193.2)	1352.76 (875.0)	1510.79 (962.7)	1231.3 (823.3)	1380.4 (920.9)
Completeness (%)	100	100	100	100	100	100	100
Mean I/sigma(I)	13.1 (1.0)	11.54 (1.11)	11.92 (1.22)	9.45 (0.83)	10.08 (1.04)	9.89 (0.85)	10.67 (1.36)
CC*	0.9988 (0.6806)	0.9982 (0.7503)	0.9985 (0.6715)	0.9974 (0.7218)	0.9977 (0.7199)	0.9972 (0.7414)	0.9979 (0.7737)
$CC_{1/2}$	0.9954 (0.3013)	0.9928 (0.3917)	0.9941 (0.2911)	0.9899 (0.3523)	0.9907 (0.3492)	0.9887 (0.3790)	0.9917 (0.4271)
R_{split} (%)	4.97 (25.57)	6.40 (31.17)	6.13 (32.13)	7.16 (32.93)	7.04 (32.09)	7.29 (32.21)	6.82 (29.77)
Wilson B-factor (Å^2)	19.21	19.09	17.62	20.53	19.48	18.17	17.60

3.2.8 Isomorphous difference maps

Fourier difference electron density maps were calculated using the phenix.fobs_minus_fobs_map program from the Phenix suite (Liebschner et al., 2019). A resolution cut-off of 1.8 Å and a sigma cut-off of 3.0 were applied and the multiscale option was used to calculate the difference maps. The presence of contamination could be observed by subtracting data collected without laser illumination (*laser-off*) from the interleaved data (*interleaved dark or light*): $F_{obs}^{\text{interleaved-dark or light}} - F_{obs}^{\text{laser-off}}$. Assuming no contamination can be observed, the signal from the $F_{obs}^{\text{interleaved-light}} - F_{obs}^{\text{laser-off}}$ should also be the same as the interleaved difference map, $F_{obs}^{\text{interleaved-light}} - F_{obs}^{\text{interleaved-dark}}$. Figures were prepared using PyMOL (DeLano, 2020).

3.3 Results and discussion

3.3.1 Pump-probe with fixed-targets

Here, we present laser-triggered, pump-probe experiments using the SwissMX endstation and MISP-chips at the SwissFEL Cristallina experimental station. To translate samples, SwissMX is equipped with two orthogonal linear stages (Parker) for *x* and *y* motions and two additional stages *z* and additional *x* motion (Standa). The MISP-chips have a reliable active area of 162 x 162 pyramidal cavities totalling 26,244 apertures per chip. All data from the chips were collected in a serpentine-like pattern. Figure 3.2 shows the final stage of the optical pump-laser coupling through the SwissMX OAV. The setup is current only used for in-air data collection. Therefore, scatter guards are required to catch the beam from the OAV to the sample and from the sample to the detector face. The total exposed length to air is approximately 15 mm.

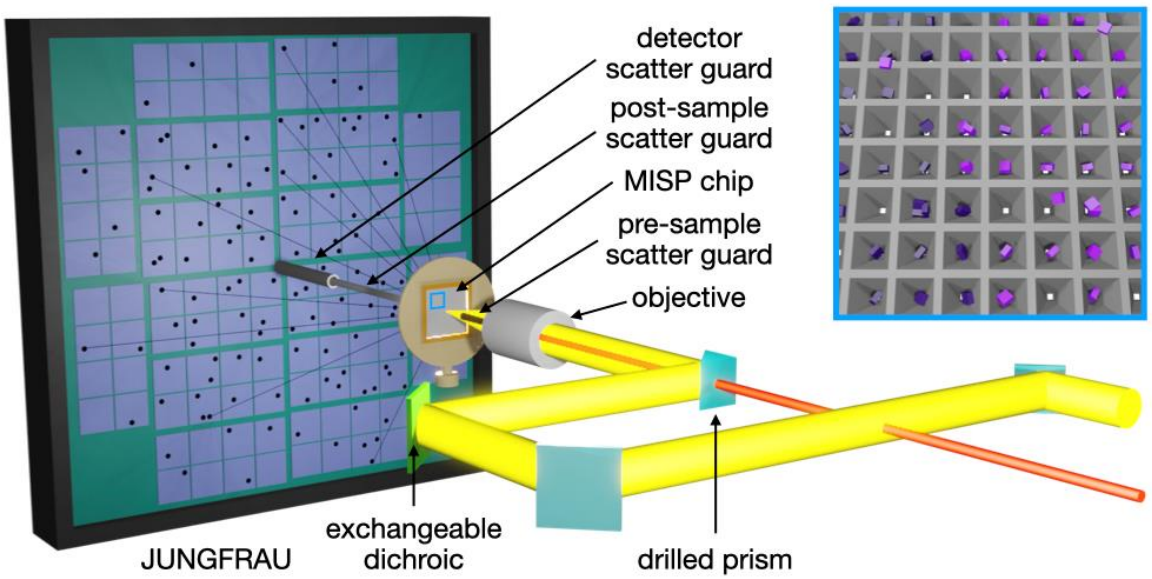

Figure 3.2: A schematic of the pump-probe experimental set-up at SwissMX endstation at the SwissFEL Cristallina experimental station. The pump laser (yellow) is coupled to the sample position *via* the endstation's on-axis viewing (OAV) system. An exchangeable dichroic mirror (light green) enables different pump wavelengths to be reflected whilst transmitting light for the chip alignment into a camera (not shown in this diagram). The X-rays pass through the centre of the drilled objective and prism of the final part of the laser coupling. Air scatter from the X-ray is minimized using pre-and post-sample scatter-guards. The blue box highlights an area of the chip showing a 1:1 interleaved light:dark scheme, where X-rays are delivered to every well and laser pump only to every other.

Data were collected on two different chip types, named *transparent* and *opaque* from their transparency to visible spectrum or lack thereof, and in two different orientations, *open* and *flat*. The transparent chips were made from commercially available 50 µm COP film, whereas the opaque chips were fabricated with an in-house cast film using COC pellets and the addition of carbon black powder (M. Carrillo et al., 2023)

Time-resolved spectroscopy experiments on *Cr*LOV1 used in this experiment indicate that it undergoes the formation of a covalent thioether bond between FMN cofactor and Cys57 10 µs after photoexcitation (Holzer et al., 2002; Kottke et al., 2003), which then persist late into the photocycle (Fedorov et al., 2003; Kottke et al., 2003) (Figure 3.3). Given the significant strength of the expected signal in the Fourier difference maps for the covalent bond formation,

a 10 µs time delay was selected to test the suitability of the *Cr*LOV1 crystals for TR-SFX experiments and to make use of their long (~ 200 s) photocycle to serve as a light contamination indicator.

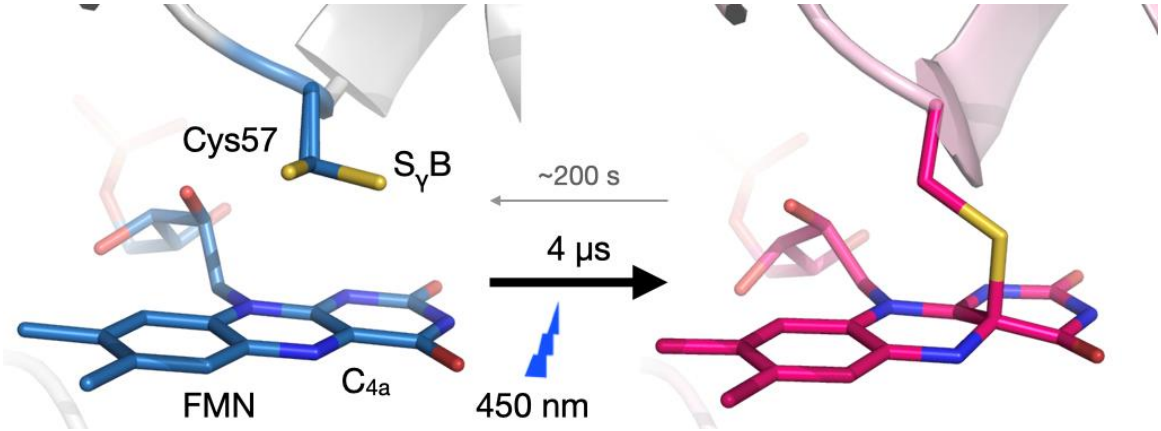

Figure 3.3: Thioadduct formation between *Cr*LOV1 and its FMN cofactor upon illumination. Crystal structures of *Chlamydomonas reindhartii* LOV1 domain in light and dark stationary states present two conformations of the binding-site cysteine (Cys57) (Fedorov et al., 2003). Blue-light absorption causes the formation of a covalent bond between the flavin C(4a) and the thiol of Cys57 within 10 □s. The reaction proceeds through an excited flavin singlet to a triplet state that then decays monotonically to the adduct (Holzer et al., 2002; Kottke et al., 2003) in which this cysteine moves ~1.5 Å closer to the FMN-C(4a) for adduct formation (Fedorov et al., 2003). Thio-adduct formation then triggers rearrangements throughout the whole LOV domain (Gotthard et al., 2023).

We employed a 1:1 interleaved light:dark experimental routine with the XFEL at 100 Hz and the pump-laser at 50 Hz. While a comprehensive analysis of the LOV-FMN light-activated structure is beyond the scope of this paper, it suffices to expect a photoactivated structure with the FMN-Cys covalent adduct formation in the laser-exposed crystals. The unpumped crystals should yield a dark state structure without the thioether bond signature. We also collected SFX data entirely without pump laser (*laser-off*) for reference as a "properly" dark state. Ideally, the *laser-off* should be indistinguishable from the dark datasets in the interleaving TR-SFX experiment.

It is important to stress the importance of delivering light-contamination-free time-resolved pump probe data. Otherwise, the crystallographic data would represent multiple overlapping protein trajectories triggered by more than one pump laser pulse, impairing correct interpretation of the electron densities. Importantly for the current work, the *Cr*LOV1 domain was specifically chosen for the fixed-target pump-probe commissioning since the 200 s resting state recovery time of the domain significantly exceeds the 10 ms interval between the consecutive XFEL pulses into the adjacent cavities of the chip. The 200 s recovery time also exceeds the time to image over half the chip, so potential light contamination in adjacent columns will also be observed.

In the quest to explore different experimental geometries of the fixed-target setup, two orientations of the opaque chips were tested with respect to the incidence pump laser and X-rays. One orientation where the chip was mounted with the pyramidal cavity facing either towards the X-ray and optical laser beams (*open* side), or in the opposite direction (*flat* side) [Figure 3.1(*d*) and (*e*)]. The transparent chip was only tested in one orientation (*open*).

3.3.2 Assessment of contamination

The TR-SFX experiment was carried out with a Δt=10 μs between the laser pump and X-ray probe pulses. Fourier difference electron density maps were evaluated in terms of photoactivation yield and potential light contamination in the nearby wells. The transparent chip setup yielded positive signal indicating thioether bond formation in $F_{obs}^{interleaved\text{-}dark} - F_{obs}^{laser\text{-}off}$ [Figure 3.4(*a*)], $F_{obs}^{interleaved\text{-}light} - F_{obs}^{laser\text{-}off}$ [Figure 3.4(*b*)] and $F_{obs}^{interleaved\text{-}light} - F_{obs}^{interleaved\text{-}dark}$ [Figure 3.4(*c*)]. While it shows features characteristic of the light activated state, the light signal present in the $F_{obs}^{interleaved\text{-}dark} - F_{obs}^{laser\text{-}off}$ indicates that each pump laser pulse did not only photoactivate a single well of the chip but that the light reached the adjacent wells leading to light contamination. Although light contamination was more likely in the transparent

chips, the extent of its prevalence was not expected. It is interesting that the signal for the $F_{obs}^{interleaved\text{-}dark} - F_{obs}^{laser\text{-}off}$ was as strong as for the $F_{obs}^{interleaved\text{-}light} - F_{obs}^{interleaved\text{-}dark}$ maps. The light contamination was likely due to the transmission of the laser light orthogonally through the chip from the scattering source, either *via* interaction with the crystal, chip or both.

Next, we performed tests using the opaque MISP-chips in two orientations. The *open* orientation, which allows the most light to reach the sample and maximizes the excited fraction of molecules, again yielded positive signal indicating the thioether bond formation in the $F_{obs}^{interleaved\text{-}dark} - F_{obs}^{laser\text{-}off}$ [Figure 3.4(*d*)]. Although yielding significantly lower signals than in the case of the transparent chips, contamination was still evident. Qualitatively similar signal was also present in the $F_{obs}^{interleaved\text{-}light} - F_{obs}^{laser\text{-}off}$ [Figure 3.4(*e*)] and $F_{obs}^{interleaved\text{-}light} - F_{obs}^{interleaved\text{-}dark}$ [Figure 3.4(*f*)].

However, in the alternative chip orientation, with the *flat* side of the cavity now facing the pump laser, no thioether signal was observed in the $F_{obs}^{interleaved\text{-}dark} - F_{obs}^{laser\text{-}off}$ [Figure 3.4(*g*)]. This lack of thioether bond signal shows that there was no detectable light contamination. At the same time, the $F_{obs}^{interleaved\text{-}light} - F_{obs}^{laser\text{-}off}$ [Figure 3.4(*h*)] and $F_{obs}^{interleaved\text{-}light} - F_{obs}^{interleaved\text{-}dark}$ [Figure 3.4(*i*)] both show the expected electron density signature for the covalent adduct formation. Therefore, the *opaque* chips with *flat* side incidence of the laser light onto the sample did prove to be a successful setup in our experiment.

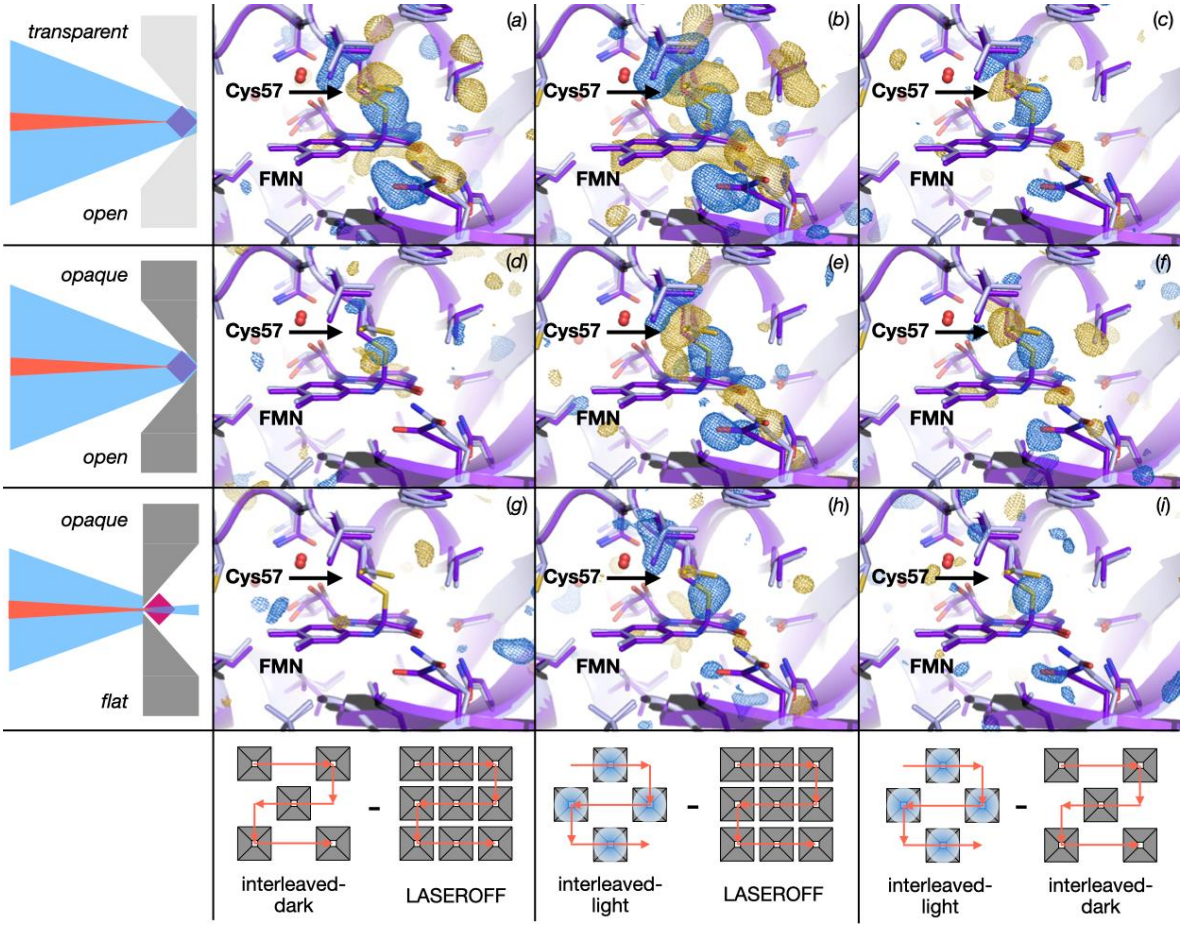

Figure 3.4: Chip placement for laser incidence and Fourier difference electron density maps for TR-SFX with *Cr*LOV1 at Δt=10 µs. Three different setups were investigated. Shown in the upper row is a *transparent chip with cavity facing the pump pulse.* This geometry yields activation signal in all three maps corresponding to thioether bond formation between the active site cysteine and FMN*:* (*a*) $F_{obs}^{interleaved\text{-}dark} - F_{obs}^{laser\text{-}off}$ (*b*) $F_{obs}^{interleaved\text{-}light} - F_{obs}^{laser\text{-}off}$ (*c*) $F_{obs}^{interleaved\text{-}light} - F_{obs}^{interleaved\text{-}dark}$. The middle row shows that data collection using the *opaque chip with cavity facing the pump pulse* yields activation signal in all three maps*:* (*d*) $F_{obs}^{interleaved\text{-}dark} - F_{obs}^{laser\text{-}off}$ (*e*) $F_{obs}^{interleaved\text{-}light} - F_{obs}^{laser\text{-}off}$ (*f*) $F_{obs}^{interleaved\text{-}light} - F_{obs}^{interleaved\text{-}dark.}$ The bottom row shows that data acquisition using the *opaque chip with aperture facing the pump pulse* yields activation signal where expected while the lack of signal in the $F_{dark} - F_{laser\text{-}off}$ indicates that in this setup light contamination was avoided: (*g*) $F_{obs}^{interleaved\text{-}dark} - F_{obs}^{laser\text{-}off}$ (*h*) $F_{obs}^{interleaved\text{-}light} - F_{obs}^{laser\text{-}off}$ and (*i*) $F_{obs}^{interleaved\text{-}light} - F_{obs}^{interleaved\text{-}dark}$. Fourier difference electron density maps show positive and negative densities as blue and gold mesh, respectively, highlighting differences between datasets. The cartoon and sticks representation show in light grey the dark state of the protein with its FMN ligand adjacent to but not covalently bound to Cys57. As a reference, the photoactivated late photocycle intermediate with FMN covalently bound to Cys57 is shown in purple. A schematic representation of the chip (grey) with a crystal sample (pink/blue) placement with respect to pump laser (blue) and XFEL pulses (red) is shown at the very left. The bottom panel shows the practical arrangement of the data from the wells contributing to the different maps.

The reason for the success of the experiment in the *flat* orientation compared to the *open* was likely due to the reduced potential exposure of the crystals in this orientation (Figure 3.5). As stated in the methods, due to issues at the beginning of beamtime, the laser beam profile could not be precisely measured, only approximately inferred from scattered light off a black film. This means that the laser profile could conceivably be larger than the 50x50 μm^2 estimate. Figure 3.5(*a*) shows how an increased laser profile could enable light contamination in the *open* chip orientation. The *flat* orientation could, by restricting the view of the crystals by the pump laser, help to prevent the contamination even with a larger laser profile. It is possible that stray scattered light of either the collimator or chip sealing film may have been a contaminating factor [Figure 3.5(*b*)]. Another potential contributing factor was the synchronization of the stage motion and XFEL pulse. Subsequent experiments have shown that the XFEL pulse was delivered approximately 1 ms (12 μm) behind its intended location, *i.e.*, the XFEL pulse was not hitting the centre of each aperture, but 12 μm off on the side of the aperture [Figure 3.5(*c*)].

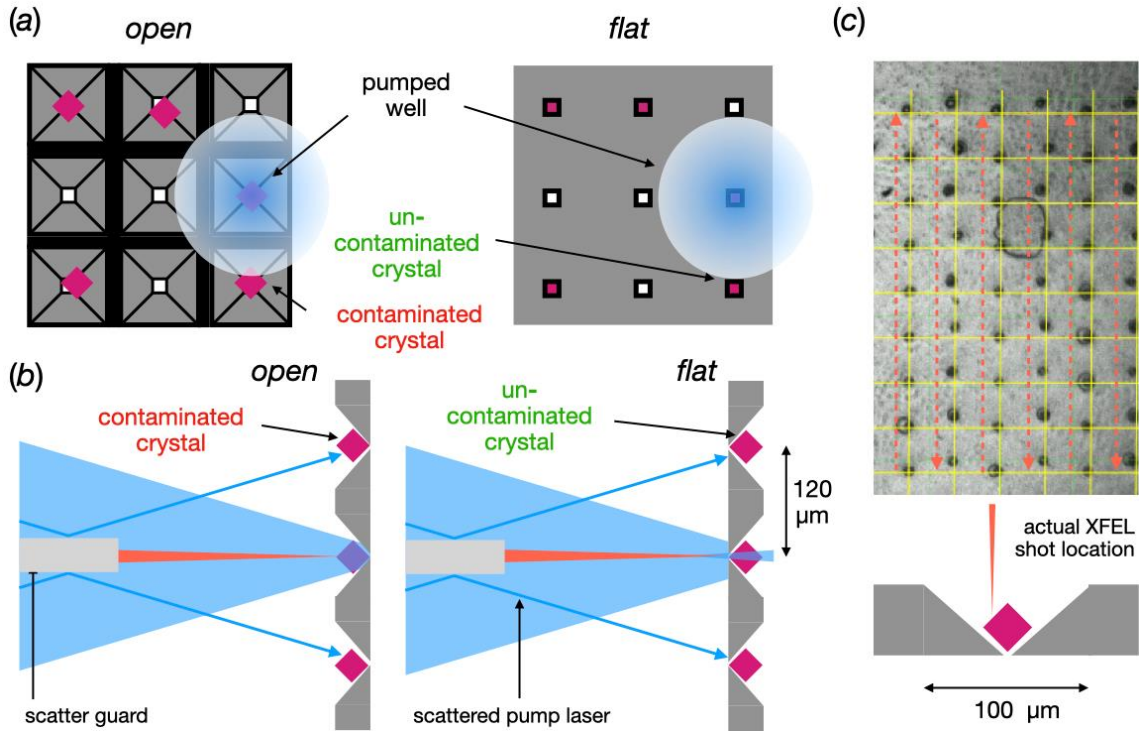

Figure 3.5. Possible explanations for the light contamination observed in the *open* orientation but not in the *flat orientation*. (*a*) Schematic of the X-ray/pump laser view of the chip in the *open* and *flat* orientation. In the *open* view, the entire crystal is visible, enabling contamination *via* a large laser profile. The same large laser profile in the *flat* orientation does not give rise to contamination due to the restricted view of the crystals. (*b*) A schematic showing how potential scattered pump laser from the pre-sample scatter guard could give rise to light contamination. Again, restricted view of the crystals in the *flat* orientation prevents contamination of crystals in adjacent well. (*c*) An image collected with the help of the Max Planck Institute, Heidelberg using a sheet an SOS chip (R. Doak et al., 2018) containing 1 M Cadium Chloride and a schematic of its implications for the MISP chip. The image was collected using the OAV camera of the SwissMX. The yellow grid shows the intended shot locations. The red arrow shows the direction of travel of the stages. Due to the 1 ms off-set of the stage motion and XFEL, the XFEL shot is 12 µm off the aperture centre.

3.3.3 Reduction in sample consumption

Sample preparation is a laborious and challenging task for TR-SFX experiments. Various sample parameters must be considered and optimized depending on the planned experiment and delivery system used. Not only does the sample need to be of high quality but the large quantities of crystalline protein can require months of sample production in preparation for every experiment. One of the attractive features of fixed-targets is their low

sample consumption when compared to other delivery methods. The sample consumption from our fixed-target TR-SFX experiment was calculated to be only ~200 μg for the collection of 10,000 indexed lattices. For comparison, Table 3.2 shows the quantities of samples consumed in several jet-based experiments with 120 Hz and lower X-ray pulse repetition rates. The development of the HVE for sample delivery was a significant improvement (>10x) when it comes to sample consumption compared to the first GDVN experiments and has now been responsible for a considerable number of successful TR-SFX epxeriments (Claesson et al., 2020; Hosaka, Nomura, et al., 2022; James et al., 2019; Li et al., 2021; Liu et al., 2022; Maestre-Reyna et al., 2022; Mous et al., 2022; Nango et al., 2016; Nass Kovacs et al., 2019; Nogly et al., 2016; Nogly et al., 2018; P. Skopintsev et al., 2020; Suga et al., 2017). However, as noted in the introduction, experiments at high pulse repetition rate XFEL facilities should reduce significantly sample consumption with GDVN delivery (S. Pandey et al., 2020).

Table 3.2: Pump-probed experiments sample consumption

Protein [pulse mode of XFEL]	**Method**	**Sample used per 10K indexed images**
Photoactivable Yellow Protein [120 Hz] (Pande et al., 2016; S. Pandey et al., 2020)	GDVN	75 mg
Bacteriorhodopsin [120 Hz] (Nogly et al., 2018), Halorhodopsin [50 Hz] (Mous et al., 2022)	HVE (LCP)	2.0-2.6 mg
Isocyanide Hydratase [n/a] (Dasgupta et al., 2019)	CoMESH	2.5-3.0 mg
Light-Oxygen-Voltage Domain 1 [100 Hz]	MISP-chip	0.20 mg

The use of the MISP-chip reported here required approximately 10 times less sample than HVE with less than 1 mg of protein required for a full dataset. With every improvement in sample delivery, TR-SFX becomes more accessible to a larger scientific community and a

wider range of interesting targets; many of which may not be easily overexpressed in greater quantities. Another practical point is that the preparation for the experiments can now be shortened in many cases from months to weeks facilitating timely completion of the TR-SFX projects.

A drawback of sample delivery using the MISP-chips includes the time that it takes for loading and mounting each chip in a humid environment and the transporting the chips in a humidity chamber from the dark room to the beamline, a procedure that took around half an hour for 5 mounted chips. In addition, light contamination was an important concern when compared to jet-based experiments, where the sample is enclosed and stored in a dark reservoir until it is finally injected in a stream. The MISP chips, and other patterned fixed-targets, are also not obviously suitable for membrane protein crystals grown in LCP. These crystals are hard to separate from the cubic phase and fail to populate the apertures. Moving the LPC-grown crystals into the much less viscous sponge phase could provide a valuable alternative. Our commissioning experiment shows that light contamination-free SFX and TR-SFX data can still be acquired using the *flat* orientation of the chip. Furthermore, there is also the potential to employ robotic systems for the chip mounting that will undoubtedly increase the efficiency of beamtime usage.

3.3 Conclusion

XFELs have allowed for the rapid growth of time-resolved structural experiments which provide crucial information on the function of biological machines' and molecular mechanisms. This is the first experiment of its type using a light-activated protein *Cr*LOV1 at the Cristallina endstation of the SwissFEL and using the novel MISP-chips for sample delivery. The light contamination present with the transparent MISP-chip was interesting to observe and showed the absolute necessity for using an opaque chip. With the opaque chips, the laser spot

size and various other parameters are still critical to the success of the experiment. Many of these, particularly the laser spot profile, undoubtably lead to the contamination observed in the *open* orientation. Future commissioning experiments will focus on enabling TR-SFX in the *open* orientation. This conformation has the greater propensity for crystal excitation as in the *flat* is very unforgiving for crystals that are not perfectly sitting inside the aperture and if the chip is slightly misaligned. The reported experiments are an important step towards a making XFEL fixed-target sample delivery compatible with pump-probe time-resolved experiments and making these experiments more sample efficient. Increasing sample and experimental time efficiency will make these experiments more attainable for the general structural biology community.

Acknowledgements

Project financed under Dioscuri, a program initiated by the Max Planck Society, jointly managed with the National Science Centre in Poland, and mutually funded by the Polish Ministry of Education and Science and the German Federal Ministry of Education and Research. This research was funded by National Science Centre, grant agreement No. UMO-2021/03/H/NZ1/00002 to P.N. We also acknowledge infrastructural support by Strategic Programme Excellence Initiative at Jagiellonian University - BioS PRA. For the purpose of Open Access, authors have applied a CC-BY public copyright licence to any Author Accepted Manuscript (AAM) version arising from this submission. Furthermore, this project was initiated with funding received from the Swiss National Science Fundation Ambizione grant PZ00P3_174169 to P.N. M.C. is supported by a studentship grant of the Swiss Nanoscience Institute, Project #1904. This project has also received funding from the European Union's HORIZON 2020 Research and Innovation Program under the Marie S. Curie grant agreement No. 701647. We acknowledge the Paul Scherrer Institute, Villigen, Switzerland for provision of free-electron laser beamtime at the Cristallina experimental station on the SwissFEL ARAMIS branch. Cristallina was realized with financial support from the Swiss National Science Foundation and the University of Zürich under Project Nr. 206021_183330.

3.5 References

Botha, S., Nass, K., Barends, T. R. M., Kabsch, W., Latz, B., Dworkowski, F., Foucar, L., Panepucci, E., Wang, M., Shoeman, R. L., Schlichting, I. & Doak, R. B. (2015). *Acta Crystallographica Section D Biological Crystallography* **71**, 387-397.

Boutet, S., Lomb, L., Williams, G. J., Barends, T. R., Aquila, A., Doak, R. B., Weierstall, U., DePonte, D. P., Steinbrener, J., Shoeman, R. L., Messerschmidt, M., Barty, A., White, T. A., Kassemeyer, S., Kirian, R. A., Seibert, M. M., Montanez, P. A., Kenney, C., Herbst, R., Hart, P., Pines, J., Haller, G., Gruner, S. M., Philipp, H. T., Tate, M. W., Hromalik, M., Koerner, L. J., van Bakel, N., Morse, J., Ghonsalves, W., Arnlund, D., Bogan, M. J., Caleman, C., Fromme, R., Hampton, C. Y., Hunter, M. S., Johansson, L. C., Katona, G., Kupitz, C., Liang, M., Martin, A. V., Nass, K., Redecke, L., Stellato, F., Timneanu, N., Wang, D., Zatsepin, N. A., Schafer, D., Defever, J., Neutze, R., Fromme, P., Spence, J. C., Chapman, H. N. & Schlichting, I. (2012). *Science* **337**, 362-364.

Brändén, G. & Neutze, R. (2021). *Science* **373**.

Carrillo, M., Beale, J. & Padeste, C. (2022). *Acta Crystallographica* **A78**, a279.

Carrillo, M., Mason, T. J., Karpik, A., Martiel, I., Kepa, M. W., McAuley, K. E., Beale, J. H. & Padeste, C. (2023). *IUCrJ* **10**, 678-693.

Chapman, H. N., Fromme, P., Barty, A., White, T. A., Kirian, R. A., Aquila, A., Hunter, M. S., Schulz, J., DePonte, D. P., Weierstall, U., Doak, R. B., Maia, F. R., Martin, A. V., Schlichting, I., Lomb, L., Coppola, N., Shoeman, R. L., Epp, S. W., Hartmann, R., Rolles, D., Rudenko, A., Foucar, L., Kimmel, N., Weidenspointner, G., Holl, P., Liang, M., Barthelmess, M., Caleman, C., Boutet, S., Bogan, M. J., Krzywinski, J., Bostedt, C., Bajt, S., Gumprecht, L., Rudek, B., Erk, B., Schmidt, C., Homke, A., Reich, C., Pietschner, D., Struder, L., Hauser, G., Gorke, H., Ullrich, J., Herrmann, S., Schaller, G., Schopper, F., Soltau, H., Kuhnel, K. U., Messerschmidt, M., Bozek, J. D., Hau-Riege, S. P., Frank, M., Hampton, C. Y., Sierra, R. G., Starodub, D., Williams, G. J., Hajdu, J., Timneanu, N., Seibert, M. M., Andreasson, J., Rocker, A., Jonsson, O., Svenda, M., Stern, S., Nass, K., Andritschke, R., Schroter, C. D., Krasniqi, F., Bott, M., Schmidt, K. E., Wang, X., Grotjohann, I., Holton, J. M., Barends, T. R., Neutze, R., Marchesini, S., Fromme, R., Schorb, S., Rupp, D., Adolph, M., Gorkhover, T., Andersson, I., Hirsemann, H., Potdevin, G., Graafsma, H., Nilsson, B. & Spence, J. C. (2011). *Nature* **470**, 73-77.

Claesson, E., Wahlgren, W. Y., Takala, H., Pandey, S., Castillon, L., Kuznetsova, V., Henry, L., Panman, M., Carrillo, M., Kubel, J., Nanekar, R., Isaksson, L., Nimmrich, A., Cellini, A., Morozov, D., Maj, M., Kurttila, M., Bosman, R., Nango, E., Tanaka, R., Tanaka, T., Fangjia, L., Iwata, S., Owada, S., Moffat, K., Groenhof, G., Stojkovic, E. A., Ihalainen, J. A., Schmidt, M. & Westenhoff, S. (2020). *Elife* **9**.

Dasgupta, M., Budday, D., de Oliveira, S., Madzelan, P., Marchany-Rivera, D., Seravalli, J., Hayes, B., Sierra, R. G., Boutet, S., Hunter, M. S., Alonso-Mori, R., Batyuk, A., Wierman, J., Lyubmiov, A., Brewster, A. S., Sauter, N. K., Applegate, G. A., Tiwari, V. K., Berkowitz, D. B., Thompson, M. C., Cohen, A. E., Fraser, J. S., Wall, M. E., van de Bedem, H. & Wilson, M. A. (2019). *PNAS* **116**, 25634-25640.

DeLano, W. (2020).

DePonte, D., Doak, R., Hunter, M., Zhenquan, L., Weierstall, U. & Spence, J. (2009). *Micron* **40**, 507-509.

Doak, R., Kovacs, G., Gorel, A., Foucar, L., Barends, T., Grünbein, M., Hilpert, M., Kloos, M., Roome, C., Shoeman, R., Stricker, M., Tono, K., You, D., Ueda, K., Sherrell, D. A., Owen, R. L. & Schlichting, I. (2018). *Acta Crystallographica* **D74**, D1000-1007.

Ebrahim, A., Appleby, M., Axford, D., Beale, J., Moreno-Chicano, T., Sherrell, D. A., Strange, R. W., Hough, M. A. & Owen, R. L. (2019). *Acta Crystallographica* **D75**, 151-159.

Fedorov, R., Schlichting, I., Hartmann, E., Domratcheva, T., Fuhrmann, M. & Hegemann, P. (2003). *Biophysics J* **84**, 2474-2482.

Fromme, R., Ishchenko, A., Metz, M., Chowdhury, S. R., Basu, S., Boutet, S., Fromme, P., White, T. A., Barty, A., Spence, J. C. H., Weierstall, U., Liu, W. & Cherezov, V. (2015). *International Union of Crystallography Journal* **2**, 545-551.

Gevorkov, Y., Yefanov, O., Barty, A., White, T. A., Mariani, V., Brehm, W., Tolstikova, A., Grigat, R. R. & Chapman, H. N. (2019). *Acta Crystallogr A Found Adv* **75**, 694-704.

Gisriel, C., Coe, J., Letrun, R., Yefanov, O. M., Luna-Chavez, C., Stander, N. E., Lisova, S., Mariani, V., Kuhn, M., Aplin, S., Grant, T. D., Dorner, K., Sato, T., Echelmeier, A., Cruz Villarreal, J., Hunter, M. S., Wiedorn, M. O., Knoska, J., Mazalova, V., Roy-Chowdhury, S., Yang, J. H., Jones, A., Bean, R., Bielecki, J., Kim, Y., Mills, G., Weinhausen, B., Meza, J. D., Al-Qudami, N., Bajt, S., Brehm, G., Botha, S., Boukhelef, D., Brockhauser, S., Bruce, B. D., Coleman, M. A., Danilevski, C., Discianno, E., Dobson, Z., Fangohr, H., Martin-Garcia, J. M., Gevorkov, Y., Hauf, S., Hosseinizadeh, A., Januschek, F., Ketawala, G. K., Kupitz, C., Maia, L., Manetti, M., Messerschmidt, M., Michelat, T., Mondal, J., Ourmazd, A., Previtali, G., Sarrou, I., Schon, S., Schwander, P., Shelby, M. L., Silenzi, A., Sztuk-Dambietz, J., Szuba, J., Turcato, M., White, T. A., Wrona, K., Xu, C., Abdellatif, M. H., Zook, J. D., Spence, J. C. H., Chapman, H. N., Barty, A., Kirian, R. A., Frank, M., Ros, A., Schmidt, M., Fromme, R., Mancuso, A. P., Fromme, P. & Zatsepin, N. A. (2019). *Nat Commun* **10**, 5021.

Gotthard, G., Mous, S., Weinert, T., Maia, R. N. A., James, D., Dworkowski, F., Gashi, D., Furrer, A., Ozerov, D., Panepucci, E., Wang, M., Schertler, G. F. X., Heberle, J., Standfuss, J. & Nogly, P. (2023). *bioRxiv* **preprint**.

Grunbein, M. L., Bielecki, J., Gorel, A., Stricker, M., Bean, R., Cammarata, M., Dorner, K., Frohlich, L., Hartmann, E., Hauf, S., Hilpert, M., Kim, Y., Kloos, M., Letrun, R., Messerschmidt, M., Mills, G., Nass Kovacs, G., Ramilli, M., Roome, C. M., Sato, T., Scholz, M., Sliwa, M., Sztuk-Dambietz, J., Weik, M., Weinhausen, B., Al-Qudami, N., Boukhelef, D., Brockhauser, S., Ehsan, W., Emons, M., Esenov, S., Fangohr, H., Kaukher, A., Kluyver, T., Lederer, M., Maia, L., Manetti, M., Michelat, T., Munnich, A., Pallas, F., Palmer, G., Previtali, G., Raab, N., Silenzi, A., Szuba, J., Venkatesan, S., Wrona, K., Zhu, J., Doak, R. B., Shoeman, R. L., Foucar, L., Colletier, J. P., Mancuso, A. P., Barends, T. R. M., Stan, C. A. & Schlichting, I. (2018). *Nat Commun* **9**, 3487.

Grunbein, M. L., Stricker, M., Nass Kovacs, G., Kloos, M., Doak, R. B., Shoeman, R. L., Reinstein, J., Lecler, S., Haacke, S. & Schlichting, I. (2020). *Nat Methods* **17**, 681-684.

Holzer, W., Penzkofer, A., Fuhrmann, M. & Hegemann, P. (2002). *Photochem Photobiol* **75**, 479-487.

Hosaka, T., Nomura, T., Kubo, M., Nakane, T., Fangjia, L., Sekine, S. I., Ito, T., Murayama, K., Ihara, K., Ehara, H., Kashiwagi, K., Katsura, K., Akasaka, R., Hisano, T., Tanaka, T., Tanaka, R., Arima, T., Yamashita, A., Sugahara, M., Naitow, H., Matsuura, Y., Yoshizawa, S., Tono, K., Owada, S., Nureki, O., Kimura-Someya, T., Iwata, S., Nango, E. & Shirouzu, M. (2022). *Proc Natl Acad Sci U S A* **119**.

Hunter, M. S., Segelke, B., Messerschmidt, M., Williams, G. J., Zatsepin, N. A., Barty, A., Benner, W. H., Carlson, D. B., Coleman, M., Graf, A., Hau-Riege, S. P., Pardini, T., Seibert, M. M., Evans, J., Boutet, S. & Frank, M. (2014). *Nature Scientific Reports* **4**, 6026.

James, D., Weinert, T., Skopintsev, P., Furrer, A., Gashi, D., Tanaka, T., Nango, E., Nogly, P. & Standfuss, J. (2019). *J Vis Exp*.

Kaminski, J. W., Vera, L., Stegmann, D. P., Vering, J., Eris, D., Smith, K. M. L., Huang, C. Y., Meier, N., Steuber, J., Wang, M., Fritz, G., Wojdyla, J. A. & Sharpe, M. E. (2022). *Acta Crystallogr D Struct Biol* **78**, 328-336.

Kottke, T., Heberle, J., Hehn, D., Dick, B. & Hegemann, P. (2003). *Biophys J*, 1192-1201.

Li, H., Nakajima, Y., Nomura, T., Sugahara, M., Yonekura, S., Chan, S. K., Nakane, T., Yamane, T., Umena, Y., Suzuki, M., Masuda, T., Motomura, T., Naitow, H., Matsuura, Y., Kimura, T., Tono, K., Owada, S., Joti, Y., Tanaka, R., Nango, E., Akita, F., Kubo, M., Iwata, S., Shen, J. R. & Suga, M. (2021). *IUCrJ* **8**, 431-443.

Liebschner, D., Afonine, P. V., Baker, M., Bunkoczi, G., Chen, V. B., Croll, T. I., Hintze, B., Hung, L.-W., Jain, S., McCoy, A. J., Moriarty, N. W., Oeffner, R. D., Poon, B. K., Prisant, M. G., Read, R. J., Richardson, J. S., Richardson, D. C., Sammito, M. D., Sobolev, O. V., Stockwell, D. H., Tervilliger, T. C., Urzhumstev, A. G., Videau, L. L., Williams, C. J. & Adams, P. D. (2019). *Acta Crystallographica* **D75**, 861-877.

Liu, X., Liu, P., Li, H., Xu, Z., Jia, L., Xia, Y., Yu, M., Tang, W., Zhu, X., Chen, C., Zhang, Y., Nango, E., Tanaka, R., Luo, F., Kato, K., Nakajima, Y., Kishi, S., Yu, H., Matsubara, N., Owada, S., Tono, K., Iwata, S., Yu, L. J., Shen, J. R. & Wang, J. (2022). *Nat Chem* **14**, 1054-1060.

Madden, J. T., Toth, S. J., Dettmar, C. M., Newman, J. A., Oglesbee, R. A., Hedderich, H. G., Everly, R. M., Becker, M., Ronau, J. A., Buchanan, S. K., Cherezov, V., Morrow, M. E., Xu, S., Ferguson, D., Makarov, O., Das, C., Fischetti, R. & Simpson, G. J. (2013). *J Synchrotron Radiat* **20**, 531-540.

Maestre-Reyna, M., Yang, C. H., Nango, E., Huang, W. C., Putu, E. P. G. N., Wu, W. J., Wang, P. H., Badur-Franz, S., Saft, M., Emmerich, H. J., Wu, H. Y., Lee, C. C., Huang, K. F., Chang, Y. K., Liao, J. H., Weng, J. H., Gad, W., Chang, C. W., Pang, A. H., Sugahara, M., Owada, S., Hosokowa, Y., Joti, Y., Yamashita, A., Tanaka, R., Tanaka, T., Luo, F., Tono, K., Hsu, K. C., Kiontke, S., Schapiro, I., Spadaccini, R., Royant, A., Yamamoto, J., Iwata, S., Essen, L. O., Bessho, Y. & Tsai, M. D. (2022). *Nat Chem* **14**, 677-685.

Mehrabi, P., Müller-Werkmeister, H. M., Leimkohl, J. P., Schikora, H., Ninkovic, J., Krivokuca, S., Andricek, L., Epp, S. W., Sherrell, D. A., Owen, R. L., Pearson, A. R., Tellkamp, F., Schulz, E. C. & Miller, R. J. D. (2020). *Journal of Synchrotron Radiation* **27**, 360-370.

Mehrabi, P., Schulz, E. C., Agthe, M., Horrell, S., Bourenkov, G., von Stetten, D., Jan-Philipp, L., Schikora, H., Schneider, T. R., Pearson, A. R., Tellkamp, F. & Miller, R. J. D. (2019). *Nature Methods* **16**, 979-982.

Mehrabi, P., Schulz, E. C., Dsouza, R., Mueller-Werkmeister, H. M., Tellkamp, F., Miller, R. J. D. & Pai, E. F. (2019). *Science* **365**, 1167-1170.

Mous, S., Gotthard, G., Ehrenberg, D., Sen, S., Weinert, T., Johnson, P. J., James, D., Nass, K., Furrer, A., Kekilli, D., Ma, P., Bruenle, S., Casadei, C. M., Martiel, I., Dworkowski, F., Gashi, D., Skopintsev, P., Wranik, M., Knopp, G., Panepucci, E., Panneels, V., Cirelli, C., Ozerov, D., Schertler, G. F. X., Wang, M., Milne, C., Standfuss, J., Schapiro, I., Heberle, J. & Nogly, P. (2022). *Science* **375**, 845-851.

Mueller, C., Marx, A., Epp, S. W., Zhong, Y., Kuo, A., Balo, A. R., Soman, J., Schotte, F., Lemke, H. T., Owen, R. L., Pai, E. F., Pearson, A. R., Olson, J. S., Anfinrud, P. A., Ernst, O. P. & Miller, R. J. D. (2015). *Structural Dynamics* **2**, 054302.

Nam, K. H., Kim, J. & Cho, Y. (2021). *Sci Rep* **11**, 13115.

Nango, E., Royant, A., Kubo, M., Nakane, T., Wickstrand, C., Kimura, T., Tanaka, T., Tono, K., Song, C., Tanaka, R., Arima, T., Yamashita, A., Kobayashi, J., Hosaka, T., Mizohata, E., Nogly, P., Sugahara, M., Nam, D., Nomura, T., Shimamura, T., Im, D., Fujiwara, T., Yamakana, Y., Jeon, B., Nishizawa, T., Oda, K., Fukuda, M., Andersson, R., Bath, P.,

Dods, R., Davidsson, J., Matsuoka, S., Kawatake, S., Murata, M., Nureki, O., Owada, S., Kameshima, T., Hatsui, T., Joti, Y., Schertler, G. F. X., Yabashi, M., Bondar, A.-N., Standfuss, J., Neutze, R. & Iwata, S. (2016). *Science* **354**, 1552-1557.

Nass Kovacs, G., Colletier, J. P., Grunbein, M. L., Yang, Y., Stensitzki, T., Batyuk, A., Carbajo, S., Doak, R. B., Ehrenberg, D., Foucar, L., Gasper, R., Gorel, A., Hilpert, M., Kloos, M., Koglin, J. E., Reinstein, J., Roome, C. M., Schlesinger, R., Seaberg, M., Shoeman, R. L., Stricker, M., Boutet, S., Haacke, S., Heberle, J., Heyne, K., Domratcheva, T., Barends, T. R. M. & Schlichting, I. (2019). *Nat Commun* **10**, 3177.

Neutze, R., Wouts, R., van der Spoel, D., Weckert, E. & Hajdu, J. (2000). *Nature* **406**, 752-757.

Nogly, P., James, D., Wang, D., White, T., Zatsepin, N., Shilova, A., Nelson, G., Liu, H., Johansson, L., Heymann, M., Jaeger, K., Metz, M., Wickstrand, C., Wenting, W., Bath, P., Berntsen, P., Oberthuer, D., Panneels, V., Cherezov, V., Chapman, H. N., Schertler, G. F. X., Neutze, R., Spence, J. C., Moraes, I., Burghammer, M., Standfuss, J. & Weierstall, U. (2015). *International Union of Crystallography Journal* **2**, 168-176.

Nogly, P., Panneels, V., Nelson, G., Gati, C., Kimura, T., Milne, C., Milathianaki, D., Kubo, M., Wu, W., Conrad, C., Coe, J., Bean, R., Zhao, Y., Bath, P., Dods, R., Harimoorthy, R., Beyerlein, K. R., Rheinberger, J., James, D., DePonte, D., Li, C., Sala, L., Williams, G. J., Hunter, M. S., Koglin, J. E., Berntsen, P., Nango, E., Iwata, S., Chapman, H. N., Fromme, P., Frank, M., Abela, R., Boutet, S., Barty, A., White, T. A., Weierstall, U., Spence, J., Neutze, R., Schertler, G. & Standfuss, J. (2016). *Nat Commun* **7**, 12314.

Nogly, P., Weinert, T., James, D., Carbajo, S., Ozerov, D., Furrer, A., Gashi, D., Borin, V., Skopintsev, P., Jaeger, K., Nass, K., Bath, P., Bosman, R., Koglin, J., Seaberg, M., Lane, T., Kekilli, D., Bruenle, S., Tanaka, T., Wu, W., Milne, C., White, T. A., Barty, A., Weierstall, U., Panneels, V., Nango, E., Iwata, S., Hunter, M., Schapiro, I., Schertler, G. F. X., Neutze, R. & Standfuss, J. (2018). *Science* **361**.

Oghbaey, S., Sarracini, A., Ginn, H. M., Pare-Labrosse, O., Kuo, A., Marx, A., Epp, S. W., Sherrell, D. A., Eger, B. T., Zhong, Y., Loch, R., Mariani, V., Alonso-Mori, R., Nelson, S., Lemke, H. T., Owen, R. L., Pearson, A. R., Stuart, D. I., Ernst, O. P., Mueller-Werkmeister, H. M. & Miller, R. J. (2016). *Acta Crystallographica* **D72**, 944-955.

Olmos, J. L., Jr., Pandey, S., Martin-Garcia, J. M., Calvey, G., Katz, A., Knoska, J., Kupitz, C., Hunter, M. S., Liang, M., Oberthuer, D., Yefanov, O., Wiedorn, M., Heyman, M., Holl, M., Pande, K., Barty, A., Miller, M. D., Stern, S., Roy-Chowdhury, S., Coe, J., Nagaratnam, N., Zook, J., Verburgt, J., Norwood, T., Poudyal, I., Xu, D., Koglin, J., Seaberg, M. H., Zhao, Y., Bajt, S., Grant, T., Mariani, V., Nelson, G., Subramanian, G., Bae, E., Fromme, R., Fung, R., Schwander, P., Frank, M., White, T. A., Weierstall, U., Zatsepin, N., Spence, J., Fromme, P., Chapman, H. N., Pollack, L., Tremblay, L., Ourmazd, A., Phillips, G. N., Jr. & Schmidt, M. (2018). *BMC Biol* **16**, 59.

Pande, K., Hutchison, C., Groenhof, G., Aquila, A., Robinson, J., Tenboer, J., Basu, S., Boutet, S., DePonte, D. P., Liang, M., White, T. A., Zatsepin, N., Yefanov, O., Morozov, D., Oberhuer, D., Gati, C., Subramanian, G., James, D., Zhao, Y., Koralek, J., Brayshaw, J., Kupitz, C., Conrad, C., Roy-Chowdhury, S., Coe, J. D., Metz, M., Xavier, P. L., Grant, T. D., Koglin, J., Ketawala, G., Fromme, R., Srajer, V., Henning, R., Spence, J. C., Ourmazd, A., Schwander, P., Weierstall, U., Frank, M., Fromme, P., Barty, A., Chapman, H. N., Moffat, K., van Thor, J. J. & Schmidt, M. (2016). *Science* **352**, 725-729.

Pandey, S., Bean, R., Sato, T., Poudyal, I., Bielecki, J., Cruz Villarreal, J., Yefanov, O., Mariani, V., White, T. A., Kupitz, C., Hunter, M., Abdellatif, M. H., Bajt, S., Bondar, V., Echelmeier, A., Doppler, D., Emons, M., Frank, M., Fromme, R., Gevorkov, Y., Giovanetti, G., Jiang, M., Kim, D., Kim, Y., Kirkwood, H., Klimovskaia, A., Knoska, J., Koua, F. H. M., Letrun, R., Lisova, S., Maia, L., Mazalova, V., Meza, D., Michelat,

T., Ourmazd, A., Palmer, G., Ramilli, M., Schubert, R., Schwander, P., Silenzi, A., Sztuk-Dambietz, J., Tolstikova, A., Chapman, H. N., Ros, A., Barty, A., Fromme, P., Mancuso, A. P. & Schmidt, M. (2020). *Nat Methods* **17**, 73-78.

Park, S.-Y., Choi, H., Eo, C., Cho, Y. & Nam, K. (2020). *Crystals* **10**, 803.

Pompidor, G., Dworkowski, F. S., Thominet, V., Schulze-Briese, C. & Fuchs, M. R. (2013). *J Synchrotron Radiat* **20**, 765-776.

Schulz, E. C., Yorke, B. A., Pearson, A. R. & Mehrabi, P. (2022). *Acta Crystallographica* **D78**, 14-29.

Sherrell, D. A., Foster, A. J., Hudson, L., Nutter, B., O'Hea, J., Nelson, S., Pare-Labrosse, O., Oghbaey, S., Miller, R. J. & Owen, R. L. (2015). *J Synchrotron Radiat* **22**, 1372-1378.

Sherrell, D. A., Lavens, A., Wilamowski, M., Kim, Y., Chard, R., Lazarski, K., Rosenbaum, G., Vescovi, R., Johnson, J. L., Akins, C., Chang, C., Michalska, K., Babnigg, G., Foster, I. & Joachimiak, A. (2022). *J Synchrotron Radiat* **29**, 1141-1151.

Sierra, R. G., Laksmono, H., Kern, J., Tran, R., Hattne, J., Alonso-Mori, R., Lassalle-Kaiser, B., Glockner, C., Hellmich, J., Schafer, D. W., Echols, N., Gildea, R., Grosse-Kunstleve, R. W., Sellberg, J., McQueen, T. A., Fry, A. R., Messerschmidt, M., Miahnahri, A., Seibert, M. M., Hampton, C. Y., Starodub, D., Loh, N. D., Sokaras, D., Weng, T.-C., Zwart, P. H., Glatzel, P., Milathianaki, D., White, W. E., Adams, P. D., Williams, G. J., Boutet, S., Zouni, A., Messinger, J., Sauter, N. K., Bergmann, E., Yano, J., Yachandra, V. K. & Bogan, M. J. (2012). *Acta Crystallographica* **D68**, 1584-1587.

Skopintsev, P., Ehrenberg, D., Weinert, T., James, D., Kar, R. K., Johnson, P. J. M., Ozerov, D., Furrer, A., Martiel, I., Dworkowski, F., Nass, K., Knopp, G., Cirelli, C., Arrell, C., Gashi, D., Mous, S., Wranik, M., Gruhl, T., Kekilli, D., Brunle, S., Deupi, X., Schertler, G. F. X., Benoit, R. M., Panneels, V., Nogly, P., Schapiro, I., Milne, C., Heberle, J. & Standfuss, J. (2020). *Nature* **583**, 314-318.

Smolentsev, G., Guda, A., Zhang, X., Haldrup, K., Andreiadis, E., Chavarot-Kerlidou, M., Canton, S. E., CNachtegaal, M., Artero, V. & Sundstrom, V. (2013). *J Phys Chem C Nanom Interf* **117**, 17367-17375.

Studier, F. (2005). *Protein Expression and Purification* **41**, 207-234.

Suga, M., Akita, F., Sugahara, M., Kubo, M., Nakajima, Y., Nakane, T., Yamashita, K., Umena, Y., Nakabayashi, M., Yamane, T., Nakano, T., Suzuki, M., Masuda, T., Inoue, S., Kimura, T., Nomura, T., Yonekura, S., Yu, L. J., Sakamoto, T., Motomura, T., Chen, J. H., Kato, Y., Noguchi, T., Tono, K., Joti, Y., Kameshima, T., Hatsui, T., Nango, E., Tanaka, R., Naitow, H., Matsuura, Y., Yamashita, A., Yamamoto, M., Nureki, O., Yabashi, M., Ishikawa, T., Iwata, S. & Shen, J. R. (2017). *Nature* **543**, 131-135.

Weierstall, U. (2014). *Philos Trans R Soc Lond B Biol Sci* **369**, 20130337.

Weierstall, U., James, D., Wang, C., White, T. A., Wang, D., Liu, W., Spence, J. C. H., Doak, R. B., Nelson, G., Fromme, P., Fromme, R., Grotjohann, I., Kupitz, C., Zatsepin, N. A., Liu, H., Basu, S., Wacker, D., Han, G. W., Katritch, V., Boutet, S., Messerschmidt, M., Williams, G. J., Koglin, J., Seibert, M. M., Klinker, M., Gati, C., Shoeman, R. L., Barty, A., Chapman, H. N., Kirian, R. A., Beyerlein, K. R., Stevens, R. C., Li, D., Shah, S. T. A., Howe, N., Caffrey, M. & Cherezov, V. (2014). *Nature Communications* **5**, 3309.

White, T. (2019). *Acta Crystallographica* **D75**, 219-233.

Wiedorn, M. O., Oberthur, D., Bean, R., Schubert, R., Werner, N., Abbey, B., Aepfelbacher, M., Adriano, L., Allahgholi, A., Al-Qudami, N., Andreasson, J., Aplin, S., Awel, S., Ayyer, K., Bajt, S., Barak, I., Bari, S., Bielecki, J., Botha, S., Boukhelef, D., Brehm, W., Brockhauser, S., Cheviakov, I., Coleman, M. A., Cruz-Mazo, F., Danilevski, C., Darmanin, C., Doak, R. B., Domaracky, M., Dorner, K., Du, Y., Fangohr, H., Fleckenstein, H., Frank, M., Fromme, P., Ganan-Calvo, A. M., Gevorkov, Y., Giewekemeyer, K., Ginn, H. M., Graafsma, H., Graceffa, R., Greiffenberg, D.,

Gumprecht, L., Gottlicher, P., Hajdu, J., Hauf, S., Heymann, M., Holmes, S., Horke, D. A., Hunter, M. S., Imlau, S., Kaukher, A., Kim, Y., Klyuev, A., Knoska, J., Kobe, B., Kuhn, M., Kupitz, C., Kupper, J., Lahey-Rudolph, J. M., Laurus, T., Le Cong, K., Letrun, R., Xavier, P. L., Maia, L., Maia, F., Mariani, V., Messerschmidt, M., Metz, M., Mezza, D., Michelat, T., Mills, G., Monteiro, D. C. F., Morgan, A., Muhlig, K., Munke, A., Munnich, A., Nette, J., Nugent, K. A., Nuguid, T., Orville, A. M., Pandey, S., Pena, G., Villanueva-Perez, P., Poehlsen, J., Previtali, G., Redecke, L., Riekehr, W. M., Rohde, H., Round, A., Safenreiter, T., Sarrou, I., Sato, T., Schmidt, M., Schmitt, B., Schonherr, R., Schulz, J., Sellberg, J. A., Seibert, M. M., Seuring, C., Shelby, M. L., Shoeman, R. L., Sikorski, M., Silenzi, A., Stan, C. A., Shi, X., Stern, S., Sztuk-Dambietz, J., Szuba, J., Tolstikova, A., Trebbin, M., Trunk, U., Vagovic, P., Ve, T., Weinhausen, B., White, T. A., Wrona, K., Xu, C., Yefanov, O., Zatsepin, N., Zhang, J., Perbandt, M., Mancuso, A. P., Betzel, C., Chapman, H. & Barty, A. (2018). *Nat Commun* **9**, 4025.

Winn, M. D., Ballard, C. C., Cowtan, K. D., Dodson, E. J., Emsley, P., Evans, P. R., Keegan, R. M., Krissinel, E. B., Leslie, A. G., McCoy, A., McNicholas, S. J., Murshudov, G. N., Pannu, N. S., Potterton, E. A., Powell, H. R., Read, R. J., Vagin, A. & Wilson, K. S. (2011). *Acta Crystallogr D Biol Crystallogr* **67**, 235-242.

Wolff, A. M., Nango, E., Young, I. D., Brewster, A. S., Kubo, M., Nomura, T., Sugahara, M., Owada, S., Barad, B. A., Ito, K., Bhowmick, A., Carbajo, S., Hino, T., Holton, J. M., Im, D., O'Riordan, L. J., Tanaka, T., Tanaka, R., Sierra, R. G., Yumoto, F., Tono, K., Iwata, S., Sauter, N. K., Fraser, J. S. & Thompson, M. C. (2023). *Nat Chem* **15**, 1549-1558.

Wranik, M., Weinert, T., Slavov, C., Masini, T., Furrer, A., Gaillard, N., Gioia, D., Ferrarotti, M., James, D., Glover, H., Carrillo, M., Kekilli, D., Stipp, R., Skopintsev, P., Brünle, S., Mühlethaler, T., Beale, J., Gashi, D., Nass, K., Ozerov, D., Johnson, P. J. M., Cirelli, C., Bacellar, C., Braun, M., Wang, M., Dworkowski, F., Milne, C., Cavalli, A., Wachtveitl, J., Steinmetz, M. O. & Standfuss, J. (2023). *Nature Communications* **14**.

Zarrine-Afsar, A., Barends, T. R. M., Müller, C., Fuchs, M. R., Lomb, L., Schlichting, I. & Miller, R. J. D. (2012). *Acta Crystallographica* **D68**, 321-323.

4

Tailoring Biotin-Streptavidin for Binding Studies Using Time-Resolved Protein Crystallography

The following section was written in a manuscript form.
It will only be used as a chapter in this thesis.
Contributions: Crystallized T7-SA, performed all cryo and room temperature studies, collected data, processed and analyzed the data.

Tailoring biotin-streptavidin for binding studies using time-resolved protein crystallography

Melissa Carrillo[1, 2, 3], John H. Beale[1], Tobias Weinert[1], Dongping Chen[2], Georgii Khusainov[1], Quentin Clément Bertrand[1], Nico Valerio Igareta[2], Yong Hua[2], Xiachun L. Blatter[2], Fabienne S. Stierli[1], Michal Kepa[1], Jörg Standfuss[1], Hannah Glover[1], Matthias Mulder[1], Thomas J. Mason[1], Thomas R. Ward[2], Celestino Padeste[1*]

[1]Paul Scherrer Institut, Forschungsstrasse 111, 5232 Villigen Switzerland,
[2]Department of Chemistry, University of Basel, Mattenstrasse 24a, 4002 Basel Switzerland
[3]Swiss Nanoscience Institute, Klingelbergstrasse 82, 4056 Basel Switzerland
[*]Email: celestinopadeste@psi.ch

Abstract

Time-resolved serial protein crystallography at X-ray free electron lasers (XFELs) and synchrotrons is a fast-emerging powerful method for obtaining structural information of protein dynamic processes at molecular resolution, e.g. using optical pump – X-ray probe experiments. The employment of photocaged ligands expands the applicability of the technology from the reaction of photosensitive bio-macromolecules to ligand-receptor binding. Due to the remarkably high affinity, the streptavidin-biotin system has widespread applications in biotechnology and bioanalytics. However, the dynamics of the binding process are still poorly understood. Here we report on the optimization of a photocaged biotin – streptavidin system for pump-probe experiments at XFELs. Specifically, we produced and characterized biotin-derivatives coupled to coumarins, which can be cleaved off using light in the 350-400nm range. We used a streptavidin T7 variant (T7-SA) with a C-terminal tail that folds back into the protein's binding pocket, which was crystallized in 15-25µm microcrystals. Cryogenic (cryo)-diffraction data acquired at the Swiss Light Source (SLS) revealed $I4_122$ as the space group and a unit cell of 57Å *57Å * 173Å. Soaking biotin into the microcrystals led to cracking and dissolving of the microcrystals, an effect that was successfully inhibited by crosslinking the crystals with glutaraldehyde, while maintaining the protein's binding affinity for biotin. After soaking the crosslinked crystals with biotin, an exchange of the C-terminal tail in the binding pocket by biotin was evident, accompanied by an expansion of the C-Axis by up to 10 Å. Initial studies also demonstrated the possibility of photocleaving the caged biotin, which was soaked into the crystal, to observe binding into the binding pocket. Initial experiments at room temperature conducted at the Swiss X-ray Free Electron laser SwissFEL validated the apo structure of T7-SA. The results indicate that, after optimizing concentrations and photo-activation/uncaging conditions, the system could potentially be well suited for time-resolved experiments, to finally allow for tracing the molecular movements during biotin-streptavidin binding.

The following people contributed by synthesizing and characterizing the caged compounds for the binding studies:

- Nico Valerio Igareta (Ward group, University of Basel)
- Dongping Chen (Ward group, University of Basel)
- Yong Hua (Ward group, University of Basel)
- Xiaochun Li Blatter (Ward group, University of Basel)

4.1 Introduction

Streptavidin is a widely used protein in molecular biology and biochemistry due to its high affinity towards biotin, a water-soluble B-vitamin. Derived from *Streptomyces avidinii,* streptavidin consists of a polypeptide composed of 159 residues (Chaiet and Wolf (1964)). However, streptavidin typically contains truncated terminal sequences after being expressed, as a result from post secretory cleavage of the terminal regions. These truncated streptavidins, also known as core-streptavidins, tend to be a less soluble form compared to non-truncated or partially truncated streptavidins, and tend to form high ordered aggregates (Argarana et al., 1986; Sano et al., 1995). Core-streptavidin consists of residues 13-139, forming a tetramer with D_2 symmetry. Each subunit contains a β-barrel structure with a biotin-binding site situated at the end of the β-barrel. The binding pocket includes several hydrogen bonding amino acid side chains (N23, S27, Y43, S45, and D128). Furthermore, residues 45-52 form a flexible binding loop that undergoes a conformation change when a ligand is present. In the absence of a ligand, this flexible binding loop is in the "open" state, with the binding pocket being exposed and unprotected. Upon the entry of a ligand into the pocket, the flexible binding loop closes over the ligand, transitioning to the "closed" state (Le Trong et al., 2011). Streptavidin has a remarkably high affinity with a dissociation constant of $K_d \sim 10^{-13}$ mol/L (Chaiet & Wolf, 1964). This strong affinity makes the streptavidin-biotin system a versatile tool in research and for biotechnical applications including labeling and transport of biochemical reagents (Bayer & Wilchek, 1990), affinity chromatography (Gretch et al., 1987), diagnostic assays and biosensors (Piketty et al., 2017; Reyes et al., 2001).

Although most cleaved streptavidin proteins report to have enhanced binding of biotin into their binding pocket (Sano et al., 1995), there are a large interest in full length streptavidin as hosts for biotinylated organometallic catalyst precursors due to their higher production levels

of protein through expression and purification (Klehr et al., 2020). These synthetic metalloenzymes exhibit favorable characteristics as hybrid catalysts for enantioselective hydrogenation and transfer hydrogenation reactions (Le Trong et al., 2006; Letondor et al., 2005; Loosli et al., 2006; Ward, 2005). To study this, a streptavidin variant was created, called T7-SA. It consists of 159 amino acid units, featuring a T7 epitope tag at the outset, encompassing 13 units, and a tail at the C-terminus (residues 130-159). This C-terminal tail forms a pliant alpha-helical segment along with an elongated peptide, directly binding within the binding site in the absence of a ligand. However, in the presence of small ligands such as biotin derivatives or strepTAG-II, the C-terminal tail exhibits flexibility, moving away from the binding site (Bayer et al., 1989; Le Trong et al., 2006). Similar to core-streptavidin, T7-SA induces analogous movements in the flexible binding loop contingent upon the presence of a ligand in the binding pocket of streptavidin.

While extensive information exists on numerous static streptavidin structures, there remains a notable gap in understanding the dynamic nature of the binding pocket during biotin binding, including molecular details of the binding process itself. Time-resolved serial crystallography (TR-SX) has become a valuable approach for experimentally exploring dynamic processes ranging from femtoseconds to millisecond capturing a range of atomic to conformational levels and, as a result, is used to solve various molecular movements and binding events (Hosaka, Katsura, et al., 2022; Josts et al., 2018). Using a pump-probe approach, a laser “pump” pulse can initiate a specific light reaction and the “probe” X-ray pulse allows to capture the structural change in specific time delays ranging from femtoseconds to milliseconds (Kubo et al., 2017; Orville, 2020; Petr Skopintsev et al., 2020). This tends to be ideal for light activated samples such as rhodopsin (Malmerberg et al., 2015; Tsai et al., 2018), phytochromes (Carrillo et al., 2021; Claesson et al., 2020), photoactivate yellow protein

(Schmidt et al., 2015), or green florescent proteins (Coquelle et al., 2018) but is more complicated for non-light sensitive proteins.

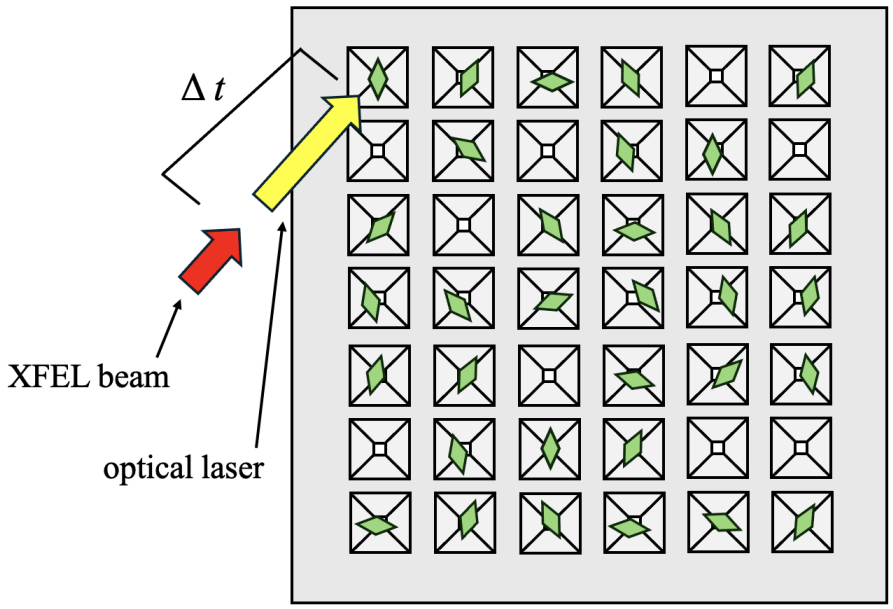

Figure 4.1: A schematic of a pump-probe experiment set-up: *A schematic of the MISP-chip membrane containing crystals in green. The scheme depicts a pump-probe pulse example involving an optical laser (indicated by a yellow arrow), followed by a time delay, and subsequently an X-ray beam (indicated by the red arrow). Varied time delays are employed to capture different timepoints within the protein's response to the laser.*

An approach to address this challenge is to precisely control the initiation of ligand binding through photocages. Photocages, also known as photolabile protecting groups or photoremovable protecting groups, are chemical compounds that can be activated through light. They are bound to a functional group such as a ligand or protein, inhibiting its reaction. Upon light exposure, the photocage absorbs photons, triggering photolysis and leading to its cleavage from the protected functional group or molecule. This, in turn, initiates binding activities. A careful selection of photocages is essential for a successful experiment. Factors such as solubility, cleavage rate (s^{-1}), extinction coefficient ($\varepsilon_{max,}$ $mM^{-1}cm^{-1}$), maximum absorption wavelength ($\lambda_{max,}$ nm), and quantum yield (ϕ) are all vital factors to consider when

designing an appropriate photocage for a time-resolved pump-probe experiment (D. C. F. Monteiro et al., 2021).

The aim of this research is to develop and test a system to study the binding interactions between streptavidin variant T7-SA and biotin using time-resolved serial femtosecond crystallography (TR-SFX). To achieve this, we have developed a protocol to micro-crystallizes the T7-SA protein suitable for TR-SX. Additionally, we've synthesized three photocaged biotin derivatives intended for soaking into these microcrystals. Through the introduction of these photocaged ligands into the crystals and employing optical lasers, our aim is to explain the dynamics and mechanisms underlying the binding of biotin to streptavidin. In order to prepare for TR-SX at Cristallina-MX, a series of experiments were done in cryo-temperature in order to obtain the parameters needed to perform TR-SX at an XFEL. A series of concentration trials of the ligands were conducted to determine what concentration would be needed to successfully soak the biotin derivate. A series of illumination tests were performed as well to determine how long it take for the photocaged biotin to cleave and bind into the pocket. Once performed, the first preliminary experiment was conducted at SwissFEL's CristallinaMX using the MISP-chips (Melissa Carrillo et al., 2023).

4.2 Materials and Methods

4.2.1 Protein production

Protein expression and purification were carried out at the University of Basel's Chemistry Department, in Thomas Ward's laboratory. A detailed description of the production of plasmid and cells can be found in ref (Mallin et al., 2016). The expression vector for the plasmids is pET-24a (Nivagen, cat. no. 69749, antibiotic: kanamycin resistance) and the *E.coli*

strain that is used is BL21(DE3). A detailed description of the large-scale overexpression of T7-SA can be found in ref. (Klehr et al., 2020).

4.2.2 Crystallization of T7-SA

Initial attempts to crystallize T7-SA consisted of performing hanging-drop vapor diffusion experiments on commercial screening crystallization trays to determine the optimal conditions. 96-well screening trays, including PACT premier, Morpheus I, Morpheus II, JCSG Plus, PEGs Suite I, and PEGs Suite II, were purchased from Molecular Dimensions for this purpose. Once crystals were obtained, optimization trays were created to fine tune crystallization conditions. Optimization trays involved varying parameters, including PEG concentrations ranging from 5% to 45%, HEPES pH levels spanning 6.5 to 8.5, salts such as Li_2SO_4, $Mg(NO_3)_2$, and NaCl at concentrations of 0.01-0.3M, drop ratios (protein: mother liquor) of 1:2, 1:1, and 2:1, and protein concentrations ranging from 17-25 mg/mL, 25 mg/mL, 50 mg/mL, 75 mg/mL to 100 mg/mL. Temperature conditions were also tested, setting crystallization trays in room temperature (20° C) and 5° C.

The refined crystallization parameters for T7-SA macro-crystals, acquired through hanging-drop vapor diffusion, involved diluting the purified protein to 25 mg/ml using a buffer composed of 50 mM Tris (pH 7.5) and 150 mM NaCl. The diluted T7-SA protein was then added into mother liquor composed of 2 M $(NH_4)_2SO_4$ and 0.1 M NaOAc pH 4.0 at a 1:1 ratio.

Micro-crystallization was carried out within an Eppendorf tube. 25 mg/ml of T7-SA protein was added to mother liquor composed of 2M $(NH_4)_2SO_4$ and 0.1 M NaOAc pH 4.0 in a 1:1 ratio. The sample was placed on a tilt platform, resulting in crystal formation within 2 hours; the crystals were then allowed to fully develop overnight. For diffraction experiments, the micro-crystal slurry was diluted with mother liquor to $1x10^5$ crystals• mL^{-1}.

4.2.3 Micro-crystal preparation for cryo- and room-temperature data collection

4.2.3.1 Crystal Preparation for Cryo-Temperature Experiments:

For samples containing ligand (biotin, PEG-biotin, and photocaged biotin), micro-crystals were soaked for 1 hr with 1% glutaraldehyde in mother liquor. Afterwards the ligand was soaked into the crystals using final concentrations varying from 100mM to 0.1mM. Samples that were for cryo-studies of pre-illuminated samples the soaked crystals were placed inside a sealed box and illuminated with a 405nm laser (Roithner LaserTechnik GmbH) for 5-30 minutes.

4.2.3.2 Crystal Loading for Cryo-Temperature Data Collection:

After immersing the samples in a solution containing both glutaraldehyde and ligand, and subjecting them to pre-illumination if required, the micro-crystal slurry were prepared for cryo-cooling. Glycerol was added as a cryoprotectant solution to the crystal slurry for 30 seconds at a final concentration of 25%. A 2µl drop of micro-crystal slurry was pipetted onto the top side of a cryo-mesh chip (Martiel et al., 2021). With a blotting paper, the excess mother liquor was blotted from the back of the cryo-mesh chip which was immediately immersed into liquid nitrogen.

4.2.3.3 Crystal Loading for Room-Temperature Data Collection:

Room temperature studies conducted on the micro-crystals consisted of loading the micro-crystal slurry onto MISP-chips (M. Carrillo et al., 2023). 200µl of prepared micro-crystal slurry was pipetted onto the top of a MISP-chip, which was placed on a loading platform under a humidity stream. The loading platform is connected to a vacuum pump controlled through a valve. Extraction of the excess mother liquor was performed by closing the valve, suctioning the liquid through the back of the MISP-chip, and pulling the crystals into the membrane's

wells. Afterward, the chip was placed on a chip holder and stored in a humidity chamber to preserve the crystals from dehydrating.

4.2.4 Photocaged Biotin

During the project's duration, considerable efforts and multiple attempts were done to formulate a functional photocaged biotin suitable for time-resolved serial protein crystallography. Photocage synthesis and production was carried out at the University of Basel's Chemistry Department, in Thomas Ward's laboratory. Three photocaged biotin compounds were designed and produced, labeled as compound **I**, **II** and **III**. The synthesis routes are shown in Figure 4.2. For compound **I**, biotin methyl ester was first reacted with triphosgene. Without purification, the resulting intermediate was added to chromophore **A**, to link the activated carboxyl group to the OH-moiety of the coumarin derivative. Compounds **II** and **III** contain a biotin with a PEG linker, which was first synthesized through esterification of biotin with triethyleneglycol monomethylether and purified using HPLC. Activation with triphosgene and linking to chromophores **I** and **II** was done analogous to compound **I**. More synthesis details and product characterizations are found in the supplementary information.

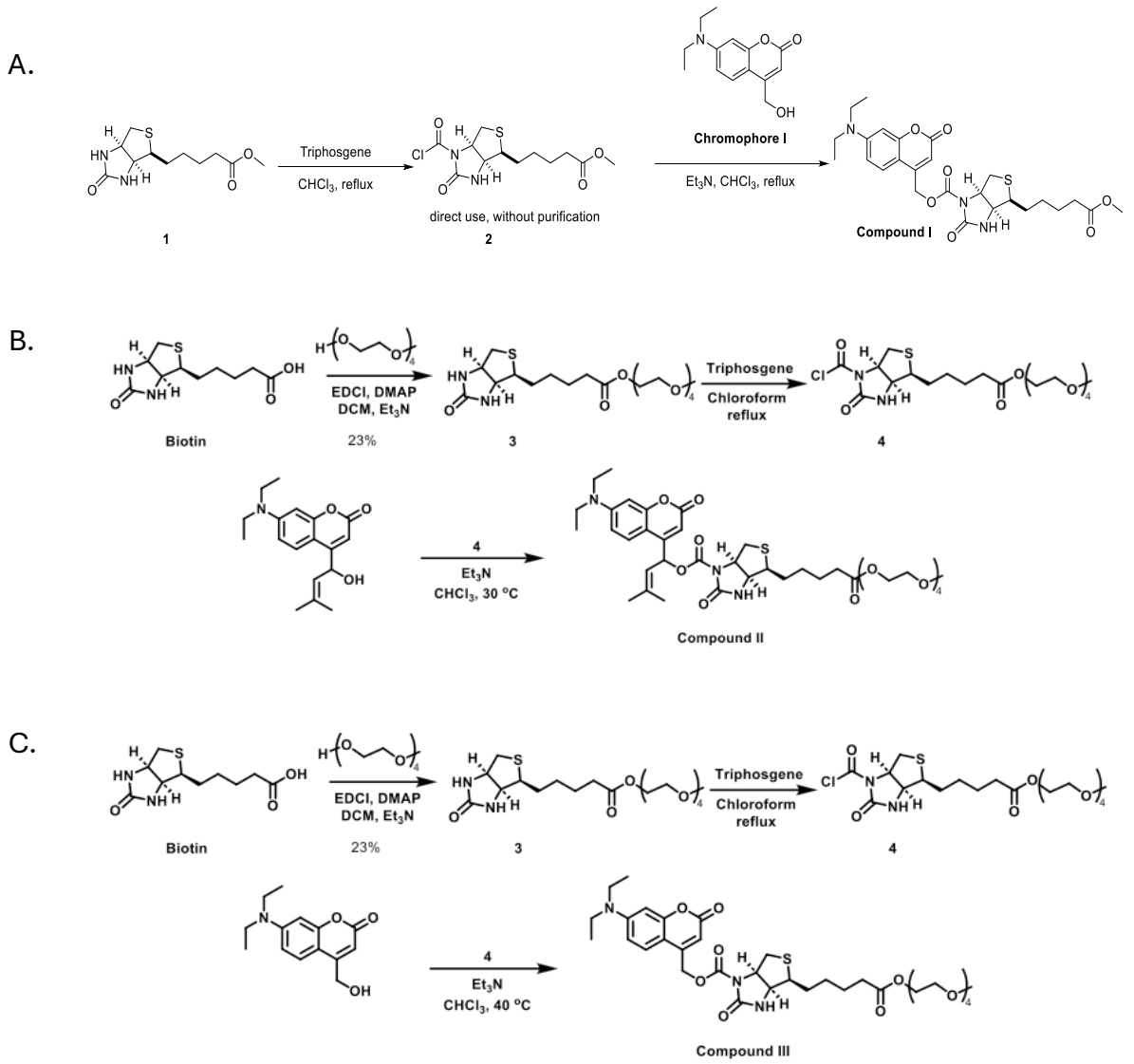

Figure 4.2: Synthesis of three photocaged biotin derivatives. *Photocaged biotin derivatives are labeled as compound* ***I-III*** *and composed of a coumarin as the photocage bound a biotin or biotin derivative containing a PEG ester tail to slow down binding rates towards streptavidin.*

4.2.5 Cryogenic Crystallography Data Collection and Data Processing

Conventional cryo-crystallography data were taken at the Swiss Light Source (SLS) at X06SA (PXI) using an EIGER 16M detector. Data was collected on the Paul Scherrer Institute (PSI) cryo-mesh chips (Martiel et al., 2021). Data was collected on a 0.1° oscillation, an exposure of 0.01s per frame at a 90° rotation range, and beam size of 10x20 μm. Automated data processing was used during the beamtime (Wojdyla et al., 2018). To solve the protein

structure, molecular replacement was used with PDB models 2BC3 and 2QCB. Afterwards, the models were refined using phenix.refine's iterative cycles as well as manual refinement (Afonine et al., 2018). Figures were prepared using PyMOL (DeLano, 2020; DeLano, 2002).

4.2.6 Time-Resolved Serial Crystallography, Data Collection and Data Processing

Time-resolved serial crystallography data were collected in June of 2023 at the SwissFEL Cristallina-MX endstation during its commissioning stages. An 8 Mpixel JUNGFRAU detector was used with X-ray pulses at 100 Hz repetition rate and 75 fs pulse duration. The beam had a photon energy of 12.45 keV, a pulse energy of 565 μJ and beam size of 1x1μm. Samples were placed on PSI's MISP-chip (M. Carrillo et al., 2023) for data collection. The optical laser was set at 10% transmission resulting in 0.5 μJ at 405 nm wavelength with a spot size of 29x29μm. Data was processed with Crystfel 0.9.1. (T. A. White, 2019; White et al., 2012). Peakfinder8 was used for peak detection, XGANDALF and MOSFLM was used for indexing and peak integration and partialator with model unity was used to merge and scale the data. Structural refinements of the models were done using PHEIX (Adams et al., 2002) with iterative cycles and manual adjustments in Coot (Emsley & Cowtan, 2004). Difference maps were produced with CCP4 suite v8.0 (Martyn D Winn et al., 2011). Figures were prepared using PyMOL (DeLano, 2020; DeLano, 2002).

4.3 Results

4.3.1 Photocaged Biotin

Three distinct photocaged biotins were synthesized for the purpose of this study labeled as compound **I**, compound **II**, and compound **III**. All three compounds contain a coumarin derived photocage attached via a carboxyl group to either a biotin or biotin with a PEG ester

tail (Figure 4.3A). Compounds **II** and **III** were designed to have a PEG ester tail at the end of biotin in order to increase the solubility of the compound.

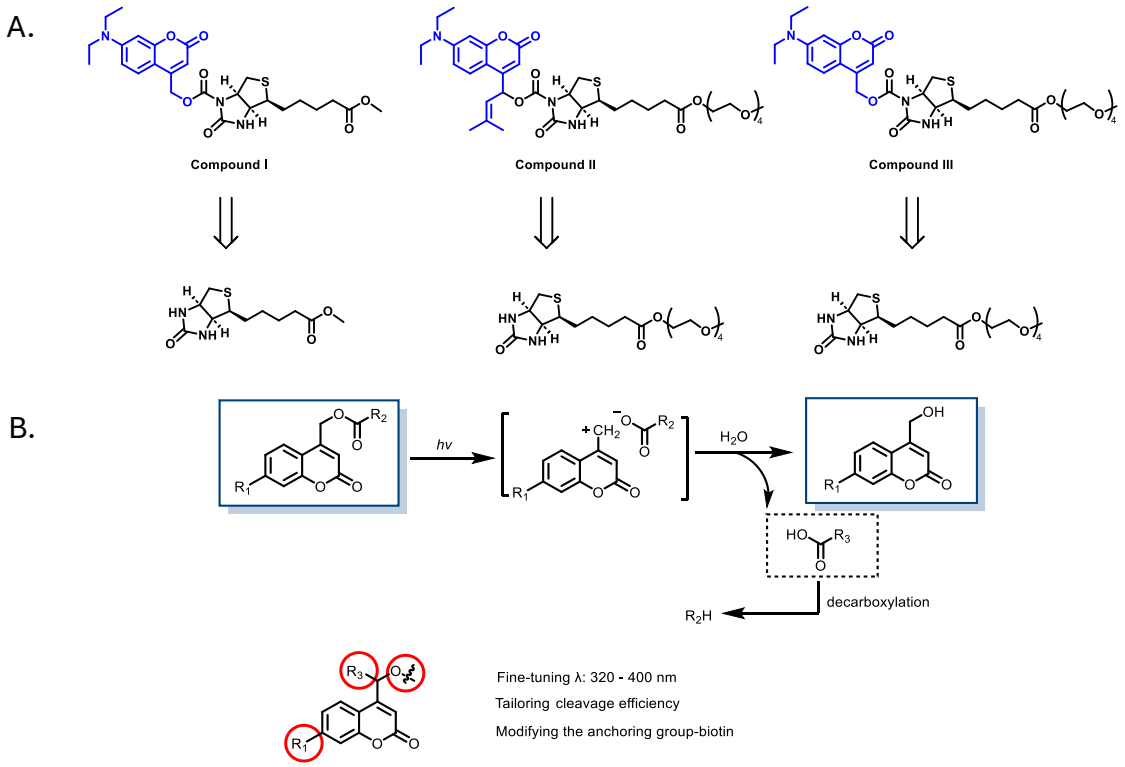

Figure 4.3: Design of photocaged biotin derivatives. *(A) The three photocaged biotin-coumarin derivative based on the selection of the chromophore, labeled as compound **I**, compound **II** and compound **III**. The coumarin photocage is highlight in blue. (B) Mechanism and selection of chromophore for the photo-uncaging reaction.*

Several studies were conducted to determine the efficacy of photocaged biotin and assess its suitability as a ligand for this study. An ultraviolet-visible spectrum of the two chromophores used for the three biotin derivates was taken in order to determine the optimal absorption wavelength. Compound **I** (containing chromophore **A**) and compound **II** (containing chromophore **B**) were dissolved and prepared for UV-vis spectrum. The corresponding spectrum were recorded, and the maximum wavelength was marked in Figure 4.4. λ_{max} of compounds **I** and **II** were recorded as 379nm and 397nm respectively.

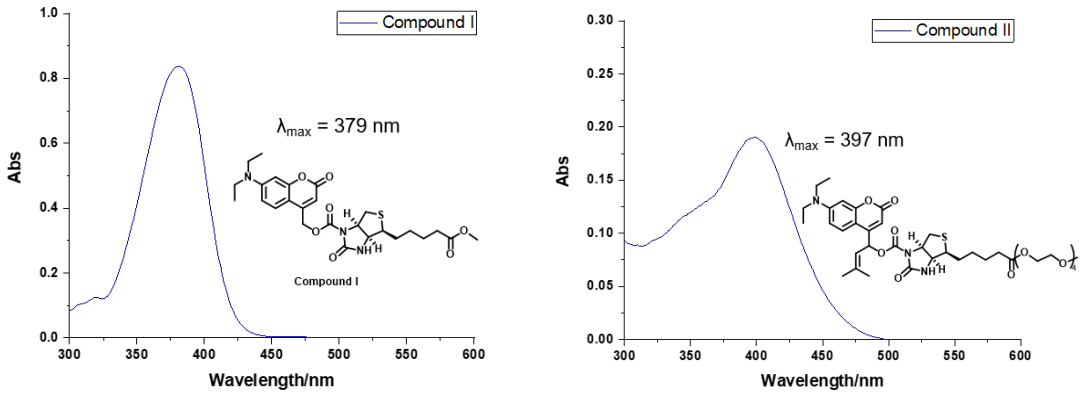

Figure 4.4: UV-Vis spectrum of compound I and II. *Compound* ***I*** *(1 mg/mL) and* ***II*** *(0.3 mg/mL) were dissolved in MeOH and used for the UV-Vis spectrum. Pure MeOH was used as the reference. Absorbance peak maximum for photocage in compound* ***I*** *is 379nm and 397nm for the photocage in compound* ***II****.*

An assessment of the uncaging efficiency of photocaged biotin was carried out through controlled exposure of the substances in solution and the utilization of liquid chromatography-mass spectrometry (LCMS) to determine the fraction of decomposed material, in order to understand the time frame of the uncaging of both photocages. Stock solutions of the photocaged compounds **I** and **II** were prepared as 0.2mg/mL in DMSO. While both photocaged stocks were being prepared for analyzes, the stock with compound **II** disintegrated within minutes, before having time to illuminate the sample and collect data. On the contrary, compound **I** survived the preparation and the decomposition time course in dependence of the illumination was recorded (Table 4.1), demonstrating a cleavage efficiency of 42% within the first 30 minutes.

Table 4.1: Uncaging efficiency of compound I measured by LC-MS after illumination of blue light

t/min	Cleavage efficiency/%
0	0
1	16
5	27
10	30
30	42
60	82

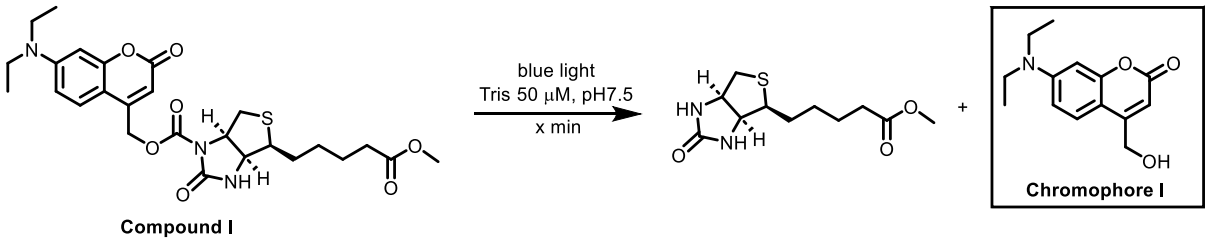

Figure 4.5: Reaction of compound I during the assessment of uncaging efficiency using blue light. *Stock solution of both compound* ***I*** *and* ***II*** *were prepared as 0.2 mg/mL in DMSO. The stock solution was 4X diluted with tris buffer (50 μM, pH 7.5). Both compounds were irradiated under blue light without shaking for the time-course detection. Uncaging efficiency was measured by LC-MS under PDA mode based on the detection of the chromophore.*

Given the instability of the chromophore in compound **II**, chromophore **A** was selected as the photocage for this study and because of the low solubility coumarins have, compound **III** was chosen as the experimental ligand due to its higher solubility.

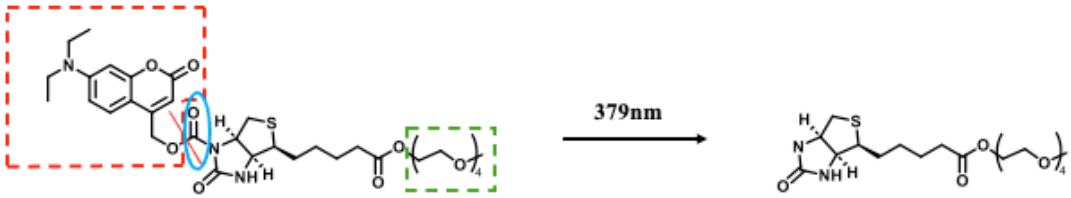

Figure 4.6: Photocaged biotin used as the experimental ligand for time-resolved serial crystallography experiments on the binding of biotin to streptavidin. *The photocage composed of a coumarin (red), which cleaves off at 379nm wavelength, followed by immediate reaction with water and decarboxylation, to yield the biotin with a PEG ester tail (green). The PEG ester tail was added to increase the ligand's solubility.*

4.3.2 Cryogenic Crystallography Measurements

Micro-crystals were grown to the sizes of 10-25µm (Figure 4.7a). T7-SA protein crystallized in space group $I4_122$. The micro-crystals diffracted to 1.98 Å resolution at 100K (Table 4.2). T7-SA forms a homotetramer with four equal subunits (Figure 4.7b). In the structure of T7-SA in its apo state, the C-terminal tail (residues 149-157) is seen inside the binding pocket and the flexible binding loop (residues 45-52) is in the "open" state (Figure 4.8a).

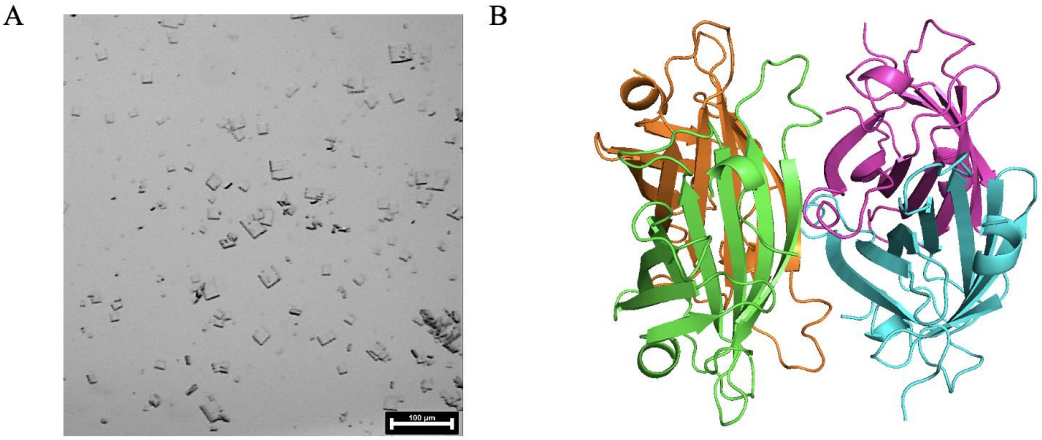

Figure 4.7: Crystallization of streptavidin (sav). (A) *Sav-T7 microcrystals slurry at 160x. Scale bar indicates 100µm. (B) Sav-Apo structure of the 4 subunits.*

In order to gain insight and understand the binding of biotin to streptavidin, initial soaking trials of the micro-crystals were conducted. A problem that arose initially was the rapid

disintegration of the micro-crystals which was occurring within seconds upon contact with biotin or biotin derived ligands. In order to combat this issue, glutaraldehyde (GA), a crosslinker, was added into the micro crystal slurry at a final concentration of 1% for an hour. The crystals containing glutaraldehyde were systematically compared with those without glutaraldehyde to assess any potential effects on the protein. However, no discernible effects were observed. Subsequently, the micro-crystals were immersed in biotin, affixed to mesh chips, and measured under cryo-cooling to investigate whether glutaraldehyde exerted any influence on the binding of biotin, or any intermolecular movements associated with the binding. The cryo-structure illustrates the successful binding of biotin within the binding pocket, accompanied by the disappearance of T7-SA's C-terminal tail as well as the flexible binding loop in the "close" state (Figure 4.8b). Interestingly enough, the unit cell shows roughly a 10Å (5%) increase in the C-axis after binding of biotin (Table 4.2). These observations indicate that the binding of biotin and the movements occurring inside the crystal were unaffected by glutaraldehyde.

As a further control, binding of biotin with the PEG ester tail (from this point onward, referred to as PEG-biotin) to GA-crosslinked T7-SA crystals was investigated. Data was collected and after analyses, PEG-biotin is observed in the binding pocket of T7-SA. Just as in the crystals soaked with biotin, PEG-biotin-soaked crystals also have the C-terminus tail displaced from the binding pocket so that PEG-biotin can be bound instead (Figure 4.8C). The flexible binding loop is also found in the "closed" state, as well as the increase in C-axis by roughly 10Å (Table 24.). The PEG residue is most probably too much disordered within the crystal to become visible in the crystal structure.

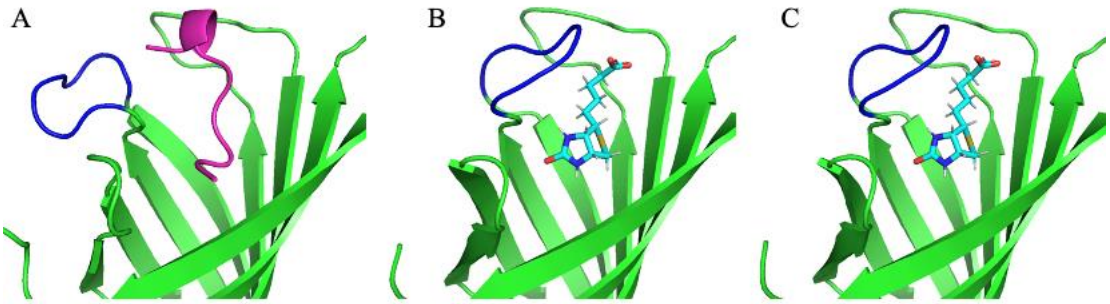

Figure 4.8. T7-SA cryo- structures. *(A) T7-SA cryo- structure in the apo state. The T7-SA tail (in pink) is found inside the binding pocket and the flexible binding loop (in royal blue) is in the "open state". (B) The cryo- structure of the biotin (baby blue) bound inside the T7-SA binding pocket. The flexible binding loop (royal blue) is in the "closed" state. (C) PEG-biotin soaked T7-SA structure, PEG-biotin (in baby blue) is found in the binding loop where the flexible binding loop is in the "closed" state, similar to biotin, however the ester tail is not visible.*

Table 4.2: Crystallographic data for all cryo- and room temperature data.

	Apo	Apo-GA	Biotin	PEG-biotin	C1	C2	C3	C4	5-minutes
Beamline	X06SA	X06SA	X06SA	X06SA	X06SA	X06SA	X06SA	X06SA	Cristallina
Resolution Limit (Å)	2.01	2.32	2.22	1.88	1.89	2.03	2.05	2.07	1.63
Temperature (K)	100	100	100	100	100	100	100	100	293
Space Group	$I4_122$	$I4_122$	$I4_122$	$I4_122$	$I4_122$	$I4_122$	$I4_122$	$I4_122$	$I4_122$
Unit-cell parameters (Å, °)	58.2 58.2 176.7 90 90 90	57.5 57.5 172.32 90 90 90	57.63 57.63 183.78 90 90 90	57.28 57.28 182.43 90 90 90	57.49 57.49 173.27 90 90 90	57.36 57.36 174.79 90 90 90	57.52 57.52 182.60 90 90 90	57.67 57.67 177.34 90 90 90	58.05 58.05 176.04 90 90 90
# of observed reflections	64949 (9449)	45237 (6814)	48065 (7416)	77904 (8912)	72617 (8513)	60393 (9290)	62527 (9875)	57977 (9010)	1589 (1409)
# of unique reflections	8528 (1302)	6059 (988)	7078 (1139)	11284 (1733)	9626 (1444)	8052 (1293)	8638 (1394)	8017 (1269)	2972 (2760)
# of possible reflections	10335 (1621)	7384 (1150)	7852 (1238)	12855 (2010)	12090 (1895)	9914 (1557)	10158 (1580)	9431 (1482)	1589 (1408)
Completeness	82.5% (80.3%)	83.2% (85.9%)	90.1% (92.1%)	87.8% (86.2%)	79.6% (76.2%)	81.2% (83.0%)	85.0% (88.2%)	85.0% (85.6%)	99.98% (99.95%)
R_{sym} (SX R_{split})	12.7% (153.2%)	7.6% (324.0%)	138.5% (18.9%)	16.0 (152.0%)	19.4% (107.8%)	20.1% (148.1%)	18.5% (124.5%)	23.0% (155.3%)	20.83% (156.13%)
I/Sigma	7.27 (1.03)	13.49 (0.40)	5.74 (1.04)	6.63 (1.05)	4.99 (0.91)	3.94 (0.74)	5.35 (1.25)	3.77 (0.68)	6.71 (0.267)
CC (1/2)	99.6* (60.0*)	99.7* (42.5*)	98.7* (42.7*)	99.5* (43.6*)	98.6* (43.8*)	99.2 (49.9%)	99.1* (53.7*)	98.9* (55.5*)	96.59* (51.35*)

4.3.4 Assessing Concentration Levels of PEG-biotin

The micro-crystals were then soaked with different PEG-biotin concentrations to determine the concentration required to successfully soak biotin into the crystal. Final soaking concentrations of PEG-biotin ligand of 100mM, 10mM, 1mM and 0.1mM were tested. Crystals soaked with 100 mM, 10 mM and 1 mM of PEG-biotin showed the ligand inside the binding pocket (Figure 4.8c) and the flexible binding loop in the closed state. However, in the trials of 0.1mM there was a spread of C-axis within the four micro-crystals, as shown in Table 4.3. Data from each crystal was individually processed, and an analysis was done on each micro-crystal to further understand this wide range of C-axis observed. T7-SA in Crystal 1 was found in its apo state, and due to this, served as a reference for comparison with the remaining three crystals, as shown in difference Fourier intensity maps (Figure 4.9). For crystal 2 (C-axis increase of 1.52Å), paired negative and positive difference electron density features in the binding pocket of T7-SA potentially reveal initiation of binding of biotin. With the expansion of the C-axis to 177.34Å, a subtle alteration is observed in the binding pocket, although its interpretation remains limited. Remarkably, despite the relatively large change along only one cell dimensions the datasets remained relatively isomorphous and it was possible to calculate isomorphous difference, which were interpretable for crystals C2 and C3. When the negative and positive electron density features in the binding pocket are looked at in the difference map of C3 compared to C1 shows negative density appearing in the region of the C-terminus tail, indicating its disappearance from the binding pocket, and positive density indicating biotin binding into the pocket.

Table 4.3: T7-SA microcrystals' unit cell after 10min soak in 0.1mM PEG-biotin.

Crystal #	A-axis	B-axis	C-axis
1	57.49	57.49	173.27
2	57.36	57.36	174.79
3	57.52	57.52	182.60
4	57.67	57.67	177.34

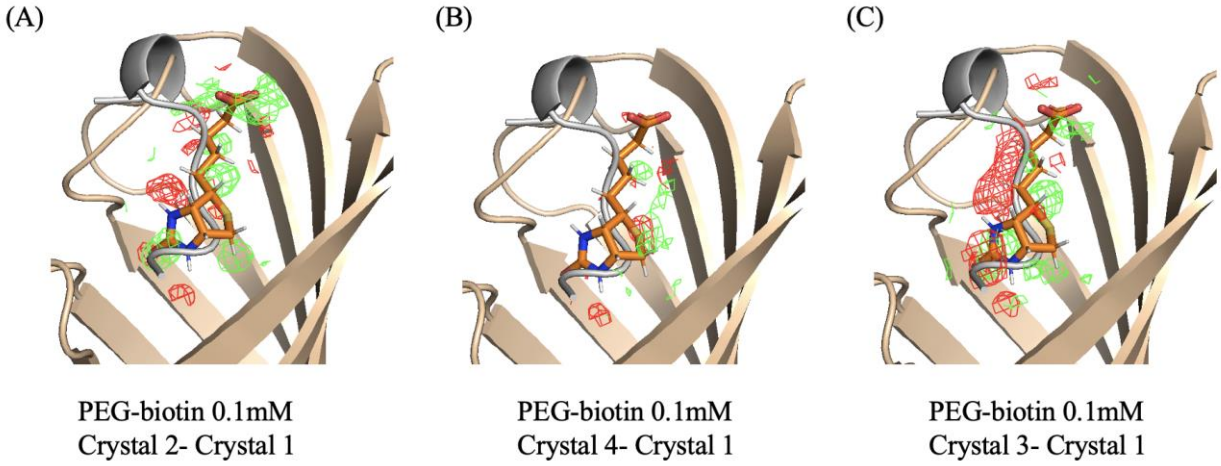

Figure 4.9. $|F_{obs}| - |F_{obs}|$ difference Fourier electron density map of the binding pocket of T7-SA at 0.1mM biotin: *(A) $|F_{obs}|^{crystal\ 2}$ - $|F_{obs}|^{crystal\ 1}$map of ΔC-axis = 1.52Å. Red indicates negative difference electron density; green denotes positive difference electron density (contoured at ±2.5 rmsd). T7-SA's tail is found in gray and biotin is found in orange. Pair negative and positive difference electron densities indicate an onset of movement occurring within the binding pocket. (B) $|F_{obs}|^{crystal\ 4}$ - $|F_{obs}|^{crystal1}$ map of ΔC-axis = 3.61Å. The pair of negative and positive difference electron densities do not clearly indicate a specific movement and can be considered as change occurring inside the pocket. (C) $|F_{obs}|^{crystal34}$ - $|F_{obs}|^{crystal\ 1}$map of ΔC-axis = 8.87Å. The negative difference electron density map indicates the tail leaving the binding pocket and the green difference electron density map indicates the biotin binding into the pocket.*

The R-factor values, which are the statistical value to assess the agreement between the observed and the calculated model electron density, were calculated and used as a measurement to distinguish between each of the four crystals' state when soaked with 0.1mM PEG-biotin. Crystals 1-4 were modeled against the apo (Figure 4.10 blue) and PEG-biotin (Figure 4.10

orange) model during refinement to observe their relativity towards either the apo or biotin bound state. Likely due to the transition of the crystals from one state to another, neither crystal 2 nor crystal 4 agreed well with the apo nor the PEG-biotin model.

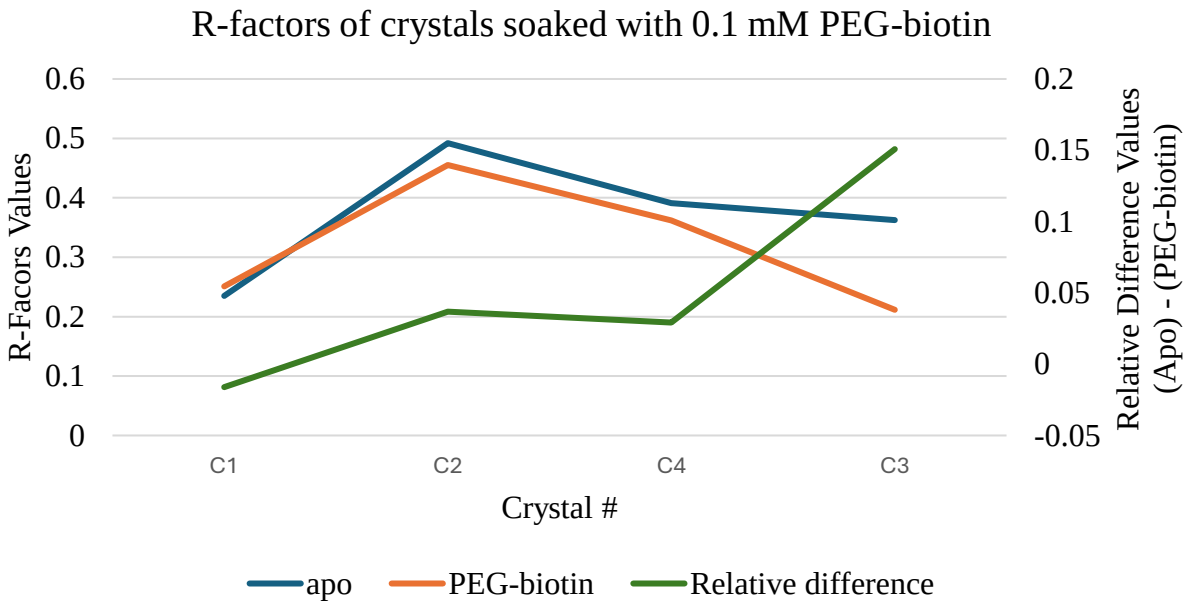

Figure 4.10: R-Factor values of crystals soaked in 0.1mM PEG-biotin for 10 minutes. *The R-factors are taken after refinement of data collected from crystals 1-4 (C1-C4) against an apo (blue) or PEG-biotin model (orange). Crystals are ordered by increasing C-axis. Relative difference plot of the R-factor values between R-Factors of crystals soaked in 0.1mM PEG-biotin for 10 minutes are found in green. The R-factors are taken after refinement between apo and PEG-biotin models for crystals C1-C4.*

The relative R-factor differences between apo and PEG-biotin models were then calculated for each of the four micro-crystals and plotted (Figure 4.10). Crystal 1 (C-axis of 173.27Å) had the lowest relative difference as it was the crystal closest to the apo state. Crystals 2 (C-axis of 174.79Å) and crystal 4 (C-axis of 177.34Å) had intermediate R-factor differences, potentially signifying the transition state from apo to bound biotin. Crystal 3 (C-axis of 182.60Å) had the highest R-factor value as it is the one that resembles closest to the biotin bound model.

4.3.5 Assessing Timeframes for Illumination

A series of illumination tests were conducted to assess the illumination time needed for the photocaged biotin to uncage and bind into the pocket of T7-SA micro-crystals. This also aimed to determine if photocaged biotin uncages and subsequently binds into the pocket. The micro-crystals were first soaked with 1% glutaraldehyde for an hour then soaked for 10 minutes with the 0.1mM photocaged biotin. Afterwards, they were illuminated for 5, 15, or 30 minutes with a 405 nm wavelength laser before cryocooling. The examination of the C-axis served as an indicator of binding interactions with biotin and streptavidin (Table 4.4). Various C-axis values were observed across all three illumination durations. However, the obtained crystallographic data did not provide any conclusive results regarding the binding of biotin to the pocket of T7-SA.

Table 4.4: T7-SA microcrystals' unit cell after being illuminated for 5, 15, or 30 minutes after a 10min soak in 0.1mM photocaged biotin (compound III).

Crystal #	C-axis at 5min (Å)
5	175.16
6	176.38
7	171.97

Crystal #	C-axis at 15min (Å)
8	181.82
9	172.96

Crystal #	C-axis at 30min (Å)
10	171.71
11	172.39
12	172.69
13	181.03
14	175.27
15	179.24

4.3.6 Serial Crystallography at SwissFEL

Serial crystallography (SX) was conducted at SwissFEL's Cristallina experimental station during its commissioning stage. Room temperature apo state of T7-SA micro-crystals diffracted to 1.63Å at 293 K. Structures of the apo state of cryo-cooled crystals and room temperature crystals were in very good agreement. Micro-crystals were then crosslinked with glutaraldehyde soaked with 0.1 mM photocaged biotin (compound **III**) for 10 minutes. Diffraction data collected in dark conditions indicated an absence of the biotin ligand in the binding pocket. Similarly prepared crystals deposited on MISP-chips were then exposed for 5-minutes to UV light at 405nm before data collection. However, no significant shift in the C-axis was observed. Difference Fourier maps obtained through thorough data analysis revealed positive and negative electron densities at similar locations as in the cryo data of PEG-biotin soaked crystals. However, the interpretation remains inconclusive due to the weak signal in the binding pocket (Figure 4.11) and noisy signal observed throughout the entire protein model.

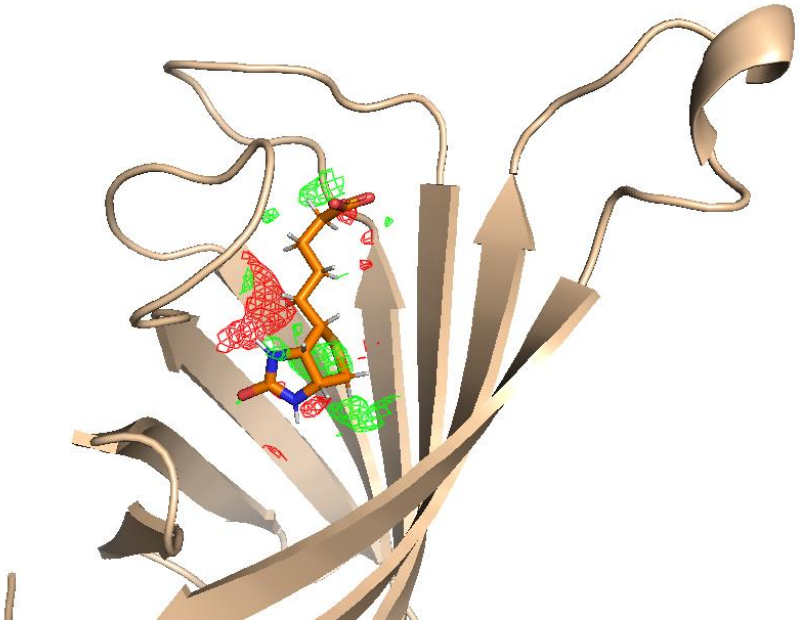

Figure 4.11. $|F_{obs}| - |F_{obs}|$ difference Fourier electron density map of the 5-minute timepoint to dark. *(A) $|F_{obs}|^{5\ min} - |F_{obs}|^{dark}$ map. Red indicates negative difference electron density; green denotes positive difference electron density (contoured at ±2.5 rmsd). Biotin model (orange) is added inside the pocket to serve as a reference. Density maps cannot be interpreted as the signals are weak and noisy.*

4.4 Discussion

4.4.1 Photocaged biotin compounds

The photocaged biotin compounds used during this study comprised two variations of coumarins (chromophore **A** and chromophore **B**), tuned to different absorption maxima of 379 and 397nm. The wavelength range of chromophore **B** be would have been more suitable for the experiments, given the current laser limitations at SwissFEL Cristallina. However, chromophore **B**, when dissolved in DMSO, disintegrated within a couple of minutes, resulting it to be a very unstable compound. Due to the instability, chromophore **B** was eliminated from this study.

As described in Monteiro et al., 2021, coumarins are classified as having poor to medium solubility. In order to combat this issue, a PEG ester tail was added onto biotin. PEG (polyethylene glycol $[-CH_2-CH_2-O-]_n$) is a hydrophilic compound due to the ability of H-

bonding that occurs between PEG and water. Both the ester and the PEG's polarity facilitates dissolution in water. The flexibility of the PEG ester tail can create steric hindrance, effectively impeding the aggregation of molecules and thereby improving solubility by minimizing intermolecular interactions that could result in precipitation. In summary, compound **III**, containing chromophore **A** and a PEG tail was chosen as the photocaged biotin ligand for this study, which is a good compromise in terms of stability and solubility, but is not optimal in the activation wavelength considering the current limitation of the laser source available at SwissFEL.

4.4.2 Biotin binding observed through Cryo-Crystallography

The micro-crystals found to dissolve upon contact with any biotin ligand, posing a significant challenge for the experiments. In order to combat this issue, glutaraldehyde was used as a crosslinker. Glutaraldehyde is a short-chain dialdehyde with 5 carbons containing a formyl group on both terminal sides serving as reactive groups. It reacts preferentially with the lysine residues located at the surface of the crystal forming covalent bonds (Yonath et al., 1977); however it can also react with other amines, thiols, and imidazoles (Habeeb & Hiramoto, 1968). The primary crosslinking mechanism of glutaraldehyde in protein crystals involves the interaction of its aldehyde groups with the ε-amino groups present in lysine residues which provides stability to the protein crystal (Habeeb & Hiramoto, 1968; Yan et al., 2015). As crosslinking predominantly takes place on the outer surface of the crystals, it should not impede intermolecular dynamics within the crystal, rendering it ideal for studying the binding interactions between T7-SA and biotin.

Because of the capability to diffuse biotin-derived ligands into T7-SA crystals stabilized by glutaraldehyde, structures of T7-SA in both the apo state and with biotin bound inside the pocket could be determined. A notable observation was the C-axis expansion bound state

compared to the apo state. The introduction of biotin onto T7-SA resulted in an increase of approximately 10Å in the C-axis (Figure 4.12). This indicates substantial rearrangements within the crystal, which can potentially be the reason why not crosslinked micro-crystals dissolve immediately upon contact with biotin.

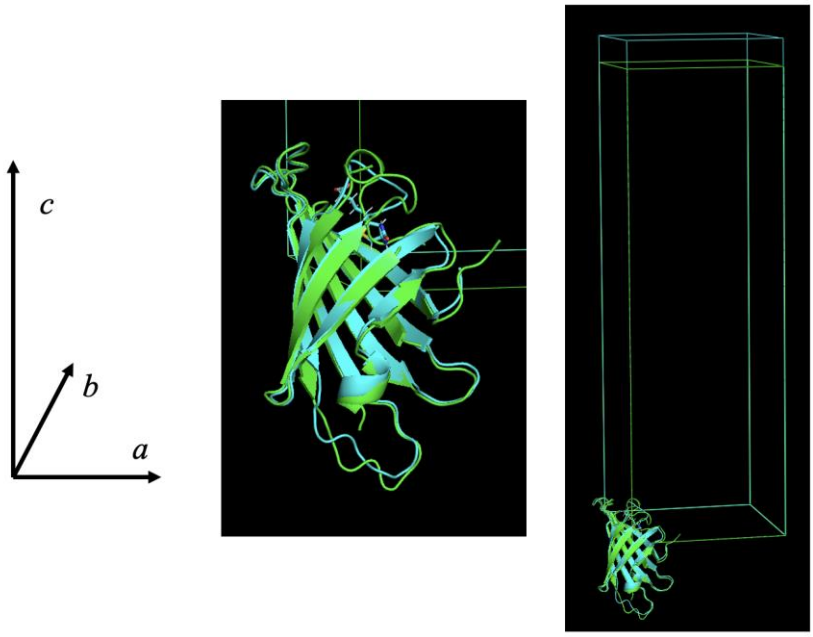

Figure 4.12: Overlay of C-axis between T7-SA apo-GA and T7-SA PEG-biotin. *Upon the binding of a biotin-derived ligand to the binding pocket of T7-SA apo (illustrated in green), there is an increase in the C-axis by approximately 10Å, depicted in teal.*

The concentration experiment that was conducted using four different PEG-biotin ligand concentrations demonstrated full binding of biotin into T7-SA's binding pocket at any concentration of 10-100mM. However, for crystals soaked with 0.1mM concentrations a variety of C-axis values were found within the four of measured crystals prepared at the same conditions: For one crystal the C-axis indicated the apo state of T7-SA (C1), another one indicated a biotin bound state (C3), and two C-axis indicated an intermediate state (C2 and C4). A possible explanation is that the reaction slows down at the surfaces of the protein crystals due to crosslinking. However, once this protective barrier is breached, the reaction accelerates significantly. In analyzing the difference Fourier electron density maps of C2-C1 (Figure 4.9A),

we noted an increase in the C-axis to 177.3Å. Despite a slight weakening of the signal, the changes observed in the binding pocket are evident. Particularly noteworthy is the robust signal observed in the analysis of C3-C1. Here, the negative electron density suggests the movement of T7-SA's tail away from the binding pocket, while the positive electron density indicates the entering of biotin. These distinct states observed within the same batch of micro-crystals soaked in 0.1mM solution may suggest that the concentration was too low for all crystals to achieve full biotin occupancy. When examining the R-factors depicted in Figure 4.10, a clear transition is evident: as the C-axis increases, so does the R-factor. This observation suggests a transition from an apo state to a biotin-bound state. This discussion underscores the dynamic nature of the binding interactions and highlights the significance of concentration levels in influencing the occupancy and behavior of ligands within protein crystals.

One drawback encountered during this experiment stemmed from the utilization of the streptavidin variant T7-SA. T7-SA features a C-terminal tail comprising residues 130-159, which forms a flexible alpha-helical segment that extends into the binding site when unoccupied by a ligand. However, when a ligand is present, this C-terminal tail displays flexibility, shifting away from the binding site. Working with a streptavidin variant containing this tail poses challenges, particularly in discerning weak electron density signals within the binding pocket, whether originating from the tail or the ligand. It is plausible to speculate that changes in electron density upon binding may be more noticeable in the absence of a ligand, when only water occupies the pocket in the apo state instead of a tail.

Illumination studies followed using compound **III** at a concentration of 0.1mM, due to the limited availability of ligand. The micro-crystals were soaked for 10 minutes then illuminated for 5, 15 or 30 minutes before cryo-cooling. Independent of the illumination time, C-axis values were distributed between what can be considered an apo state to a transitional

state, and the data was inconclusive due to the weak signals in the binding pocket, which may be explained as a result of the low concentration of photocaged biotin after diffusion into the crosslinked crystals and the limited uncaging efficiency.

4.4.3 TR-SX at SwissFEL

An opportunity arose during the commissioning stages of the MISP-chip at Cristallina to try capturing TR-SX of the uncaging and binding events of photocaged biotin (compound **III**) into T7-SA. The ability to crosslink T7-SA to determine the room temperature structure provides a solid basis for upcoming experiments. By establishing a solid protocol for room temperature studies, it paves the road and allows for further studies to be conducted in order to understand the structural dynamics performed at room temperature during the uncaging events occurring.

4.5 Further experiments

To proceed with this experiment, various adjustments or attempts can be made to capture the time points of biotin binding to T7-SA. To start off, further experiments should have ligand soaking concentrations of 1mM or higher to assure that biotin binds into streptavidin based on of the concentration trails. An adequate wavelength of 380nm should be used to further proceed uncaging experiments as 405nm may be too high for the coumarin caged biotin. During the commissioning stage of Cristallina, wavelengths below 405 were unattainable due to the prevailing circumstances. However, with Cristallina now operational, it is feasible to reach wavelengths as low as 380nm.

An alternate approach for capturing time-resolved data on the binding of biotin to T7-SA might involve employing a droplet ejector instead of a photocage. By removing pump-probe studies, along with the photocage, you eliminate any issues that may arise with either the

methodology or the specific photocage. Instead, one can opt for a droplet ejector set up where diffusion studies can be performed on this model system. Biotin has an extremely high affinity towards streptavidin, and due to this, makes it a great candidate for diffusion studies. At Cristallina, commissioning of the droplet ejector will begin in the Spring of 2024, providing a great new alternative to capture the timepoints of biotin binding into streptavidin.

4.6 Conclusion

This study aimed to optimize a photocaged biotin-streptavidin system for pump-probe TR-SX experiments in attempt to reveal the structural dynamics of the binding events by using coumarins as the photocage. We were able to successfully capture the apo and biotin bound states of T7-SA, however, we were not able to capture time-resolved data. The photocage chosen for this project was a coumarin since they are classified to have a higher cleavage rate and absorbance maximum, however, coumarins are inherently low in solubility. We were able to overcome this issue by incorporating a PEG ester tail onto the photocaged biotin, resulting in a successful enhancement of the solubility of the photocaged biotin. Although coumarins are classified as having one of the highest cleavage rate among other photocages, photodecaging was not efficient enough in our case for time-resolved measurements. Further optimization will be needed in the design of the molecules, was well as in the experimental set-up to reach a better overlap of laser emission and photocage absorption wavelengths.

The glutaraldehyde-crosslinked T7-SA proved to be well suited for the intended studies. The exchange of the C-terminal tail to the biotin bound in the binding pocket was recorded along with the expansion of the crystal lattice. However, a streptavidin variant without the tail binding back into the biding pocket in the apo state might be more suitable for such experiments, as changes in electron density upon biotin binding might be easier to record and interpret. It also became clear that a certain threshold concentration of biotin is needed to

reproducibly induce binding. In time-resolved measurements, suitable concentrations might be easier to achieve using mixing experiments, e.g. using a drop ejector, than with photocages. Such experiments appear as the logic intermediate step towards further exploration of biding dynamics.

While further time is necessary to fully unlock the potential of this study, the investigations highlighted above present an exciting opportunity to determine the suitability of a coumarin-based photocaged biotin in order to capture the structural dynamics that occur while biotin binds into the binding pocket.

4.7 References

Adams, P. D., Grosse-Kunstleve, R. W., Hung, L.-W., Ioerger, T. R., McCoy, A. J., Moriarty, N. W., Read, R. J., Sacchettini, J. C., Sauter, N. K., & Terwilliger, T. C. (2002). PHENIX: building new software for automated crystallographic structure determination. *Acta Crystallographica Section D: Biological Crystallography*, *58*(11), 1948-1954.

Afonine, P. V., Poon, B. K., Read, R. J., Sobolev, O. V., Terwilliger, T. C., Urzhumtsev, A., & Adams, P. D. (2018). Real-space refinement in PHENIX for cryo-EM and crystallography. *Acta Crystallographica Section D: Structural Biology*, *74*(6), 531-544.

Altarelli, M. (2011). The European X-ray free-electron laser facility in Hamburg. *Nuclear Instruments and Methods in Physics Research Section B: Beam Interactions with Materials and Atoms*, *269*(24), 2845-2849.

Ankenbruck, N., Courtney, T., Naro, Y., & Deiters, A. (2018). Optochemical control of biological processes in cells and animals. *Angewandte Chemie International Edition*, *57*(11), 2768-2798.

Argarana, C. E., Kuntz, I. D., Birken, S., Axel, R., & Cantor, C. R. (1986). Molecular cloning and nucleotide sequence of the streptavidin gene. *Nucleic acids research*, *14*(4), 1871-1882.

Bandara, H. D., & Burdette, S. C. (2012). Photoisomerization in different classes of azobenzene. *Chemical Society Reviews*, *41*(5), 1809-1825.

Barends, T. R., Stauch, B., Cherezov, V., & Schlichting, I. (2022). Serial femtosecond crystallography. *Nature Reviews Methods Primers*, *2*(1), 59.

Baxter, E. L., Aguila, L., Alonso-Mori, R., Barnes, C. O., Bonagura, C. A., Brehmer, W., Brunger, A. T., Calero, G., Caradoc-Davies, T. T., & Chatterjee, R. (2016). High-density grids for efficient data collection from multiple crystals. *Acta Crystallographica Section D: Structural Biology*, *72*(1), 2-11.

Bayer, E. A., & Wilchek, M. (1990). Application of avidin-biotin technology to affinity-based separations. *J Chromatogr*, *510*, 3-11. https://doi.org/10.1016/s0021-9673(01)93733-1

Beale, J. H., Bolton, R., Marshall, S. A., Beale, E. V., Carr, S. B., Ebrahim, A., Moreno-Chicano, T., Hough, M. A., Worrall, J. A., & Tews, I. (2019). Successful sample preparation for serial crystallography experiments. *Journal of Applied Crystallography*, *52*(6), 1385-1396.

Beale, J. H., & Marsh, M. E. (2021). Optimizing the Growth of Endothiapepsin Crystals for Serial Crystallography Experiments. *JoVE (Journal of Visualized Experiments)*(168), e61896.

Botha, S., Nass, K., Barends, T. R. M., Kabsch, W., Latz, B., Dworkowski, F., Foucar, L., Panepucci, E., Wang, M., Shoeman, R. L., Schlichting, I., & Doak, R. B. (2015). Room-temperature serial crystallography at synchrotron X-ray sources using slowly flowing free-standing high-viscosity microstreams. *Acta Crystallographica Section D Biological Crystallography*, *71*(2), 387-397. https://doi.org/10.1107/s1399004714026327

Boutet, S., Lomb, L., Williams, G. J., Barends, T. R., Aquila, A., Doak, R. B., Weierstall, U., DePonte, D. P., Steinbrener, J., Shoeman, R. L., Messerschmidt, M., Barty, A., White, T. A., Kassemeyer, S., Kirian, R. A., Seibert, M. M., Montanez, P. A., Kenney, C., Herbst, R., . . . Schlichting, I. (2012). High-resolution protein structure determination by serial femtosecond crystallography. *Science*, *337*(6092), 362-364. https://doi.org/10.1126/science.1217737

Bragg, W. L. (1913). The structure of some crystals as indicated by their diffraction of X-rays. *Proceedings of the Royal Society of London. Series A, Containing papers of a mathematical and physical character*, *89*(610), 248-277.

Brändén, G., & Neutze, R. (2021). Advances and challenges in time-resolved macromolecular crystallography. *Science*, *373*(6558). https://doi.org/10.1126/science.aba0954

Carrillo, M., Beale, J., & Padeste, C. (2022). Fixed-targets for serial protein crystallography at SwissFEL. *Acta Crystallographica*, *A78*, a279.

Carrillo, M., Mason, T. J., Karpik, A., Martiel, I., Kepa, M. W., McAuley, K. E., Beale, J. H., & Padeste, C. (2023). Micro-structured polymer fixed targets for serial crystallography at synchrotrons and XFELs. *IUCrJ*, *10*(6).

Carrillo, M., Mason, T. J., Karpik, A., Martiel, I., Kepa, M. W., McAuley, K. E., Beale, J. H., & Padeste, C. (2023). Micro-structured polymer fixed targets for serial crystallography at synchrotrons and XFELs. *IUCrJ*, *10*(Pt 6), 678-693. https://doi.org/10.1107/S2052252523007595

Carrillo, M., Pandey, S., Sanchez, J., Noda, M., Poudyal, I., Aldama, L., Malla, T. N., Claesson, E., Wahlgren, W. Y., & Feliz, D. (2021). High-resolution crystal structures of transient intermediates in the phytochrome photocycle. *Structure*, *29*(7), 743-754. e744.

Chaiet, L., & Wolf, F. J. (1964). The Properties of Streptavidin, a Biotin-Binding Protein Produced by Streptomycetes. *Arch Biochem Biophys*, *106*, 1-5. https://doi.org/10.1016/0003-9861(64)90150-x

Chapman, H. N., Caleman, C., & Timneanu, N. (2014). Diffraction before destruction. *Philos Trans R Soc Lond B Biol Sci*, *369*(1647), 20130313. https://doi.org/10.1098/rstb.2013.0313

Chapman, H. N., Fromme, P., Barty, A., White, T. A., Kirian, R. A., Aquila, A., Hunter, M. S., Schulz, J., DePonte, D. P., & Weierstall, U. (2011). Femtosecond X-ray protein nanocrystallography. *Nature*, *470*(7332), 73-77.

Chapman, H. N., Fromme, P., Barty, A., White, T. A., Kirian, R. A., Aquila, A., Hunter, M. S., Schulz, J., DePonte, D. P., Weierstall, U., Doak, R. B., Maia, F. R., Martin, A. V., Schlichting, I., Lomb, L., Coppola, N., Shoeman, R. L., Epp, S. W., Hartmann, R., . . . Spence, J. C. (2011). Femtosecond X-ray protein nanocrystallography. *Nature*, *470*(7332), 73-77. https://doi.org/10.1038/nature09750

Chayen, N. E. (2005). Methods for separating nucleation and growth in protein crystallisation. *Progress in biophysics and molecular biology*, *88*(3), 329-337.

Chayen, N. E., & Saridakis, E. (2008). Protein crystallization: from purified protein to diffraction-quality crystal. *Nature methods*, *5*(2), 147-153.

Claesson, E., Wahlgren, W. Y., Takala, H., Pandey, S., Castillon, L., Kuznetsova, V., Henry, L., Panman, M., Carrillo, M., Kubel, J., Nanekar, R., Isaksson, L., Nimmrich, A., Cellini, A., Morozov, D., Maj, M., Kurttila, M., Bosman, R., Nango, E., . . . Westenhoff, S. (2020). The primary structural photoresponse of phytochrome proteins captured by a femtosecond X-ray laser. *Elife*, *9*. https://doi.org/10.7554/eLife.53514

Coquelle, N., Sliwa, M., Woodhouse, J., Schirò, G., Adam, V., Aquila, A., Barends, T. R., Boutet, S., Byrdin, M., & Carbajo, S. (2018). Chromophore twisting in the excited state of a photoswitchable fluorescent protein captured by time-resolved serial femtosecond crystallography. *Nature Chemistry*, *10*(1), 31-37.

Dasgupta, M., Budday, D., de Oliveira, S., Madzelan, P., Marchany-Rivera, D., Seravalli, J., Hayes, B., Sierra, R. G., Boutet, S., Hunter, M. S., Alonso-Mori, R., Batyuk, A., Wierman, J., Lyubmiov, A., Brewster, A. S., Sauter, N. K., Applegate, G. A., Tiwari, V. K.,

Berkowitz, D. B., . . . Wilson, M. A. (2019). Mix-and-inject XFEL crystallography reveals gated conformational dynamics during enzyme catalysis. *PNAS*, *116*(51), 25634-25640.

DeLano, W. (2020). The PyMOL Molecular Graphics System, Version 2.0 Schrödinger, LLC.

DeLano, W. L. (2002). Pymol: An open-source molecular graphics tool. *CCP4 Newsl. Protein Crystallogr*, *40*(1), 82-92.

DePonte, D., Doak, R., Hunter, M., Zhenquan, L., Weierstall, U., & Spence, J. (2009). SEM imaging of liquid jets. *Micron*, *40*(4), 507-509.

DePonte, D., Weierstall, U., Schmidt, K., Warner, J., Starodub, D., Spence, J., & Doak, R. (2008). Gas dynamic virtual nozzle for generation of microscopic droplet streams. *Journal of Physics D: Applied Physics*, *41*(19), 195505.

Dessau, M. A., & Modis, Y. (2011). Protein crystallization for X-ray crystallography. *JoVE (Journal of Visualized Experiments)*(47), e2285.

Doak, R., Kovacs, G., Gorel, A., Foucar, L., Barends, T., Grünbein, M., Hilpert, M., Kloos, M., Roome, C., Shoeman, R., Stricker, M., Tono, K., You, D., Ueda, K., Sherrell, D. A., Owen, R. L., & Schlichting, I. (2018). Crystallography on a chip - without the chip: sheet-on-sheet sandwich. *Acta Crystallographica*, *D74*(10), D1000-1007.

Doak, R. B., Nass Kovacs, G., Gorel, A., Foucar, L., Barends, T. R., Grünbein, M. L., Hilpert, M., Kloos, M., Roome, C. M., & Shoeman, R. L. (2018). Crystallography on a chip–without the chip: Sheet-on-sheet sandwich. *Acta Crystallographica Section D: Structural Biology*, *74*(10), 1000-1007.

Doerr, A. (2011). Diffraction before destruction. *Nature methods*, *8*(4), 283-283.

Drenth, J., Jansonius, J., Koekoek, R., Swen, H., & Wolthers, B. (1968). Structure of papain. *Nature*, *218*(5145), 929-932.

Ducruix, A., & Giegé, R. (1999). *Crystallization of nucleic acids and proteins: a practical approach* (Vol. 210). OUP Oxford.

Ebrahim, A., Appleby, M., Axford, D., Beale, J., Moreno-Chicano, T., Sherrell, D. A., Strange, R. W., Hough, M. A., & Owen, R. L. (2019). Resolving polymorphs and radiation-driven effects in microcrystals using fixed-target serial synchrotron crystallography. *Acta Crystallographica*, *D75*(2), 151-159.

Edwards, D. A., & Syphers, M. J. (2008). *An introduction to the physics of high energy accelerators*. John Wiley & Sons.

Emma, P., Akre, R., Arthur, J., Bionta, R., Bostedt, C., Bozek, J., Brachmann, A., Bucksbaum, P., Coffee, R., & Decker, F.-J. (2010). First lasing and operation of an ångstrom-wavelength free-electron laser. *nature photonics*, *4*(9), 641-647.

Emsley, P., & Cowtan, K. (2004). Coot: model-building tools for molecular graphics. *Acta Crystallographica Section D: Biological Crystallography*, *60*(12), 2126-2132.

Eriksson, M., Al-Dmour, E., Andersson, Å., Johansson, M., Leemann, S., Malmgren, L., Tavares, P., & Thorin, S. (2016). *Commissioning of the MAX IV light source*. eScholarship, University of California.

Fedorov, R., Schlichting, I., Hartmann, E., Domratcheva, T., Fuhrmann, M., & Hegemann, P. (2003). Crystal structures and molecular mechanism of a light induced signaling switch: the Phot-LOV1 domain from Chlamydomonas reinhardtii. *Biophysics J*, *84*, 2474-2482.

Fromme, R., Ishchenko, A., Metz, M., Chowdhury, S. R., Basu, S., Boutet, S., Fromme, P., White, T. A., Barty, A., Spence, J. C. H., Weierstall, U., Liu, W., & Cherezov, V. (2015).

Serial femtosecond crystallography of soluble proteins in lipidic cubic phase. *International Union of Crystallography Journal*, *2*(5), 545-551.

Gevorkov, Y., Yefanov, O., Barty, A., White, T. A., Mariani, V., Brehm, W., Tolstikova, A., Grigat, R. R., & Chapman, H. N. (2019). XGANDALF - extended gradient descent algorithm for lattice finding. *Acta Crystallogr A Found Adv*, *75*(Pt 5), 694-704. https://doi.org/10.1107/S2053273319010593

Gisriel, C., Coe, J., Letrun, R., Yefanov, O. M., Luna-Chavez, C., Stander, N. E., Lisova, S., Mariani, V., Kuhn, M., Aplin, S., Grant, T. D., Dorner, K., Sato, T., Echelmeier, A., Cruz Villarreal, J., Hunter, M. S., Wiedorn, M. O., Knoska, J., Mazalova, V., . . . Zatsepin, N. A. (2019). Membrane protein megahertz crystallography at the European XFEL. *Nat Commun*, *10*(1), 5021. https://doi.org/10.1038/s41467-019-12955-3

Gotthard, G., Mous, S., Weinert, T., Maia, R. N. A., James, D., Dworkowski, F., Gashi, D., Furrer, A., Ozerov, D., Panepucci, E., Wang, M., Schertler, G. F. X., Heberle, J., Standfuss, J., & Nogly, P. (2023). Capturing the blue-light activated state of the Phot-LOV1 domain from Chlamydomonas reinhardtii using time-resolved serial synchrotron crystallography. *bioRxiv*, *preprint*. https://doi.org/10.1101/2023.11.06.565770

Gretch, D., Suter, M., & Stinski, M. (1987). The use of biotinylated monoclonal antibodies and streptavidin affinity chromatography to isolate herpesvirus hydrophobic proteins or glycoproteins. *Analytical biochemistry*, *163*(1), 270-277.

Grunbein, M. L., Bielecki, J., Gorel, A., Stricker, M., Bean, R., Cammarata, M., Dorner, K., Frohlich, L., Hartmann, E., Hauf, S., Hilpert, M., Kim, Y., Kloos, M., Letrun, R., Messerschmidt, M., Mills, G., Nass Kovacs, G., Ramilli, M., Roome, C. M., . . . Schlichting, I. (2018). Megahertz data collection from protein microcrystals at an X-ray free-electron laser. *Nat Commun*, *9*(1), 3487. https://doi.org/10.1038/s41467-018-05953-4

Grunbein, M. L., Stricker, M., Nass Kovacs, G., Kloos, M., Doak, R. B., Shoeman, R. L., Reinstein, J., Lecler, S., Haacke, S., & Schlichting, I. (2020). Illumination guidelines for ultrafast pump-probe experiments by serial femtosecond crystallography. *Nat Methods*, *17*(7), 681-684. https://doi.org/10.1038/s41592-020-0847-3

Haas, D., & Rossmann, M. (1970). Crystallographic studies on lactate dehydrogenase at–75° C. *Acta Crystallographica Section B: Structural Crystallography and Crystal Chemistry*, *26*(7), 998-1004.

Haas, D. J. (2020). The early history of cryo-cooling for macromolecular crystallography. *IUCrJ*, *7*(2), 148-157.

Habeeb, A., & Hiramoto, R. (1968). Reaction of proteins with glutaraldehyde. *Archives of biochemistry and biophysics*, *126*(1), 16-26.

Hadian-Jazi, M., Messerschmidt, M., Darmanin, C., Giewekemeyer, K., Mancuso, A. P., & Abbey, B. (2017). A peak-finding algorithm based on robust statistical analysis in serial crystallography. *Journal of Applied Crystallography*, *50*(6), 1705-1715.

Hansen, S., Hough, E., & Andersen, K. (1999). Purification, crystallization and preliminary X-ray studies of two isoforms of Rubisco from Alcaligenes eutrophus. *Acta Crystallographica Section D: Biological Crystallography*, *55*(1), 310-313.

Holzer, W., Penzkofer, A., Fuhrmann, M., & Hegemann, P. (2002). Spectroscopic characterization of flavin mononucleotide bound to the LOV1 domain of phototropin from Chlamydomonas reinhardtii. *Photochem Photobiol*, *75*, 479-487.

Hosaka, T., Katsura, K., Ishizuka-Katsura, Y., Hanada, K., Ito, K., Tomabechi, Y., Inoue, M., Akasaka, R., Takemoto, C., & Shirouzu, M. (2022). Crystal Structure of an Archaeal Tyrosyl-tRNA Synthetase Bound to Photocaged L-Tyrosine and Its Potential Application to Time-Resolved X-ray Crystallography. *Int J Mol Sci*, *23*(18). https://doi.org/10.3390/ijms231810399

Hosaka, T., Nomura, T., Kubo, M., Nakane, T., Fangjia, L., Sekine, S. I., Ito, T., Murayama, K., Ihara, K., Ehara, H., Kashiwagi, K., Katsura, K., Akasaka, R., Hisano, T., Tanaka, T., Tanaka, R., Arima, T., Yamashita, A., Sugahara, M., . . . Shirouzu, M. (2022). Conformational alterations in unidirectional ion transport of a light-driven chloride pump revealed using X-ray free electron lasers. *Proc Natl Acad Sci U S A*, *119*(9). https://doi.org/10.1073/pnas.2117433119

Huang, N., Deng, H., Liu, B., Wang, D., & Zhao, Z. (2021). Features and futures of X-ray free-electron lasers. *The Innovation*, *2*(2).

Hunte, C., Von Jagow, G., & Schagger, H. (2003). *Membrane protein purification and crystallization: a practical guide*. Elsevier.

Hunter, M. S., Segelke, B., Messerschmidt, M., Williams, G. J., Zatsepin, N. A., Barty, A., Benner, W. H., Carlson, D. B., Coleman, M., Graf, A., Hau-Riege, S. P., Pardini, T., Seibert, M. M., Evans, J., Boutet, S., & Frank, M. (2014). Fixed-target protein serial microcrystallography with an X-ray free-electron laser. *Nature Scientific Reports*, *4*, 6026.

James, D., Weinert, T., Skopintsev, P., Furrer, A., Gashi, D., Tanaka, T., Nango, E., Nogly, P., & Standfuss, J. (2019). Improving High Viscosity Extrusion of Microcrystals for Time-resolved Serial Femtosecond Crystallography at X-ray Lasers. *J Vis Exp*(144). https://doi.org/10.3791/59087

Ji, G., Wang, N., Yin, X., & Chen, P. (2020). Substituent Effect Induces Emission Modulation of Stilbene Photoswitches by Spatial Tuning of the N/B Electronic Constraints. *Organic Letters*, *22*(15), 5758-5762.

Josts, I., Niebling, S., Gao, Y., Levantino, M., Tidow, H., & Monteiro, D. (2018). Photocage-initiated time-resolved solution X-ray scattering investigation of protein dimerization. *IUCrJ*, *5*(Pt 6), 667-672. https://doi.org/10.1107/S2052252518012149

Kaminski, J. W., Vera, L., Stegmann, D. P., Vering, J., Eris, D., Smith, K. M. L., Huang, C. Y., Meier, N., Steuber, J., Wang, M., Fritz, G., Wojdyla, J. A., & Sharpe, M. E. (2022). Fast fragment- and compound-screening pipeline at the Swiss Light Source. *Acta Crystallogr D Struct Biol*, *78*(Pt 3), 328-336. https://doi.org/10.1107/S2059798322000705

Kang, H.-S., Min, C.-K., Heo, H., Kim, C., Yang, H., Kim, G., Nam, I., Baek, S. Y., Choi, H.-J., & Mun, G. (2017). Hard X-ray free-electron laser with femtosecond-scale timing jitter. *nature photonics*, *11*(11), 708-713.

Karpik, A., Martiel, I., Kristiansen, P. M., & Padeste, C. (2020). Fabrication of ultrathin suspended polymer membranes as supports for serial protein crystallography. *Micro and Nano Engineering*, *7*, 100053.

Kendrew, J. C., Bodo, G., Dintzis, H. M., Parrish, R., Wyckoff, H., & Phillips, D. C. (1958). A three-dimensional model of the myoglobin molecule obtained by x-ray analysis. *Nature*, *181*(4610), 662-666.

Kendrew, J. C., & Parrish, R. (1957). The crystal structure of myoglobin III. Sperm-whale myoglobin. *Proceedings of the Royal Society of London. Series A. Mathematical and Physical Sciences*, *238*(1214), 305-324.

Kim, Y., Babnigg, G., Jedrzejczak, R., Eschenfeldt, W. H., Li, H., Maltseva, N., Hatzos-Skintges, C., Gu, M., Makowska-Grzyska, M., & Wu, R. (2011). High-throughput protein purification and quality assessment for crystallization. *Methods*, *55*(1), 12-28.

Klehr, J., Zhao, J., Kron, A. S., Ward, T. R., & Köhler, V. (2020). Streptavidin (Sav)-based artificial Metalloenzymes: cofactor design considerations and large-scale expression of host protein variants. *Peptide and Protein Engineering: From Concepts to Biotechnological Applications*, 213-235.

Kottke, T., Heberle, J., Hehn, D., Dick, B., & Hegemann, P. (2003). Phot LOV1: photocycle of a blue-light receptor domain from the green alga Chlamydomonas reinhardtii. *Biophys J*, 1192-1201.

Kubo, M., Nango, E., Tono, K., Kimura, T., Owada, S., Song, C., Mafune, F., Miyajima, K., Takeda, Y., Kohno, J. Y., Miyauchi, N., Nakane, T., Tanaka, T., Nomura, T., Davidsson, J., Tanaka, R., Murata, M., Kameshima, T., Hatsui, T., . . . Iwata, S. (2017). Nanosecond pump-probe device for time-resolved serial femtosecond crystallography developed at SACLA. *J Synchrotron Radiat*, *24*(Pt 5), 1086-1091. https://doi.org/10.1107/S160057751701030X

Labrou, N. E. (2014). Protein purification: an overview. *Protein Downstream Processing: Design, Development and Application of High and Low-Resolution Methods*, 3-10.

Le Trong, I., Humbert, N., Ward, T. R., & Stenkamp, R. E. (2006). Crystallographic analysis of a full-length streptavidin with its C-terminal polypeptide bound in the biotin binding site. *J Mol Biol*, *356*(3), 738-745. https://doi.org/10.1016/j.jmb.2005.11.086

Le Trong, I., Wang, Z., Hyre, D. E., Lybrand, T. P., Stayton, P. S., & Stenkamp, R. E. (2011). Streptavidin and its biotin complex at atomic resolution. *Acta Crystallogr D Biol Crystallogr*, *67*(Pt 9), 813-821. https://doi.org/10.1107/S0907444911027806

Lee, D., Baek, S., Park, J., Lee, K., Kim, J., Lee, S. J., Chung, W. K., Lee, J.-L., Cho, Y., & Nam, K. H. (2019). Nylon mesh-based sample holder for fixed-target serial femtosecond crystallography. *Scientific reports*, *9*(1), 6971.

Letondor, C., Humbert, N., & Ward, T. R. (2005). Artificial metalloenzymes based on biotin-avidin technology for the enantioselective reduction of ketones by transfer hydrogenation. *Proc Natl Acad Sci U S A*, *102*(13), 4683-4687. https://doi.org/10.1073/pnas.0409684102

Li, H., Nakajima, Y., Nomura, T., Sugahara, M., Yonekura, S., Chan, S. K., Nakane, T., Yamane, T., Umena, Y., Suzuki, M., Masuda, T., Motomura, T., Naitow, H., Matsuura, Y., Kimura, T., Tono, K., Owada, S., Joti, Y., Tanaka, R., . . . Suga, M. (2021). Capturing structural changes of the S(1) to S(2) transition of photosystem II using time-resolved serial femtosecond crystallography. *IUCrJ*, *8*(Pt 3), 431-443. https://doi.org/10.1107/S2052252521002177

Li, Y., Wang, M., Wang, F., Lu, S., & Chen, X. (2023). Recent progress in studies of photocages. *Smart Molecules*, e20220003.

Liebschner, D., Afonine, P. V., Baker, M., Bunkoczi, G., Chen, V. B., Croll, T. I., Hintze, B., Hung, L.-W., Jain, S., McCoy, A. J., Moriarty, N. W., Oeffner, R. D., Poon, B. K., Prisant, M. G., Read, R. J., Richardson, J. S., Richardson, D. C., Sammito, M. D., Sobolev, O. V., . . . Adams, P. D. (2019). Macromolecular structure determination using X-rays, neutrons and electrons: recent developments in Phenix. *Acta Crystallographica*, *D75*, 861-877.

Liu, X., Liu, P., Li, H., Xu, Z., Jia, L., Xia, Y., Yu, M., Tang, W., Zhu, X., Chen, C., Zhang, Y., Nango, E., Tanaka, R., Luo, F., Kato, K., Nakajima, Y., Kishi, S., Yu, H., Matsubara, N., . . . Wang,

J. (2022). Excited-state intermediates in a designer protein encoding a phototrigger caught by an X-ray free electron laser. *Nat Chem*, *14*, 1054-1060.

Loosli, A., Rusbandi, U. E., Gradinaru, J., Bernauer, K., Schlaepfer, C. W., Meyer, M., Mazurek, S., Novic, M., & Ward, T. R. (2006). (Strept)avidin as host for biotinylated coordination complexes: stability, chiral discrimination, and cooperativity. *Inorg Chem*, *45*(2), 660-668. https://doi.org/10.1021/ic051405t

Madden, J. T., Toth, S. J., Dettmar, C. M., Newman, J. A., Oglesbee, R. A., Hedderich, H. G., Everly, R. M., Becker, M., Ronau, J. A., Buchanan, S. K., Cherezov, V., Morrow, M. E., Xu, S., Ferguson, D., Makarov, O., Das, C., Fischetti, R., & Simpson, G. J. (2013). Integrated nonlinear optical imaging microscope for on-axis crystal detection and centering at a synchrotron beamline. *J Synchrotron Radiat*, *20*(Pt 4), 531-540. https://doi.org/10.1107/S0909049513007942

Maestre-Reyna, M., Yang, C. H., Nango, E., Huang, W. C., Putu, E. P. G. N., Wu, W. J., Wang, P. H., Badur-Franz, S., Saft, M., Emmerich, H. J., Wu, H. Y., Lee, C. C., Huang, K. F., Chang, Y. K., Liao, J. H., Weng, J. H., Gad, W., Chang, C. W., Pang, A. H., . . . Tsai, M. D. (2022). Serial crystallography captures dynamic control of sequential electron and proton transfer events in a flavoenzyme. *Nat Chem*, *14*, 677-685.

Mallin, H., Hestericová, M., Reuter, R., & Ward, T. R. (2016). Library design and screening protocol for artificial metalloenzymes based on the biotin-streptavidin technology. *Nature protocols*, *11*(5), 835-852.

Malmerberg, E., M. Bovee-Geurts, P. H., Katona, G., Deupi, X., Arnlund, D., Wickstrand, C., Johansson, L. C., Westenhoff, S., Nazarenko, E., & X. Schertler, G. F. (2015). Conformational activation of visual rhodopsin in native disc membranes. *Science signaling*, *8*(367), ra26-ra26.

Martiel, I., Beale, J. H., Karpik, A., Huang, C. Y., Vera, L., Olieric, N., Wranik, M., Tsai, C. J., Muhle, J., Aurelius, O., John, J., Hogbom, M., Wang, M., Marsh, M., & Padeste, C. (2021). Versatile microporous polymer-based supports for serial macromolecular crystallography. *Acta Crystallogr D Struct Biol*, *77*(Pt 9), 1153-1167. https://doi.org/10.1107/S2059798321007324

Mehrabi, P., Müller-Werkmeister, H. M., Leimkohl, J. P., Schikora, H., Ninkovic, J., Krivokuca, S., Andricek, L., Epp, S. W., Sherrell, D. A., Owen, R. L., Pearson, A. R., Tellkamp, F., Schulz, E. C., & Miller, R. J. D. (2020). The HARE chip for efficient time-resolved serial synchrotron crystallography. *Journal of Synchrotron Radiation*, *27*(2), 360-370.

Mehrabi, P., Schulz, E. C., Agthe, M., Horrell, S., Bourenkov, G., von Stetten, D., Jan-Philipp, L., Schikora, H., Schneider, T. R., Pearson, A. R., Tellkamp, F., & Miller, R. J. D. (2019). Liquid application method for time-resolved analyses by serial synchrotron crystallography. *Nature Methods*, *16*, 979-982.

Mehrabi, P., Schulz, E. C., Dsouza, R., Mueller-Werkmeister, H. M., Tellkamp, F., Miller, R. J. D., & Pai, E. F. (2019). Time-resolved crystallography reveals allosteric communication aligned with molecular breathing. *Science*, *365*, 1167-1170.

Monteiro, D. C., Amoah, E., Rogers, C., & Pearson, A. R. (2021). Using photocaging for fast time-resolved structural biology studies. *Acta Crystallographica Section D: Structural Biology*, *77*(10), 1218-1232.

Monteiro, D. C. F., Amoah, E., Rogers, C., & Pearson, A. R. (2021). Using photocaging for fast time-resolved structural biology studies. *Acta Crystallogr D Struct Biol*, *77*(Pt 10), 1218-1232. https://doi.org/10.1107/S2059798321008809

Mous, S., Gotthard, G., Ehrenberg, D., Sen, S., Weinert, T., Johnson, P. J., James, D., Nass, K., Furrer, A., Kekilli, D., Ma, P., Bruenle, S., Casadei, C. M., Martiel, I., Dworkowski, F., Gashi, D., Skopintsev, P., Wranik, M., Knopp, G., . . . Nogly, P. (2022). Dynamics and mechanism of a light-driven chloride pump. *Science*, *375*, 845-851.

Mueller, C., Marx, A., Epp, S. W., Zhong, Y., Kuo, A., Balo, A., Soman, J., Schotte, F., Lemke, H., & Owen, R. (2015). Fixed target matrix for femtosecond time-resolved and in situ serial micro-crystallography. *Structural Dynamics*, *2*(5).

Mueller, C., Marx, A., Epp, S. W., Zhong, Y., Kuo, A., Balo, A. R., Soman, J., Schotte, F., Lemke, H. T., Owen, R. L., Pai, E. F., Pearson, A. R., Olson, J. S., Anfinrud, P. A., Ernst, O. P., & Miller, R. J. D. (2015). Fixed target matrix for femtosecond time-resolved and in situ serial micro-crystallography. *Structural Dynamics*, *2*(5), 054302.

Nam, K. H. (2023). Real-time monitoring of large-scale crystal growth using batch crystallization for serial crystallography. *Journal of Crystal Growth*, *614*, 127219.

Nam, K. H., Kim, J., & Cho, Y. (2021). Polyimide mesh-based sample holder with irregular crystal mounting holes for fixed-target serial crystallography. *Sci Rep*, *11*(1), 13115. https://doi.org/10.1038/s41598-021-92687-x

Nango, E., Kubo, M., Tono, K., & Iwata, S. (2019). Pump-probe time-Resolved serial femtosecond crystallography at SACLA: current status and data collection strategies. *Applied Sciences*, *9*(24), 5505.

Nango, E., Royant, A., Kubo, M., Nakane, T., Wickstrand, C., Kimura, T., Tanaka, T., Tono, K., Song, C., Tanaka, R., Arima, T., Yamashita, A., Kobayashi, J., Hosaka, T., Mizohata, E., Nogly, P., Sugahara, M., Nam, D., Nomura, T., . . . Iwata, S. (2016). A three-dimensional movie of structural changes in bacteriorhodopsin. *Science*, *354*(6319), 1552-1557.

Nass Kovacs, G., Colletier, J. P., Grunbein, M. L., Yang, Y., Stensitzki, T., Batyuk, A., Carbajo, S., Doak, R. B., Ehrenberg, D., Foucar, L., Gasper, R., Gorel, A., Hilpert, M., Kloos, M., Koglin, J. E., Reinstein, J., Roome, C. M., Schlesinger, R., Seaberg, M., . . . Schlichting, I. (2019). Three-dimensional view of ultrafast dynamics in photoexcited bacteriorhodopsin. *Nat Commun*, *10*(1), 3177. https://doi.org/10.1038/s41467-019-10758-0

Neutze, R., Wouts, R., van der Spoel, D., Weckert, E., & Hajdu, J. (2000). Potential for biomolecular imaging with femtosecond X-ray pulses. *Nature*, *406*(6797), 752-757.

Nogly, P., James, D., Wang, D., White, T., Zatsepin, N., Shilova, A., Nelson, G., Liu, H., Johansson, L., Heymann, M., Jaeger, K., Metz, M., Wickstrand, C., Wenting, W., Bath, P., Berntsen, P., Oberthuer, D., Panneels, V., Cherezov, V., . . . Weierstall, U. (2015). Lipidic cubic phase serial milisecond crystallography using synchrotron radiation. *International Union of Crystallography Journal*, *2*(2), 168-176.

Nogly, P., Panneels, V., Nelson, G., Gati, C., Kimura, T., Milne, C., Milathianaki, D., Kubo, M., Wu, W., Conrad, C., Coe, J., Bean, R., Zhao, Y., Bath, P., Dods, R., Harimoorthy, R., Beyerlein, K. R., Rheinberger, J., James, D., . . . Standfuss, J. (2016). Lipidic cubic phase injector is a viable crystal delivery system for time-resolved serial crystallography. *Nat Commun*, *7*, 12314. https://doi.org/10.1038/ncomms12314

Nogly, P., Weinert, T., James, D., Carbajo, S., Ozerov, D., Furrer, A., Gashi, D., Borin, V., Skopintsev, P., Jaeger, K., Nass, K., Bath, P., Bosman, R., Koglin, J., Seaberg, M., Lane, T., Kekilli, D., Bruenle, S., Tanaka, T., . . . Standfuss, J. (2018). Retinal isomerization in bacteriorhodopsin captured by a femtosecond X-ray laser. *Science*, *361*(6398).

Oberthuer, D., Knoška, J., Wiedorn, M. O., Beyerlein, K. R., Bushnell, D. A., Kovaleva, E. G., Heymann, M., Gumprecht, L., Kirian, R. A., & Barty, A. (2017). Double-flow focused liquid injector for efficient serial femtosecond crystallography. *Scientific reports*, *7*(1), 44628.

Oghbaey, S., Sarracini, A., Ginn, H. M., Pare-Labrosse, O., Kuo, A., Marx, A., Epp, S. W., Sherrell, D. A., Eger, B. T., Zhong, Y., Loch, R., Mariani, V., Alonso-Mori, R., Nelson, S., Lemke, H. T., Owen, R. L., Pearson, A. R., Stuart, D. I., Ernst, O. P., . . . Miller, R. J. (2016a). Fixed target combined with spectral mapping: approaching 100% hit rates for serial crystallography. *Acta Crystallogr D Struct Biol*, *72*(Pt 8), 944-955. https://doi.org/10.1107/S2059798316010834

Oghbaey, S., Sarracini, A., Ginn, H. M., Pare-Labrosse, O., Kuo, A., Marx, A., Epp, S. W., Sherrell, D. A., Eger, B. T., Zhong, Y., Loch, R., Mariani, V., Alonso-Mori, R., Nelson, S., Lemke, H. T., Owen, R. L., Pearson, A. R., Stuart, D. I., Ernst, O. P., . . . Miller, R. J. (2016b). Fixed target combined with spectral mapping: approaching 100% hit rates for serial crystallography. *Acta Crystallographica*, *D72*(Pt 8), 944-955. https://doi.org/10.1107/S2059798316010834

Olmos, J. L., Jr., Pandey, S., Martin-Garcia, J. M., Calvey, G., Katz, A., Knoska, J., Kupitz, C., Hunter, M. S., Liang, M., Oberthuer, D., Yefanov, O., Wiedorn, M., Heyman, M., Holl, M., Pande, K., Barty, A., Miller, M. D., Stern, S., Roy-Chowdhury, S., . . . Schmidt, M. (2018). Enzyme intermediates captured "on the fly" by mix-and-inject serial crystallography. *BMC Biol*, *16*(1), 59. https://doi.org/10.1186/s12915-018-0524-5

Orville, A. M. (2020). Recent results in time resolved serial femtosecond crystallography at XFELs. *Curr Opin Struct Biol*, *65*, 193-208. https://doi.org/10.1016/j.sbi.2020.08.011

Pande, K., Hutchison, C., Groenhof, G., Aquila, A., Robinson, J., Tenboer, J., Basu, S., Boutet, S., DePonte, D. P., Liang, M., White, T. A., Zatsepin, N., Yefanov, O., Morozov, D., Oberhuer, D., Gati, C., Subramanian, G., James, D., Zhao, Y., . . . Schmidt, M. (2016). Femtosecond structural dynamics drives the trans/cis isomerization in photoactive yellow protein. *Science*, *352*(6286), 725-729.

Pandey, S., Bean, R., Sato, T., Poudyal, I., Bielecki, J., Cruz Villarreal, J., Yefanov, O., Mariani, V., White, T. A., Kupitz, C., Hunter, M., Abdellatif, M. H., Bajt, S., Bondar, V., Echelmeier, A., Doppler, D., Emons, M., Frank, M., Fromme, R., . . . Schmidt, M. (2020). Time-resolved serial femtosecond crystallography at the European XFEL. *Nat Methods*, *17*(1), 73-78. https://doi.org/10.1038/s41592-019-0628-z

Pandey, S., Poudyal, I., & Malla, T. N. (2020). Pump-probe time-resolved serial femtosecond crystallography at X-ray free electron lasers. *Crystals*, *10*(7), 628.

Panneels, V., Wu, W., Tsai, C.-J., Nogly, P., Rheinberger, J., Jaeger, K., Cicchetti, G., Gati, C., Kick, L. M., & Sala, L. (2015). Time-resolved structural studies with serial crystallography: A new light on retinal proteins. *Structural Dynamics*, *2*(4).

Park, S.-Y., Choi, H., Eo, C., Cho, Y., & Nam, K. (2020). Fixed-Target Serial Synchrotron Crystallography Using Nylon Mesh and Enclosed Film-Based Sample Holder. *Crystals*, *10*(9), 803.

Perutz, M. (1990). How WL Bragg invented X-ray analysis. *Acta Crystallographica Section A: Foundations of Crystallography*, *46*(8), 633-643.

Perutz, M. F. (1963). X-ray Analysis of Hemoglobin: The results suggest that a marked structural change accompanies the reaction of hemoglobin with oxygen. *Science*, *140*(3569), 863-869.

Piketty, M.-L., Polak, M., Flechtner, I., Gonzales-Briceño, L., & Souberbielle, J.-C. (2017). False biochemical diagnosis of hyperthyroidism in streptavidin-biotin-based immunoassays: the problem of biotin intake and related interferences. *Clinical Chemistry and Laboratory Medicine (CCLM)*, *55*(6), 780-788.

Pompidor, G., Dworkowski, F. S., Thominet, V., Schulze-Briese, C., & Fuchs, M. R. (2013). A new on-axis micro-spectrophotometer for combining Raman, fluorescence and UV/Vis absorption spectroscopy with macromolecular crystallography at the Swiss Light Source. *J Synchrotron Radiat*, *20*(Pt 5), 765-776. https://doi.org/10.1107/S0909049513016063

Powell, H. R. (2017). X-ray data processing. *Bioscience reports*, *37*(5), BSR20170227.

Powell, H. R. (2021). A beginner's guide to X-ray data processing. *The Biochemist*, *43*(3), 46-50.

Reyes, F. D., Romero, J. F., & de Castro, M. L. (2001). Determination of biotin in foodstuffs and pharmaceutical preparations using a biosensing system based on the streptavidin–biotin interaction. *Analytica chimica acta*, *436*(1), 109-117.

Rhodes, G. (2010). *Crystallography made crystal clear: a guide for users of macromolecular models*. Elsevier.

Robinson, A., & Booklet, X.-r. D. (2001). Section 2.2 History of synchrotron radiation. *X-ray data booklet*, *2*.

Rodgers, D. W. (1994). Cryocrystallography. *Structure*, *2*(12), 1135-1140.

Roedig, P., Ginn, H. M., Pakendorf, T., Sutton, G., Harlos, K., Walter, T. S., Meyer, J., Fischer, P., Duman, R., & Vartiainen, I. (2017). High-speed fixed-target serial virus crystallography. *Nature methods*, *14*(8), 805-810.

Rupp, B. (2015). Origin and use of crystallization phase diagrams. *Acta Crystallographica Section F: Structural Biology Communications*, *71*(3), 247-260.

Safo, M. K., & Abraham, D. J. (2003). X-ray crystallography of hemoglobins. *Hemoglobin Disorders: Molecular Methods and Protocols*, 1-19.

Sano, T., Pandori, M. W., Chen, X., Smith, C. L., & Cantor, C. R. (1995). Recombinant core streptavidins. A minimum-sized core streptavidin has enhanced structural stability and higher accessibility to biotinylated macromolecules. *J Biol Chem*, *270*(47), 28204-28209. https://doi.org/10.1074/jbc.270.47.28204

Schluenzen, F., Tocilj, A., Zarivach, R., Harms, J., Gluehmann, M., Janell, D., Bashan, A., Bartels, H., Agmon, I., & Franceschi, F. (2000). Structure of functionally activated small ribosomal subunit at 3.3 Å resolution. *cell*, *102*(5), 615-623.

Schmidt, M. (2013). Mix and inject: Reaction initiation by diffusion for time-resolved macromolecular crystallography. *Advances in Condensed Matter Physics*, *2013*.

Schmidt, M., Pande, K., Basu, S., & Tenboer, J. (2015). Room temperature structures beyond 1.5 Å by serial femtosecond crystallography. *Structural Dynamics*, *2*(4).

Schulz, E. C., Yorke, B. A., Pearson, A. R., & Mehrabi, P. (2022). Best practices for time-resolved serial synchrotron crystallography. *Acta Crystallographica*, *D78*(Pt 1), 14-29. https://doi.org/10.1107/S2059798321011621

Sherrell, D. A., Foster, A. J., Hudson, L., Nutter, B., O'Hea, J., Nelson, S., Pare-Labrosse, O., Oghbaey, S., Miller, R. J., & Owen, R. L. (2015). A modular and compact portable mini-endstation for high-precision, high-speed fixed target serial crystallography at FEL and synchrotron sources. *J Synchrotron Radiat*, *22*(6), 1372-1378. https://doi.org/10.1107/S1600577515016938

Sherrell, D. A., Lavens, A., Wilamowski, M., Kim, Y., Chard, R., Lazarski, K., Rosenbaum, G., Vescovi, R., Johnson, J. L., & Akins, C. (2022). Fixed-Target Serial Crystallography at Structural Biology Center. *bioRxiv*, 2022.2004. 2006.487333.

Sherrell, D. A., Lavens, A., Wilamowski, M., Kim, Y., Chard, R., Lazarski, K., Rosenbaum, G., Vescovi, R., Johnson, J. L., Akins, C., Chang, C., Michalska, K., Babnigg, G., Foster, I., & Joachimiak, A. (2022). Fixed-target serial crystallography at the Structural Biology Center. *J Synchrotron Radiat*, *29*(Pt 5), 1141-1151. https://doi.org/10.1107/S1600577522007895

Sierra, R. G., Laksmono, H., Kern, J., Tran, R., Hattne, J., Alonso-Mori, R., Lassalle-Kaiser, B., Glöckner, C., Hellmich, J., & Schafer, D. W. (2012). Nanoflow electrospinning serial femtosecond crystallography. *Acta Crystallographica Section D: Biological Crystallography*, *68*(11), 1584-1587.

Sierra, R. G., Laksmono, H., Kern, J., Tran, R., Hattne, J., Alonso-Mori, R., Lassalle-Kaiser, B., Glockner, C., Hellmich, J., Schafer, D. W., Echols, N., Gildea, R., Grosse-Kunstleve, R. W., Sellberg, J., McQueen, T. A., Fry, A. R., Messerschmidt, M., Miahnahri, A., Seibert, M. M., . . . Bogan, M. J. (2012). Nanoflow electrospinning serial femtosecond crystallography. *Acta Crystallographica*, *D68*, 1584-1587.

Skopintsev, P., Ehrenberg, D., Weinert, T., James, D., Kar, R. K., Johnson, P. J., Ozerov, D., Furrer, A., Martiel, I., & Dworkowski, F. (2020). Femtosecond-to-millisecond structural changes in a light-driven sodium pump. *Nature*, *583*(7815), 314-318.

Skopintsev, P., Ehrenberg, D., Weinert, T., James, D., Kar, R. K., Johnson, P. J. M., Ozerov, D., Furrer, A., Martiel, I., Dworkowski, F., Nass, K., Knopp, G., Cirelli, C., Arrell, C., Gashi, D., Mous, S., Wranik, M., Gruhl, T., Kekilli, D., . . . Standfuss, J. (2020). Femtosecond-to-millisecond structural changes in a light-driven sodium pump. *Nature*, *583*(7815), 314-318. https://doi.org/10.1038/s41586-020-2307-8

Smolentsev, G., Guda, A., Zhang, X., Haldrup, K., Andreiadis, E., Chavarot-Kerlidou, M., Canton, S. E., CNachtegaal, M., Artero, V., & Sundstrom, V. (2013). Pump-flow-probe X-ray absorption spectroscopy as a tool for studying intermediate states of photocatalytic systems. *J Phys Chem C Nanom Interf*, *117*(34), 17367-17375.

Sorigué, D., Hadjidemetriou, K., Blangy, S., Gotthard, G., Bonvalet, A., Coquelle, N., Samire, P., Aleksandrov, A., Antonucci, L., & Benachir, A. (2021). Mechanism and dynamics of fatty acid photodecarboxylase. *Science*, *372*(6538), eabd5687.

Stevens, R. C. (2000). High-throughput protein crystallization. *Current opinion in structural biology*, *10*(5), 558-563.

Studier, F. (2005). Protein production by auto-induction in high-density shaking cultures. *Protein Expression and Purification*, *41*(1), 207-234.

Suga, M., Akita, F., Sugahara, M., Kubo, M., Nakajima, Y., Nakane, T., Yamashita, K., Umena, Y., Nakabayashi, M., Yamane, T., Nakano, T., Suzuki, M., Masuda, T., Inoue, S., Kimura, T., Nomura, T., Yonekura, S., Yu, L. J., Sakamoto, T., . . . Shen, J. R. (2017). Light-induced structural changes and the site of O=O bond formation in PSII caught by XFEL. *Nature*, *543*(7643), 131-135. https://doi.org/10.1038/nature21400

Tsai, C.-J., Pamula, F., Nehmé, R., Mühle, J., Weinert, T., Flock, T., Nogly, P., Edwards, P. C., Carpenter, B., & Gruhl, T. (2018). Crystal structure of rhodopsin in complex with a mini-Go sheds light on the principles of G protein selectivity. *Science advances*, *4*(9), eaat7052.

Villarón, D., & Wezenberg, S. J. (2020). Stiff-stilbene photoswitches: from fundamental studies to emergent applications. *Angewandte Chemie*, *132*(32), 13292-13302.

Ward, T. R. (2005). Artificial metalloenzymes for enantioselective catalysis based on the noncovalent incorporation of organometallic moieties in a host protein. *Chemistry*, *11*(13), 3798-3804. https://doi.org/10.1002/chem.200401232

Weierstall, U. (2014). Liquid sample delivery techniques for serial femtosecond crystallography. *Philos Trans R Soc Lond B Biol Sci*, *369*(1647), 20130337. https://doi.org/10.1098/rstb.2013.0337

Weierstall, U., James, D., Wang, C., White, T. A., Wang, D., Liu, W., Spence, J. C. H., Doak, R. B., Nelson, G., Fromme, P., Fromme, R., Grotjohann, I., Kupitz, C., Zatsepin, N. A., Liu, H., Basu, S., Wacker, D., Han, G. W., Katritch, V., . . . Cherezov, V. (2014). Lipidic cubic phase injector facilitates membrane protein serial femtosecond crystallography. *Nature Communications*, *5*, 3309.

White, T. (2019). Processing serial crystallography data with CrystFEL: a step-by-step guide. *Acta Crystallographica*, *D75*, 219-233.

White, T. A. (2019). Processing serial crystallography data with CrystFEL: a step-by-step guide. *Acta Crystallographica Section D: Structural Biology*, *75*(2), 219-233.

White, T. A., Kirian, R. A., Martin, A. V., Aquila, A., Nass, K., Barty, A., & Chapman, H. N. (2012). CrystFEL: a software suite for snapshot serial crystallography. *Journal of Applied Crystallography*, *45*(2), 335-341.

Wiedorn, M. O., Oberthur, D., Bean, R., Schubert, R., Werner, N., Abbey, B., Aepfelbacher, M., Adriano, L., Allahgholi, A., Al-Qudami, N., Andreasson, J., Aplin, S., Awel, S., Ayyer, K., Bajt, S., Barak, I., Bari, S., Bielecki, J., Botha, S., . . . Barty, A. (2018). Megahertz serial crystallography. *Nat Commun*, *9*(1), 4025. https://doi.org/10.1038/s41467-018-06156-7

Winn, M. D., Ballard, C. C., Cowtan, K. D., Dodson, E. J., Emsley, P., Evans, P. R., Keegan, R. M., Krissinel, E. B., Leslie, A. G., & McCoy, A. (2011). Overview of the CCP4 suite and current developments. *Acta Crystallographica Section D: Biological Crystallography*, *67*(4), 235-242.

Winn, M. D., Ballard, C. C., Cowtan, K. D., Dodson, E. J., Emsley, P., Evans, P. R., Keegan, R. M., Krissinel, E. B., Leslie, A. G., McCoy, A., McNicholas, S. J., Murshudov, G. N., Pannu, N. S., Potterton, E. A., Powell, H. R., Read, R. J., Vagin, A., & Wilson, K. S. (2011). Overview of the CCP4 suite and current developments. *Acta Crystallogr D Biol Crystallogr*, *67*(Pt 4), 235-242. https://doi.org/10.1107/S0907444910045749

Wojdyla, J. A., Kaminski, J. W., Panepucci, E., Ebner, S., Wang, X., Gabadinho, J., & Wang, M. (2018). DA+ data acquisition and analysis software at the Swiss Light Source macromolecular crystallography beamlines. *J Synchrotron Radiat*, *25*(Pt 1), 293-303. https://doi.org/10.1107/S1600577517014503

Wolff, A. M., Nango, E., Young, I. D., Brewster, A. S., Kubo, M., Nomura, T., Sugahara, M., Owada, S., Barad, B. A., & Ito, K. (2023). Mapping protein dynamics at high spatial resolution with temperature-jump X-ray crystallography. *Nature Chemistry*, *15*(11), 1549-1558.

Wolff, A. M., Nango, E., Young, I. D., Brewster, A. S., Kubo, M., Nomura, T., Sugahara, M., Owada, S., Barad, B. A., Ito, K., Bhowmick, A., Carbajo, S., Hino, T., Holton, J. M., Im, D., O'Riordan, L. J., Tanaka, T., Tanaka, R., Sierra, R. G., . . . Thompson, M. C. (2023). Mapping protein dynamics at high spatial resolution with temperature-jump X-ray crystallography. *Nat Chem*, *15*(11), 1549-1558. https://doi.org/10.1038/s41557-023-01329-4

Wranik, M., Weinert, T., Slavov, C., Masini, T., Furrer, A., Gaillard, N., Gioia, D., Ferrarotti, M., James, D., & Glover, H. (2023). Watching the release of a photopharmacological drug from tubulin using time-resolved serial crystallography. *Nature communications*, *14*(1), 903.

Wranik, M., Weinert, T., Slavov, C., Masini, T., Furrer, A., Gaillard, N., Gioia, D., Ferrarotti, M., James, D., Glover, H., Carrillo, M., Kekilli, D., Stipp, R., Skopintsev, P., Brünle, S., Mühlethaler, T., Beale, J., Gashi, D., Nass, K., . . . Standfuss, J. (2023). Watching the release of a photopharmacological drug from tubulin using time-resolved serial crystallography. *Nature Communications*, *14*(1). https://doi.org/10.1038/s41467-023-36481-5

Yan, E.-K., Cao, H.-L., Zhang, C.-Y., Lu, Q.-Q., Ye, Y.-J., He, J., Huang, L.-J., & Yin, D.-C. (2015). Cross-linked protein crystals by glutaraldehyde and their applications. *Rsc Advances*, *5*(33), 26163-26174.

Yonath, A., Sielecki, A., Moult, J., Podjarny, A., & Traub, W. (1977). Crystallographic studies of protein denaturation of renaturation. 1. Effects of denaturants on volume and x-ray pattern of crosslinked triclinic lysozyme crystals. *Biochemistry*, *16*(7), 1413-1417.

Zarrine-Afsar, A., Barends, T. R. M., Müller, C., Fuchs, M. R., Lomb, L., Schlichting, I., & Miller, R. J. D. (2012). Crystallography on a chip. *Acta Crystallographica*, *D68*(3), 321-323.

Zhang, F., Shan, B., Wang, Y., Zhu, Z., Yu, Z.-Q., & Ma, C. Y. (2021). Progress and opportunities for utilizing seeding techniques in crystallization processes. *Organic Process Research & Development*, *25*(7), 1496-1511.

4.8 Appendix: Supplementary Information

Supplementary information is provided by the Ward team.

*A. 4.1. Synthesis of photocaged biotin ester compound **I**.*

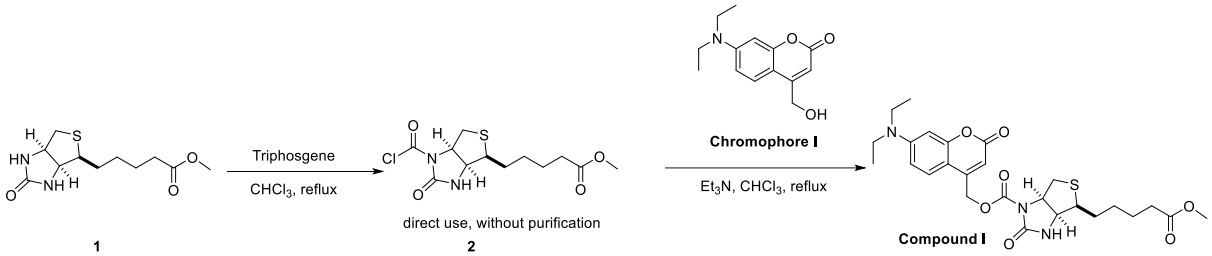

The intermediate "Compound **II"** was synthesized following a reported procedure (Chen 2022, supplementary info, synthesis of compounds 7 and 11). The resulting compound mix was used directly for the next step.

Compound **I**: The compound **II** was dissolved in $CHCl_3$. To the chromophore **I** (0.081 mmol, 1.0 eq) in the round bottom flask, compound **II** (0.16 mmol, 2.0 eq) and triethyl amine (0.24 mmol, 3.0 eq) were added at room temperature. The reaction mixture was heated at 80 °C overnight. After removing the solvent, the residue was redissolved in 5 mL MeOH. Precipitates were filtered using a 0.2 µM syringe. The compound was purified using a BUCHI C18 reverse phase column: elution A: water, elution B: acetonitrile. 0-5 min 20% B, 5-23 min, gradient to 80% B, 23-28 min, gradient to 100% B, 28-29min 100%B, 29-30min, gradient to 20%B, 30-32min. 20%. Retention time at 21.3 min. The product was lyophilized as yellow powder, 3 mg, yield: 6.9%. ^{1}H NMR (600 MHz, DMSO) δ 7.83 (s, 1H), 7.46 (d, *J* = 9.0 Hz, 1H), 6.69 (dd, *J* = 9.3, 2.3 Hz, 1H), 6.55 (d, *J* = 2.5 Hz, 1H), 6.21 (s, 1H), 5.40 (d, *J* = 2.7 Hz, 2H), 4.81 (dd, *J* = 7.6, 5.3 Hz, 1H), 4.17 (dd, *J* = 7.8, 4.3 Hz, 1H), 3.43 (q, *J* = 7.1 Hz, 4H), 3.21 (dt, *J* = 9.9, 5.2 Hz, 1H), 3.03 – 2.89 (m, 2H), 2.31 (t, *J* = 7.5 Hz, 2H), 1.70 – 1.42 (m, 4H), 1.12 (t, *J* = 7.0 Hz, 6H). ^{13}C NMR (151 MHz, DMSO) δ 173.32, 160.75, 155.74, 154.59, 150.52, 150.44, 125.39, 108.73, 105.03, 104.82, 96.83, 62.67, 61.97, 57.39, 54.79, 51.24, 44.01, 37.89, 33.07, 28.01, 27.77, 24.40, 12.33.

*A. 4.2. Synthesis of photocaged biotin PEG esters, compounds **II** and **III**.*

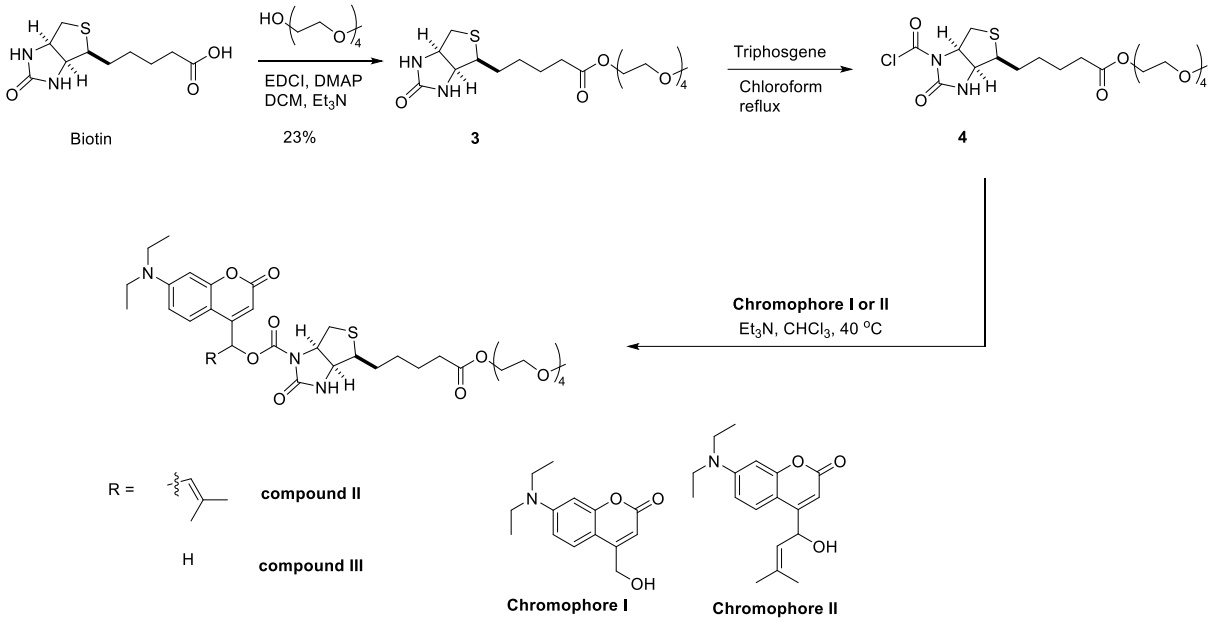

Biotin PEG ester III: EDCI (6 mmol), DMAP (1 mmol) and triethyleneglycol monomethylether (7.1 mmol) were added to a stirred suspension of *D*-biotin (5 mmol) in dry DCM (100 mL). The mixture was stirred for 2 days at room temperature. The solvent was evaporated under vacuum. The residues were taken up in water/acetonitrile 9:1 (total volume 36 mL). Precipitation was filtered off by 0.2 µM syringe filter. Biotin PEG ester **III** was purified by preparative HPLC on a C18 column. The product was lyophilized as white solid, yield: 23%. ^{1}H NMR (500 MHz, DMSO) δ 6.42 (t, *J* = 1.9 Hz, 1H), 6.35 (s, 1H), 4.30 (ddt, *J* = 7.5, 5.2, 1.1 Hz, 1H), 4.17 – 4.05 (m, 3H), 3.63 – 3.56 (m, 2H), 3.54 – 3.47 (m, 10H), 3.45 – 3.39 (m, 2H), 3.24 (s, 3H), 3.13 – 3.04 (m, 1H), 2.82 (dd, *J* = 12.4, 5.1 Hz, 1H), 2.58 (d, *J* = 12.4 Hz, 1H), 2.31 (t, *J* = 7.5 Hz, 2H), 1.66 – 1.24 (m, 6H). ^{13}C NMR (126 MHz, DMSO) δ 173.32, 163.15, 71.75, 70.28, 70.25, 70.22, 70.06, 68.78, 63.55, 61.49, 59.64, 58.53, 55.82, 33.71, 28.46, 28.44, 24.96. MS[M+H]$^{+}$ = 532.2.

The intermediate "compound **IV"** was synthesized following the reported procedure (Chen 2022). The resulting compound mix was used directly for the next step.

Compound **II** and compound **III**: The compound 4 mix was dissolved in $CHCl_3$. 20 mL stock solution (0.308 mmol) were transferred to round bottom reaction flasks. Chromophores **I** or **II** (0.077 mmol) and triethylamine (0.924 mmol) were added at room temperature. The reaction mixture was heated at 40 °C overnight. After removing the solvent, the residue was re-dissolved in 10 mL MeOH. Precipitates were filtered off using a 0.2 µM syringe. The residue was purified by reverse phase chromatography.

Compound **II** was isolated as yellow solid. ^{1}H NMR (600 MHz, MeOD) δ 7.49 (dd, *J* = 10.8, 9.2 Hz, 1H), 6.82 – 6.68 (m, 2H), 6.55 (d, *J* = 2.6 Hz, 1H), 6.26 (d, *J* = 11.9 Hz, 1H), 5.40 – 5.31 (m, 1H), 4.92 (d, *J* = 5.1 Hz, 0H), 4.25 (ddd, *J* = 7.7, 5.8, 4.3 Hz, 1H), 4.25 – 4.13 (m, 2H), 3.70 (t, *J* = 4.8 Hz, 2H), 3.64 – 3.58 (m, 11H), 3.57 – 3.52 (m, 2H), 3.48 (q, *J* = 7.1 Hz, 4H), 3.35 (d, *J* = 1.0 Hz, 3H), 3.12 – 2.93 (m, 2H), 2.44 – 2.34 (m, 2H), 2.03 – 1.96 (m, 3H), 1.77 – 1.42 (m, 6H), 1.21 (t, *J* = 7.1 Hz, 6H). ^{13}C NMR (151 MHz, MeOD) δ 173.83, 163.19, 156.49, 156.45, 156.31, 156.23, 154.95, 154.86, 150.97, 141.90, 141.57, 125.57, 125.45, 120.57, 120.51, 108.96, 108.94, 105.37, 104.45, 104.07, 96.97, 71.57, 70.84, 70.60, 70.17, 70.16, 70.15, 70.11, 69.96, 68.74, 63.22, 62.71, 58.01, 57.97, 57.70, 55.16, 55.14, 44.20, 38.19, 38.14, 33.30, 28.23, 27.95, 24.58, 24.54, 24.43, 17.70, 17.65, 11.32. LC-MS $[M+H]^{+}$ = 762.40.

Compound **III** was purified by BUCHI C18 reverse phase column: elution A: water with 3% acetonitrile, elution B: acetonitrile. 0-17 min linear increase to 95% elution B, 17-18 min, 95% elution B, 18-19 min, gradient to 20% B, retention time at 13.7 min. The product compound **III** was lyophilized as yellow solid 20 mg, yield: 9.1%. ^{1}H NMR (500 MHz, MeOD) δ 7.49 (dt, *J* = 9.0, 2.1 Hz, 1H), 6.83 – 6.66 (m, 1H), 6.55 (q, *J* = 2.3 Hz, 1H), 6.21 (t, *J* = 1.2 Hz, 1H), 5.44 (dd, *J* = 4.0, 2.1 Hz, 2H), 4.93 (ddd, *J* = 7.8, 4.3, 1.9 Hz, 1H), 4.27 (dd, *J* = 7.7, 4.4 Hz, 1H), 4.24 – 4.11 (m, 2H), 3.69 (dd, *J* = 4.0, 2.5 Hz, 2H), 3.64 – 3.58 (m, 12H), 3.56 – 3.51 (m, 2H), 3.48 (qd, *J* = 7.0, 1.7 Hz, 5H), 3.35 (s, 3H), 3.31 (p, *J* = 1.6 Hz, 6H), 3.12 – 3.03 (m, 2H), 2.38 (t, *J* = 7.3 Hz, 2H), 1.84 – 1.40 (m, 7H), 1.26 – 1.15 (m, 7H). ^{13}C NMR (126 MHz, MeOD) δ 175.24, 164.30, 157.63, 157.53, 152.52, 152.49, 152.36, 126.17, 110.47, 106.99, 106.35, 98.30, 72.98, 71.58, 71.58, 71.56, 71.53, 71.37, 70.15, 64.64, 64.23, 64.19, 59.46, 59.10, 56.57, 45.63, 39.43, 34.71, 29.64, 29.36, 25.84, 12.73. LC-MS $[M+H]^{+}$ = 708.30.

*A.4.3. NMR spectra of compound **I**:*

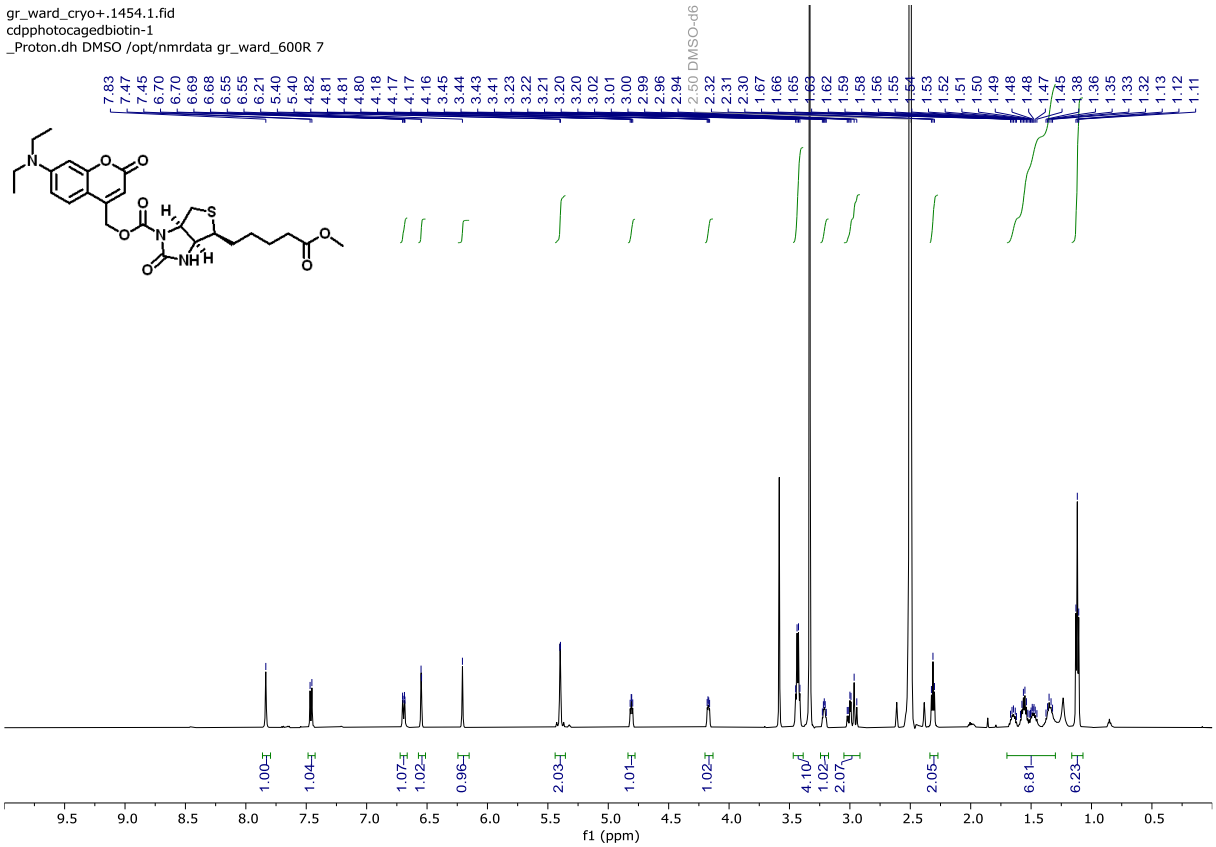

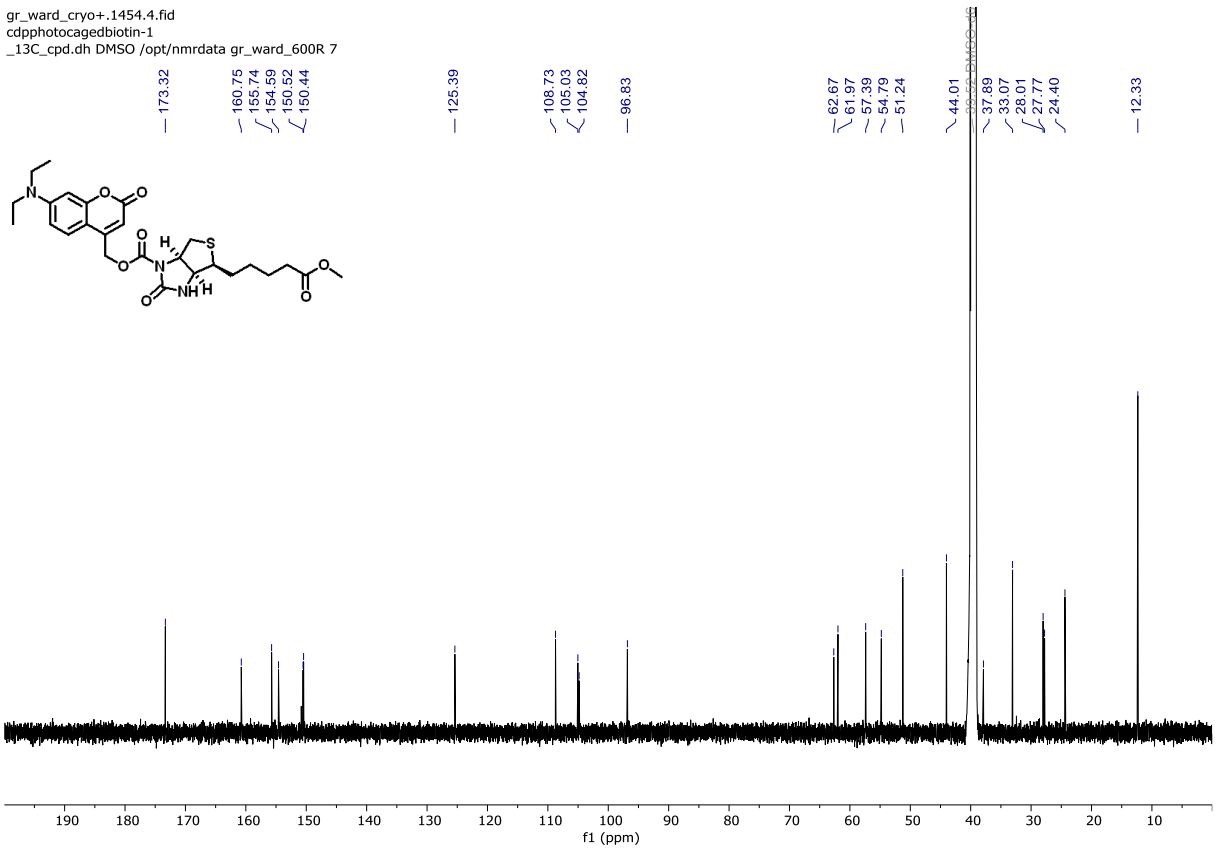

A.4.4. NMR spectra of PEG-Biotin

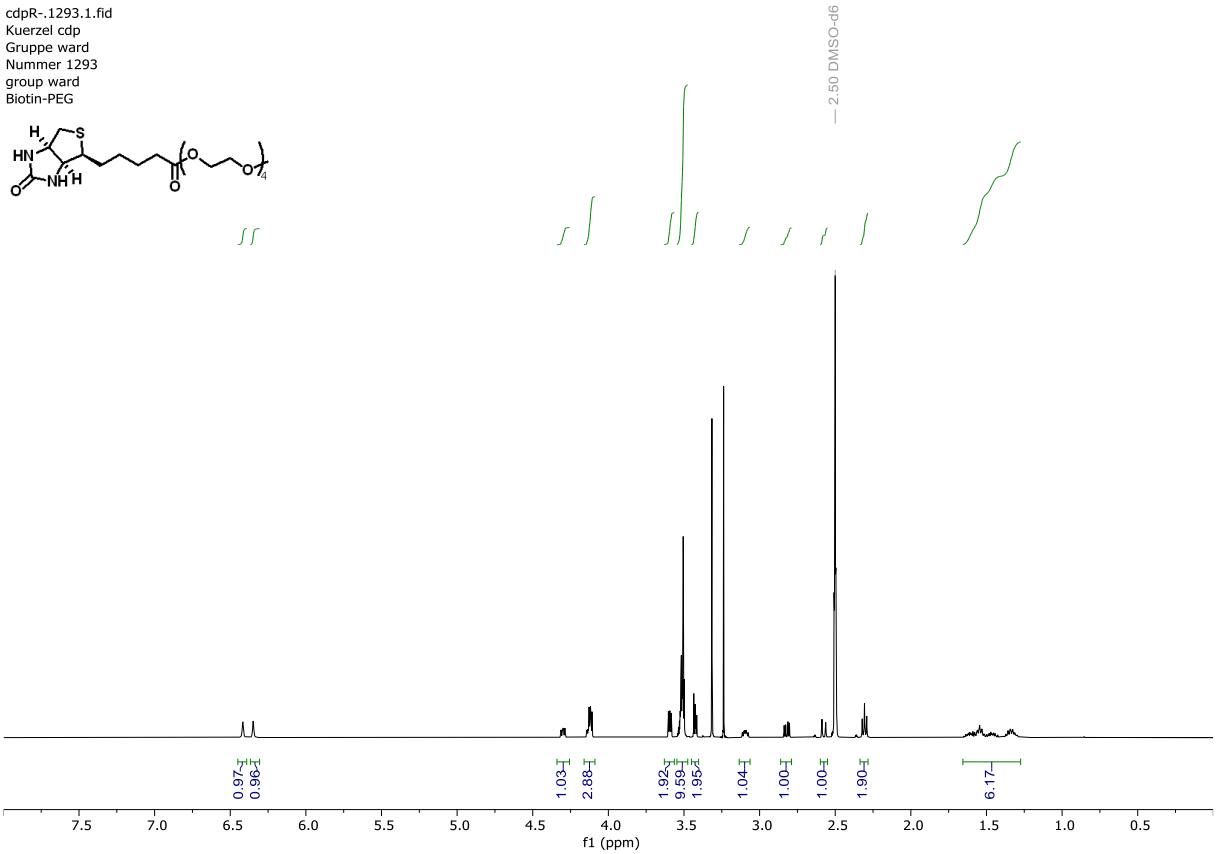

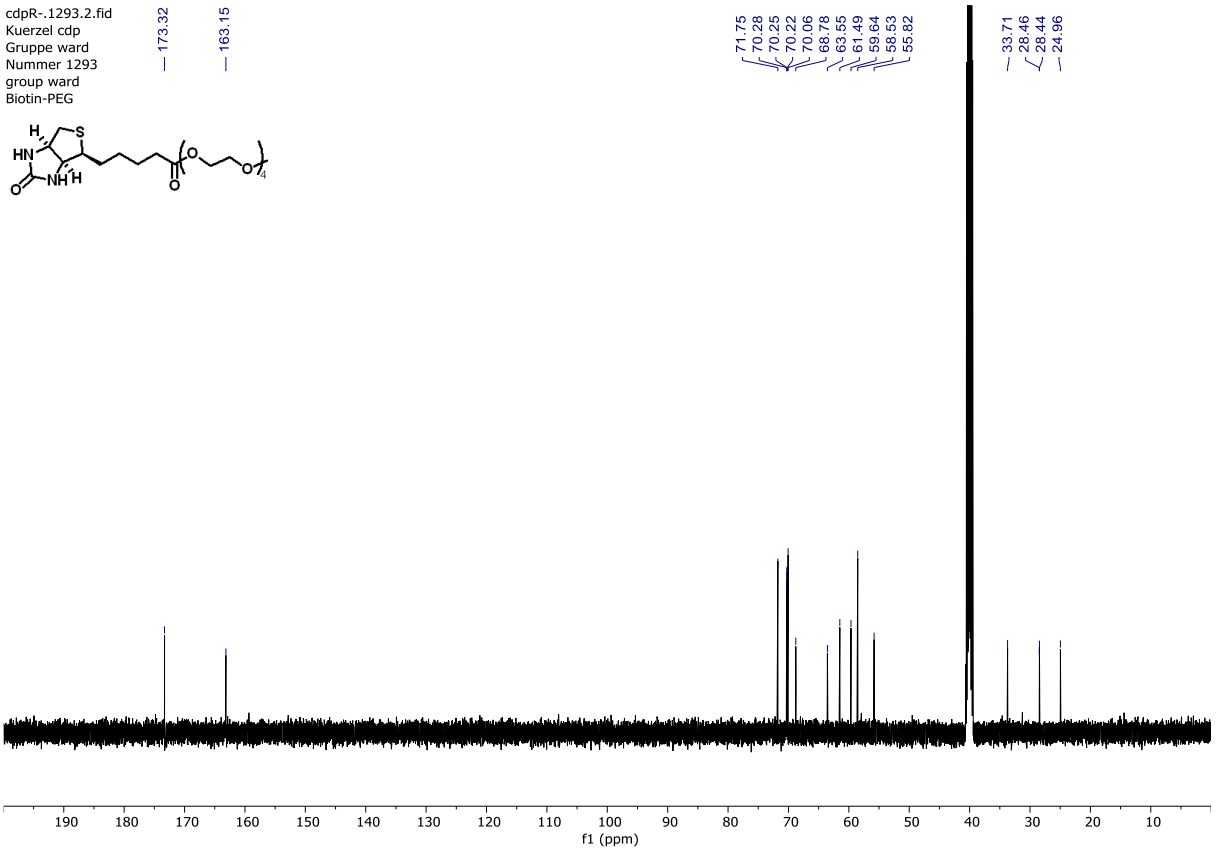

A.4.5. NMR Spectra of compound ***II***

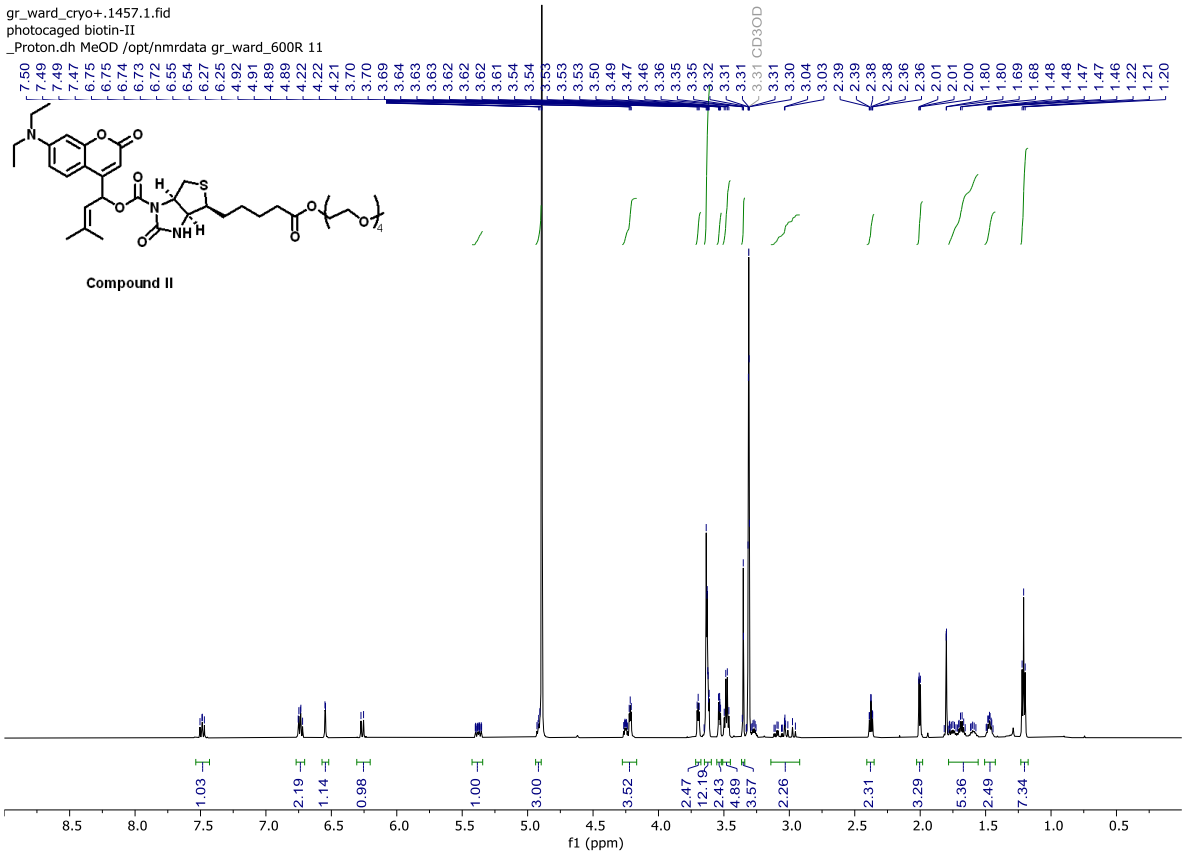

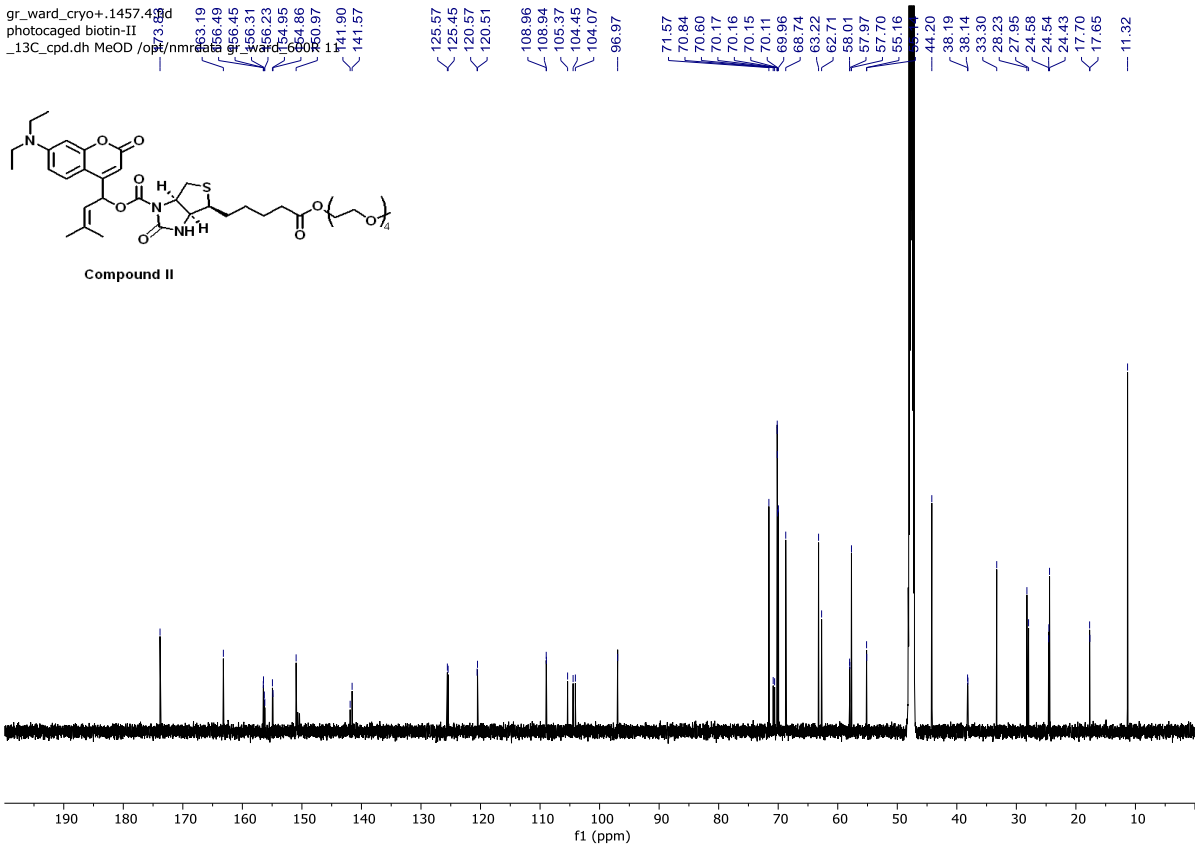

*A.4.6. NMR Spectra of compound **III***

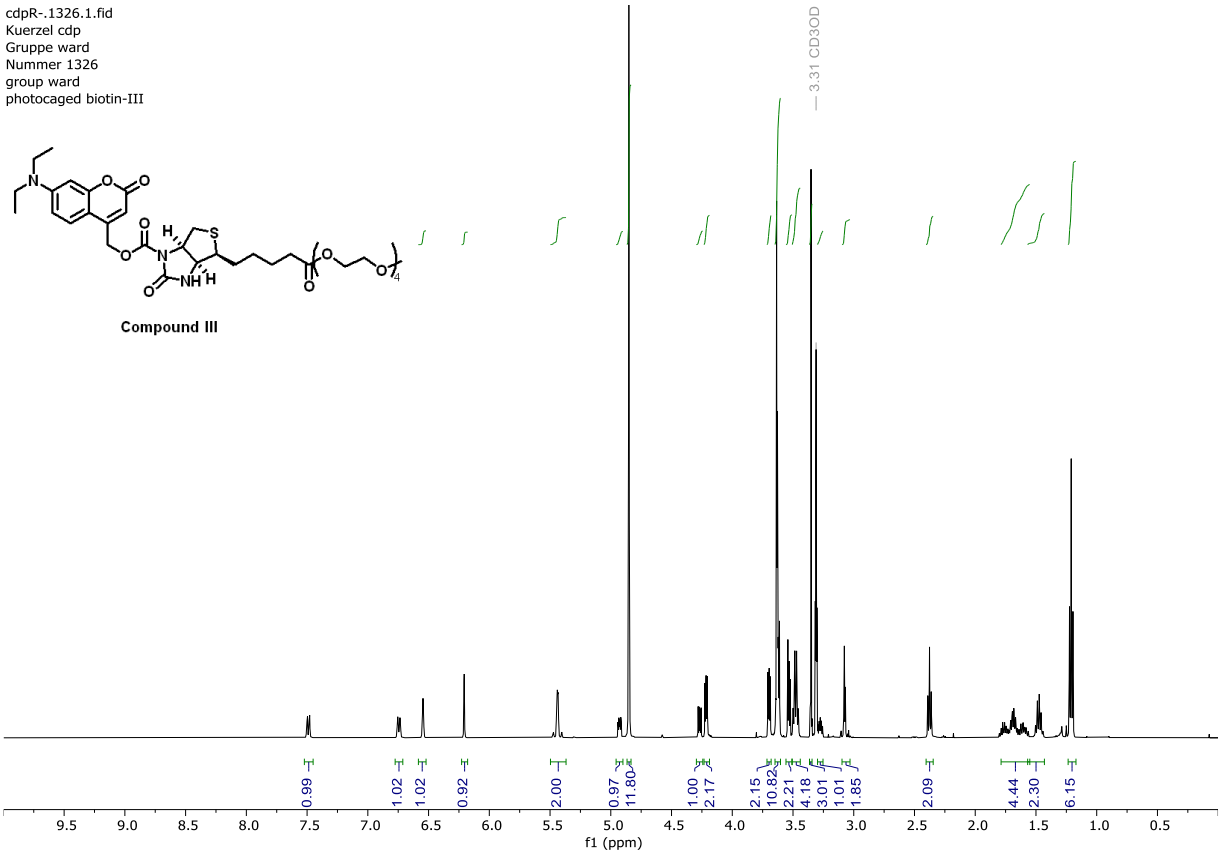

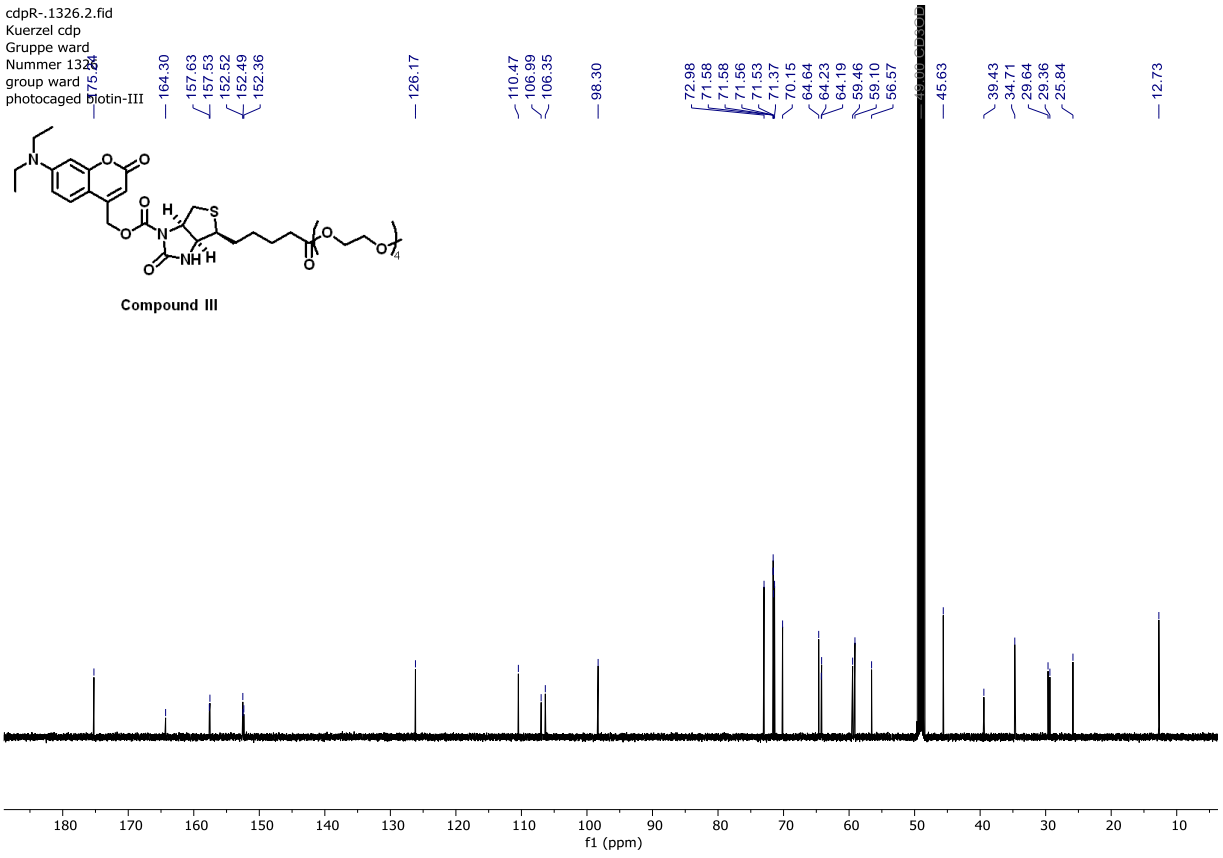

*A.4.7. LC-MS traces of the photocaged biotin derivatives **I** to **III**.*

Compound **I**

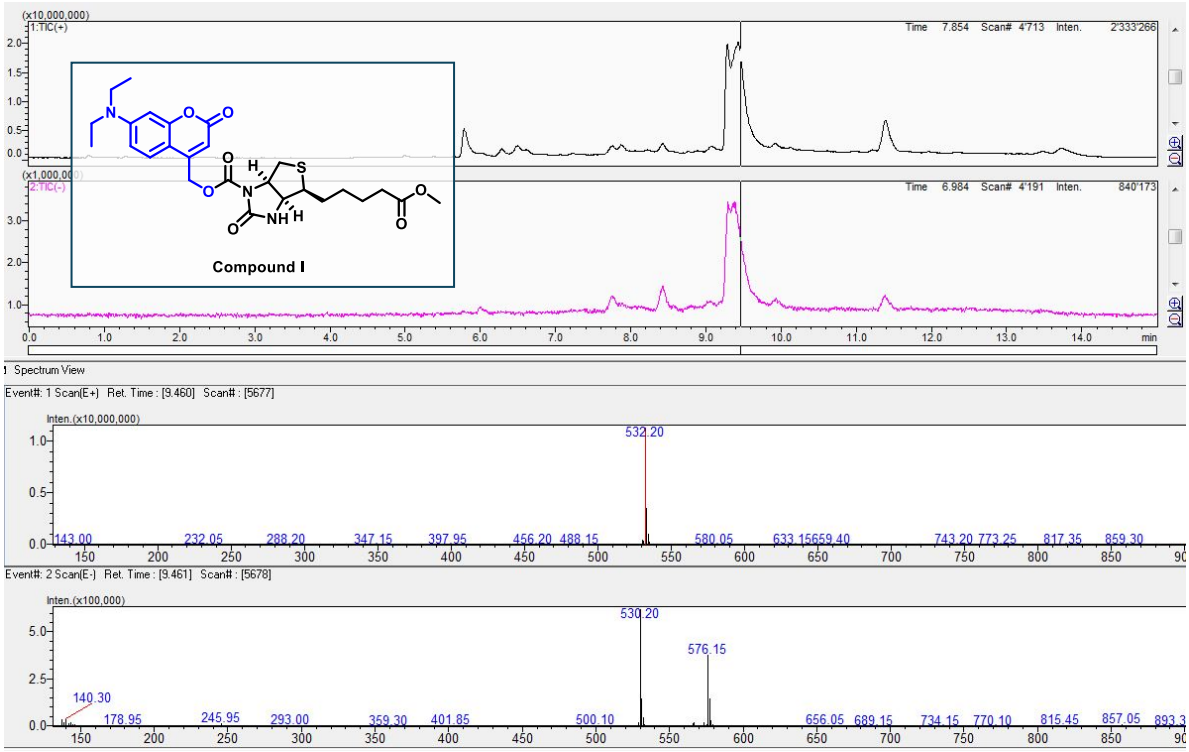

Compound **II**

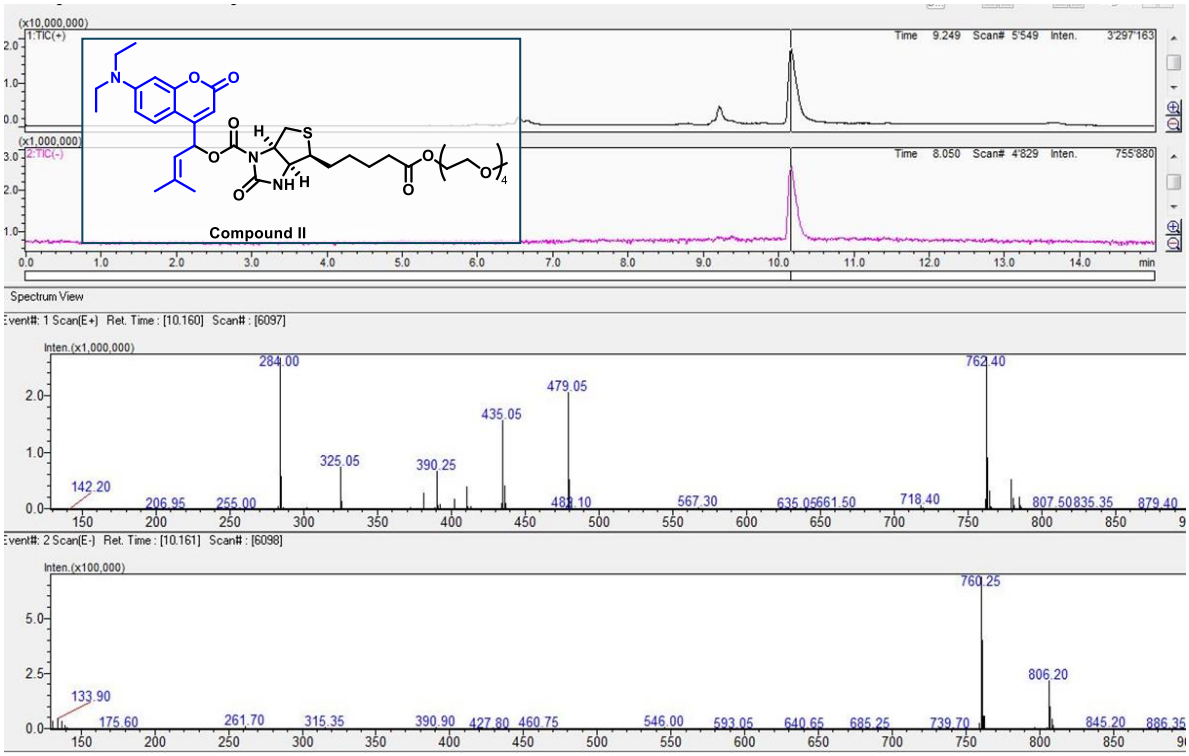

Compound **III**

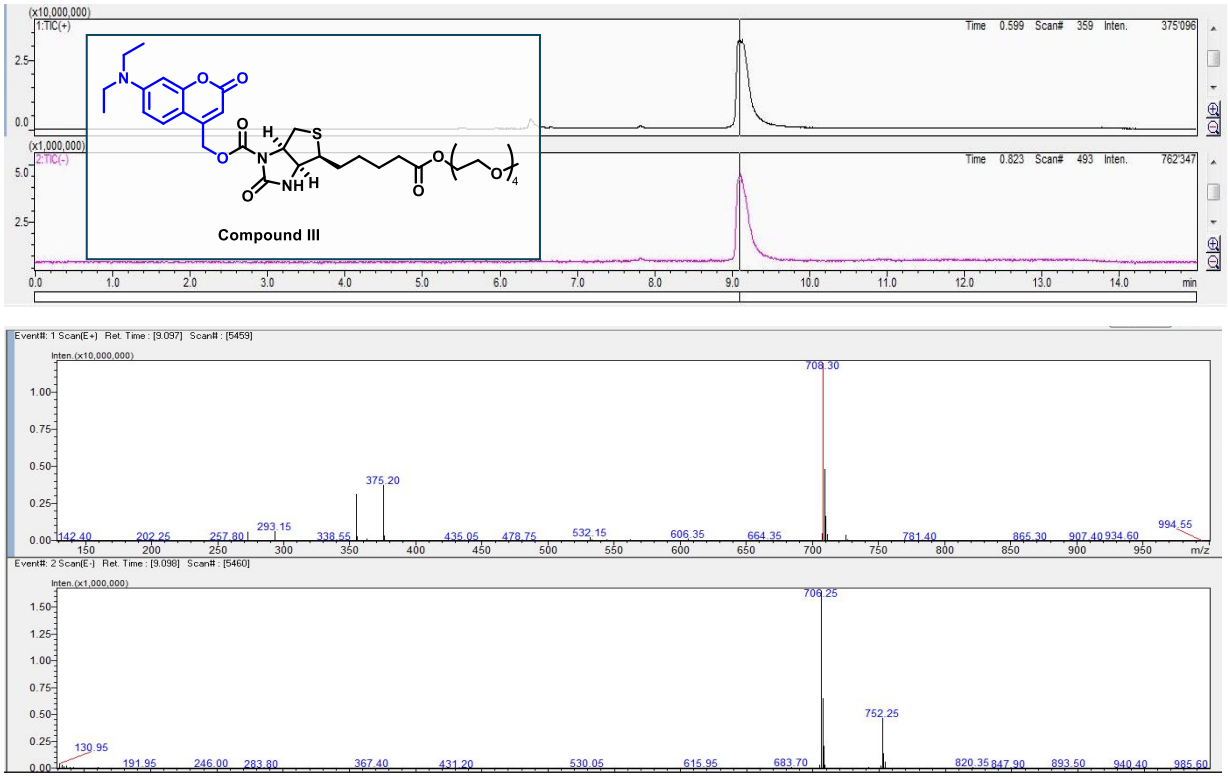

*A.4.8. Time-course experiment of uncaging efficiency of compound **I** after the irradiation with blue LED:*

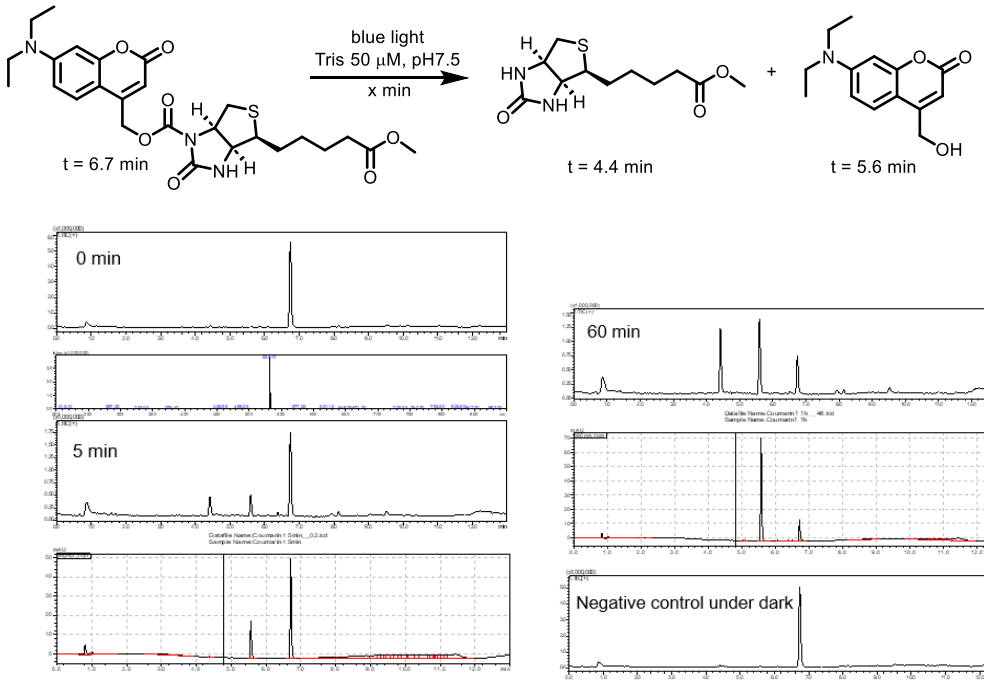

Decompostion of compound **I**. The product is unstable even under dark conditions.

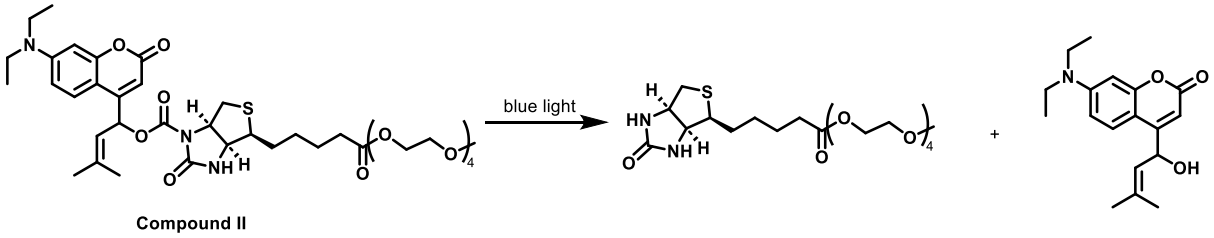

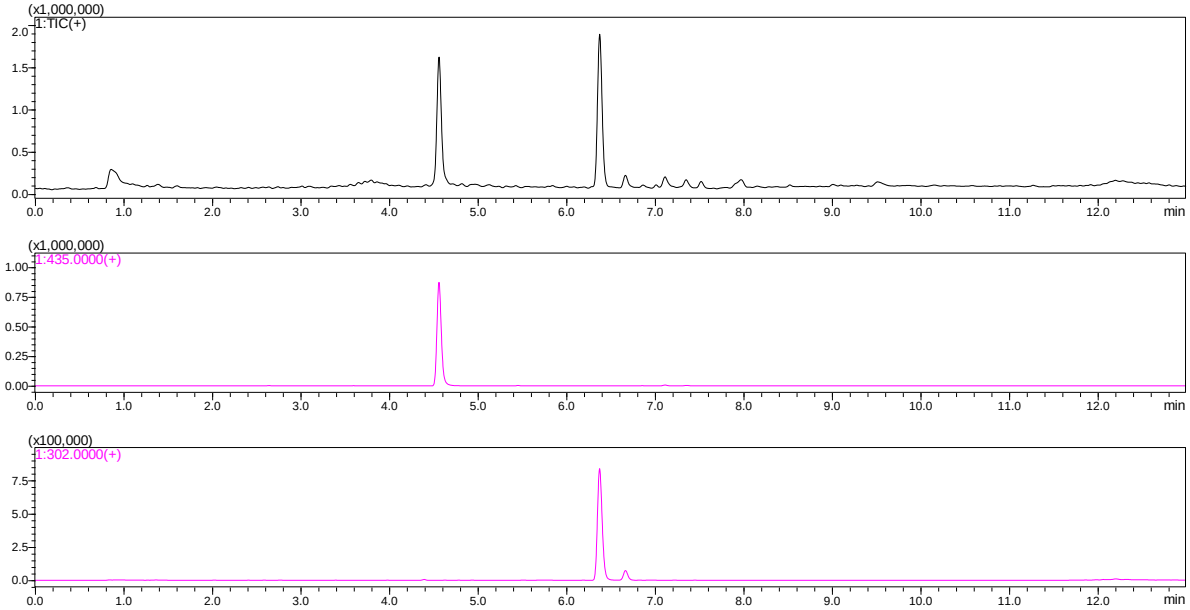

Reference:
(1) Chen, Y.-H. Signal Amplification and Detection of Small Molecules via the Activation of Streptavidin and Biotin Recognition. *Anal. Chem.* **2019**, *91*, 12461−12467. Schulte, A. M. Strategy for Engineering High Photolysis Efficiency of Photocleavable Protecting Groups through Cation Stabilization. *J. Am. Chem. Soc.* **2022**, *144*, 12421-12430.

5

Alternative Sample Delivery Methods: Extruder Jets

The following section has been published in
Nature Communications. ***2024***
DOI: 10.1038/s41557-023-01413-9
Contributions: Participated during the beamtime by preparing and loading the sample onto the beamline, managing the controls systems for alignment and running the jet, assisted with troubleshooting during the beamtime

Directed ultrafast conformational changes accompany electron transfer in a photolyase as resolved by serial crystallography

Andrea Cellini[1] , Madan Kumar Shankar[1,2], Amke Nimmrich[1,8], Leigh Anna Hunt [3], Leonardo Monrroy [2], Jennifer Mutisya[1,2], Antonia Furrer[4], Emma V. Beale[4], **Melissa Carrillo[4]**, Tek Narsingh Malla[5], Piotr Maj[1,2], Lidija Vrhovac[1,2], Florian Dworkowski[4], Claudio Cirelli[4], Philip J. M. Johnson[4], Dmitry Ozerov[4], Emina A. Stojković[6], Leif Hammarström[3], Camila Bacellar[4], Jörg Standfuss[4], Michał Maj[3], Marius Schmidt[5], Tobias Weinert[4], Janne A. Ihalainen[7], Weixiao Yuan Wahlgren[1,9] & Sebastian Westenhoff [1,2]

[1]Department of Chemistry and Molecular Biology, University of Gothenburg, Gothenburg, Sweden.
[2]Department of Chemistry – BMC, Uppsala University, Uppsala, Sweden.
[3]Department of Chemistry – Ångström Laboratory, Uppsala University, Uppsala, Sweden.
[4]Paul Scherrer Institut, Villigen, Switzerland.
[5]Physics Department, University of Wisconsin-Milwaukee, Milwaukee, WI, USA.
[6]Department of Biology, Northeastern Illinois University, Chicago, IL, USA.
[7]Department of Biological and Environmental Sciences, Nanoscience Center, University of Jyvaskyla, Jyvaskyla, Finland.
[8]Present address: Department of Chemistry, University of Washington, Seattle, WA, USA.
[9]Present address: Department of Chemistry and Molecular Biology and the Swedish NMR Centre, University of Gothenburg, Gothenburg, Sweden.
e-mail: sebastian.westenhoff@kemi.uu.se

Abstract

Charge-transfer reactions in proteins are important for life, such as in photolyases which repair DNA, but the role of structural dynamics remains unclear. Here, using femtosecond X-ray crystallography, we report the structural changes that take place while electrons transfer along a chain of four conserved tryptophans in the Drosophila melanogaster (6-4) photolyase. At femto- and picosecond delays, photoreduction of the favin by the frst tryptophan causes directed structural responses at a key asparagine, at a conserved salt bridge, and by rearrangements of nearby water molecules. We detect charge-induced structural changes close to the second tryptophan from 1 ps to 20 ps, identifying a nearby methionine as an active participant in the redox chain, and from 20 ps around the fourth tryptophan. The photolyase undergoes highly directed and carefully timed adaptations of its structure. This questions the validity of the linear solvent response approximation in Marcus theory and indicates that evolution has optimized fast protein fuctuations for optimal charge transfer.

The following section has been published in
Nature Communications. ***2023***
DOI: 10.1038/s41467-023-36481-5
Contributions: Assisted with crystallization and harvesting. Participated during the beamtime by preparing and loading the sample onto the beamline, managing the controls systems for alignment and running the jet, assisted with troubleshooting during the beamtime

Watching the release of a photopharmacological drug from tubulin using time-resolved serial crystallography

Maximilian Wranik[1], Tobias Weinert[1], Chavdar Slavov[2], Tiziana Masini[3], Antonia Furrer[1], Natacha Gaillard[1], Dario Gioia[3], Marco Ferrarotti[3], Daniel James[1], Hannah Glover[1], **Melissa Carrillo[1]**, Demet Kekilli[1], Robin Stipp[1], Petr Skopintsev[1], Steffen Brünle[1], Tobias Mühlethaler[1], John Beale[1], Dardan Gashi[4], Karol Nass[4], Dmitry Ozerov[5], Philip J. M. Johnson[4], Claudio Cirelli[4], Camila Bacellar[4], Markus Braun[2], Meitian Wang[4], Florian Dworkowski[4], Chris Milne[4], Andrea Cavalli[3,6], Josef Wachtveitl[2], Michel O. Steinmetz[1,7] & Jörg Standfuss[1]

[1]Division of Biology and Chemistry, Paul Scherrer Institut, 5232 Villigen, Switzerland.
[2]Institute of Physical and Theoretical Chemistry, Goethe University, Frankfurt am Main, Germany.
[3]Computational & Chemical Biology, Istituto Italiano di Tecnologia, 16163 Genova, Italy.
[4]Photon Science Division, Paul Scherrer Institut, 5232 Villigen, Switzerland.
[5]Scientific Computing, Theory and Data, Paul Scherrer Institut, 5232 Villigen, Switzerland.
[6]Department of Pharmacy and Biotechnology, University of Bologna, 40126 Bologna, Italy.
[7]Biozentrum, University of Basel, 4056 Basel, Switzerland.
e-mail: michel.steinmetz@psi.ch; joerg.standfuss@psi.ch

Abstract

The binding and release of ligands from their protein targets is central to fundamental biological processes as well as to drug discovery. Photopharmacology introduces chemical triggers that allow the changing of ligand affinities and thus biological activity by light. Insight into the molecular mechanisms of photopharmacology is largely missing because the relevant transitions during the light-triggered reaction cannot be resolved by conventional structural biology. Using time-resolved serial crystallography at a synchrotron and X-ray free-electron laser, we capture the release of the anti-cancer compound azo-combretastatin A4 and the resulting conformational changes in tubulin. Nine structural snapshots from 1 ns to 100 ms complemented by simulations show how cisto-trans isomerization of the azobenzene bond leads to a switch in ligand affinity, opening of an exit channel, and collapse of the binding pocket upon ligand release. The resulting global backbone rearrangements are related to the action mechanism of microtubuledestabilizing drugs.

The following section has been published in
Nature Communications. ***2023***
DOI: 10.1038/s41467-023-43523-5
Contributions: Participated during the beamtime by preparing and loading the sample onto the beamline, managing the controls systems for alignment and running the jet, assisted with troubleshooting during the beamtime

A multi-reservoir extruder for time-resolved serial protein crystallography and compound screening at X-ray free-electron lasers

Maximilian Wranik[1,12], Michal W. Kepa[1,12], Emma V. Beale[2,12], Daniel James[1], Quentin Bertrand[1], Tobias Weinert[1], Antonia Furrer[1], Hannah Glover[1], Dardan Gashi[2], **Melissa Carrillo[3]**, Yasushi Kondo[1], Robin T. Stipp[1], Georgii Khusainov[1], Karol Nass[4], Dmitry Ozerov[5], Claudio Cirelli[2], Philip J. M. Johnson[6], Florian Dworkowski[4], John H. Beale[4], Scott Stubbs[7], Thierry Zamofing[7], Marco Schneider[7], Kristina Krauskopf[8], Li Gao[8], Oliver Thorn-Seshold[8], Christoph Bostedt[2,9], Camila Bacellar[2], Michel O. Steinmetz[1,10], Christopher Milne[11] & Jörg Standfuss[1]

[1]Laboratory of Biomolecular Research, Division of Biology and Chemistry, Paul Scherrer Institut, Villigen-PSI, Villigen 5232, Switzerland.
[2]Laboratory for Synchrotron Radiation and Femtochemistry, Photon Science Division, Paul Scherrer Institut, Villigen-PSI, 5232 Villigen, Switzerland.
[3]Laboratory of Nanoscale Biology, Photon Science Division, Paul Scherrer Institut, Villigen-PSI, 5232 Villigen, Switzerland.
[4]Laboratory for Macromolecules and Bioimaging, Photon Science Division, Paul Scherrer Institut, Villigen-PSI, 5232 Villigen, Switzerland.
[5]Scientific Computing, Theory and Data Division, Paul Scherrer Institut, Villigen-PSI, 5232 Villigen, Switzerland.
[6]Laboratory for Nonlinear Optics, Photon Science Division, Paul Scherrer Institut, Villigen-PSI, 5232 Villigen, Switzerland.
[7]Large Research Facilities Division, Paul Scherrer Institut, Villigen-PSI, 5232 Villigen, Switzerland.
[8]Department of Pharmacy, LudwigMaximilians University of Munich, Butenandtstr. 7, Munich 81377, Germany.
[9]LUXS Laboratory for Ultrafast X-ray Sciences, Institute of Chemical Sciences and Engineering, École Polytechnique Fédérale de Lausanne (EPFL), CH-1015 Lausanne, Switzerland.
[10]Biozentrum, University of Basel, 4056 Basel, Switzerland.
[11]Femtosecond X-ray Experiments Instrument, European XFEL GmbH, Schenefeld, Germany.
[12]These authors contributed equally: Maximilian Wranik, Michal W. Kepa, Emma V. Beale. e-mail: maximilian.wranik@psi.ch; mwranik@stanford.edu; michal.kepa@psi.ch

Abstract

Serial crystallography at X-ray free-electron lasers (XFELs) permits the determination of radiation-damage free static as well as time-resolved protein structures at room temperature. Efficient sample delivery is a key factor for such experiments. Here, we describe a multi-reservoir, high viscosity extruder as a step towards automation of sample delivery at XFELs. Compared to a standard single extruder, sample exchange time was halved and the workload of users was greatly reduced. In-built temperature control of samples facilitated optimal extrusion and supported sample stability. After commissioning the device with lysozyme crystals, we collected timeresolved data using crystals of a membrane-bound, light-driven sodium pump. Static data were also collected from the soluble protein tubulin that was soaked with a series of small molecule drugs. Using these data, we identify low occupancy (as little as 30%) ligands using a minimal amount of data from a serial crystallography experiment, a result that could be exploited for structure-based drug design.

The following section is under review in
Nature.
Contributions: Participated during the beamtime by preparing and loading the sample onto the beamline, managing the controls systems for alignment and running the jet, assisted with troubleshooting during the beamtime

Direct observation of coherent azobenzene photochemistry

Tobias Weinert[1], Maximillian Wranik[1], Jonathan Church[2], Hans-Peter Seidel[1], Chavdar Slavov[3], Tiziana Masini[4], Daniel James[1], Hannah Glover[1], **Melissa Carrillo[1]**, Demet Kekilli[1], Robin Stipp[1], Petr Skopintsev[1], Steffen Brünle[1], Natacha Gaillard[1], Antonia Furrer[1], Dardan Gashi[5], Tobias Mühlethaler[1], John Beale[1], Karol Nass[5], Philip J.M. Johnson[5], Claudio Cirelli[5], Dmitry Ozerov[6], Florian Dworkowski[5], Camila Bacellar[5], Chris Milne[5], Michel O. Steinmetz[1,7], Josef Wachtveitl[3], Igor Schapiro[2], Joerg Standfuss[1*]

[1]Division of Biology and Chemistry, Paul Scherrer Institut, Villigen PSI, Switzerland.
[2]Institute for Chemistry, The Hebrew University of Jerusalem, Jerusalem, Israel
[3]Institute of Physical and Theoretical Chemistry, Goethe University, Frankfurt am Main, Germany.
[4]Computational & Chemical Biology, Instituto Italiano di Tecnologia, Genova, Italy. 5
[5]Photon Science Division, Paul Scherrer Institut, Villigen PSI, Switzerland.
[6]Scientific Computing, Theory and Data, Paul Scherrer Institut, Villigen PSI, Switzerland.
[7]Biozentrum, University of Basel, Basel, Switzerland.
Email: Joerg.standfuss@psi.ch

Abstract

Molecular photoswitches are versatile natural or synthetic molecules that undergo reversible conformational changes in response to light. In chemistry azobenzenes act as ubiquitous synthetic photoswitches1 with applications ranging from opto-electronics2, over molecular machines3 to photopharmacology4 . Their isomerization mechanism defines their molecular properties and yet is controversially debated, as the underlying ultrafast photochemistry is challenging to resolve in time and space. In this study, we have used an X-ray Free Electron Laser to observe coherent structural transitions in the prototypical photoswitch azocombretastatin A4 bound to its protein target tubulin. A molecular movie assembled from a crystallographic femtosecond scan and snapshots of kinetic intermediates in the femto-tonanosecond range show how the cis isomer overcomes energy barriers in the excited state, traverses the conical intersection into a twisted ground state conformation, cools, stretches and finally relaxes into a planarized trans conformer. Our crystallographic data at near-atomic resolution contrasted with femtosecond transient absorption spectroscopic data and quantum chemical trajectories provides an experimental and theoretical description of the ultrafast azobenzene photoreaction. These fundamental insights reveal surprising parallels between natural and synthetic photoswitches opening a route for the design of artificial photoswitching proteins.

The following section has been submitted to
Nature Communications.
Contributions: Participated during the beamtime by preparing and loading the sample onto the beamline, managing the controls systems for alignment and running the jet, assisted with troubleshooting during the beamtime

Photochemical affinity switches to resolve ligand dissociation from a G5 protein-coupled receptor by time-resolved serial crystallography

Hannah Glover[1], Torben Sassmannshausen[2], Quentin Bertrand[1], Matilde Trabuco[3], Chavdar Slavov[2], Arianna Bacchin[3], Fabio Andres[3], Yasushi Kondo[1], Robin Stipp[1], Maximilian Wranik[1], Georgii Khusainov[1], **Melissa Carrillo[1]**, Demet Kekilli[1], Jie Nan[5], Ana Gonzalez[5], Robert Cheng[3], Werner Neidhart[3], Tobias Weinert[1], Filip Leonarski[6], Florian Dworkowski[6], Michal Kepa[1], Josef Wachtveitl[2], Michael Hennig[3], Joerg Standfuss[1,*]

[1]Division of Biology and Chemistry, Paul Scherrer Institut, Villigen PSI, Switzerland
[2]Institute of Physical and Theoretical Chemistry, Goethe University, Frankfurt, Germany
[3]LeadXpro Biotech AG, Park Innovaare, Villigen PSI, Switzerland
[4]Department of Chemistry, University of South Florida, Tampa, United States
[5]MaxIV Laboratory, Lund University, Lund, Sweden
[6]Photon Science Division, Paul Scherrer Institut, Villigen PSI, Switzerland
Email: Joerg.standfuss@psi.ch

Abstract

G protein-coupled receptors (GPCRs) are the largest family of cell surface receptors in humans and are important drug targets. Inherent conformational dynamics allow them to adopt various functional states, tuned by ligand binding. We designed seven photochemical affinity switches derived from the anti-Parkinson's drug istradefylline, to study the dynamics of ligand dissociation from the human adenosine A2A receptor. The new ligands were characterized by UV/Vis spectroscopy, time-resolved absorption spectroscopy, differential scanning fluorimetry, cryo-crystallography and time-resolved serial crystallography. Our findings provide a foundation for selecting photoswitchable ligands to study protein-ligand interaction dynamics in proteins lacking endogenous light triggers. Probing millisecond-scale dynamics of selected ligand-receptor complexes revealed how a single methyl group alteration shifted the position of istradefylline derivatives after photoisomerization. The corresponding changes in hydrogen bonding networks disrupt an interaction between extracellular loops 2 and 3 that act as a lid regulating ligand confinement within the binding pocket. This original approach to study GPCR dynamics on the atomic level may contribute to the development of innovative compounds for pharmaceutical interventions.

6

Conclusion

Time-resolved serial crystallography (TR-SX) for dynamic studies of bio-molecular interactions is a powerful but also challenging emerging technique. The ability to perform successful experiments is dependent on different workgroups and disciplines working reliably and effectively in coordination with each other. Components such as reliability of sample delivery methods, precision of sample location in regard to the X-ray beam, quality of the crystalline sample as well as the characteristics of biological system investigated are crucial for a successful time-resolved experiment. This PhD thesis covers contributions to different areas within time-resolved serial crystallography such as endeavors ranging from experimental support during beamtimes using extruder jets as the sample delivery method for TR-SX to the development and implementation of a novel polymer-based fixed-target sample delivery method to the investigation on a photocaged biotin – streptavidin system for time resolved measurements.

The development, commissioning, and implementation of the MIcro-Structure Polymer-based fixed-target (MISP-chip) for SwissFEL's newly constructed experimental station Cristallina-MX marks a significant advancement in the capabilities of sample delivery methods for time-resolved serial crystallography. The MISP-chip is classified as an aperture-aligned fixed-target which is composed of a membrane containing pre-determined wells optimally designed for the deposition of crystal samples. Such a membrane allows for an optimized hit-rate, decrease in sample consumption and waste, and minimized crosstalk in pump-probe experiments by providing an optical barrier between deposited crystals. The chip is designed to facilitate an effective and optimized alignment procedure at the beamline. With the collaboration of the beamline scientists at Cristallina-MX, the development and optimization of the corner fiducials were carried out during the commissioning of the chip and beamline in order to assure precise alignment. Due to its polymer-based membrane, this fixed-target offers durability, user-friendliness, reusability, and is cost-effective during production.

The MISP-chip has now become the working horse for SwissFEl's Cristallina-MX and has been distributed to various facilities in the world for potential usage at other beamlines.

In addition, advancements were done to study the binding of biotin to streptavidin. A streptavidin variant, known as T7-SA, was used in this study, demonstrating ideal micro-crystallization properties suitable for time-resolved experiments. Due to its noticeable axis expansion upon the binding of biotin, this system became ideal for fast onsite analysis. The closure of its binding loop is visible, however since the C-terminus tail tucks into the binding pocket in its apo state, it causes issues distinguishing the binding of biotin from the C-terminus tail. It is hypothesized that the reason why crystals dissolve upon soaking of biotin is due to the ~10Å expansion in the C-axis upon biotin binding within the pocket. To resolve this issue, we soaked the crystals with glutaraldehyde serving as a crosslinker. As a result, we were able to demonstrate that crosslinking the crystals with glutaraldehyde does not hinder biotin binding and molecular movement. On the contrary, it allowed binding experiments to proceed, serving as a potential strategy also for other systems to use. In order to conduct pump-probe studies, as a way to capture the binding events of biotin to streptavidin, three photocage biotin derivates were developed and synthesized. Reasonable solubility was obtained by linking a PEG-tail the photocaged biotin derivatives, which showed a range of wavelengths suitable for XFELs. However, additional refinement is required to enhance uncaging efficiency. Overall, the investigated system demonstrated a great potential for elucidating the binding interactions of biotin and streptavidin.

7

Curriculum Vitae

Melissa Carrillo

Education

Ph.D., Nanoscience
May, 2024
Paul Scherrer Institute & University of Basel
Villigen, Switzerland
Thesis: Sample delivery development for serial crystallography at XFELs and synchrotrons: micro-structured, polymer based, fixed-targets and their applications for crystallography
Supervisor: Dr. Celestino Padeste, Dr. Thomas Ward

M.Sc., Biology
May, 2020
Northeastern Illinois University (NEIU)
Chicago, IL
Thesis: Development of myxobacterial phytochrome as a model system for X-ray Free Electron Lasers (XFELs)
Supervisor: Dr. Emina Stojkovic

BASc, Biology
May, 2016
University of Illinois at Chicago (UIC)
Chicago, IL

Research Experience

Graduate Student
Oct. 2020 – March 2024
Paul Scherrer Institute (PSI)
Laboratory of Nanoscale Biology

- Successfully designed, developed, produced, tested, and commissioned micro-structured, polymer-based, fixed-targets for serial crystallography.
- Assisted with commissioning beamtimes of SwissFEL's newly constructed beamline for serial protein crystallography on fixed-targets.
- Provided user support for internal and external beamtimes at SwissFEL and Swiss Light Source (SLS).
- Conducted beamtimes at Swiss Light Source (SLS), SwissFEL, Linac Coherent Light Source (LCLS), Pohang Accelerator Laboratory (PAL) and European XFEL (EuXFEL) through protein crystallization, sample preparation and data collection, on soluble and membrane proteins.
- Crystallized protein, soaked and co-crystallized ligands and protein crystals, harvesting crystals for cryo and room temperature crystallography at synchrotrons, cryo-cooled crystals, collected cryo and room temperature data at SLS and pump-probe TR-SX data at SwissFEL on binding activities of soaked photocaged biotin onto streptavidin, processed and analyzed synchrotron and FEL data.

Research Assistant **May 2018 – Aug. 2020**	**Northeastern Illinois University** **Biology Department** • Expression and protein purification, crystallization and optimization, crystal harvesting for cryo and room temperature crystallography at synchrotrons, micro-crystallization, trained students, created crystallization protocols, coordinated beamtimes and shipments. • Collected data at the Advanced Photon Source (APS) – Sectors 14 & 19 and Spring-8 Angstrom Compact free electron Laser (SACLA).
Research Coordinator **Feb. 2017 – May 2017**	**University of Chicago Medicine Comer's Children Hospital** **Pediatric Intensive Care Unit** • Effectively communicated with families, providers, and medical staff to efficiently coordinate study. Met deadlines and consistently exceeded expectations for timely data collection, coding, and submissions. Collaborated with medical staff to build and manage treatment plans. Coded and analyzed data.
Research Intern **Jan. 2016 – May 2016**	**University of Illinois at Chicago** **Jane Addams College of Social Work** • Transcribed both Spanish and English interviews for future coding. Coded data and preformed data analysis.
Research Intern **Aug. 2014-Aug. 2015**	**Feinberg School of Medicine** **Department of Medical Social Sciences** • Developed research aims and research structure for a psychosocial research study on primary outcomes, health-related quality of life and symptom burden among Hispanic breast cancer patients to develop a smartphone psychoeducational and psychosocial intervention program. • Created protocols, assessments, questioners, and coding books. Trained, guided, and evaluated new interns, screened patients, coded interviews, data analysis.
Researcher **Aug. 2012-May 2013**	**University of Illinois at Chicago** **Latino Recruitment and Academic Assistance Program** • Conducted independent research on holistic vs western healthcare practices of Mexican migrants and their Mexican-American children to understand healthcare outcomes within this community. • Created protocols, assessments, questioners, and coding books. Screened patients, conducted both Spanish and English interviews, translated, transcribed, and coded interviews, performed data analysis.

Key Research Skills

Protein Chemistry	Expression and purification of proteins. Enzyme assay design. Western blot analyses.
Protein Crystallography	Crystallization methods (manual, mosquito). Co-crystallization and soaking of ligands. Optimization of single protein crystals into micro-crystal slurries for serial X-ray diffraction. Crystal harvesting/cryo-cooling for synchrotron data collection. Ligand soaking for crystals.
X-ray Crystallography	Single crystal rotation and serial data collection on cryo and room temperature samples at synchrotrons and XFELs. Experience with fixed-targets, liquid and viscous jetting, and rotation data collections. Data processing, model building and structural analysis. User support at SwissFEL and Swiss Light Source (SLS).
Micro-Fabrication & Polymer Processing	Designed and developed SwissFEL's Micro-Structures Polymer fixed-targets (MISP-chips). Laser lithography, reactive ion etching, KOH etching, hot embossing, 3D printing.
Synchrotrons & XFELs	User support for: SwissFEL's CristallinaMX serial- and time-resolved serial crystallography beamtime with fixed-targets, SwissFEL's Alvra and Bernina beamtimes with viscous extruder jet, SLS VESPA beamtime with extruder jet, SLS PX1 and PX2 cryo beamtime with chips and loops, SLS acoustic levitator with droplet ejector diffusion study beamtime. Supported on membrane, soluble and anerobic samples.
Facilities Used	APS, SLS, ESRF, MAX IV, SACLA, SwissFEL, PAL, LCLS, EuXFEL
Languages	English, Spanish

Publications

2024	Cellini, A., Shankar, M.K., Nimmrich, A., Mutisya, J., Furrer, A., Beale, E., **Carrillo, M.**, Malla, T.N., Maj, P., Vrhovac, L. and Dworkowskic, F., …, Westenhoff, S., *Directed ultrafast conformational changes accompany electron transfer in a photolyase as resolved by seral crystallography.* Nature Communications
2024 (Accepted)	Gotthard, G.*, Flores-Ibarra, A.*, **Carrillo, M.** *, Kepa, M., Mason, T.J., Stegmann, D., Olasz, B., Pachota, M., Dworkowski, F., …, Nogly, P., *Fixed-target time-resolved crystallography at XFELs: the scourge of light contamination but reduced sample consumption.* IUCrJ
2024 (Submitted)	Glover, H., Sassmannshausen, T., Bertrand, Q., Trabuco, M., Slavov, C., Bacchin, A., Andres, F., Kondo, Y., Stipp, R., Wranik, M., Khusainov, G., **Carrillo, M.**, … Standfuss, J.,

Photochemical affinity switches to resolve ligand dissociation from a G protein-coupled receptor by time-resolved serial crystallography. Nature Communications

2023 **Carrillo, M.**, Mason, T.J., Karpik, A., Martiel, I., Kepa, M.W., McAuley, K.E., Beale, J.H. and Padeste, C., 2023. *Micro-structured polymer fixed targets for serial crystallography at synchrotrons and XFELs.* IUCrJ, 10(6).

2023 Wranik, M., Weinert, T., Slavov, C., Masini, T., Furrer, A., Gaillard, N., Gioia, D., Ferrarotti, M., James, D., Glover, H., **Carrillo, M.**, …, Standfuss, J., *Watching the release of a photopharmacological drug from tubulin using time-resolved serial crystallography.* Nature Communications, 14(1), p.903.

2023 Wranik, M., Kepa, M., Beale, E., James, D., Bertrand, Q., Weinert, T., Furrer, A., Glover, H., Gashi, D., **Carrillo, M.**, Kondo, Y., …, Standfuss, J., *A multi-reservoir extruder for time-resolved serial protein crystallography and compound screening at X-ray free-electron lasers.* Nature Communications, 14(1), p7956.

2023 (Under Review) Weinert, T., Wranik, M., Church, J., Seidel, H., Slavov, C., Masini, T., James, D., Glover, H., **Carrillo, M.**, Kekilli, D., Stipp, R., …, Standfuss, J., *Direct observation of coherent azobenzene photochemistry.* Nature

2021 Kraskov, A., Buhrke, D., Scheerer, P., Shaef, I., Sanchez, J.C., **Carrillo, M.**, Noda, M., Feliz, D., Stojković, E.A. and Hildebrandt, P. *On the role of the conserved histidine at the chromophore isomerization site in phytochromes.* The Journal of Physical Chemistry B, 125(50), pp.13696-13709.

2021 **Carrillo, M.**, Pandey, S., Sanchez, J., Noda, M., Poudyal, I., Aldama, L., Malla, T.N., Claesson, E., Wahlgren, W.Y., Feliz, D., Šrajer, V., ..., Schmidt, M. *High-resolution crystal structures of transient intermediates in the phytochrome photocycle*. Structure, 29(7), pp.743-754.

2020 Claesson, E., Wahlgren, W.Y., Takala, H., Pandey, S., Castillon, L., Kuznetsova, V., Henry, L., Panman, M., **Carrillo, M.**, Kübel, J., Nanekar, R., ..., Westenhoff, S. *The primary structural photoresponse of phytochrome proteins captured by a femtosecond X-ray laser.* Elife, 9, p.e53514.

2019 Sanchez, J.C., **Carrillo, M.**, Pandey, S., Noda, M., Aldama, L., Feliz, D., Claesson, E., Wahlgren, W.Y., Tracy, G., Duong, P., Nugent, A.C., ..., Stojkovic, E. *High-resolution crystal structures of a myxobacterial phytochrome at cryo and room temperatures.* Structural Dynamics, 6(5).

Conferences

2023	**Carrillo, M.** *Micro-structured Polymer Based Fixed-Targets (MISP-Chips) for Serial Crystallography at Synchrotrons and XFELs.* American Crystallography Association Conference **(Oral Presentation – Student Lecturer Award)**
2023	**Carrillo, M.** *The use of fixed-targets for biological applications.* DESY Photon Science User Meeting European XFEL Users 2023 **(Invited speaker)**
2023	**Carrillo, M.** Micro-patterned, polymer based fixed-targets for serial crystallography at synchrotrons and XFELs. IUCr Conference. (Poster)
2022	**Carrillo, M.** *Fixed-targets for Protein Dynamic Studies at SwissFEL,* BioXFEL (Poster)
2022	**Carrillo, M.** *Fixed-targets for Serial Crystallography at SwissFEL,* American Crystallography Association Conference, (Poster)
2022	**Carrillo, M.** *Fixed-targets for Serial Crystallography at SwissFEL,* Swiss Nanoconvention (Poster)
2021	**Carrillo M.** *Towards Molecular Movies: Studying Protein Binding Dynamics at SwissFEL,* 6th European Crystallography School (Poster)
2020	**Carrillo M**. *Time Resolved SRX on a Classical Phytochrome from S. aurantiaca.* BioXFEL (Poster)
2019	**Carrillo M**. *Crystal Structures of a Phytochrome from the Non-Photosynthetic Myxobacterium S. aurantiaca.* Northeastern Illinois University 27th Annual Student Symposium (Poster)
2019	**Carrillo M**. *Crystal Structures of a Phytochrome from the Non-Photosynthetic Myxobacterium S. aurantiaca.* Presented at BioXFEL (Poster)
2016	**Carrillo M.** *Adherence to Endocrine Therapy among Hispanic Women: Finds from a Pilot Study*. Lewis Landsberg Research Day (Poster)
2016	**Carrillo M.** *Adherence to Endocrine Therapy among Hispanic Women: Finds from a Pilot Study*. UIC's Student Research Forum (Poster)
2013	**Carrillo M.** *From Traditional to Western Medicine: Health Care Practice Among Mexican Americans.* Illinois African American and Latino Higher Education Alliance (IALHEA) (Poster)